Global- and local-scale environmental change in an ancient high-elevation lake basin; carbonates and microbialites from the latest Cretaceous to middle Eocene Sheep Pass Formation, Nevada, USA

by

JULIANA OLSEN-VALDEZ

B.A., Lawrence University, 2018

A thesis submitted to the

Faculty of the Graduate School of the

University of Colorado in partial fulfillment

of the requirement for the degree of

Doctor of Philosophy

Department of Geological Sciences

2025

Committee Members:

Kathryn Snell

Elizabeth Trower

Thomas Marchitto

Miquela Ingalls

Isabella Oleksy

Abstract

Olsen-Valdez, Juliana (Ph.D., Geological Sciences)

Global- and local-scale environmental change in an ancient high-elevation lake basin; carbonates and microbialites from the latest Cretaceous to middle Eocene Sheep Pass Formation, Nevada, USA

Thesis directed by Professors Kathryn Snell and Elizabeth Trower

The Sheep Pass Formation type section in east-central Nevada preserves lacustrine (lake), palustrine (wetland), and microbialite carbonates deposited within a high-elevation lake basin between the latest Cretaceous and middle Eocene. This interval spans a pivotal time in geologic history; it encompasses the Cretaceous-Paleogene (K-Pg) mass extinction, as well as long-term greenhouse conditions and rapid warming events that serve as some of our best analogs for future climate change under un-mitigated anthropogenic warming. Understanding terrestrial records from this time contributes an invaluable perspective beyond the better-constrained marine realm. However, continental settings are complex and variable, requiring a diverse range of paleoenvironmental proxies and settings to holistically describe this climate response on land.

Characterizing the carbonate sedimentology and stable isotope geochemistry of the Sheep Pass Formation type section has the potential to provide a nuanced record of environmental change in a high-elevation setting during this crucial past climate interval. My dissertation work combines transmitted light and cathodoluminescence petrography, X-ray diffraction mineralogy, and various stable isotope geochemistry tools ($\delta^{13}C$, $\delta^{18}O$, and Δ_{47}) to describe the paleoenvironmental trends preserved in the

Sheep Pass Basin. I find that the Sheep Pass Formation type section preserves a dynamic and sensitive lake basin due to its small size, with evidence that microbialites – lithified microbial mats – thrived in place of a more complex metazoan food web. I also find sedimentological and geochemical evidence for the potential expression of both long-term and short-term global climate signals, including warming from the late Paleocene to early Eocene, as well as abrupt climate transitions like the K-Pg boundary and early Paleogene hyperthermal climate events. Lastly, carbonate microbialites from the Sheep Pass Formation type section preserve geochemical evidence for local-scale photosynthetic carbon cycling, similar to both modern and modeled observations. In full, this work highlights that the careful characterization of ancient carbonates from the Sheep Pass Formation type section reveals a new and unique record of global- and local-scale environmental change during an important geologic climate interval.

Acknowledgements

My family – composed of friends, siblings, parents, my beloved partner and our dog, lab mates, science community members and mentors, my incomparable advisors, and so many others – has worked in both direct and often invisible ways to get me to this point. They have shaped me and, therefore, this PhD; I write this with so much love and gratitude for all of them. Thank you also to my thoughtful and encouraging committee members and the Geological Sciences department staff for the immeasurable amount of time and energy they have poured into this effort.

Table of Contents

List of Tables

List of Figures

Chapter I: Introduction

Characterizing the evolution of the earth – including its climate and biosphere – over geologic time is a fundamental objective for the field of Geology. As we face dramatic environmental and ecosystem change in response to anthropogenic warming (10-100s yrs), looking to the geologic past provides a long-term perspective (kyrs to myrs and more) on the response of diverse environments to changing climate. These comparisons ultimately strengthen predictions for the modeled trajectory of future climate, providing invaluable context for the policy choices and mitigation actions we need to make.

The Cenozoic era (66 Ma to present) is one of the best studied geologic time intervals because it encompasses the recent geologic past and preserves a range of global climate states, from ice ages to major warming events (Fig. 1; Zachos et al., 2001, 2008; Westerhold et al., 2020; The Cenozoic CO Proxy Integration Project (CenCOPIP) Consortium et al., 2023). The most comprehensive records for this time come from deep ocean cores and sea surface proxies, which provide an exceptional marine perspective on global climate change over the last ~66 million years (Westerhold et al., 2020). The Paleocene (~66-56 Ma) and Eocene (~56-34 Ma) epochs (i.e., the early Paleogene) have received particular attention because they reflect global mean temperatures not unlike what we may expect in the next hundred years given certain climate projections (Burke et al., 2018; Westerhold et al., 2020).

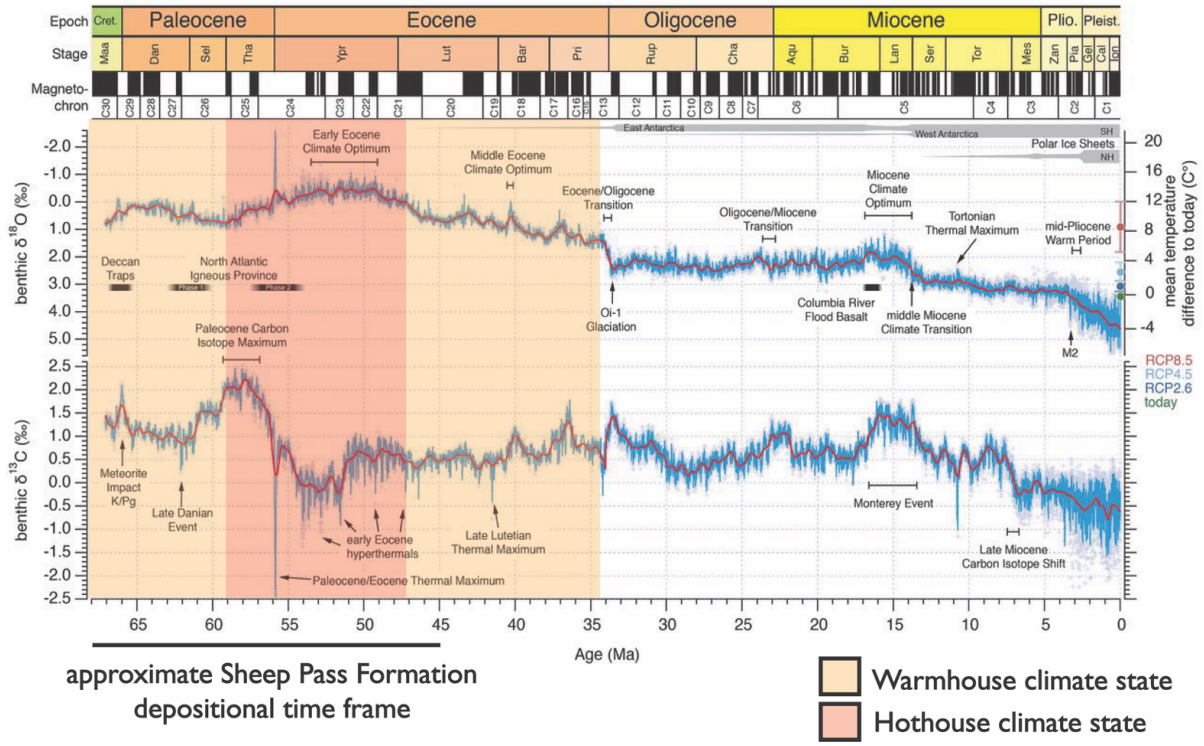

Figure 1-1: Benthic stable carbon and oxygen isotopes across the Cenozoic era highlighting warmhouse and hothouse climate states that characterized the Paleocene and Eocene (modified from Westerhold et al., 2020).

The early Paleogene includes both warmhouse and hothouse climate states, including long-term warming in the Paleocene that made way for the Early Eocene Climatic Optimum, the period of most sustained warmth during the entire Cenozoic. Superimposed on this warming trend were transient (<100 kyrs) hyperthermal climate events characterized by increased pCO_2 and abrupt warming at a time scale most similar (though still orders of magnitude longer) to what we are observing today (Fig. 1-1; Zachos et al., 2001, 2008; Pagani et al., 2014; Westerhold et al., 2020; The Cenozoic CO Proxy Integration Project (CenCOPIP) Consortium et al., 2023).

Terrestrial (on land) records from this time are especially important because they provide the best analogs for characterizing climate-driven environmental change in settings where much of the population lives today. They also refine our understanding of climate change in continental settings, which respond differently and more variably compared to the marine realm, making it difficult to accurately model terrestrial environments (Thrasher and Sloan, 2009; Byrne and O'Gorman, 2015; Carmichael et al., 2016).

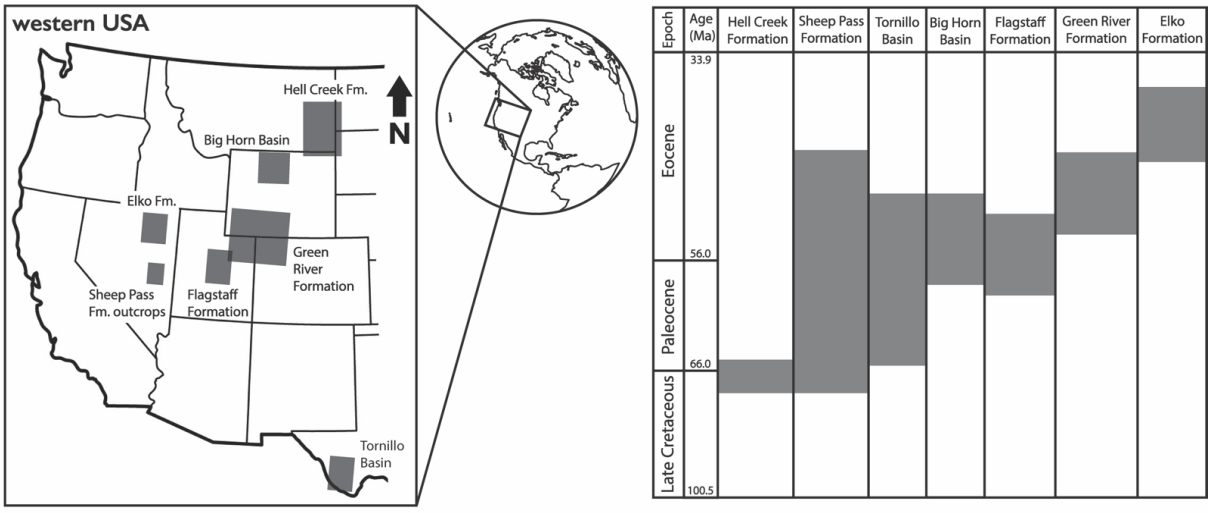

Figure 1-2: Geographic and temporal distribution of notable Late Cretaceous, Paleocene, and Eocene sedimentary basins in the western USA.

The western United States (western USA) is one of the most extensively studied regions with respect to early Paleogene terrestrial climate records. It preserves several sedimentary basins spanning the Late Cretaceous through middle Eocene (Fig. 2). Most of these basins have been well-characterized and provide detailed records of paleobiological, paleohydrological, and paleotemperature change in response to global climate during this time, especially hyperthermal climate events

and extreme warmth in the early Eocene (PETM; Wilf, 2000; Wilf et al., 2003; Kraus et al., 2013; Frantz et al., 2014; Widlansky et al., 2022). The Sheep Pass Formation type section in east-central Nevada is one of these western USA archives. It's existing age framework suggests it spanned this full climate interval, from the Late Cretaceous through middle Eocene (Druschke et al., 2009a), meaning it has the potential to preserve a more continuous record of climate change during this time. It is also unique in that it reflects a high-elevation setting compared to most of these other western USA records. The range of its depositional time frame and high-elevation perspective, as well as its context within a well-constrained comparative framework of both coeval marine and regional terrestrial records provides a promising opportunity to investigate the expression of climate in the Sheep Pass Formation, with the potential for the creation of a new paleoclimate record spanning an important geologic climate interval.

The primary goal of this dissertation is to characterize the sedimentological and geochemical expression of local- and global-scale processes on the Sheep Pass lake basin. The best paleoclimate records are rooted in a detailed sedimentological and stratigraphic framework. In Chapter 2, I describe the sedimentology, stratigraphy, and environmental evolution of the >1 km-thick Sheep Pass Formation across two measured transects. I find that the Sheep Pass Formation records a dynamic and sensitive lake basin setting where microbialites – microbially-associated sedimentary deposits – thrived in place of a more complex metazoan food web. I also identify four stratigraphic intervals that preserve notable environmental change,

reflecting the most promising target points for future chemo- and chronostratigraphic studies.

In Chapter 3, I pair this detailed sedimentological framework with geochemical records of carbon and oxygen, as well as paleotemperatures from carbonate clumped isotopes spanning the full range of sedimentary facies in the Sheep Pass Formation type section. These stratigraphically comprehensive records are the first of their kind in the Sheep Pass Formation. Comparison of their trends to global marine and regional terrestrial records, aided by the application of a dynamic time warping algorithm for stratigraphic correlation, indicates that both long-term and short-term climate signals may be expressed in the Sheep Pass Basin. First, an interval of gradual warming in the Sheep Pass Formation most likely corresponds to warming in the later Paleocene and early Eocene, possibly punctuated by short-term hyperthermal climate events during this time. Peak warming in the Sheep Pass Basin is also associated with sedimentological and geochemical evidence for drying, which has been recognized in other western USA records from this time. Further, a marked shift in both carbon isotopes and clumped isotope temperature estimates in the lower part of the Sheep Pass Formation type section appears most similar to short-term climate signals from around the K-Pg boundary.

In Chapter 4, I focus in on the isotopic signals preserved within the Sheep Pass Formation microbialites. I leverage the carbon isotopic composition of distinct textural components in these carbonate microbialites, identifying an isotopic 'biosignature' of photosynthetic carbon cycling. I interpret that the consistent fabric-

driven carbon isotope variations are the product of microbial metabolisms influencing the dissolved inorganic carbon pool in the micro-environment around these mats as they lithified. These carbon isotope results are compelling because they preserve similar magnitudes to values documented in modern microbialite-forming lakes around the world, and they indicate that the Sheep Pass Formation type section captures local-scale geobiological processes in addition to global-scale climate change, the former of which is often hard to preserve and/or measure in the geologic record.

This range of spatial scales that biological and physicochemical change is expressed in the Sheep Pass Formation type section is an exciting finding. It highlights that the high-elevation Sheep Pass Basin preserves a complex paleoenvironmental and paleoclimatic record for this time. This work provides nuance for climate model inputs and data-model comparisons, paves the way for future investigations into the specific role of elevation in shaping these records, and continues to build our understanding of the response of terrestrial (and high-elevation) settings to greenhouse climate in the past, present, and future.

1.1 Works Cited

Burke, K.D., Williams, J.W., Chandler, M.A., Haywood, A.M., Lunt, D.J., and Otto-Bliesner, B.L., 2018, Pliocene and Eocene provide best analogs for near-future climates: Proceedings of the National Academy of Sciences, v. 115, p. 13288–13293, doi:10.1073/pnas.1809600115.

Byrne, M.P., and O'Gorman, P.A., 2015, The Response of Precipitation Minus Evapotranspiration to Climate Warming: Why the "Wet-Get-Wetter, Dry-Get-Drier" Scaling Does Not Hold over Land*: Journal of Climate, v. 28, p. 8078–8092, doi:10.1175/JCLI-D-15-0369.1.

Carmichael, M.J. et al., 2016, A model–model and data–model comparison for the early Eocene hydrological cycle: Climate of the Past, v. 12, p. 455–481, doi:10.5194/cp-12-455-2016.

Druschke, P., Hanson, A.D., and Wells, M.L., 2009, Structural, stratigraphic, and geochronologic evidence for extension predating Palaeogene volcanism in the Sevier hinterland, east-central Nevada: International Geology Review, v. 51, p. 743–775, doi:10.1080/00206810902917941.

Frantz, C.M., Petryshyn, V.A., Marenco, P.J., Tripati, A., Berelson, W.M., and Corsetti, F.A., 2014, Dramatic local environmental change during the Early Eocene Climatic Optimum detected using high resolution chemical analyses of Green River Formation stromatolites: Palaeogeography, Palaeoclimatology, Palaeoecology, v. 405, p. 1–15, doi:10.1016/j.palaeo.2014.04.001.

Kraus, M.J., McInerney, F.A., Wing, S.L., Secord, R., Baczynski, A.A., and Bloch, J.I., 2013, Paleohydrologic response to continental warming during the Paleocene–Eocene Thermal Maximum, Bighorn Basin, Wyoming: Palaeogeography, Palaeoclimatology, Palaeoecology, v. 370, p. 196–208, doi:10.1016/j.palaeo.2012.12.008.

Pagani, M., Huber, M., and Sageman, B., 2014, Greenhouse Climates, *in* Treatise on Geochemistry, Elsevier, p. 281–304, doi:10.1016/B978-0-08-095975-7.01314-0.

The Cenozoic CO Proxy Integration Project (CenCOPIP) Consortium et al., 2023, Toward a Cenozoic history of atmospheric CO_2: Science, v. 382, p. 5177, doi:10.1126/science.adi5177.

Thrasher, B.L., and Sloan, L.C., 2009, Carbon dioxide and the early Eocene climate of western North America: Geology, v. 37, p. 807–810, doi:10.1130/G30090A.1.

Westerhold, T. et al., 2020, An astronomically dated record of Earth's climate and its predictability over the last 66 million years: Science, v. 369, p. 1383–1387, doi:10.1126/science.aba6853.

Widlansky, S.J., Secord, R., Snell, K.E., Chew, A.E., and Clyde, W.C., 2022, Terrestrial carbon isotope stratigraphy and mammal turnover during post-PETM hyperthermals in the Bighorn Basin, Wyoming, USA: Climate of the Past, v. 18, p. 681–712, doi:10.5194/cp-18-681-2022.

Wilf, P., 2000, Late Paleocene–early Eocene climate changes in southwestern Wyoming: Paleobotanical analysis: Geological Society of America Bulletin, v. 112, p. 292–307.

Wilf, P., Johnson, K.R., and Huber, B.T., 2003, Correlated terrestrial and marine evidence for global climate changes before mass extinction at the Cretaceous–Paleogene boundary: Proceedings of the National Academy of Sciences, v. 100, p. 599–604, doi:10.1073/pnas.0234701100.

Zachos, J.C., Dickens, G.R., and Zeebe, R.E., 2008, An early Cenozoic perspective on greenhouse warming and carbon-cycle dynamics: Nature, v. 451, p. 279–283, doi:10.1038/nature06588.

Zachos, J., Pagani, M., Sloan, L., Thomas, E., and Billups, K., 2001, Trends, Rhythms, and Aberrations in Global Climate 65 Ma to Present: Science, v. 292, p. 686–693, doi:10.1126/science.1059412.

Chapter II: Carbonates and microbialites record a dynamic lake basin evolution in the Late Cretaceous to Eocene Sheep Pass Formation, Nevada, USA

Juliana Olsen-Valdez[1], Sarah Widlansky[2], Elizabeth Trower[1], Kathryn Snell[1], William Clyde[3]

[1]Department of Geological Sciences, University of Colorado Boulder, Benson Earth Sciences Building, 2200 Colorado Ave., Boulder, Colorado 80309, USA

[2]Department of Earth Sciences, University of New Hampshire, 56 College Road, 214 James Hall, Durham, New Hampshire 03824, USA. Now at: Woods Hole Coastal and Marine Science Center, U.S. Geological Survey, 360 Woods Hole Road, Woods Hole, Massachusetts 02543, USA

[3]Department of Earth Sciences, University of New Hampshire, 56 College Road, 214 James Hall, Durham, New Hampshire 03824, USA

2.1 Abstract

Ancient terrestrial sediments provide critical information about the responses of continental environments to global scale climate and tectonic perturbations, which are vastly understudied relative to marine archives. The >1-km-thick Sheep Pass Formation type section in east-central Nevada preserves non-marine carbonates, including microbialites, and lesser siliciclastics deposited in a tectonically active,

This chapter is published:
Olsen-Valdez, J., Widlansky, S., Trower, E., Snell, K., and Clyde, W., 2025, Carbonates and microbialites record a dynamic lake basin evolution in the Late Cretaceous to Eocene Sheep Pass Formation, Nevada, USA: Sedimentology, p. sed.13264, doi:10.1111/sed.13264.

high-elevation basin during the latest Cretaceous through to middle Eocene time, an interval spanning major global greenhouse climate states and warming events. This study combines outcrop and hand-sample observations, thin section petrography, and X-ray diffraction mineralogical analyses to create a facies framework and interpreted environmental evolution for the Sheep Pass Basin. Together, these observations portray the Sheep Pass Formation type section as a dynamic and highly sensitive basin due to its small size. The dominance of thrombolite boundstones compared to metazoan fossils, which sets the Sheep Pass Formation type section apart from other Palaeogene-aged lake basins in the western United States, reflects the resilience of microbial mats compared to metazoans in this dynamic setting. The major lacustrine phase of the Sheep Pass Basin records three intervals: a shallow lake with few microbialites, followed by abundant microbialites, before the transition to a marginal setting with evaporative conditions, marking the culmination of this major lacustrine phase. The transition to a microbialite-dominated interval was likely driven by physicochemical conditions (for example, higher alkalinity), paired with lower competition from metazoan grazers. Although the Sheep Pass Formation type section preserves environmental change in response to both tectonics and climate, similar trends in facies, mineralogy, and invertebrate abundance compared to other sedimentary basins from this time suggests that global climate also influenced environmental shifts in the Sheep Pass Basin. This work provides a detailed sedimentological framework for a new, high-elevation paleoclimate record during a pivotal geological climate interval.

Key words: Microbialite, non-marine carbonate, paleoclimatology, sedimentology, western USA

2.2 Introduction

The latest Cretaceous to middle Eocene (*ca* 70 Ma to 45 Ma) Sheep Pass Formation (SPF) type section in east-central Nevada, western USA, preserves a rich and varied terrestrial sedimentary record of a syn-tectonic, high-elevation lake basin spanning a global greenhouse climate interval and several hyperthermal climate events (Winfrey, 1960; Kellogg, 1964; Fouch, 1979; Druschke et al., 2009b; Snell et al., 2014; Westerhold et al., 2020). The SPF type section is also unique in that its palaeobiological record is largely limited to microbialites and invertebrates, with localized frog fossil horizons, in contrast to the presence of diverse vertebrate and invertebrate fossil records in many similarly aged lake basins in the western USA (e.g., Buchheim & Surdam, 1977; Emry & Korth, 1989; Henrici et al., 2018; Bonde et al., 2020). How did this changing tectonic and climatic setting influence the high-elevation Sheep Pass basin and its carbonate facies, including its microbialites? And why does the Sheep Pass Formation type section lack the diversity of metazoans seen in other contemporaneous systems from this time?

To help address these overarching research questions, this study focused on characterizing the decimetre to metre-scale sedimentology of the SPF type section, with particular focus on the carbonate and microbialite facies from the major lacustrine phase of the basin (Member B). This research presents sedimentological

descriptions and interpretations of carbonates – including microbialites – to develop a facies framework and describe the environmental evolution in the SPF type section, with the ultimate goal of providing a comprehensive understanding of environmental change in the Sheep Pass Basin and its relationship to climate, tectonics, and lake ecosystem shifts. This work will also provide critical structure for a new, high-elevation Palaeogene climate record in the western USA.

2.3 Background

2.3.1 Sheep Pass Formation Geological Background

The Sheep Pass Formation comprises several latest Cretaceous to middle Eocene non-volcanic sedimentary successions spread over a >15,000 km^2 area in east-central Nevada, USA (Winfrey, 1960; Kellogg, 1964; Fouch, 1979; Fouch et al., 1991; Druschke et al., 2011). Although Winfrey (1958) originally interpreted the SPF as a single, large basin, more recent sedimentological work suggests SPF deposits reflect discrete sedimentary basins of variable age (Druschke et al., 2011). The Sheep Pass Formation type section area, located in the southern Egan Range (Fig. 1), provides the best exposure of these strata; it rests unconformably on upper Palaeozoic limestones, sandstones, and shales, and is unconformably overlain by late Eocene to Oligocene volcaniclastic deposits of the Garrett Ranch Group (Winfrey, 1960; Kellogg, 1964; Fouch, 1979; Fouch et al., 1991; Druschke et al., 2009b, 2009a). The SPF type section is characterized by six lithologically distinct members, A-F (Fig. 1B) (Winfrey, 1960; Kellogg, 1964; Fouch, 1979; Good, 1987; Druschke et al., 2009a). Member B in

the SPF type section primarily comprises carbonate and microbial carbonate lithologies that record the major lacustrine phase of the Sheep Pass Basin and is the focus of this study (Fouch, 1979; Druschke et al., 2009a).

Originally, age constraints for the SPF were based on biostratigraphy and palynology, which bracketed Members A-C between the Maastrichtian and Palaeocene (70-55 Ma) and identified Member E as middle Eocene (Bridgerian, 50.5-45.4 Ma) (Fouch, 1979; Good, 1987). More recently, U-Pb dating of detrital zircons in the SPF type section suggests that the top of Member A has a maximum depositional age between *ca* 68 to 70 Ma ± 1 Ma, and a calcite U-Pb age from near the base of Member B constrains the depositional age for that interval to 66.1 ± 5.4 Ma (Druschke et al., 2009b). Local Upper Eocene volcanics, including ash-flow tuffs and siliciclastic beds overlying SPF strata, were deposited between 35 Ma and 38 Ma based on $^{40}Ar/^{39}Ar$ and detrital zircon age peaks, respectively (Winfrey, 1960; Kellogg, 1964; Fouch, 1979; Druschke et al., 2009a, 2011).

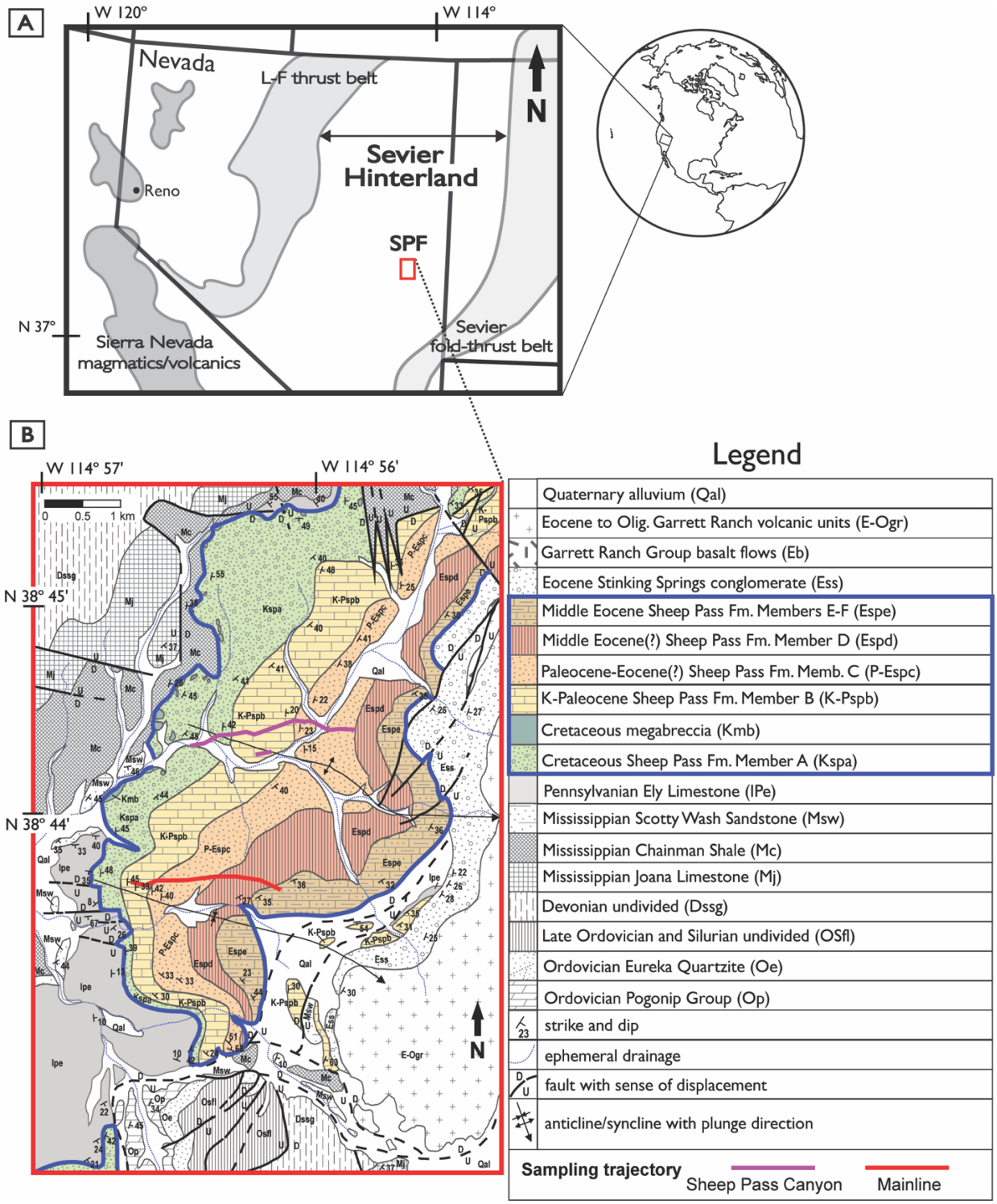

Figure 2-1: A) Sheep Pass Formation (SPF) type section (red box) in the context of prevalent western USA tectonic features during its formation (modified from Druschke et al., 2009a) with present-day city of Reno, Nevada and B) geological map of the SPF type section exposures, shown in color and outlined in blue (modified from Druschke et al., 2009b). LF = Luning-Fencemaker.

2.3.2 Sheep Pass Formation Palaeontology

Charophytes and other unidentified algae are abundant in Member B (Fouch, 1979). Bonde et al. (2020) also noted unidentified plant fossils, including body impressions, a single angiosperm leaf, and a partial gymnosperm leaf, in isolated horizons. They interpret these horizons to reflect intervals when low lake levels allowed for plants to subsist in the lake basin, most likely near the shoreline. Lastly, Member B contains potential decapod carapace impressions and vertical burrows (Bonde et al., 2020).

Invertebrates are dominated by two molluscan associations based on ostracod and mollusc shells in Members B, C, and E (Good, 1987). Both associations indicate a shallow, low-energy, freshwater setting, with modern molluscan analogs residing in lakes in Canada and northern USA (Good, 1987). The first association (Valvata-Hydrobia-*Sphaeriidae*, VHS, found in Members B and C) has analogs common in deeper water with no emergent vegetation. The second association (*Lymnaeidae*-Biomphalaria, LB, found in Member E) has analogs common in ponds or small lakes with emergent vegetation (Good, 1987).

Frog fossils (*Eorubeta nevadensis*), preserved as both isolated fossil specimens and bonebeds in Members B and C, serve as the only vertebrate fossils found in the SPF type section to date, and their body size is larger than most frogs in the fossil record (Henrici et al., 2018; Bonde et al., 2020). Bonde et al. (2020) concluded that the frog fossils found in Member B reflect natural attrition through time, while the bonebeds found in Member C reflect discrete mortality events. Notably, the

preservational modes of all frog fossils indicate a natural settling to the lake bottom in relatively cool lake water, without extensive transport or subaerial exposure (Bonde et al., 2020).

2.3.3 Tectonic Setting

Subduction of the Farallon Plate under the western North American continent led to continuous deformation associated with the Sevier and later Laramide orogenies from at least the Late Jurassic (*ca* 155 Ma) until the early Eocene (*ca* 55 Ma) (DeCelles, 2004; Dickinson, 2004; DeCelles and Coogan, 2006; Druschke et al., 2011; Long, 2015). A high-elevation orogenic plateau, similar to that of the Andean Puna-Altiplano, developed by the Late Cretaceous within the Sevier hinterland region of Nevada and western Utah (termed the 'Nevadaplano') (Coney and Harms, 1984; Jones et al., 1998; DeCelles, 2004; Dickinson, 2004; Druschke et al., 2011; Snell et al., 2014; Long, 2015).

Within the type section, the SPF was deposited in a local high-relief, extensional half-graben basin, likely formed by movement along the Ninemile normal fault (Winfrey, 1960; Kellogg, 1964; Vandervoort and Schmitt, 1990; Druschke et al., 2009b, 2009a, 2011). The Ninemile Fault created up to 3 km of movement in the Late Cretaceous and Palaeocene, and an additional 1 km of movement during later reactivation, the exact timing of which is unknown (Druschke et al., 2009a). The Ninemile Fault also served as the basin-bounding fault in the east, evidenced by: (i) megabreccia and gravity slide deposits extending over 1 km laterally in the Sheep Pass Canyon and (ii) the presence of alluvial fan deposits within Member A that show

greatest accumulation in the east and thin out to the west (Winfrey, 1960; Kellogg, 1964; Fouch, 1979; Fouch et al., 1991; Druschke et al., 2009a). Variability in the thickness of Member A – with *ca* 250 m in Sheep Pass Canyon and complete pinch-out just 2 km south – suggests syn-tectonic fault-controlled deposition during this time (Winfrey, 1960; Fouch, 1979; Druschke et al., 2009a). Further, Druschke et al. (2009a) interpreted that soft-sediment deformation features, including rip-up clasts, load casts, slump folds and flame structures, fluidization pipes, ball-and-pillow structures, and ruptured, contorted, or overturned bedding in Members B and C, reflect syn-tectonic deposition.

2.3.4 Climatic Setting

Most of the Cretaceous to Palaeogene interval is characterized as a time of greenhouse climate, reflecting higher atmospheric CO_2 concentrations and elevated global mean temperatures compared with today (Pagani et al., 2014; Westerhold et al., 2020; The Cenozoic CO Proxy Integration Project (CenCOPIP) Consortium et al., 2023). Within this long-term warmhouse climate interval, a global warming trend beginning in the Palaeocene led into an early Eocene hothouse climate state (i.e., the Early Eocene Climatic Optimum, EECO, *ca* 49-53 Ma), the period of most sustained extreme warmth in the entire Cenozoic Era (Zachos et al., 2001, 2008; Pagani et al., 2014; Westerhold et al., 2020). Superimposed on these warmhouse and hothouse climate states were abrupt and transient (tens to hundreds kyr) hyperthermal events, which affected both the marine and terrestrial realm on a global scale (e.g., the Palaeocene-Eocene Thermal Maximum, PETM, at *ca* 56 Ma and early Eocene

hyperthermals) (Koch et al., 2003; Zachos et al., 2008; Lauretano et al., 2015; Abels et al., 2016; Westerhold et al., 2020).

In the western USA, the early Palaeogene, which has been described generally as a 'warm and wet' greenhouse climate state (e.g., Greenwood and Wing, 1995; Wilf, 2000; Bowen et al., 2004) was also characterized by an intensified hydrological cycle that led to periods of increased drying and evaporation (Pagani et al., 2014; Carmichael et al., 2016). In the Bighorn Basin (north-central Wyoming), various proxies (paleosols, paleobotany, etc.) suggest warm temperatures in the early Palaeogene (e.g., Wing et al., 2005; Snell et al., 2013), as well as transient drying, more episodic or seasonal rainfall changes, and wet/dry cycles leading up to and associated with the PETM (Greenwood & Wing, 1995; Kraus & Riggins, 2007; Kraus et al., 2013; Baczynski et al., 2017). Late Palaeocene and early Eocene records from the Green River Formation (Colorado, Wyoming, and Utah) and Flagstaff Formation (central Utah) show evidence for progressive warming and drying, seasonally-driven runoff, as well as highly fluctuating lake levels associated with an arid climate in response to hyperthermal events and/or the EECO during this time (Bowen et al., 2008; Smith et al., 2008; Tänavsuu-Milkeviciene & Sarg, 2012; Frantz et al., 2014; Birgenheier et al., 2020; Ingalls et al., 2022).

2.4 Methods

The SPF type section area, as described in this study, includes the Sheep Pass Canyon transect of Fouch et al. (1991) together with outcrops from the surrounding

ca 2 km. Two stratigraphic transects in the SPF type section area - the Mainline in 2019 and the Sheep Pass Canyon in 2020 - were measured, described, and sampled (Fig. 1B, Table 1), as well as a smaller (*ca* 40-meter-thick) stratigraphic transect termed the Member B Slope south of the Sheep Pass Canyon transect. A total of 148 (97 from the Mainline, 42 from the Sheep Pass Canyon and nine from the Member B Slope), >20 cm sized samples were collected with corresponding field photographs and GPS coordinates at a resolution of <1 m in Member B and *ca* 5 m Members A, C, D, and E from either outcrops or shallow trenches (in the case of Member D). Member F was not sampled due to poor exposure and limited stratigraphic extent (<50 m; Winfrey, 1960; Fouch, 1979). Through-going, post-depositional faults and folding within the SPF type section area made stratigraphic correlation between transects difficult.

Fifty-six thin sections were prepared by Spectrum Petrographics (Vancouver, WA, USA) and Grindstone Laboratory (Portland, OR, USA) for petrographic analyses on a Zeiss Axio Imager M2 (Zeiss, Jena, Germany) with an attached 6 MP 33 fps Axiocam 506 colour camera. Facies were defined based on the Carbonate Classification Scheme from Dunham (1962) and build on the existing SPF sedimentological classification framework developed by Fouch (1979), Fouch et al. (1991), Druschke et al. (2009a, b, 2011), and Snell (2011).

Thirty-one carbonate sample powders, spanning the stratigraphic range of the SPF type section, were drilled for bulk mineralogy from cut and polished sample surfaces, homogenized with a mortar and pestle, and analyzed on a Bruker D8

Advance X-Ray Diffractometer (Bruker, Billerica, MA, USA) at 40 kV power and 40 mA current. The samples were scanned from 2θ = 10° to 50°, with a 4 second time step at 0.01° increments (default number of steps). Mineral phase identification was completed using the DIFFRAC.EVA software (Bruker, V.5.0) based on reference intensity ratio values, with simultaneous comparison to the International Centre for Diffraction Data PDF-4/Minerals database. Based on the results, the dominant mineralogy was grouped into calcite, dolomite and quartz, and other minor phases were not considered.

Detrital zircon U-Pb analyses were carried out on a 5 kg sample consisting of material collected from coarse-grained sand layers within an *ca* 5 m thick channel deposit in Member C of the Mainline transect (see Supplemental Materials). Once prepared, U-Pb geochronology of zircons was conducted by laser ablation-multicollector-inductively coupled plasma mass spectrometry (LA-MC-ICPMS) at the Arizona LaserChron Center (Gehrels et al., 2006, 2008, see Supplemental Materials). The maximum depositional age was determined by taking a weighted mean of the youngest population of grains, using the AgeCalcML software (Sundell et al., 2021). This method provides a conservative estimate to avoid underestimation of the maximum depositional age that often comes from using a single youngest grain approach (Dickinson and Gehrels, 2009). Data points were weighted by the inverse-square of their assigned errors (1σ) and the resulting mean is shown with a 2σ (i.e., 95%) confidence interval.

Measured Transect	Transect Base		Transect Top	
	Latitude (°)	Longitude (°)	Latitude (°)	Longitude (°)
Mainline (ML)	N 38.73816	W 114.96495	N 38.72544	W 114.95823
Sheep Pass Canyon (SPC)	N 38.72538	W 114.97237	N 38.73936	W 114.94920
Member B Slope	N 38.73737	W 114.95876	N38.73733	W 114.95754

Table 2-1: GPS coordinates (WGS 84 datum) for the base and top of the Mainline and Sheep Pass Canyon measured transects. Member B Slope is a sub-transect within the Sheep Pass Canyon.

2.5 Results and Interpretation

2.5.1 Facies Characterization

This study described 15 facies and their corresponding interpreted depositional settings, constituting the range of unique matrix composition, fabrics and grains (Table 2). Facies were classified through depositional features observed in outcrop, hand sample and thin section. Facies were grouped broadly into five categories: (i) boundstones, (ii) grainstones, (iii) packstones, (iv) mudstones and wackestones, and (v) siliciclastics - with several facies in each group.

Facies name (and abbreviation)	Geometry and sedimentary structures	Facies description	Associated facies	Depositional interpretation*
Thombolite Boundstone (Thrombolite BS)	*ca* 10 cm thick structureless or internally laminated beds with wavy contacts (Fig. 2A to D)	Dark bluish clots in a surrounding beige matrix, clots vary in size from micron to centimetre-scale (Fig. 2C to K)	Micro-clotted Microbial BS, Bioturbated PS, Laminated PS	Shallow lacustrine, littoral zone; microbial mats in the photic zone
Micro-clotted Microbial Boundstone (Micro-clotted Microbial BS)	*ca* 10 to 60 cm-thick internally laminated beds, often stratigraphically underlying Thrombolite BS beds (Fig. 2L)	Heterogeneous micron-scale clotted matrix with rare clots (Fig. 2M and N)	Thrombolite BS, Bioturbated PS, Laminated PS	Shallow lacustrine, littoral zone; preceded stages of well-developed microbial mat growth

Oncoid Packstone to Grainstone (Oncoid PS/GS)	*ca* 20 to 30 cm thick beds sometimes with millimetre-scale horizontal or cross-laminations visible (Fig. 3A)	Spheroidal and fragmented millimetre-scale oncoids surrounded by in-filling calcite or micritic matrix (Fig. 3B to E)	Ooid GS	Shallow lacustrine, littoral zone; bedload transport under higher water energy
Ooid Grainstone (Ooid GS)	*ca* 10 cm thick beds with horizontal to sub-horizontal millimetre-scale laminations (Fig. 3F)	Sub-mm-scale radial ooids surrounded by in-filling calcite and pore space in cross-laminated beds (Fig. 3G to I)	Oncoid PS/GS	Shallow lacustrine, littoral zone; bedload transport under transiently higher water energy
Peloidal Grainstone (Peloidal GS)	*ca* 20 to 80 cm thick mostly structureless beds (Fig. 3J and K)	Grain-supported peloids surrounded by in-filling calcite and chalcedony cement (Fig. 3L to O)	Micro-clotted Microbial BS, Thrombolite BS, Vuggy WS, Siliciclastic facies	Transitional shoreline; shallow lacustrine and palustrine, littoral to eulittoral zone
Laminated Peloidal Packstone (Laminated PS)	*ca* 10 to 30 cm thick planar beds with internal horizontal layering and some ripple-scale cross-laminations (Fig. 4A and B)	Micritic peloids in uniform planar beds with some bioclast fragments present (Fig. 4C to F)	Bioturbated PS, Thromoblite BS, Micro-clotted Microbial BS, Siliciclastic facies	Shallow lacustrine, littoral zone; higher energy setting lacking bioturbation
Bioturbated Peloidal Packstone (Bioturbated PS)	*ca* 10 cm up to metre-scale irregular and structureless beds (Fig. 4G)	Micritic peloids in a biogenically mottled matrix with bioclast fragments (Fig. 4H and I)	Laminated PS, Thrombolite BS, Micro-clotted Microbial BS	Shallow lacustrine, littoral zone; lower energy setting dominated by bioturbation
Bioclast-rich Wackestone to Packstone (Bioclast-rich WS/PS)	Rare centimetre up to metre-scale beds with internal centimetre-scale layering and some cross-cutting micro veins (Fig. 4J)	Unoriented ostracods, charophyte algae, bivalves and rare gastropods in a somewhat biogenically mottled micritic matrix (Fig. 4K and L)	Laminated PS, Bioturbated PS	Varied, but relatively shallow (likely sublittoral zone or shallower); driven largely by water chemistry
Undifferentiated Mudstone to Wackestone (Undiff. MS/WS)	*ca* 1 to 30 cm thick often laterally discontinuous beds with vertical, cross-cutting micro veins (Fig. 5A)	Micrite exhibiting mottling, rare bioclasts and peloids, gypsum pseudomorphs and length-slow chalcedony (Fig. 5B to E)	Vuggy WS	Palustrine, eulittoral to supralittoral zone; with rare evaporite deposition
Vuggy Wackestone (Vuggy WS)	*ca* 1 to 15 cm thick often laterally discontinuous beds (Fig. 5F)	Abundant millimetre to centimetre-scale vugs somewhat resembling alveolar structures in a mottled micritic matrix with rare bioclasts and peloids (Fig. 5G to J)	Undiff. MS/WS	Palustrine, eulittoral to supralittoral zone; with microkarstification and /or desiccation and fissuring in the vadose zone
Matrix-supported Conglomerate (Matrix-supported Congl.)	*ca* 20 to 40 cm thick structureless beds (Fig. 6A)	Angular to subrounded, poorly sorted, very fine to coarse cobble	Clast-supported Congl., Fine-grained SS	Debris flow

		conglomerate with lithic pebbles (Fig. 6A)		
Clast-supported Conglomerate (Clast-supported Congl.)	*ca* 20 cm up to metre-scale structureless or cross-bedded and crudely graded beds with erosive basal contact and gradational top contact with fine sands (Fig. 6A to D)	Angular to subrounded, very fine pebble to coarse cobble conglomerate with lithic pebbles (Fig. 6B)	Fine-grained SS, Matrix-supported Congl.	Gravel-bedded braided rivers
Fine-grained Sandstone (Fine-grained SS)	*ca* 10 to 30 cm thick beds, structureless to crudely horizontally bedded, present as lenses within or capping Clast-supported Congl. (Fig. 6A)	Fine to rare coarse sand-sized detrital quartz grains in a carbonate-cemented sandstone	Clast-supported Congl., Matrix-supported Congl.	Bar top of gravel-bedded braided rivers
Fine to Coarse-grained Sandstone (Coarse-grained SS)	*ca* 5 cm to <metre-scale beds with horizontal bedding, dune-scale planar cross-bedding and less common ripple-scale cross-laminations (Fig. 6E)	Fine to coarse sand-sized detrital quartz grains in a carbonate-cemented sandstone	Very fine-grained SS	Sand-bedded braided rivers
Very fine to Fine-grained Sandstone (Very fine-grained SS)	~2-30 cm-thick structureless or horizontally laminated beds, sometimes with ripple-scale cross-laminations present (Fig. 6B, F and G)	Angular to subrounded, very fine to fine sand-sized detrital quartz grains in a carbonate mud matrix with few peloids, intraclasts and bioclast fragments (Fig. 6H and I)	Coarse-grained SS, Clast-supported Congl.	Low-energy within alluvial fan, fluvial, or deltaic setting

Table 2-2: Various descriptions and corresponding interpreted depositional setting for all facies in the Sheep Pass Formation type section. *See Fig. 12 for more specific depositional interpretations.

2.5.1.1 Boundstones

Thrombolite Boundstone (Thrombolite BS):

Description –

The thrombolite boundstone facies is characterized by dark bluish grey or brown clots in a surrounding beige micritic matrix. Beds range in thickness from 10 cm up to metre-scale in rare occurrences (Fig. 2A to D). Beds are either structureless or have internal laminations between *ca* 1 to 5 cm thick. Wavy contacts often define the base and top of beds. Clots have irregular but distinct boundaries (Fig. 2E to G). In many cases, the clots are elongated with their longest axis in the horizontal direction (Fig. 2G). The clots are composed of homogeneous micrite and microsparite with crystal grains no larger than *ca* 25 μm in diameter (Fig. 2I and J). Very fine sand-sized detrital quartz grains and smaller than millimetre-scale bioclast fragments are rare within the clots. The surrounding matrix is heterogeneous, with majority micrite and lesser microsparite. Very fine sand-sized, subangular to subrounded detrital quartz grains and bioclasts are more common in the matrix compared to the clots (Fig. 2J). Although uncommon overall, irregularly shaped micron-scale voids are more abundant in the matrix compared to the clots. Both the clots and matrix also exhibit rare calcitic micro veins and micron-scale patchy coarse, cross-cutting cement with crystal grains up to *ca* 150 μm in diameter. The clots vary in size from the micron-scale up to the centimetre-scale. This study defines small clots as between micron-scale up to *ca* 2 mm on their longest axis (Fig. 2E and F) and large clots as *ca* 2 mm up to the centimetre-scale on their longest axis (Fig. 2G, I and J). The micron-scale clots appear to be most associated with the matrix component. Rarely, the clots are bound together in a framework of clots up to 3 cm in height and >10 cm wide (Fig. 2H and K). Generally, as clots increase in size, they become more

regularly arranged and weakly laminated; bedding thickness usually increases with clot size as well. In the SPF type section, clot size usually increases with stratigraphic level among groups of thrombolite boundstone beds.

Interpretation –

The thrombolite boundstone facies is characteristic of a microbially influenced carbonate containing an internal clotted fabric and is consistent with definitions of thrombolitic textures by Aitken (1967), Kennard & James (1986), and Shapiro (2000). The clots reflect microbially-associated *in situ* calcification, while the matrix reflects a heterogeneous, interstitial component containing carbonate, detrital grains, and/or reworked micron-scale clot fragments (Kennard & James, 1986; Harwood Theisen and Sumner, 2016; Mei et al., 2020). Generally, lacustrine thrombolites are interpreted as growing in shallow, submerged water where sunlight promotes photosynthesis (Aitken, 1967; Kennard & James, 1986; Riding, 2011). In the geologic record, the spatial and temporal distribution of thrombolites, as well as their clotted fabric, have been associated with the presence of colonizing algae (Feldmann & Mckenzie, 1998; Pruss & Knoll, 2017; Cantine et al., 2020). Cantine et al. (2020) suggested that thrombolitic textures are most common in the rock record when early lithification and penecontemporaneous cementation is absent, allowing for the continued development of clotted textures from fabric-disrupting processes. Further, Gischler et al. (2008) argued that microbialite accretion is largely dependent on carbonate-rich water chemistry promoting lithification over bioerosion from metazoan grazers. We interpret that the thrombolite boundstone facies formed in a

shallow, littoral (Scott et al., 2012) lacustrine depositional setting reflecting microbial mats in the photic zone, with influences from both physicochemical conditions and biological processes. The observed relationship between clot size, bedding thickness, and weak laminations suggests that there are variations in the level of development in the thrombolite boundstone facies.

Micro-clotted Microbial Boundstone (Micro-clotted Microbial BS):

Description –

The micro-clotted microbial boundstone facies is characterized by a micron-scale clotted texture containing a mix of grains and rare clots. Beds are beige to dark bluish grey and range in thickness from 10-60 cm, up to 1 m in rare occurrences (Fig. 2L). Most beds have internal laminations between 1 to 5 cm thick (Fig. 2M). The matrix of the micro-clotted microbial boundstone has interspersed patches of micrite and microsparite, which defines the micron-scale heterogeneous clotted texture in this facies (Fig. 2N). This matrix is different from the thrombolite boundstone matrix, which does not have a micron-scale clotted texture. When present, clots are identical to those in the thrombolite boundstone but only range in size from the micron-scale up to millimetre-scale (Fig. 2M). Clots are composed of microsparite with crystal grains up to 150 μm in diameter (Fig. 2N). Unlike the thrombolite boundstone facies, clots in the micro-clotted microbial boundstone facies never become regularly arranged or weakly laminated. Irregularly shaped voids between 10 to 200 μm are dispersed throughout the matrix. Angular to rounded, very fine sand and silt-sized

detrital quartz grains are present but uncommon (Fig. 2N). Bivalve and ostracod fragments are rare (Fig. 2N). The lack of abundant clots and micron-scale clotted texture of the matrix differentiates the micro-clotted microbial boundstone from the thrombolite boundstone facies. Micro-clotted microbial boundstone beds are closely associated with thrombolite boundstone beds, often stratigraphically underlying the more developed thrombolite boundstone beds.

Interpretation –

The micro-clotted microbial boundstone facies reflects an incipient stage of thrombolite development in a shallow, littoral lacustrine depositional setting. The similarities in clot morphology between both boundstone facies support that the same microbial processes influenced formation of micro-clotted microbial boundstone beds and thrombolite boundstone beds. However, the lack of either abundant or regularly arranged clots suggests that this facies likely reflects a phase that preceded stages of well-developed microbial mat growth like that preserved in the thrombolite boundstone facies. This interpretation is supported by the association of micro-clotted microbial boundstone beds stratigraphically underlying more developed thrombolite boundstone beds. Further, the μm-scale clotted texture in the matrix suggests that microbial activity, including microbially-mediated carbonate precipitation, dominated within the sediment (Dupraz et al., 2009).

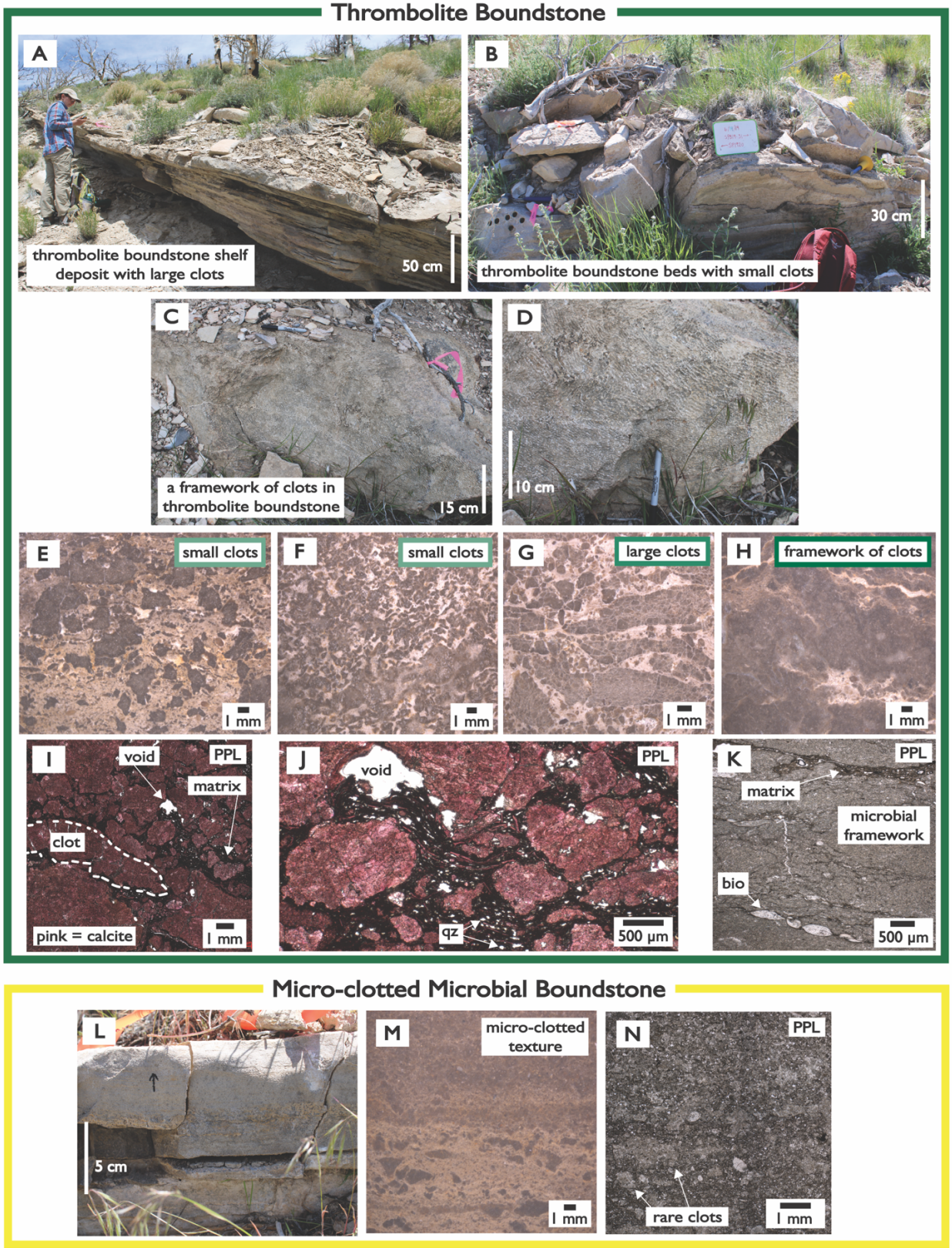

Figure 2-2: Boundstone Facies Plate – Thrombolite Boundstone facies: (A) to (D)

representative beds in outcrop with varying scales of bedding and clot size; (E) to (G) representative hand samples highlighting dark bluish small and large clots in a light beige matrix; and (H) the rare framework of clots, (I) representative thin section image in plane polarized light (PPL) illustrating a clot (white dashed outline) and surrounding dark micritic matrix with rare voids; and (J) same sample in PPL at higher magnification highlighting clots comprised of micrite and microsparite and the dark matrix that contains detrital quartz grains (qz), note that thin section was stained with alizarin red so pink regions in (I) and (J) are calcitic; (K) representative thin section image in PPL of rare framework of clots with little dark micritic matrix and bioclasts (bio) within the matrix. The thrombolite boundstone facies is further colour-coded by small clots (light green), large clots (medium green), or a framework of clots (dark green); Micro-clotted Microbial Boundstone facies: (L) representative bed in outcrop, (M) representative hand sample illustrating micro-clotted texture in matrix, (N) representative thin section image in PPL highlighting rare clots composed of micrite and microsparite, within micron-scale clotted matrix.

2.5.1.2 Grainstones

Oncoid Packstone to Grainstone (Oncoid PS/GS):

Description –

The oncoid packstone to grainstone facies is dominated by grain-supported oncoids in a surrounding sparry cement with local zones of micritic matrix. Beds are light beige to dark grey. Bedding ranges in thickness from *ca* 20 to 30 cm, sometimes with millimetre-scale horizontal or cross-laminations visible (Fig. 3A). The oncoids are between 2 mm and 1.5 cm in diameter, with multiple irregular crinkly coatings between 1 to 2 mm wide (Fig. 3B). Oncoids are spheroidal to ellipsoidal and largely fully intact; in rare cases oncoids are fragmented (Fig. 3C). Oncoid cortices are characterized by a patchy fabric of dark micrite interspersed with fabric-cross-cutting, irregular microsparite composed of crystals between 10 to 20 μm in diameter (Fig. 3D). Silt-sized detrital quartz grains are present within and along the edge of

oncoid cortices (Fig. 3D). Oncoid nuclei contain bioclast fragments, peloids and coarse, equant calcite crystals between 100 μm and 300 in diameter. When present, the surrounding micritic matrix contains bioclasts and peloids, and is often irregularly laminated, bending around oncoids (Fig. 3B and D). Peloids within the oncoid packstone to grainstone have micritic centres and sparry outer rims, with a similar texture to microsparitic patches in oncoid cortices (Fig. 3E). These peloids are similar to those described in the laminated peloidal packstone and bioturbated peloidal packstone facies (see Packstones). Oncoid packstone to grainstone beds are closely associated with ooid grainstone beds and laminated peloidal packstone beds, and lesser bioturbated peloidal packstone beds.

Interpretation –

The oncoid packstone to grainstone facies reflects deposition in a mid to high-energy shallow lacustrine setting with abundant microbes in the littoral zone. Many of the facies characteristics reflect higher water energy where bedload transport of gravel-sized grains via rolling would have occurred: the spheroidal to ellipsoidal morphologies, the presence of oncoid fragments, cross-laminations in beds, and the close association with ooid grainstone beds and laminated peloidal packstone beds. The presence of silt-sized detrital quartz grains and peloids within the cortices of the micritic oncoids indicates that trapping and binding contributed to oncoid growth (Pentecost, 1978). The microsparitic patches within oncoid cortices likely reflect early cementation within the oncoid microstructures due to their isolated, irregular, and fabric-cross-cutting character (Freytet, 1965; Pentecost, 1978; Nickel, 1983).

Ooid Grainstone (Ooid GS):

Description –

The ooid grainstone facies comprises grain-supported, radial ooids surrounded by sparry calcite cement and pore space. Beds are light beige to buff coloured. Bedding thickness is *ca* 10 cm, with horizontal to sub-horizontal millimetre-scale laminations (Fig. 3F and G). The ooids are uniform in size, commonly between *ca* 500 to 700 μm, with a few grains just over 1 mm in diameter (Fig. 3G). The spaces between ooids are filled by either sparry cement or preserved pore space. Rare very fine sand to silt-sized detrital quartz grains are present between ooids. The edges of ooids are slightly irregular; many appear compressed against adjacent grains making grain boundaries hard to discern (Fig. 3H). Where present, cement is composed of coarse, poikilotopic calcite with crystal diameters between 100 μm and >500 μm, and rare patches of in-filling microcrystalline quartz (Fig. 3H and I). In cross-polarized light, ooids exhibit a radial calcitic cortical fabric (Fig. 3I). The compositions of ooid nuclei were not identifiable.

Interpretation –

The ooid grainstone facies reflects deposition in a shallow, littoral lacustrine environment with lake water relatively supersaturated with respect to calcite. The radial calcitic cortical fabric in these ooids is commonly considered a primary texture in lacustrine depositional settings and is indicative of relatively quiet water conditions (Heller et al., 1980). The shallow cross-laminations, reflecting migration

of ripples, suggests that water energy was, at times, high enough to create bedforms via bedload transportation of coarse sand.

Peloidal Grainstone (Peloidal GS):

Description –

The peloidal grainstone facies comprises peloids and lesser bioclasts in a sparry cement with minor pore space. Beds are light beige to dark grey. Bedding ranges in thickness between *ca* 20 cm and 80 cm (Fig. 3J). Peloidal grainstone beds are mostly structureless, though some beds have laminations between *ca* 2 cm and 10 cm thick. In outcrop, peloidal grainstone beds have a granular texture (Fig. 3K). Peloids are angular to rounded, and between 100 μm and 500 μm in diameter (Fig. 3L and N). The peloids differ from clots in the thrombolite boundstone facies because of their less distinct grain boundaries and smaller diameters. In-filling cement is composed of both calcite and chalcedony in close association (Fig. 3O). Calcite in-fills as patches of microspar with crystal grains around 10 μm, as well as rare coarse crystals up to 100 μm in diameter. Calcite microspar and coarse crystals are almost always in direct contact with peloid boundaries, whereas chalcedony cement uniformly in-fills between all grains. Some samples exhibit birdseye structures (i.e., fenestral pores), which appear circular in cross-section (Fig. 3M). Distinct bioturbation features are absent in peloidal grainstone beds. The peloidal grainstone facies is commonly associated with siliciclastic facies beds, mudstone or wackestone facies beds, and some packstone or boundstone facies beds.

Interpretation –

The peloidal grainstone facies reflects deposition in a transitional shoreline environment; characteristics of the peloidal grainstone facies are consistent with either a shallow lacustrine or palustrine setting within the littoral or eulittoral zone (Scott et al., 2012). The association of some peloidal grainstone beds with boundstone beds suggests that peloidal grainstone deposition was, at times, in a shallow, littoral lacustrine environment. The largely structureless nature of the peloidal grainstone also reflects that this shallow depositional environment was not wave-influenced given the absence of bedforms like cross-laminations. The lack of uniformity in peloid diameter and roundness suggests that these grains are not faecal pellets, but rather the product of a mechanical process (for example, reworking of mud) (Fahraeus et al., 1974; Freytet and Verrecchia, 2002). The birdseye structures in some beds also support deposition in a shallow subaqueous and ephemerally exposed eulittoral setting, possibly with root colonization that resulted in pseudomicrokarst features (Choquette & Pray, 1970; Freytet & Plaziat, 1982; Shinn, 1983; Platt, 1989; Alonso Zarza et al., 1992; Freytet & Verrecchia, 2002; Alonso-Zarza & Wright, 2010). The association of peloidal grainstone beds with vuggy wackestone beds or siliciclastic facies further supports a transitional depositional regime, which spans beyond just a lacustrine setting.

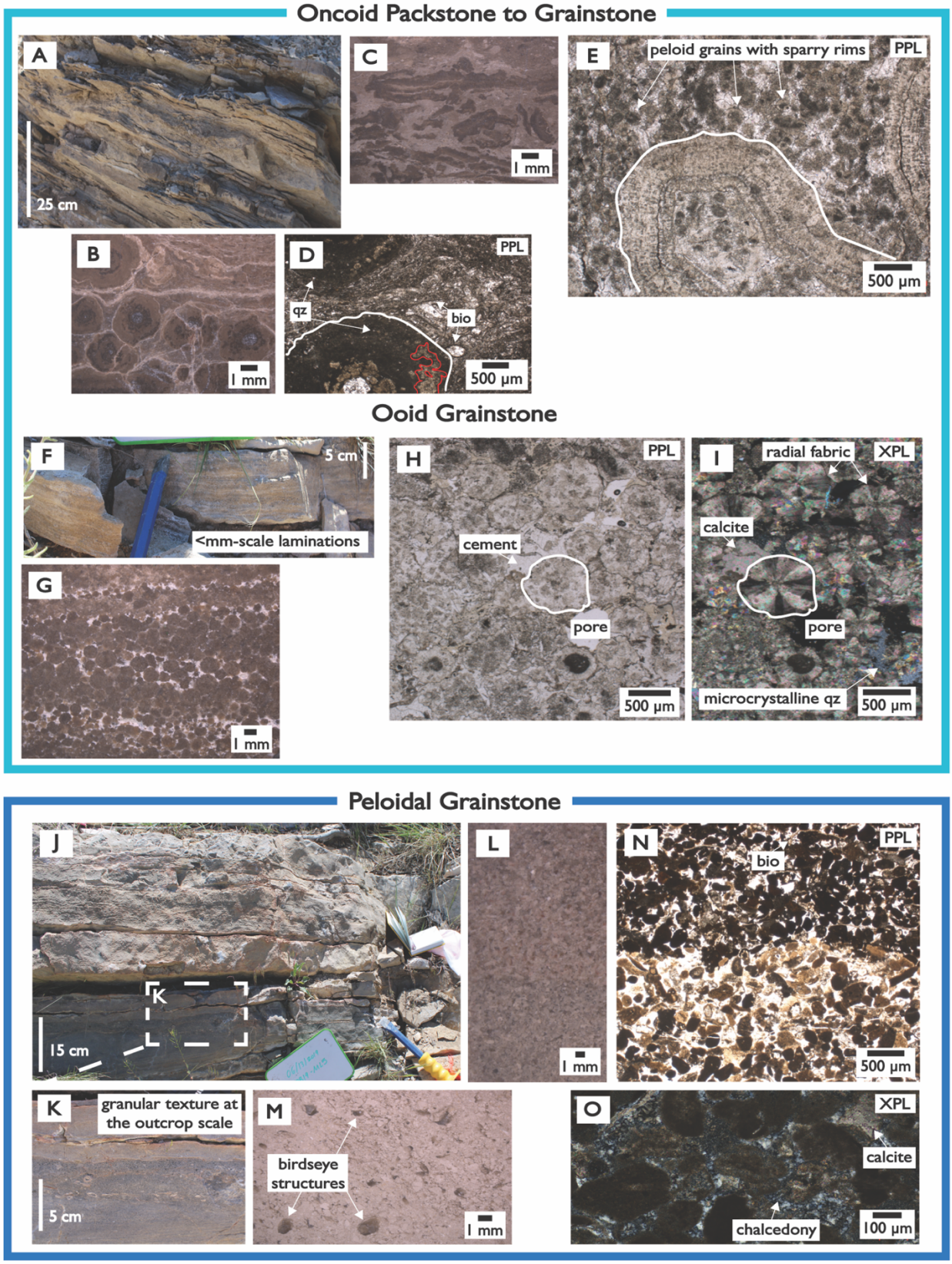

Figure 2-3: Grainstone Facies Plate – Oncoid Packstone to Grainstone facies: (A)

representative bed in outcrop, (B) representative hand samples illustrating crinkly spheroidal oncoids and (C) oncoid fragments, (D) representative thin section image in PPL illustrating an oncoid grain with detrital quartz grains (qz) in oncoid cortices and bioclasts (bio) in the surrounding matrix, as well as patchy micrite and irregular microsparite (red outline) within the oncoid cortices, (E) an outlined oncoid grain surrounded by peloids with sparry rims; Ooid Grainstone facies: F) <millimetre-scale laminations in outcrop, (G) representative hand sample with millimetre-scale ooids, (H) representative thin section image in PPL illustrating an outlined ooid grain in the densely packed sample, and (I) same field of view in cross polarized light (XPL) highlighting radial fabric in the ooid grain as well as the calcite cement, microcrystalline quartz (qz), and pore; Peloidal Grainstone facies: (J) representative bed in outcrop with laminations and (K) granular texture at the centimetre-scale, (L) representative hand sample illustrating peloids in surrounding cement and (M) birdseye structures in cross-section, (N) representative thin section in PPL illustrating peloids with rare bioclasts (bio), and (O) same field of view in XPL highlighting calcite and chalcedony cement between peloids.

2.5.1.3 Packstones

Laminated Peloidal Packstone (Laminated PS):

Description –

The laminated peloidal packstone facies largely comprises peloids, detrital quartz grains and minor bioclasts. Beds are light beige and grey, or brown in rare instances. Bedding ranges in thickness between 2 cm and 40 cm, though beds 10 to 30 cm are most common (Fig. 4A). Beds are planar, with internal horizontal layering defined mostly by the collection of bioclast fragments and sometimes ripple-scale cross-laminations in outcrop (Fig. 4B and C). Peloids are between *ca* 100 µm and 500 µm in diameter, subangular to rounded, and beige or brown (Fig. 4C and E). Peloids are composed of fine, homogeneous micrite and lesser microsparite (Fig. 4D and F). In some cases, peloid edges are characterized by 10 to 30 µm thick rims of coarser microspar crystals (Fig. 4D). Generally, peloids in the laminated peloidal packstone

facies are less angular than those in the peloidal grainstone facies. Angular to subrounded, very fine sand to silt-sized detrital quartz grains are present in all laminated peloidal packstone beds but are most common when associated with rare siliciclastic facies beds (Fig. 4F). Bioclast fragments, dominantly from ostracods but also including rare bivalves, gastropods or charophyte algae, are present but not abundant. Micrite and patchy microsparite comprise the matrix surrounding grains; the micritic texture and crystal sizes closely resemble those which comprise the peloids. Laminated peloidal packstone beds are associated with boundstone facies beds and the bioturbated peloidal packstone facies.

Interpretation –

The laminated peloidal packstone facies reflects deposition in a high-energy shallow, littoral lacustrine setting lacking bioturbation. The preserved internal horizontal and ripple-scale cross-laminations suggest formation of bedforms in a mid to high-energy shoreline environment. The uniform texture within this facies suggests that bioturbation was largely absent (Freytet & Verrecchia, 2002). This interpretation is also consistent with the paucity of bioclasts in laminated peloidal packstone beds. Lastly, the association of laminated peloidal packstone beds with boundstone beds further supports a shallow lacustrine depositional interpretation; these facies were likely spatially adjacent to each other. The more uniform roundness of peloids in laminated peloidal packstone beds compared to the peloidal grainstone facies may reflect a faecal pellet origin for these grains (Freytet & Verrecchia, 2002). Carbonate was likely derived, in part, from invertebrate bioclast material and calcification

associated with charophyte algae (Platt & Wright, 1991; Freytet & Verrecchia, 2002). Variations in detrital quartz grain content in the laminated peloidal packstone facies reflects differences in the amount of siliciclastic input into the lake basin; this is reflected in the increase in detrital quartz content when laminated peloidal packstone beds are associated with siliciclastic facies beds.

Bioturbated Peloidal Packstone (Bioturbated PS):

Description –

The bioturbated peloidal packstone facies has a distinct, bioturbated texture containing peloids and bioclasts. Beds are light beige to grey. Bedding ranges in thickness from 10 cm up to the metre-scale. Beds are irregular and structureless at the outcrop scale and lack internal laminations (Fig. 4G). These features differentiate the bioturbated peloidal packstone from the laminated peloidal packstone. Although burrowing features are absent, the bioturbated peloidal packstone facies exhibits biogenic mottling visible at both the hand sample and thin section-scale (Fig. 4H and I). This texture is characterized by an irregular distribution of matrix and grains, giving the facies a mottled appearance at the millimetre to micron-scale. Peloids are between 50 to 150 μm in diameter, subangular to rounded, and beige or brown. These grains are identical to those found in the laminated peloidal packstone apart from their smaller size range. Bioclast fragments, namely from ostracods, charophyte algae and less abundant gastropods, are present throughout the matrix, although not as common compared to the bioclast-rich wackestone to packstone facies (see

description below; Fig. 4I). The matrix is composed of patchy microsparite and micrite. Regions of coarse, drusy spar cement with crystals up to 100 μm in diameter are common throughout the matrix (Fig. 4I). Bioturbated peloidal packstone beds are closely associated with boundstone facies beds and the laminated peloidal packstone facies.

Interpretation –

The bioturbated peloidal packstone facies reflects deposition in a biologically active shallow, littoral lacustrine setting. The similarity of the peloids in bioturbated peloidal packstone beds to those in laminated peloidal packstone beds suggests that the main depositional difference between these two facies is in the intensity of bioturbation. This interpretation is also consistent with the greater abundance of bioclasts in bioturbated peloidal packstone beds. This facies likely reflects a more protected, lower energy setting favorable for aquatic invertebrates (Platt & Wright, 1991). The close association of bioturbated peloidal packstone beds with boundstone facies beds suggests that both facies reflect a biologically productive, shallow lacustrine setting, with the bioturbated peloidal packstone representing productivity largely driven by invertebrate metazoans versus microbial or algal processes as in the thrombolite boundstone facies.

Bioclast-rich Wackestone to Packstone (Bioclast-rich WS/PS):

Description –

The bioclast-rich wackestone to packstone facies contains abundant bioclasts in a micritic matrix with sparse in-filling sparry cement. Beds are light beige, grey, or buff coloured. Bedding ranges from rare centimetre-scale, up to *ca* 3 m (Fig. 4J). Beds often have internal layering at the centimetre-scale. Some beds have millimetre- to centimetre-scale, cross-cutting micro veins. At the millimetre-scale and smaller, the bioclast-rich wackestone to packstone facies exhibits biogenic mottling, but to a lesser degree compared to the bioturbated peloidal packstone facies. Bioclasts are <millimetre to millimetre-scale, and include ostracods, charophyte algae, bivalves and rare gastropods in an unoriented fossil hash (Fig. 4K). Ostracods are fragmented or rarely fully articulated. Charophyte algae have preserved stem fragments or oogonia. Bivalves and rare gastropods occur as fragments. Bioclasts exhibit either intragranular porosity, complete in-fill of coarse, equant sparry calcite, or isopachous calcite rims in-filling intragranular pore space (Fig. 4K and L). In rare instances, <millimetre-scale peloids or other <millimetre-scale bioclasts are preserved within intragranular pore space. Peloids in the bioclast-rich wackestone to packstone facies are similar to those in the peloidal packstone facies, although in some cases the shapes of peloids are more ellipsoidal (Fig. 4L). Sparry cement is present but less common in the matrix compared to the sparry in-fill within bioclasts. The bioclast-rich wackestone to packstone is mostly associated with the peloidal packstones.

Interpretation –

The bioclast-rich wackestone to packstone facies reflects deposition in freshwater of varying depth. The abundance of ostracods, charophyte algae, bivalves

and gastropods suggests that this facies marks periods when aquatic invertebrates and algae were thriving, likely in a freshwater environment (García, 1994; Palacios-Festa et al., 1994). This interpretation is supported by past work that interpreted a freshwater palaeoecological setting for specific species of ostracods, bivalves and gastropods in the SPF (Good, 1987; Swain, 1987). The range in grain abundance (wackestone to packstone), as well as the presence of both fragmented and fully articulated bioclasts, suggests that water energy and/or water depth varied within this facies, although deposition was likely in the sublittoral zone or shallower (Scott et al., 2012), given the association of this facies with shallow lacustrine peloidal packstone facies beds. Further, the presence of bioclast-rich wackestone to packstone beds across almost every single member, including Members B, C, D, and E, supports the interpretation that deposition of the bioclast-rich wackestone to packstone facies was probably driven more by water chemistry rather than being associated with specific water energy or depth constraints given that depositional environments vary widely across SPF type section members.

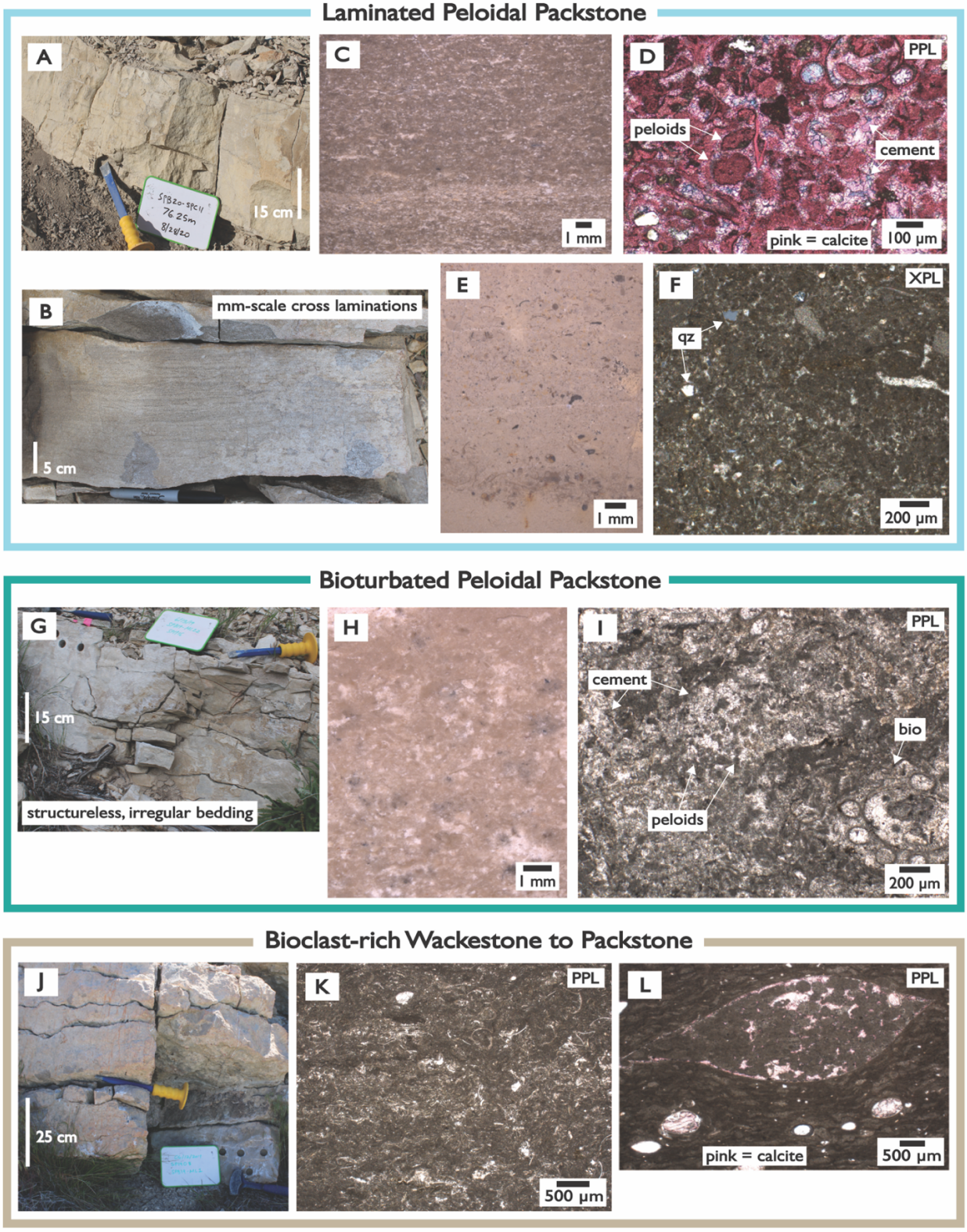

Figure 2-4: Packstone Facies Plate – Laminated Peloidal Packstone facies: (A) representative bed in outcrop, (B) millimetre-scale cross-laminations, (C) and (E)

representative hand samples with faint internal laminations, (D) representative thin section image in PPL illustrating peloids and cement, (F) representative thin section image in XPL illustrating detrital quartz grains (qz); Bioturbated Peloidal Packstone facies: (G) irregular and structureless beds, (H) representative hand sample with bioturbated internal texture, (I) representative thin section image in PPL illustrating peloids, bioclasts, including a charophyte algae oogonia (bio), and interspersed cement; Bioclast-rich Wackestone to Packstone facies: (J) representative bed in outcrop, (K) representative thin section image in PPL illustrating an unoriented bioclast fossil hash in a micritic matrix, (L) bioclast grains in-filled with calcite cement, pore space, or peloids; note alizarin red stain in (D) and (L).

2.5.1.4 Mudstones and Wackestones

Undifferentiated Mudstone to Wackestone (Undiff. MS/WS):

Description –

The undifferentiated mudstone to wackestone facies comprises non-laminated mottled micrite with detrital quartz grains. Beds are light whitish grey to beige. Bedding ranges in thickness between *ca* 1 to 30 cm and is often laterally discontinuous (Fig. 5A). Vertical, cross-cutting, millimetre-scale micro veins are common. Light mottling is common at both the thin section-scale and in hand samples; diffuse, darker patches or haloes are visible at the micron-scale and polished hand samples display irregular lighter-darker colour variations (Fig. 5B and C). This type of mottling is distinct from the biogenic mottling observed in the bioturbated peloidal packstone facies. Interspersed micrite and less abundant microsparite comprise the matrix. Subangular to rounded, very-fine to silt-sized detrital quartz grains are evenly distributed throughout the matrix (Fig. 5C). Ostracod and bivalve fragments are very rare. Millimetere-scale curved cracks are present but rare and associated with more nodular matrix components (Fig. 5C). Gypsum pseudomorphs,

which often form rosettes with individual lenticular blades <1 mm on their shortest axis and 2 to 3 mm on their longest axis, are present but uncommon in the matrix (Fig. 5D). The pseudomorphs are in-filled with coarse calcite as well as lesser microcrystalline quartz and chalcedony (Fig. 5D and E). In-filling calcite has equant crystals up to 300 μm in diameter. Some pseudomorphs exhibit geopetal structures or minor porosity. In-filling chalcedony is composed of fibrous (i.e., quartzine) radial crystals up to 100 μm in length with moderate relief (Fig. 5E).

Interpretation –

Although fine-grained carbonates are common in both lacustrine and palustrine depositional environments (Freytet & Verrecchia, 2002; Alonso-Zarza & Wright, 2010; Gierlowski-Kordesch, 2010), the undifferentiated mudstone to wackestone facies reflects palustrine deposition in a low-energy wetland setting. Palustrine deposition occurs in freshwater wetland systems, as well as in ponds and along the fringes of lakes, where sediments are modified through subaerial exposure and pedogenic (soil) processes in both coastal and continental settings, with a strong influence from groundwater (Platt & Wright, 1991, 2023; Wright & Platt, 1995; Freytet & Verrecchia, 2002; Alonso-Zarza & Wright, 2010). Wetting and drying is a common physical process that occurs in palustrine systems, often reflecting seasonal fluctuations in the groundwater aquifer, and can preserve several alteration characteristics associated with pedogenic modification (Wright & Platt, 1995). Mottling like that observed in the undifferentiated mudstone to wackestone facies is a common textural characteristic that forms from desiccation and iron mobilization

(Freytet & Verrecchia, 2002; Alonso-Zarza & Wright, 2010). The curved cracks in the undifferentiated mudstone to wackestone facies likely developed as a result of early modification, and resemble circumgranular cracking features found in other palustrine carbonate archives (Freytet & Plaziat, 1982; Platt, 1989; Freytet & Verrecchia, 2002). Modified lenticular gypsum is also common in hydrologically-closed, evaporitic basin settings (Rodriguez-Aranda & Calvo, 1998). Euhedral gypsum rosettes likely formed subaqueously in highly saline water and were later dissolved and in-filled with calcite and chalcedony in the vadose zone (Mees et al., 2012). Further, the presence of length-slow chalcedony – with fibrous quartzine crystals – has been previously identified as a common genetic marker of silicified evaporites (Folk & Pittman, 1971). Overall, the micritic matrix in the undifferentiated mudstone to wackestone is likely to have formed from inorganic subaqueous precipitation given the relative absence of bioclast fragments or bioturbation features; this matrix was subsequently reworked through subaerial exposure processes, likely over multiple oscillations in the water table (Alonso-Zarza & Wright, 2010).

Vuggy Wackestone (Vuggy WS):

Description –

The vuggy wackestone facies comprises abundant vugs in a non-laminated micritic matrix. Beds are light grey, beige or buff coloured. Bedding ranges in thickness between 1 to 15 cm and is often laterally discontinuous (Fig. 5F). Vugs are

subangular to rounded and are between 1 mm and 2 cm on their longest axis. Smaller vugs are often spherical, while large vugs have more elongated shapes with their longest axis trending towards vertical (Fig. 5G). Some vugs are in-filled with coarse chalcedony cement and lesser micrite or peloids, some of which have a geopetal structure (Fig. 5H). When present, peloids are subangular to rounded and range in size between 50 μm to 100 μm in diameter. Mottling like that observed in the undifferentiated mudstone to wackestone facies is also common. Subrounded to rounded, silt-sized and very fine sand-sized detrital quartz grains are evenly distributed throughout the matrix. Ostracod fragments are very rare. In a single occurrence, the vuggy wackestone facies is brecciated at the top of a bed; the breccia is composed of millimetre-scale, angular and curvilinear intraclasts surrounded by coarse drusy calcite spar cement with crystal grains between 20 μm and 500 μm (Fig. 5I and J). The vuggy wackestone facies is closely associated with the undifferentiated mudstone to wackestone facies.

Interpretation –

The vuggy wackestone facies is interpreted to reflect palustrine deposition in a low-energy wetland setting within the eulittoral to supralittoral zone. This facies appears similar to Alonso-Zarza & Wright's (2010) 'limestones with vertical root cavities' facies. The characteristics of the vugs in the vuggy wackestone, some of which resemble alveolar structures (Wright, 1986; Alonso Zarza et al., 1992; Alonso-Zarza & Wright, 2010), suggest a similar formation mechanism through the vertical penetration of roots and/or rhizomes into carbonate mud, which leave root hollows

that can remain open (i.e., pseudomicrokarst) or be subsequently in-filled (Freytet, 1973; Freytet & Plaziat, 1982; Platt, 1989; Alonso Zarza et al., 1992; Freytet & Verrecchia, 2002; Alonso-Zarza & Wright, 2010). In-filling of vugs by spar cement, micrite, and/or peloids in a geopetal structure reflect modification in the vadose zone. The brecciated or grainified fabric preserved as a single occurrence within the vuggy wackestone facies resembles features that result from either desiccation and fissuring during subaerial exposure (Freytet, 1973; Freytet & Verrecchia, 2002; Alonso-Zarza & Wright, 2010) or through the development of pseudomicrokarst as a result of root colonization and subsequent exposure (Freytet and Plaziat, 1982; Platt, 1989; Alonso Zarza et al., 1992; Freytet and Verrecchia, 2002; Alonso-Zarza and Wright, 2010). Although the angular and curvilinear nature of intraclasts within the rare breccia is most reminiscent of desiccation and fissuring, the authors hypothesize that microkarstification likely also contributed to the development of this texture; these features are common and often co-occur in palustrine depositional settings (e.g., Alonso Zarza et al., 1992; Dunagan & Turner, 2004).

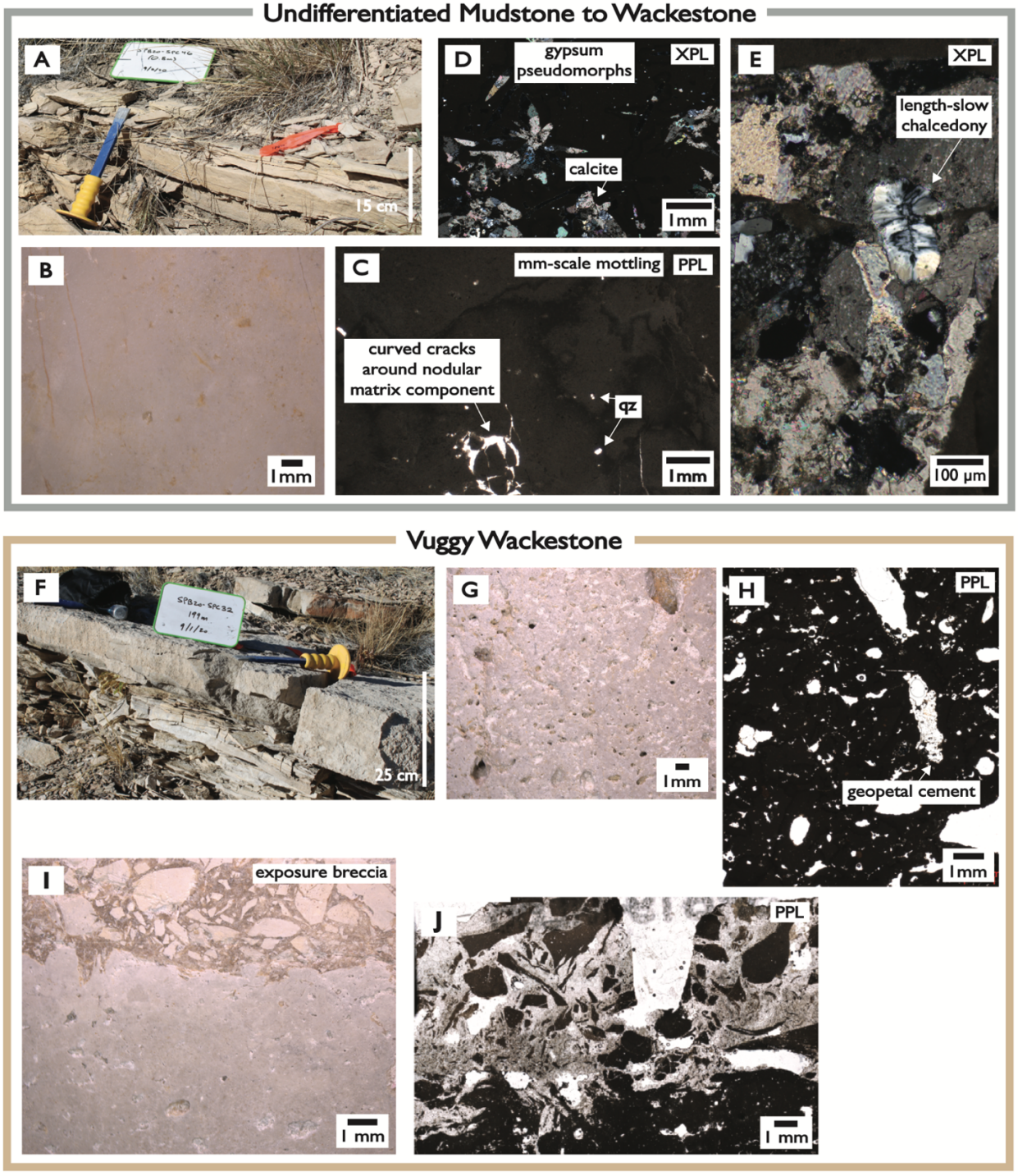

Figure 2-5: Mudstone and Wackestone Facies Plate – Undifferentiated Mudstone to Wackestone facies: (A) representative bed in outcrop, (B) representative hand sample with faint mottling, (C) representative thin section image in PPL illustrating mottling with diffuse, darker patches and detrital quartz grains (qz), (D) thin section image in XPL highlighting gypsum pseudomorphs comprised of calcite and chalcedony, (E) length-slow chalcedony within a gypsum pseudomorph; Vuggy Wackestone facies: (F)

representative bed in outcrop, (G) representative hand sample exhibiting millimetre to centimetre-scale vugs, (H) representative thin section image in PPL with geopetal structures in a vug, (I) hand sample with rare exposure breccia, and (J) thin section image in PPL illustrating angular and curvilinear exposure breccia clasts in-filled with cement.

2.5.1.5 Siliciclastics

Matrix-supported Conglomerate (Matrix-supported Congl.):

Description –

The matrix-supported conglomerate facies is a structureless, angular to subrounded, very fine to coarse pebble conglomerate (Fig. 6A). Beds are beige to reddish pink. Bedding ranges in thickness between 20 to 40 cm. The matrix comprises abundant silt-sized detrital quartz grains and other <millimetre-scale lithic fragments in a carbonate mud. The matrix-supported conglomerate is poorly sorted. Chert clasts up to centimetre-scale are present but rare. Lithic pebbles that are mostly sedimentary in nature vary in colour between grey, beige, pink and white, often with marine bioclast fragments (for example, coral).

Interpretation –

The matrix-supported conglomerate facies reflects rapid deposition by a debris flow, due to its matrix-supported, structureless nature and extremely poor sorting. The lithic pebbles, as well as the finer grains within the matrix, appear to be locally sourced from the Ely Limestone and Scotty Wash Sandstone, as previously documented by Winfrey (1960) and Kellogg (1964).

Clast-supported Conglomerate (Clast-supported Congl.):

Description –

The clast-supported conglomerate facies is structureless to cross-bedded, with angular to subrounded very fine pebbles to large cobbles (Fig. 6A and B). Beds are beige to red. Bedding ranges in thickness from 20 cm up to 2 m. Some beds exhibit crude grading. Beds have erosive basal contacts, including rare scours and coarse basal lags (Fig. 6A). The clast-supported conglomerate usually has an erosive basal contact with either conglomerate or fine sand beds and a gradational top contact with fine sands. In some cases, beds grade upward. Lithic pebbles and cobbles within the conglomerate either contain marine bioclast fragments or are composed of a homogeneous beige or tan carbonate mud matrix (Fig. 6B). The finest-grained end member of the clast-supported conglomerate facies, only present in Member C of the Mainline transect, contains minor coarse and very coarse sand grains, as well as abundant trough cross-bedding (Fig. 6C and D).

Interpretation –

The clast-supported conglomerate facies reflects deposition of gravel bars within a gravel-bedded braided river due to its clast-supported nature, pebble to cobble grain size, and erosive basal contacts. The trough cross-bedding reflects subaqueous dune formation as mid-channel bars within the braided river. Scours and coarse basal lag features in the conglomerate beds reflect deposition at the base of the channel. The range in grain size, from very fine pebble to large cobble, correlates

to proximity to the sediment source; coarser grain sizes were deposited more proximal to the sediment source while finer grained beds were deposited more distal from the sediment source (i.e., in Member C of the Mainline transect).

Fine-grained Sandstone (Fine-grained SS):

Description –

The fine-grained sandstone facies is structureless to crudely horizontally bedded, with fine to rare coarse sand-sized and lesser silt-sized detrital quartz grains. Beds are beige and red. Bedding ranges in thickness between 10 to 30 cm and is often laterally discontinuous (Fig. 6A). Beds are carbonate-cemented and contain minor angular to subrounded, very fine to medium lithic pebbles. The fine-grained sandstone often caps clast-supported conglomerate beds. Top contacts are most commonly erosive with either the matrix-supported conglomerate or clast-supported conglomerate facies. Smaller than metre-scale lenses of fine-grained sandstone sometimes occur within the clast-supported conglomerate (Fig. 6A). Conversely, lenses of clast-supported conglomerate can occur within fine-grained sandstone beds, though it is uncommon. In rare instances, load casts from overlying conglomerate beds are also present in the fine-grained sandstone.

Interpretation –

The fine-grained sandstone facies reflects the waning stages of deposition associated with migration of a gravel-bedded braided river. The close association of fine-grained sandstone beds, which often cap clast-supported conglomerate beds,

suggests that this facies marks the fining-up of the bar deposit. A drop in water energy likely led to deposition of finer sands and silts as the bar was abandoned and the channel migrated.

Fine to Coarse-grained Sandstone (Coarse-grained SS):

Description –

The fine- to coarse-grained sandstone facies is carbonate-cemented, with fine to coarse sand-sized detrital quartz grains. Beds are orangey beige to red. Bedding ranges in thickness from 5 cm up to 0.5 m (Fig. 6E). Fine- to coarse-grained sandstone beds have horizontal bedding and dune-scale planar cross-bedding, as well as less common ripple-scale cross-laminations. Fine- to coarse-grained sandstone beds are associated with the very fine- to fine-grained sandstone facies and clast-supported conglomerate facies.

Interpretation –

The fine- to coarse-grained sandstone facies reflects deposition of sandy bars in a sand-bedded braided river. Horizontal bedding and dune-scale planar cross-bedding suggests that water energy was lower than that required to form the clast-supported conglomerate facies; sands were likely deposited in shallower water close to the edge of channel bars versus within gravel-bedded channels. The association of the clast-supported conglomerate and very fine- to fine-grained sandstone facies supports that this braided river system regularly migrated to deposit sediments at both higher and lower water energy.

Very fine to Fine-grained Sandstone (Very fine-grained SS):

Description –

The very fine- to fine-grained sandstone facies is structureless to horizontally laminated, with abundant very fine to fine sand-sized detrital quartz grains in a carbonate mud matrix. Beds are beige or reddish buff. Bedding ranges in thickness between 2 cm and 30 cm, sometimes with internal layering 1 to 10 cm thick (Fig. 6B, F and G). Bedding is sometimes irregular or laterally discontinuous. Scoured bases are present but rare. Ripple-scale cross-laminations are present in some beds. Detrital quartz grains are angular to subrounded, and evenly distributed throughout the matrix (Fig. 6H). The carbonate mud matrix is composed of both micrite and silt-sized carbonate grains (Fig. 6I). Although the very fine to fine-grained sandstone is largely matrix-supported, certain regions are clast-supported where detrital quartz grains are closely packed together. Peloids are present but uncommon; they are usually subangular to rounded and between 50 to 100 μm in diameter. The peloids in the very fine- to fine-grained sandstone closely resemble those in packstone facies beds. When present, carbonate intraclasts are angular to subrounded and between 1 to 5 mm in diameter. Intraclast grain boundaries are distinct, and the matrix is composed of micrite with few detrital quartz grains. Ostracod and bivalve fragments are rare. Very fine to fine-grained sandstone beds are often inter-bedded with the fine- to coarse-grained sandstone. The facies is also associated with clast-supported conglomerate beds and lesser carbonate facies beds.

Interpretation –

The very fine to fine-grained sandstone facies reflects a range of low-energy depositional settings; the type of depositional setting changes with spatial distance from the alluvial fan versus the lake basin and is differentiated through facies associations. First, the association of very fine to fine-grained sandstone beds with clast-supported conglomerate beds suggests that deposition was, at times, near gravel-bedded braided rivers in a fluvial setting more proximal to the alluvial fan. Conversely, the close association of very fine to fine-grained sandstone beds with cross-bedded sandstone beds and lesser carbonate facies beds suggests that deposition also occurred near sandy-bedded braided rivers more distal from the alluvial fan, and possibly even in a deltaic setting. The irregular and largely structureless nature of very fine to fine-grained sandstone beds may reflect the role of bioturbation in disrupting internal structures (Freytet & Verrecchia, 2002; Gingras et al., 2015). The carbonate mud matrix in the very fine to fine-grained sandstone facies is likely a mix of both detrital and authigenic components, the amount of which may also vary with proximity to the alluvial fan.

Siliciclastic Facies

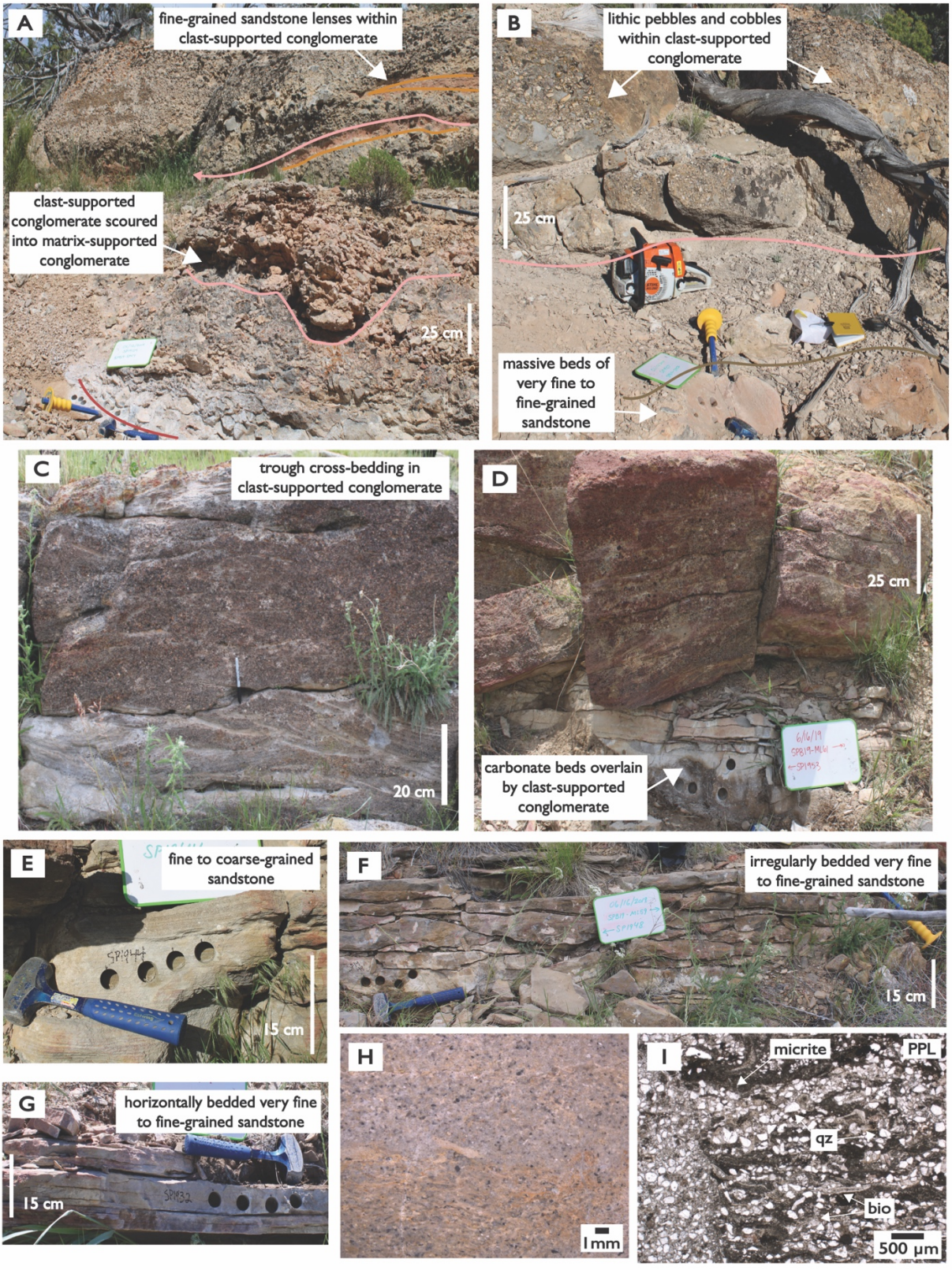

Figure 2-6: Siliciclastic Facies Plate – (A) to (D) representative beds in outcrop highlighting stratigraphic relationship between matrix-supported conglomerate, clast-supported conglomerate, fine-grained sandstone and very fine- to fine-grained sandstone beds, (E) representative fine to coarse-grained sandstone beds in outcrop, (F) and (G) representative very fine to fine-grained sandstone beds in outcrop with various bedding, (H) representative hand sample of very fine to fine-grained sandstone and, (I) paired thin section image in PPL illustrating micritic matrix, bioclasts (bio), and detrital quartz grains (qz). Note that the detrital zircon U-Pb sample was derived from coarse sand layers in a *ca* 5 m thick channel deposit that included the conglomerate shown in (C).

2.5.2 Environmental Evolution of the Sheep Pass Formation

This study investigated the environmental evolution of the Sheep Pass Basin by characterizing the sedimentological and stratigraphic changes within and between Members A to E, with particular focus on Member B. The common facies, mineralogy, and interpreted depositional environment were summarized for each member using a stratigraphic overview with mineralogical data (Fig. 7), member-specific stratigraphic columns (Figs 8 to 11), and a Sheep Pass Basin depositional model (Fig. 12).

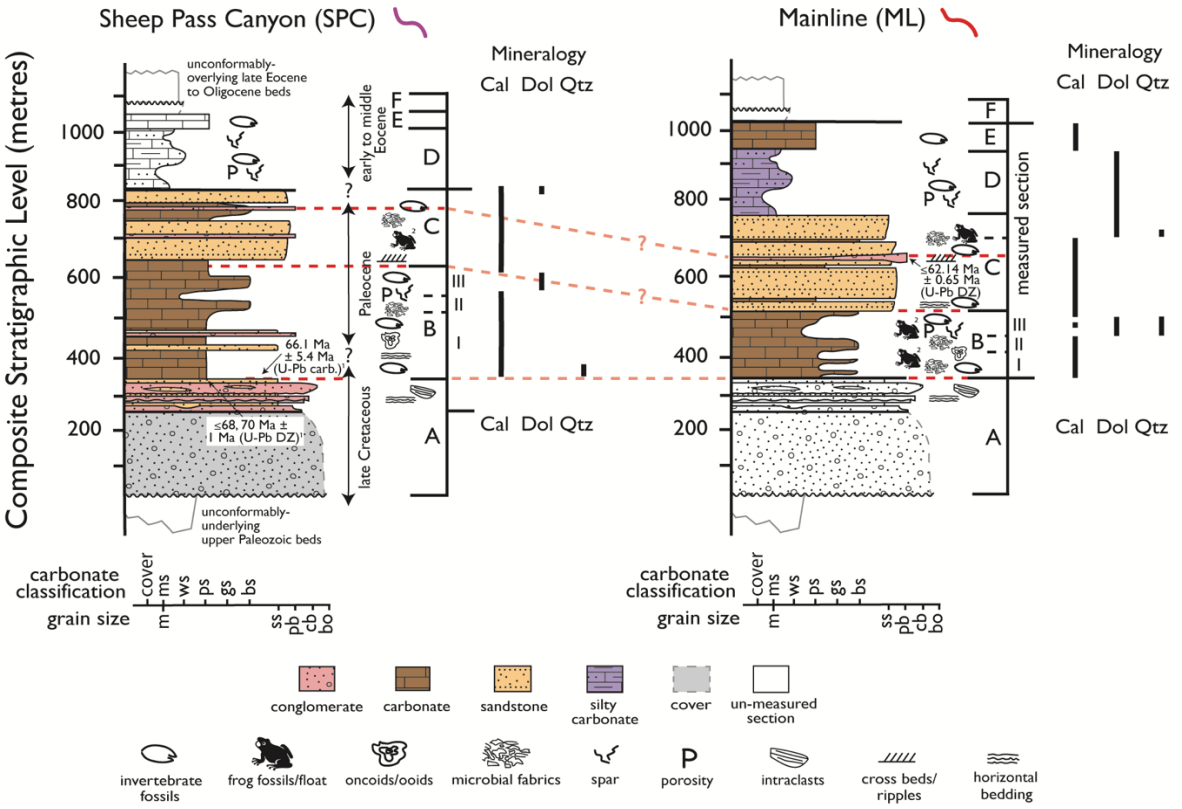

Figure 2-7: Simplified stratigraphic columns for the Sheep Pass Canyon and Mainline measured transects. Roman numerals I to III and black dashed lines in Member B reflect Member B Intervals I, II, and III. Black dashed line in Member C (Mainline) denotes transition between lower and upper Member C. Black vertical lines represent the presence of calcite (Cal), dolomite (Dol), and quartz (Qtz) based on dominant mineralogy. Red dashed lines reflect approximate stratigraphic correlations. Included dates are from this study (U-Pb detrital zircon date in the Mainline transect) and [1]Druschke et al. (2009b). The stratigraphic positions of frog fossils/float were approximated from [2]Henrici et al. (2018), except for in Member C of the Mainline transect where frog float was directly observed. Note Member F was not measured in this study due to poor exposure.

2.5.2.1 Member A – Alluvio-fluvial stage:

Member A largely comprises interbedded matrix-supported conglomerates and clast-supported conglomerates that grade into fine sandstones, matching previous observations by Winfrey (1960), Kellogg (1964), and Fouch (1979) (Fig. 8). These facies are interpreted as having formed in a depositional environment that included

an alluvial fan and an adjacent down slope fluvial system (Fig. 12, Member A). The presence of decametre-scale blocks and megabreccias in lower Member A of the Sheep Pass Canyon transect, composed of underlying Mississippian-aged Scotty Wash Sandstone and Pennsylvanian-aged Ely Limestone (Fig. 7; Kellogg, 1964; Fouch et al., 1991; Druschke et al., 2009b), as well as the size of lithic pebbles and cobbles within the Member A conglomerates, suggests that topographic relief was significant. Consistent with previous interpretations, these characteristics indicate that detritus was shed off of steep, fault-bounded margins at the onset of deposition (Kellogg, 1964; Vandervoort & Schmitt, 1990; Fouch et al., 1991; Druschke et al., 2009b). Palaeocurrent measurements from Druschke et al. (2009a) indicate a dominant westward direction of transport. Very fine to fine-grained sandstones towards the top of the member suggest that the depositional environment also encompassed a deltaic setting towards the culmination of Member A, likely due to the emergence of a shallow lake that made way for the lacustrine system in Member B (Fig. 12, Member A).

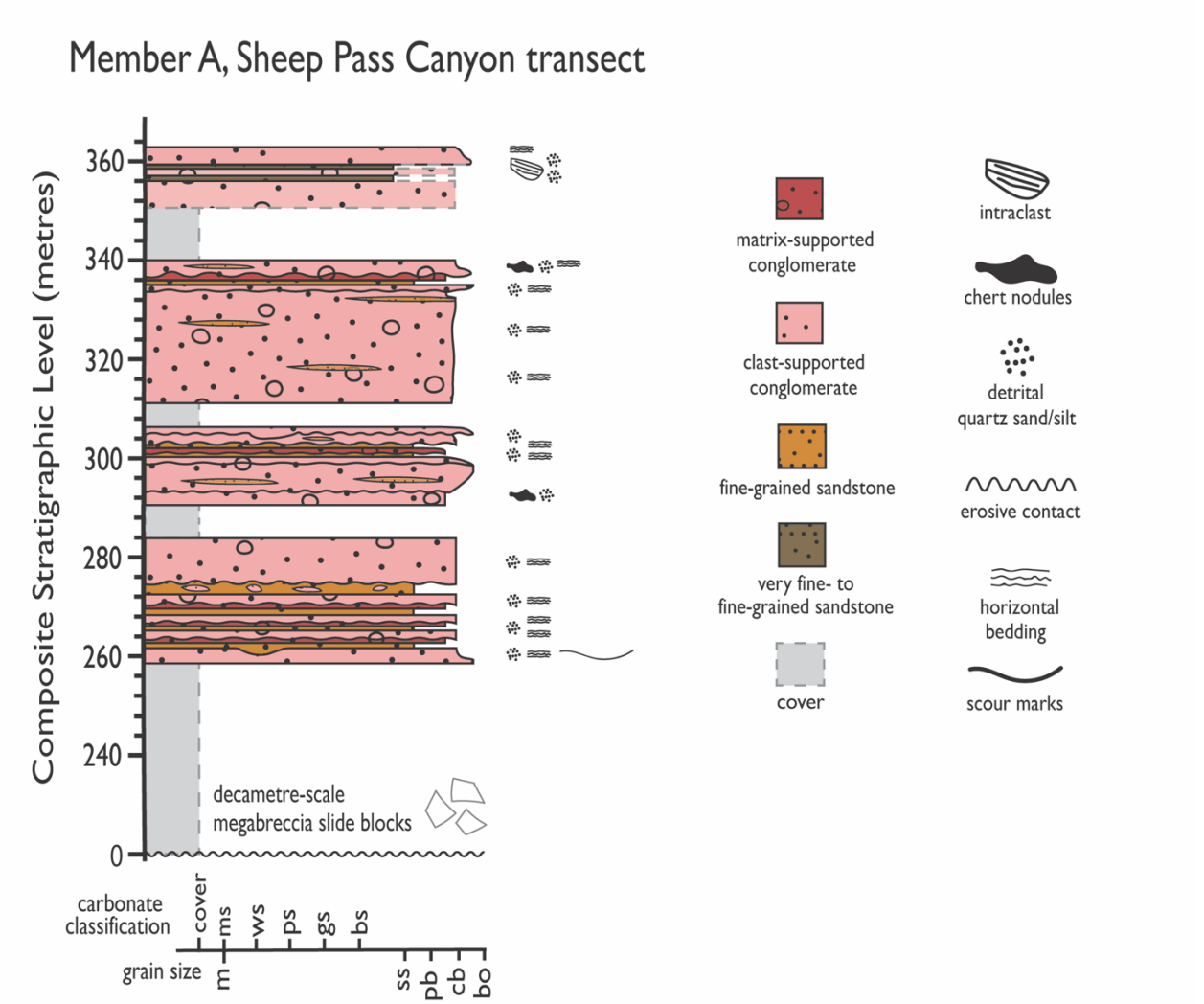

Figure 2-8: Composite stratigraphic column of Member A, Sheep Pass Canyon measured transect.

2.5.2.2 Member B – Major lacustrine stage:

Member B records a variety of facies, including packstones (laminated peloidal packstone, bioturbated peloidal packstone, bioclast-rich wackestone to packstone), boundstones (thrombolite boundstone, micro-clotted microbial boundstone), and grainstones (peloidal grainstone, ooid grainstone, oncoid packstone to grainstone), as well as less abundant siliciclastic facies (clast-supported conglomerate, fine-grained

sandstone, very fine to fine-grained sandstone) and mudstones or wackestones (undifferentiated mudstone to wackestone, vuggy wackestone) (Fig. 9).

The basal part of Member B has a transitional contact with underlying conglomerates and sandstones in Member A. Overall, Member B is interpreted to reflect deposition in a shallow lacustrine (sublittoral to eulittoral) setting (Fig. 12, Member B). The Mainline and Sheep Pass Canyon transects generally record parallel changes in facies and mineralogy, indicating that they both preserve deposition in a single, low-gradient, lake basin (Platt & Wright, 1991). However, the authors interpret the greater abundance of siliciclastic facies in the Sheep Pass Canyon transect, particularly in lower Member B, to signify that the Sheep Pass Canyon transect preserves a more shoreward depositional setting compared to the Mainline transect (Fig. 9).

Detailed analysis of facies trends and paired mineralogical data indicate three main depositional intervals within Member B (Figs 9 and 12):

Member B Interval I – Freshwater, high-energy shoreline setting:

Lower Member B, from the base to approximately 420 m in the Mainline transect, is mostly composed of the laminated peloidal packstone, bioturbated peloidal packstone, and bioclast-rich wackestone to packstone (Fig. 9, Interval I). Micro-clotted microbial boundstone beds also outcrop several times, and thrombolite boundstone beds are present but uncommon. Grainstone beds are present but rare. Interval I is characterized by calcitic mineralogy (Fig. 7). This, as well as the presence

of facies with abundant charophyte algae (for example, bioclast-rich wackestone to packstone), suggest that calcite was forming in fresh, carbonate-supersaturated lake water (Kelts & Hsü, 1978).

Laminated peloidal packstone beds, which dominate for much of Interval I, indicate that the first stage of the lacustrine basin was characterized by a mid to high-energy shoreline environment with well-developed bedforms and limited bioturbation in the littoral zone (Fig. 12, Member B – Interval I). The Sheep Pass Canyon transect contains siliciclastic facies, including clast-supported conglomerate, fine-grained sandstone, and very fine to fine-grained sandstone beds, towards the base of Member B. These occurrences suggest that alluvial, fluvial, and deltaic deposition, which characterized Member A, continued as the basin initially expanded into its major lacustrine phase. These characteristics are consistent with deposition in a hydrologically open (Platt & Wright, 1991), balanced-fill (Carroll & Bohacs, 1999) lake basin.

Common, metre-scale stratigraphic transitions between the various facies highlight the dynamic (i.e., frequently changing) nature of the shallow lacustrine setting preserved in Interval I. For example, bioclast-rich wackestone to packstone beds interbedded with laminated peloidal packstone beds throughout Interval I suggest that there were times when the environment was characterized by abundant invertebrates, likely in response to distinct freshening episodes (Fig. 9). Further, micro-clotted microbial boundstone beds and rare thrombolite boundstone beds interspersed within Interval I indicate that, at times, microbial mats began to develop

in the lacustrine setting. However, the relative absence of more developed thrombolite boundstone beds suggests that conditions – whether driven by water chemistry, water energy, and/or metazoan competition – were not conducive to their proliferation during this interval. Cyclicity or other consistent stratal stacking patterns like those resolved in some lacustrine carbonate strata (e.g., Kelts & Hsü, 1978; Fischer & Roberts, 1991; Drummond et al., 1996; Tänavsuu-Milkeviciene et al., 2017) are not observed in Interval I. The dominance of bioturbated peloidal packstone beds and absence of boundstone beds towards the top of Interval I indicates that biological productivity was high during the culmination of Interval I (Fig. 9).

Member B Interval II – Alkaline, microbialiate-dominated setting:

Thrombolite boundstone beds and less abundant micro-clotted microbial boundstone beds are the only facies present between approximately 420 m and 450 m in the Mainline transect (Fig. 9, Interval II). This interval, in both the Mainline and Sheep Pass Canyon transects, is also marked by a general absence in all other facies, as well as a notable decrease in bioclasts (i.e., ostracods, gastropods, bivalves and charophyte algae) compared to Interval I. Overall, this interval is interpreted as a relatively stable and shallow, littoral lacustrine setting with few invertebrates or charophyte algae (Fig. 12, Member B – Interval II).

The presence of boundstone beds spanning the Mainline to Sheep Pass Canyon transects highlights the lateral extent of microbial mat development in the SPF type section during this time. The Member B Slope transect also includes some laminated

peloidal packstone beds (Fig. 9). This suggests that in certain parts of the depositional environment, mid to high water energy promoted the formation of bedforms and limited thrombolite development. The succession of development observed in thrombolite boundstone beds indicates that thrombolite bioherms experienced continuous and more complex growth over time. Overall, Interval II is interpreted as a simpler shallow lacustrine setting compared to the more varied and dynamic depositional environment in Interval I, though both reflect balanced-fill lake basins (Carroll & Bohacs, 1999). Interval II is characterized by calcitic mineralogy like Interval I (Fig. 7). However, the absence of calcifying bioclasts and charophyte algae suggest distinct water chemistry compared to Interval I (see Discussion).

Member B Interval III – Evaporitic, marginal shoreline setting:

Upper Member B, from 450 m to the Member B-C contact, is composed of a mix of facies including mudstones to wackestones (undifferentiated mudstone to wackestone, vuggy wackestone), packstones (laminated peloidal packstone, bioturbated peloidal packstone), grainstones (peloidal grainstone), and less abundant boundstones (micro-clotted microbial boundstone, thrombolite boundstone) (Fig. 9, Interval III). Notably, the bioclast-rich wackestone to packstone facies is absent. Given this, Interval III is interpreted to reflect fluctuation between a shallow lake shoreline and a low-energy wetland setting (littoral to eulittoral); these facies transitions highlight that Interval III experienced periodic fluctuations in lake level, which included episodes of subaerial exposure (Fig. 12, Member B – Interval III).

These characteristics are consistent with deposition in a hydrologically closed, underfilled lake basin (Platt & Wright, 1991; Carroll & Bohacs, 1999). The presence of clast-supported conglomerate beds in the Member B Slope indicates that the more shoreward sections included fluvial deposition at times.

Mineralogy from Interval III strata is dominantly characterized by dolomite and quartz, with a rare occurrence of calcite (Fig. 7). The authors interpret the dolomite to be likely non-diagenetic (i.e., either primary or penecontemporaneous, *sensu* Wolfbaur & Surdam (1974)) and a reflection of precipitation in a shallow, at least periodically evaporative setting, much like saline and highly alkaline lake systems where modern dolomite is forming (De Deckker & Last, 1988, 1989; Rosen et al., 1989; Last, 1990; Last & De Deckker, 1990; Warren, 1990; Alonso Zarza et al., 1992; Meister et al., 2011; Mather et al., 2018). Dolomite has also been associated with evaporative conditions in ancient lake systems (Wolfbauer & Surdam, 1974; Arenas et al., 1997; García Del Cura et al., 2001; Arribas et al., 2004; Bowen et al., 2008; Sarg et al., 2013; Casado et al., 2014; Wanas & Sallam, 2016; Guo et al., 2023; Pommer et al., 2023). Given that Interval III includes palustrine deposition, dolomite formation was also likely influenced by the mixing of surface water and groundwater (Alonso-Zarza, 2003). This dolomite formation mechanism has been documented in both modern and ancient settings (Folk & Land, 1975; García Del Cura et al., 2001; Guo et al., 2023; McCormack et al., 2024).

Fine-grained, euhedral crystals with no cement characterize the primary dolomite in modern settings (De Deckker & Last, 1988, 1989; Rosen et al., 1989;

Meister et al., 2011) and homogeneous, densely packed micritic dolomite lacking coarse crystalline textures is a common characteristic of dolomite interpreted to be primary to penecontemporaneous in the geologic record (Wolfbauer & Surdam, 1974; e.g., Sarg et al., 2013; Wanas & Sallam, 2016; Guo et al., 2023); these characteristics are similar to dolomite in the SPF type section. Microbially-mediated processes can also influence dolomite formation (García Del Cura et al., 2001; Wright & Wacey, 2004; Li et al., 2020; Mather et al., 2023; Pommer et al., 2023). The stratigraphic distribution of dolomite (i.e., in distinct intervals rather than associated with a specific facies such as the thrombolite boundstone) suggests that this mechanism may not have been a major driver of dolomite formation in the SPF type section, although it cannot be ruled out as a possible contributor. At the very top of Member B near the Member B-C contact, poorly developed thrombolite boundstone beds present in both the Mainline and Sheep Pass Canyon transect revert to calcitic mineralogy (Fig. 7). This shift suggests that a final transition to less evaporatively-influenced lake water marked the culmination of this major lacustrine phase in the Sheep Pass Basin.

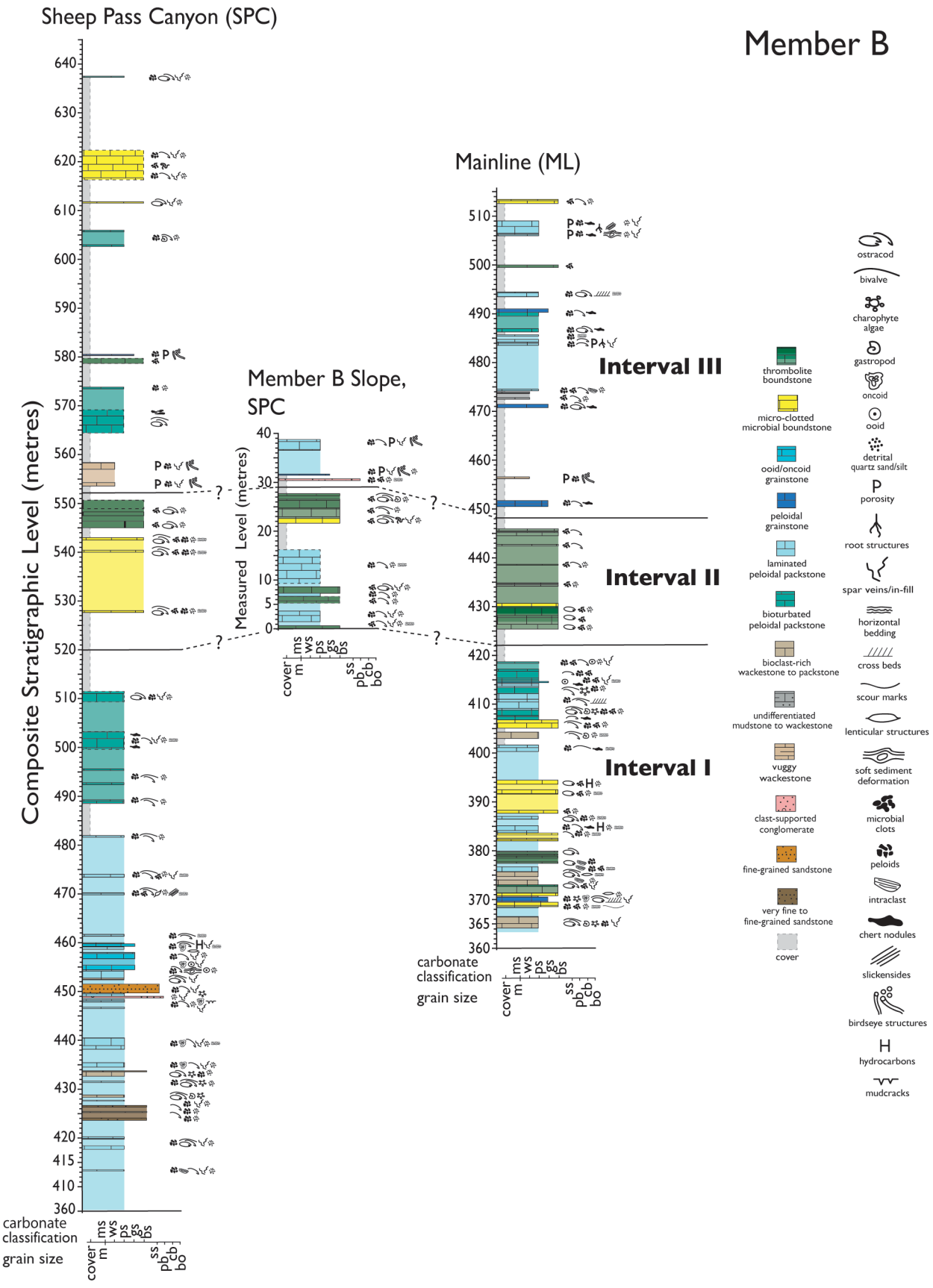
Sheep Pass Canyon (SPC)
Member B
Composite Stratigraphic Level (metres)
Member B Slope, SPC
Measured Level (metres)
Mainline (ML)
Interval III
Interval II
Interval I
carbonate classification
grain size
cover
m
ms
ws
ps
gs
bs
ss
pb
cb
bo
thrombolite boundstone
micro-clotted microbial boundstone
ooid/oncoid grainstone
peloidal grainstone
laminated peloidal packstone
bioturbated peloidal packstone
bioclast-rich wackestone to packstone
undifferentiated mudstone to wackestone
vuggy wackestone
clast-supported conglomerate
fine-grained sandstone
very fine to fine-grained sandstone
cover
ostracod
bivalve
charophyte algae
gastropod
oncoid
ooid
detrital quartz sand/silt
P
porosity
root structures
spar veins/in-fill
horizontal bedding
cross beds
scour marks
lenticular structures
soft sediment deformation
microbial clots
peloids
intraclast
chert nodules
slickensides
birdseye structures
H
hydrocarbons
mudcracks

Figure 2-9: Composite stratigraphic column of Member B for Sheep Pass Canyon, Member B Slope, and Mainline measured transects. Tie-lines indicate observed transitions between Intervals I to III in each transect but are not stratigraphically correlated. Shading in thrombolite boundstone facies denotes beds with majority small clots (light green), large clots (medium green) or a framework of clots (dark green).

2.5.2.3 Member C – Fluvio-deltaic stage:

Member C largely comprises siliciclastic facies beds (fine to coarse-grained sandstone, very fine to fine-grained sandstone, clast-supported conglomerate) and less abundant interbedded carbonates (laminated peloidal packstone, bioturbated peloidal packstone, bioclast-rich wackestone to packstone, micro-clotted microbial boundstone, peloidal grainstone, oncoid packstone to grainstone, undifferentiated mudstone to wackestone) (Figs 10 and S1). Given this, Member C is interpreted as reflecting deposition in a dominantly fluvial environment, likely with adjacent deltaic or rare shallow lacustrine deposition similar to previous interpretations by Fouch (1979) (Fig. 12, Member C).

The abundance of fine to coarse-grained sandstones is interpreted to reflect deposition within sandy-bedded braided rivers. Rare metre-scale, laterally traceable, clast-supported conglomerate channel deposits with basal scours suggest that, at times, the gravel-sand transition migrated down-dip, perhaps in response to higher flow conditions. Previous studies inferred a dominantly westward direction of transport in Member C rivers, consistent with transport directions in Member A (Druschke et al., 2009a). The interbedded nature of very fine to fine-grained sandstones and less abundant carbonates with the fine to coarse-grained sandstone

and clast-supported conglomerate beds is interpreted to reflect lower-energy depositional environments adjacent to the fluvial environment; deposition was either in an overbank environment adjacent to the river channels or possibly in a deltaic setting. The presence of shallow lacustrine facies supports the interpretation that there was still a lake that resulted in transient expansions into the Mainline transect area during Member C time.

Member C carbonates are composed of calcite from the base of Member C up to 693 m in the Mainline transect (Fig. 7; Fig. 12, lower Member C). At 693 m, dolomite dominates for the remainder of Member C. The authors interpret this as a shift to more saline or highly alkaline water, which can occur in response to groundwater mixing or evaporative concentration of surface waters like in Member B Interval III (Fig. 7; Fig. 12, upper Member C) (Alonso-Zarza, 2003; Guo et al., 2023). Interestingly, this mineralogical transition corresponds to the approximate stratigraphic level of a frog fossil deathbed horizon (see Taphonomic Mode 5 in Bonde et al., 2020). Thus, this water chemistry change and the cause of the mass die-off of the frog population associated with this horizon in Member C could be causally related.

The detrital zircon sample from Member C showed peaks in U-Pb ages between 1 to 2 Ga, *ca* 500 Ma, and *ca* 150 Ma. This sample also contained a small population of zircons (n = 3) that cluster around 62 Ma (62.2 ± 0.4 Ma, 63.3 ± 0.8 Ma, and 58.5 ± 1.3 Ma, 1σ internal uncertainty; Supplemental Materials). The weighted mean age of this youngest population gives a maximum depositional age of 62.14 ± 0.65 Ma (± 2σ) for this interval within Member C (Fig. 7).

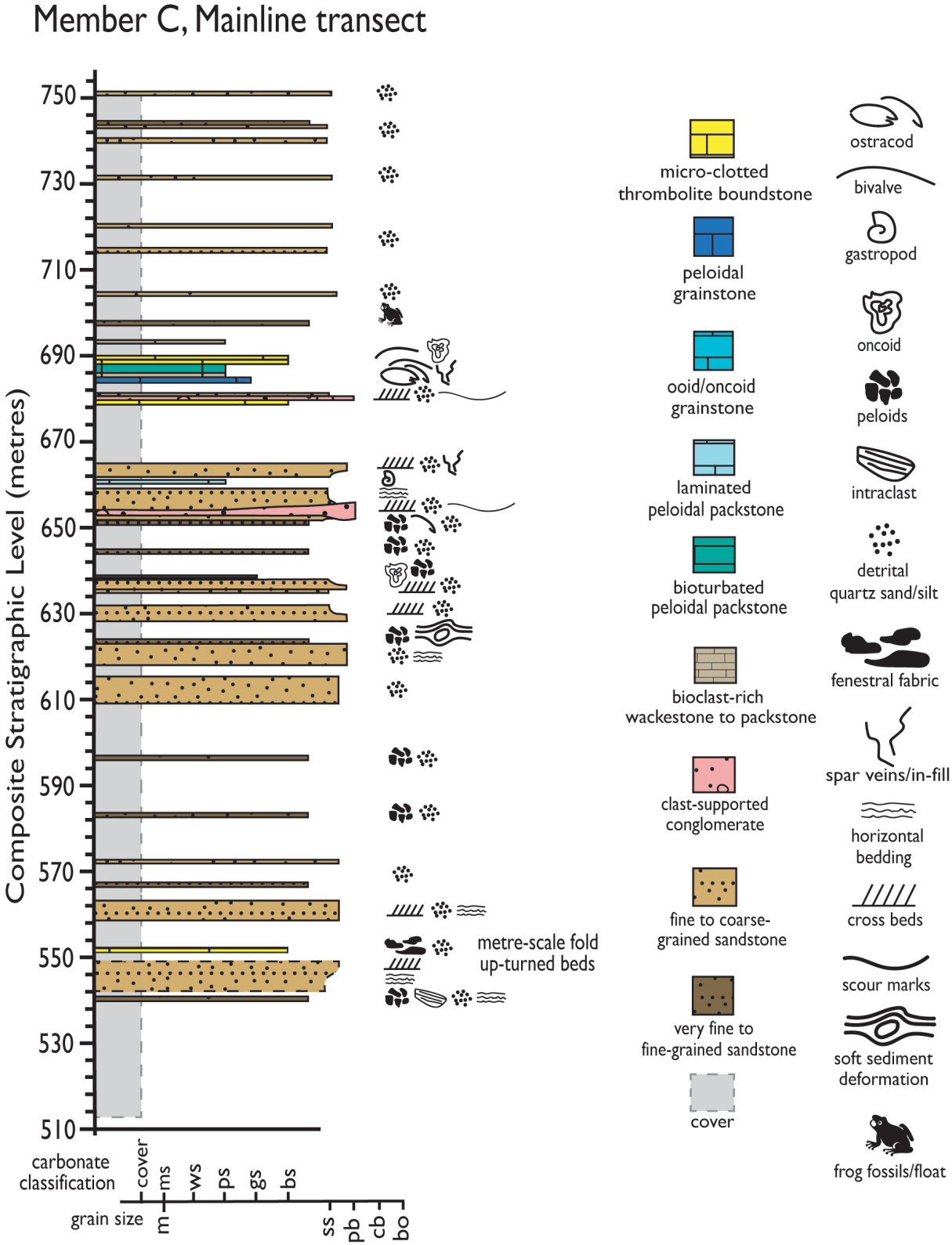

Figure 2-10: Composite stratigraphic column of Member C, Mainline measured transect.

2.5.2.4 Member D – Major palustrine stage:

Member D has a sharp basal contact with underlying Member C, which was previously interpreted as a depositional hiatus by Druschke et al. (2011). Member D also has a markedly different lithology compared to all other members in the SPF type section. Outcropping beds are sparse, and outcrops were often best observed from pits dug through the modern colluvium. Dominant facies include the mudstones to wackestones (undifferentiated mudstone to wackestone and vuggy wackestone) with rare occurrences of the bioclast-rich packstone to wackestone facies or laminated peloidal packstone facies (Fig. 11). Together, these facies are interpreted as reflecting palustrine deposition in a shallow, low-energy wetland setting that experienced frequent subaerial exposure within the eulittoral to supralittoral zone (Fig. 12, Member D). Evidence for evaporite minerals in the undifferentiated mudstone to wackestone facies (for example, gypsum pseudomorphs and length-slow chalcedony) suggests that evaporative conditions were also common at times. Mineralogy of Member D samples is characterized by dolomite, which is interpreted to indicate more saline or highly alkaline conditions in response to evaporative conditions and groundwater mixing during this time, similar to Member B Interval III (Fig. 7; Alonso-Zarza, 2003; Guo et al., 2023). A close association between dolomite and evaporite minerals like gypsum or halite has also been recognized in modern and ancient lacustrine settings (Warren, 1990; Arenas et al., 1997). Thus, Member D is

interpreted to reflect a depositional setting comprising a sparse wetland terrain with at least periodically evaporative conditions.

2.5.2.5 Member E – Ephemeral lacustrine stage:

Member E has a gradational lithological contact with underlying Member D and comprises bioclast-rich wackestone to packstone beds (Fig. 11). Mineralogically, Member E is characterized by calcite (Fig. 7). Given this, as well as the presence of charophyte algae in the bioclast-rich wackestone to packstone, the authors interpret that deposition was occurring in fresh, carbonate-supersaturated lake water similar to Member B Interval I. Despite a superficial similarity in facies and mineralogy between Members B and E, the dominance of bioclast-rich wackestone to packstone beds, along with its limited stratigraphic extent (<20 m) suggests that the depositional setting in Member E is distinct from Member B. Past work by Good (1987) used modern analogs of molluscan associations in Member E to characterize the depositional setting as that of an expansive freshwater wetland terrain comprised of isolated ponds rather than a single, large lake as in Member B. However, Member E lacks palustrine facies (for example, undifferentiated mudstone to wackestone) or any other subaerial exposure and modification features common in freshwater wetland settings (Wright & Platt, 1995; Alonso-Zarza & Wright, 2010). Thus, Member E is interpreted to reflect a depositional setting limited to freshwater ponds or a small lake, rather than an expansive lake basin as in Member B or a wetland terrain as in Member D (Fig. 12, Member E).

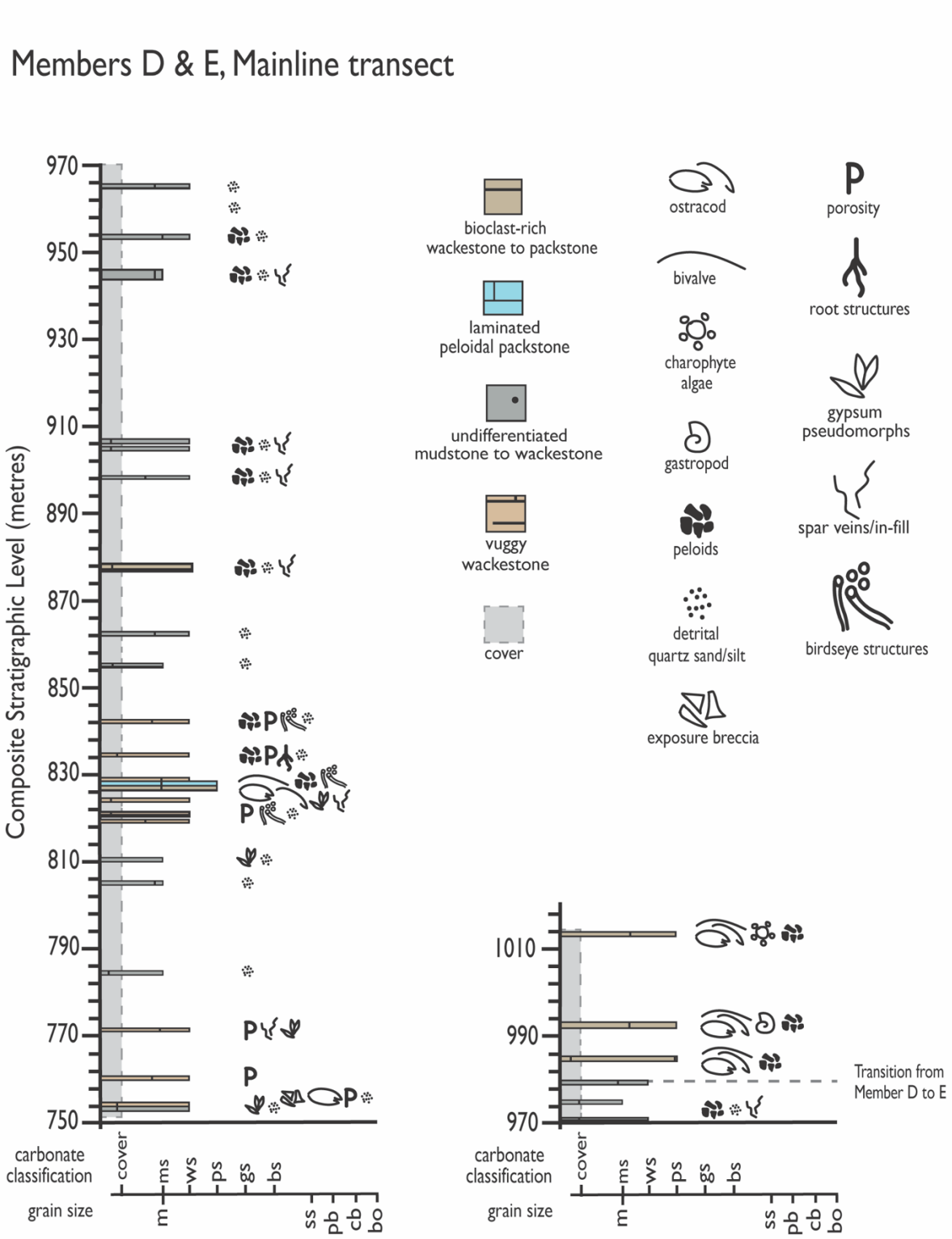

Figure 2-11: Composite stratigraphic column of Members D and E, Mainline measured transect. Note the grey dashed line marking the Member D to Member E transition.

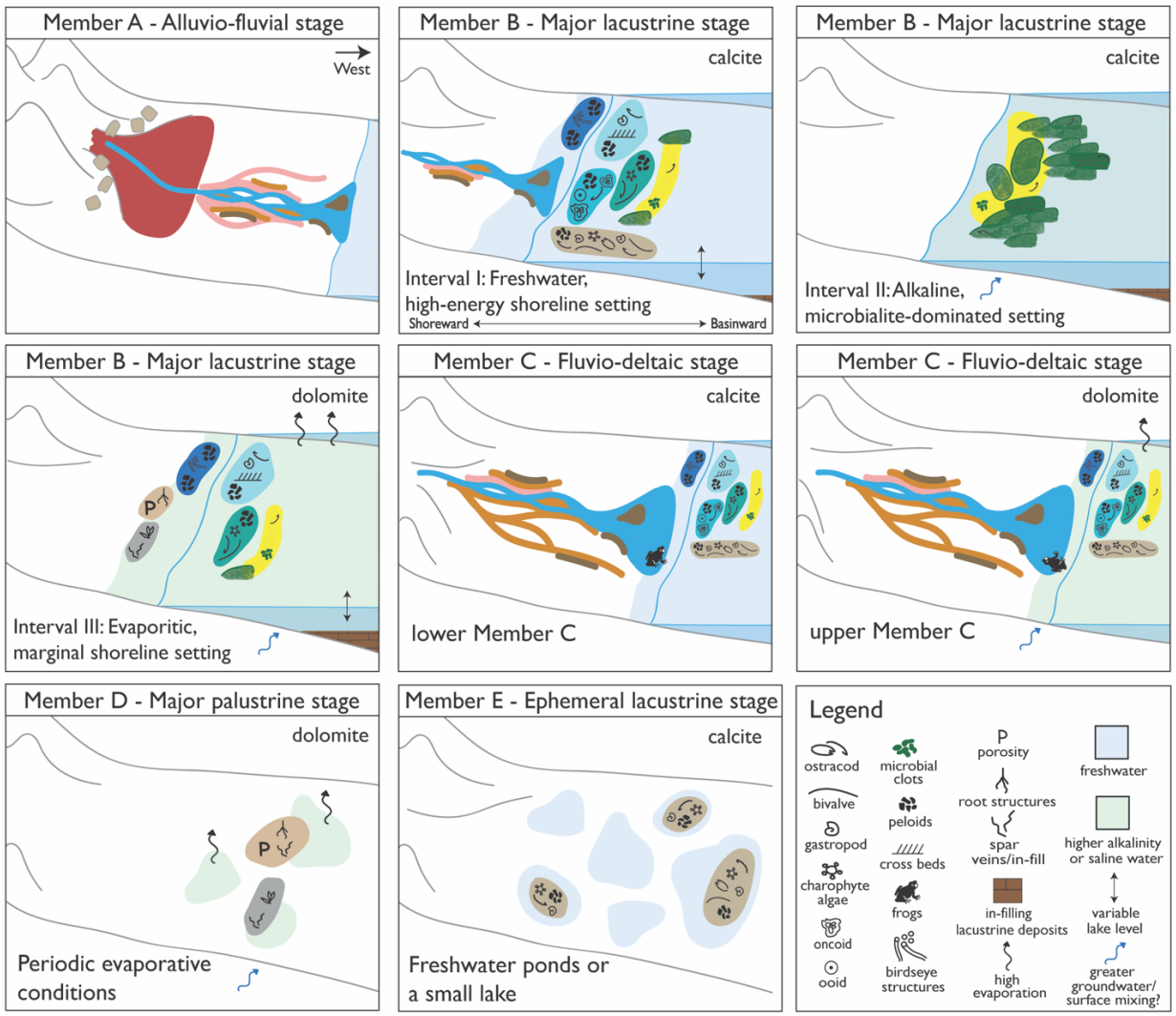

Figure 2-12: Environmental evolution of the Sheep Pass Formation (SPF) lake basin between each member, including within Member B (Intervals I to III) and at lower and upper Member C. Facies colours map to those in Figs 2 to 11. Labeled west arrow represents the approximate palaeo-west direction based on interpretations of palaeoflow indicators from Drushke et al. (2009a) and references therein.

2.6 Discussion

2.6.1 Thrombolite Persistence in a Dynamic Sheep Pass Basin

Although the sedimentology of the SPF type section closely resembles that of other Paleogene-aged lacustrine basins in the western USA (for example, the Green River Formation or the Flagstaff Formation), its paleobiological record is notably different from these other formations (Bowen et al., 2008; Smith et al., 2008). For example, the Green River Formation contains invertebrate shells, insect and insect casing fossils, plant and fish fossils, rare mammalian, bird, and reptile fossils, and microbialites (Hanley, 1976; Buchheim & Surdam, 1977; Greenwood & Wing, 1995; Smith et al., 2008; Seard et al., 2013; Smith & Carroll, 2015). Even the Elderberry Canyon section, a small succession of middle Eocene carbonates only *ca* 50 km north of the SPF type section, preserves diverse fauna comprising birds, frogs, reptiles, and mammals (Fouch, 1979; Emry & Korth, 1989; Emry, 1990). In contrast, the SPF type section is largely limited to invertebrate shells, isolated plant fossil horizons, and frog fossil bonebed horizons; it is the abundant thrombolite boundstones within Member B that define the paleobiological record in the SPF type section (Fouch, 1979; Good, 1987; Swain, 1987; Henrici et al., 2018; Bonde et al., 2020).

The dynamic environmental evolution of the Sheep Pass Basin – with evidence for frequent and major transitions in the depositional setting both between and within members – suggests that this shallow lake ecosystem was extremely sensitive to small-scale environmental changes. The relatively small extent of the Sheep Pass Basin (kilometre-scale) made it susceptible to even minor shifts in basin hydrology (Platt & Wright, 1991). Abrupt, and sometimes episodic, changes to hydrological basins can lead to shifts in water chemistry or other physicochemical controls that

affect metazoan populations (e.g., Wrona et al., 2006; Bergner et al., 2009; Woolway et al., 2020; Frantz et al., 2023). The proliferation of microbial mats in place of a more complex metazoan food web supports the interpretation that the Sheep Pass basin hosted a dynamic, isolated lake system that was unable to sustain diverse metazoan populations for extended periods of time. This interpretation is supported by evidence from Bonde et al. (2020) for multiple frog fossil mortality events that suggest metazoan populations thrived in the Sheep Pass Basin at times, but also experienced episodes of significant population collapse.

The proliferation of SPF type section thrombolite boundstones, particularly in Interval II of Member B, suggests that the microbial mats benefited from: (i) physicochemical conditions that favored their accretion and cementation; paired with (ii) lower predation from metazoan grazers as evidenced by a general absence of invertebrate fossils and freshwater charophyte algae compared to Interval I.

Previous work has demonstrated that ancient microbialites persisted in a range of physicochemical conditions in lakes. For example, Green River Formation microbialites have been interpreted as reflecting nearshore growth in clear, warm, saline to alkaline lake water (Buchheim & Surdam, 1977; Surdam & Stanley, 1979; Roehler, 1993; Schieber, 2007; Awramik & Buchheim, 2015; Tänavsuu-Milkeviciene et al., 2017; Birgenheier et al., 2020; Eljalafi & Sarg, 2021; Ingalls et al., 2022; Pommer et al., 2023). Eljalafi & Sarg (2021) found a positive correlation between the abundance and diversity of Green River Formation microbialite morphologies with periods of higher salinity and alkalinity, likely driven by greater erosion of carbonate

bedrock and more evaporative conditions (Pommer et al., 2023). Frantz et al. (2014) also showed evidence for significant changes in lake volume, depth, and chemistry over the time scale of microbialite growth, suggesting Green River Formation microbialites persisted despite major hydrological changes to the basin. Lastly, Ingalls et al. (2022) argued that low lake levels and warm temperatures were critical in reaching the carbonate saturation state needed to rapidly precipitate giant Green River Formation stromatolites.

Modern lacustrine microbialites are also observed in a variety of conditions, including fresh to hypersaline water (Gischler et al., 2008; Chagas et al., 2016). For example, Fayetteville Green Lake (New York) hosts thrombolites in freshwater where mound growth is largely driven by light availability (Thompson & Ferris, 1990). Interestingly, Fayetteville Green Lake has a paucity of macroscopic invertebrates despite its freshwater littoral setting (Harman & Jackson, 1967; Thompson & Ferris, 1990). Great Salt Lake (Utah) also hosts thrombolitic microbialites, but in hypersaline water with a limited metazoan aquatic ecological web mostly comprising small arthropods. The shallowly graded Great Salt Lake basin also experiences dramatic shifts in lake shoreline, which subaerially expose microbialites at different times of the year (Frantz *et al.*, 2023). Further, microbialites in Laguna Bacalar (Mexico) thrive in carbonate-rich waters that Gischler et al. (2008) argue are crucial for microbialite accretion and cementation to outweigh bioerosion from metazoan grazers. In fact, alkaline water chemistry is a common trait among modern microbialite lakes, and has been found to be associated with microbialite size (Iniesto

et al., 2021; Caumartin et al., 2023). Lastly, a comparison of modern microbialite-forming environments by Gischler et al. (2008) concluded that most freshwater lacustrine settings contain abundant grazers. However, both Fayetteville Green Lake and Great Salt Lake highlight that microbialites, whether in fresh or saline water, may also benefit from environments with lower predation pressure from metazoan grazers.

Thus, this study interprets the stratigraphic distribution and morphology of thrombolite boundstones, particularly in Interval II of the major lacustrine phase in the Sheep Pass basin (Figs 2, 9 and 12), to reflect microbial mat accretion and cementation under unique physicochemical conditions (for example, higher alkalinity compared to Interval I), paired with lower competition from metazoan grazers under these conditions. This niche depositional environment led to the proliferation of microbialites during this time.

Interestingly, recent work by Frantz et al. (2023) highlights that, even in a hypersaline environment, modern microbialite persistence can be limited by increased salinity and prolonged exposure from lake level changes. The transition into Interval III, a marginal setting with evaporative conditions, suggests that the microbialite-dominated Interval II ultimately concluded in response to yet another change in physicochemical conditions in this dynamic lake basin. Thus, the microbialite-dominated interval marks a transitional stage in the major lacustrine phase from a hydrologically open to closed lake basin. Microbialite-rich intervals have been associated with transitional lake stages in other ancient lacustrine basins like

the Green River Formation (Tänavsuu-Milkeviciene & Sarg, 2012; Sarg et al., 2013; Seard et al., 2013; Eljalafi & Sarg, 2021; Ingalls et al., 2022). The recognition and characterization of microbialite-abundant intervals in palaeo-lake archives could help constrain the drivers of microbialite proliferation and better leverage these intervals as recorders of paleoenvironmental change.

2.6.2 Drivers of Environmental Change in the Sheep Pass Basin

In lacustrine systems, both tectonics and climate influence basin hydrology and morphology through the iterative balance between potential accommodation space, erosion and sediment supply, and water input (Carroll and Bohacs, 2000; Platt and Wright, 1991). Potential accommodation space is mostly controlled by tectonics, while climate largely affects sediment and water supply, as well as biological productivity (Platt & Wright, 1991; Carroll & Bohacs, 1999). Given that the SPF type section reflects a synorogenic basin deposited during a time of known greenhouse climate (Druschke et al., 2009a, 2011), it is likely that both tectonics and climate drove environmental changes at various stages in the evolution of the Sheep Pass Basin. Here, we lay out the most likely drivers for the environmental changes observed throughout the SPF type section, with particular focus on the major lacustrine phase represented by Member B.

Deposition began within an alluvial fan and fluvial system in Member A time, with strong topographic relief and a water source that, together, drove erosion and sediment transport (Fig. 12, Member A). An increase in accommodation space from basin initiation (driven by localized extension described previously by Druschke et al.

(2009a, 2009b)) limited the output of water from the basin and eventually led to the formation of a shallow, carbonate-forming lake (Member B), whose water chemistry was likely influenced by the surrounding Paleozoic carbonate bedrock in the catchment area (Platt & Wright, 1991).

This dynamic, low-gradient lacustrine environment was highly sensitive to external changes; it began as a mid to high-energy, invertebrate-abundant, calcite-forming, freshwater balanced-fill lake basin with evidence for multiple shifts in dominant shoreline facies, as well as several episodes of lake water freshening (Fig. 12, Member B – Interval I). A notable shift to an invertebrate-poor, microbialite-dominated setting was likely in response to a change in physicochemical conditions (for example, higher alkalinity and/or salinity) in the lake basin (Fig. 12, Member B – Interval II). Lastly, the transition to a marginal lake to wetland setting with dominant dolomitic mineralogy marked the end of abounding thrombolites, and a shift to periodically evaporative conditions in an underfilled lake basin during the culmination of the major lacustrine phase (Fig. 12, Member B – Interval III).

Given previously described evidence for syn-tectonic deposition – including mass movement of transported sediment during the major lacustrine phase (Druschke et al., 2009a) – changes in accommodation space likely exerted a dominant control on the frequent shifts between depositional settings in the initial high-energy shoreline lake environment (Fig. 12, Member B – Interval I). The contribution of minor siliciclastic beds and lack of subaerial exposure features suggests consistent water and sediment input into the basin during this time. Overall, this dynamic

lacustrine shoreline setting resembles freshwater lake stages characterized in the Green River Formation (fresh lake; Tänavsuu-Milkeviciene & Sarg, 2012; Sarg et al., 2013) and Flagstaff Formation (early highstand; Bowen et al., 2008). However, the absence of observed climate-driven cyclicity, although common in other larger sedimentary basins (e.g., Green River Formation, see Tänavsuu-Milkeviciene et al., 2017), indicates that the preservation of contemporaneous climate-driven depositional trends at the beginning of the major lacustrine phase was likely overshadowed by tectonically driven changes (Keighley et al., 2003).

The shift to a more stable microbialite-dominated setting (Fig. 12, Member B – Interval II) suggests that changes in accommodation space, though still present, may have been less influential in this depositional stage. The interpreted shift in physicochemical conditions (for example, higher alkalinity and/or salinity) could have been driven by a greater contribution of groundwater versus surface or meteoric water (Alonso-Zarza, 2003; Platt & Wright, 2023), greater erosion of the carbonate bedrock, or a shift to lower sediment and water supply under more arid climatic conditions (Eljalafi & Sarg, 2021). Overall, these variables suggest a climate-driven change in water chemistry; this agrees with previous interpretations that climate largely drove microbialite distribution in the Green River Formation (Tänavsuu-Milkeviciene & Sarg, 2012; Sarg et al., 2013; Birgenheier et al., 2020; Eljalafi & Sarg, 2021; Pommer et al., 2023). Notably, the calcitic mineralogy recorded in this depositional interval indicates that the climate-driven physicochemical change in water chemistry appears to have not affected primary mineralogy.

The transition to a marginal lacustrine to wetland setting (Fig. 12, Member B – Interval III) suggests that fluctuations in lake level, to the point of subaerial exposure and periodic evaporative conditions, characterized this depositional interval (Alonso-Zarza & Wright, 2010). This indicates that either there was little to no new accommodation space being created through tectonic activity, or that water and sediment input had drastically decreased due to climatic forcing. In low-gradient basins, palustrine deposition can occur in response to even subtle decreases in accommodation space and/or aquifer rise and groundwater emergence, the latter of which can be both climatically or tectonically driven (Wright & Platt, 1995; Platt & Wright, 2023). However, climate also causes frequent shoreline fluctuations and has been cited as an important driver in many ancient palustrine systems that resemble this depositional interval (Platt, 1989; Alonso-Zarza, 2003; Dunagan & Turner, 2004). It is possible that the rate of deposition over the major lacustrine phase eventually outpaced the rate that accommodation space formed. However, the dolomitic mineralogy that characterizes this stage suggests that likely climate-driven evaporative conditions, paired with contributions from groundwater, were also common during this time. Thus, the marginal lacustrine to wetland setting may have formed in response to some accommodation space-related changes but was largely influenced by climate.

The shift to a fluvio-deltaic setting in Member C time marked the return to a siliciclastic-dominated system (Fig. 12, lower Member C). According to Druschke et al. (2009a), new accommodation space was likely being created, but not at the rate

needed to accommodate a lake such as in Member B. Tectonic activity could have also affected the position of the lake basin outlet, leading to the draining of the vestiges of the lake. However, the calcitic mineralogy and rare shallow lacustrine facies within this majority fluvial environment support the presence of a transient freshwater lake whose locus of deposition had shifted basinward. In the Green River Formation, fluvial intervals like this are associated with climatically driven cyclic deposition and high rates of precipitation and erosion (e.g., Tänavsuu-Milkeviciene et al., 2017; Birgenheier et al., 2020). Thus, a coupled response to climate and tectonics is likely reflected in Member C. Notably, the transition from calcitic to dolomitic mineralogy towards the top of this depositional interval suggests that there was a change in groundwater mixing and/or more evaporative concentration of surface waters which lead to saline or highly alkaline conditions (Fig. 12, upper Member C) (Alonso-Zarza, 2003; Guo et al., 2023). Similar to the mineralogical shift in Member B Interval III, we interpret the transition to dolomitic mineralogy in upper Member C to have been largely driven by climate.

The fluvio-deltaic system was followed by a wetland setting (Member D) characterized by frequent subaerial exposure and the continuation of dolomitic mineralogy under periodically evaporative conditions, possibly with a marked depositional hiatus between these two environments (Fig. 12, Member D). Like in Member B Interval III, the dominant wetland setting with dolomitic mineralogy suggests fluctuations in water level were common, but under very limited accommodation space. The absence of a more long-lived lacustrine setting during this

depositional interval also indicates that little to no accommodation space was being created by this time and that water and sediment input may have also been limited. The Jurassic Morrison Formation (USA) preserves an ancient groundwater-fed wetland setting under arid conditions with only intermittent meteoric or surface water input (Dunagan & Turner, 2004). The wetland setting in Member D, with features characteristic of the Morrison Formation, could reflect a similar mechanism, ultimately indicating that climate exerted a dominant control on this depositional setting.

Lastly, Member E time marked a Sheep Pass Basin depositional environment confined to isolated freshwater ponds or a small lake with many invertebrates and charophyte algae like in Member B Interval I (Fig. 12, Member E). However, the limited extent of this depositional setting compared to the major lacustrine phase suggests that even with sufficient sediment and water supply, accommodation space was extremely limited, possibly due to minimal local tectonic activity during this time. This aligns with previous conclusions by Druschke et al. (2009a) that following tectonic activity during deposition of Members A to C, the basin-bounding fault in the SPF type section locality did not reactivate until middle to late Eocene time.

2.6.3 The Expression of Global Climate Change in the Sheep Pass Basin

Given the existing SPF age framework, it is reasonable to infer that global climate change – including changes associated with the Cretaceous-Palaeogene (K-Pg) mass extinction or hyperthermals such as the PETM, and long-term warming from the mid-Palaeocene to the EECO – played a role in environmental change in the

Sheep Pass Basin. Previous studies have concluded that the SPF type section formed in a temperate, freshwater lake environment, with relatively cool temperatures resulting from the high-elevation of the Sheep Pass Basin (Good, 1987; Druschke et al., 2009a, b; Snell et al., 2014; Bonde et al., 2020). This current work suggests that, at least during certain intervals, the Sheep Pass Basin also experienced significant changes to its metazoan populations and physicochemical conditions likely associated with a climate forcing. Given that high-elevation settings are particularly sensitive to climate change (Rangwala et al., 2013; Pepin et al., 2015), characterizing the expression of global climate in the Sheep Pass Basin has the potential to add a nuanced perspective to existing paleoclimate records from this time.

Four environmental intervals stand out as major focus points for future work constraining the role of global climate events in environmental change within the Sheep Pass Basin: (i) the microbialite-dominated interval, with evidence for a change in physicochemical conditions that allowed for the accretion and lake basin-wide expansion of thrombolites without significant competition from metazoan grazers; (ii) the underfilled lake basin interval following the microbialite-dominated interval, with evidence for lower lake levels and dolomite formation under more evaporative conditions, ultimately leading to the culmination of the major lacustrine phase; (iii) the shift to dolomitic mineralogy in upper Member C that is stratigraphically adjacent to a previously documented frog fossil deathbed horizon (Bonde et al., 2020); and (iv) a sustained transition to a wetland terrain in Member D, with evidence for persistent alteration from subaerial exposure, limited meteoric or surface water

input, and dolomite and evaporite deposition under periodically evaporative conditions.

The new U-Pb detrital zircon age in the SPF type section (62.14 ± 0.65 Ma) provides a mid-Palaeocene or younger age constraint within Member C of the Mainline transect (Fig. 7). This new date suggests that, if recorded in the SPF type section, the K-Pg boundary likely lies somewhere between the base of Member B and middle Member C. The microbialite-dominated interval in Member B, associated with niche physicochemical conditions paired with low invertebrate abundance, could reflect an environmental change in response to the K-Pg mass extinction. In fact, others have suggested that a mass extinction event could drive extensive microbialite development in response to environmental exclusion or the complete absence of competitor organism abundance (Riding, 2006; Mata & Bottjer, 2012; Chen & Lee, 2014). However, this speculation warrants further investigation and highlights the critical need for additional chronostratigraphic constraints so that the SPF type section sedimentological framework can be put into a more precise temporal context.

Several studies from Palaeogene-aged lake basins in the western USA have documented notable shifts in palaeobiological, palaeohydrological, and/or palaeotemperature records in response to hyperthermal climate events during this time. Overall, warm temperatures, transient drying, and seasonal rainfall changes are associated with the PETM in the Bighorn Basin and Flagstaff Formation (see Background; Greenwood & Wing, 1995; Kraus & Riggins, 2007; Bowen et al., 2008; Kraus et al., 2013; Baczynski et al., 2017). Studies have also observed major faunal

transition and turnover in association with the onset and recovery of the PETM and early Eocene hyperthermals (e.g., ETM2 and H2) in the Bighorn Basin (Clyde & Gingerich, 1998; Van Der Meulen et al., 2020; Widlansky et al., 2022). The Green River Formation preserves evidence for a warm, arid, and monsoonal climate during the Early Eocene Climatic Optimum (Surdam & Stanley, 1979; Smith et al., 2008; Tänavsuu-Milkeviciene & Sarg, 2012; Seard et al., 2013; Frantz et al., 2014; Tänavsuu-Milkeviciene et al., 2017; Birgenheier et al., 2020; Pommer et al., 2023). This led to highly cyclic sedimentation of fluvio-deltaic and marginal lacustrine facies, similar to the deposition of fluvial facies in response to early Eocene hyperthermal events in the Bighorn Basin during this time (Abels et al., 2016). Evaporite deposition was also common in parts of the Greater Green River Basin during the early Eocene; notably, some major periods of evaporite deposition are associated with the disappearance of freshwater molluscsan assemblages (Roehler, 1993; Smith et al., 2008; Tänavsuu-Milkeviciene et al., 2017). A more stable, cooler, and humid climate led to high lake level conditions in the Green River Formation following the early Eocene hyperthermal climate events and EECO (Smith et al., 2008; Tänavsuu-Milkeviciene & Sarg, 2012; Tänavsuu-Milkeviciene et al., 2017; Birgenheier et al., 2020; Pommer et al., 2023).

The major environmental intervals identified in Member B Interval III, upper Member C, and Member D all share characteristics indicative of evaporative conditions and a shift to more saline or alkaline water chemistry. Importantly, these SPF type section intervals also share similar sedimentological attributes associated

with environmental change in response to early Paleogene climate, the PETM, and early Eocene climate, as observed in other western USA terrestrial records. Further, the stratigraphic proximity of upper Member C (shift to dolomitic mineralogy) with a frog fossil deathbed horizon (Bonde et al., 2020) could suggest that the climate forcing that drove environmental change in Member C may have significantly affected metazoan populations as well. Given the current age framework in the SPF type section, constraining each of these intervals to specific time periods or events is not possible. However, geochemical evidence for high rates of evaporation (for example, higher $\delta^{18}O_{water}$ values) or warmer temperatures (for example, through carbonate clumped isotope Δ_{47} thermometry) have been found in records like the Green River Formation and Flagstaff Formation (Bowen et al., 2008; Sarg et al., 2013; Frantz et al., 2014; Ingalls et al., 2022; Pommer et al., 2023). Development of a similar geochemical record in the SPF type section would help deconvolve the relative role of tectonics and climate on environmental change within the Sheep Pass Basin. Ultimately, these key environmental intervals should serve as the focus for future studies aiming to better constrain both the chronostratigraphic and paleoclimatic record in the SPF type section.

2.7 Conclusions

The Sheep Pass Formation type section in east-central Nevada is a promising site for the ongoing development of a new, Late Cretaceous to middle Eocene high-elevation paleoclimate record. A detailed study of facies and lake basin evolution,

with particular focus on the carbonates and microbialites in the major lacustrine phase of the basin, establishes four key takeaways:

- The Sheep Pass Formation (SPF) type section reflects a dynamic and extremely sensitive high-elevation lake basin, susceptible to even subtle shifts in accommodation space and sediment/water input due to the basin's relatively small (kilometre-scale) lateral extent.
- The thrombolite boundstones that define the SPF type section palaeobiological record reflect the resilience of microbial mats compared to metazoans in this dynamic setting, and their stratigraphic distribution and morphology during the major lacustrine phase in the Sheep Pass Basin suggests that the thrombolites thrived in response to a change in physicochemical conditions (for example, higher alkalinity) paired with lower competition from metazoan grazers under these conditions.
- The major lacustrine phase (Member B) of the Sheep Pass Basin shows evidence for three distinct environmental intervals: (i) a freshwater, high-energy shoreline setting with few microbialites that transitioned to; (ii) an alkaline, microbialite-dominated interval with relatively low invertebrate abundance, before; (iii) the shift to a marginal lacustrine and wetland setting with evaporative conditions that marked the culmination of this major lacustrine phase in the basin.
- Major shifts in invertebrate abundance, dominant facies, and/or mineralogy – namely in the microbialite-dominated interval, the culmination of the major

lacustrine phase, as well as upper Member C and Member D – serve as focus points for future studies investigating the expression of global climate change in the Sheep Pass Basin. These intervals share close characteristics with other terrestrial records from this time that are known to preserve palaeobiological, palaeohydrological, and/or palaeotemperature changes in response to global greenhouse climate.

2.8 Acknowledgements

Field work and sample collection was conducted on the current and ancestral homelands, including unceded territory, of the Western Shoshone, Goshute, and Timpanogos peoples. Sedimentological and petrographic characterizations were completed at the University of Colorado Boulder, which operates on the ancestral land and unceded territory of the Arapaho, Ute, and Cheyenne peoples. We thank A. Henrici, J. Bonde, and P. Druschke for their field guidance during the planning and reconnaissance stages of this research. We also thank P. Haber for assistance with field work and A. Bell for XRD training. This work was funded by the National Science Foundation under EAR 1826850 (Snell and Trower) and 1826769 (Clyde). Additional support was provided through the National Science Foundation Graduate Research Fellowship (Olsen-Valdez). Thank you to N. Platt, M. Pommer, one anonymous reviewer, Associate Editor C. Arenas, and Chief Editor G. Mángano for their feedback which improved this manuscript.

2.9 Data Availability Statement

All additional, relevant sample data is included in a published folder on the Open Science Framework. Appendix S1, additional petrographic images, XRD spectra, and additional U-Pb data information can be found in this OSF repository (https://doi.org/10.17605/OSF.IO/3HA6X).

2.10 Works Cited

Abels, H.A., Lauretano, V., van Yperen, A.E., Hopman, T., Zachos, J.C., Lourens, L.J., Gingerich, P.D. and Bowen, G.J. (2016) Environmental impact and magnitude of paleosol carbonate carbon isotope excursions marking five early Eocene hyperthermals in the Bighorn Basin, Wyoming. *Clim. Past*, 12, 1151–1163.

Aitken, J.D. (1967) Classification and Environmental Significance of Cryptalgal Limestones and Dolomites, with Illustrations from the Cambrian and Ordovician of Southwestern Alberta. SEPM JSR. doi: 10.1306/74D7185C-2B21-11D7-8648000102C1865D

Alonso Zarza, A.M., Calvo, J.P. and García Del Cura, M.A. (1992) Palustrine sedimentation and associated features—grainification and pseudo-microkarst—in the Middle Miocene (intermediate unit) of the Madrid Basin, Spain. *Sedimentary Geology*, 76, 43–61.

Alonso-Zarza, A.M. (2003) Palaeoenvironmental significance of palustrine carbonates and calcretes in the geological record. *Earth-Science Reviews*, 60, 261–298.

Alonso-Zarza, A.M. and Wright, V.P. (2010) Palustrine Carbonates. In: *Developments in Sedimentology - Carbonates in Continental Settings: Facies, Environments, and Processes*, *Elsevier*, 61, 103–131.

Arenas, C., Casanova, J. and Pardo, G. (1997) Stable-isotope characterization of the Miocene lacustrine systems of Los Monegros (Ebro Basin, Spain): palaeogeographic and palaeoclimatic implications. *Palaeogeography, Palaeoclimatology, Palaeoecology*, 128, 133–155.

Arribas, M.E., Bustillo, A. and Tsige, M. (2004) Lacustrine chalky carbonates: origin, physical properties and diagenesis (Palaeogene of the Madrid Basin, Spain). *Sedimentary Geology*, 166, 335–351.

Awramik, S.M. and Buchheim, H.P. (2015) Giant stromatolites of the Eocene Green River Formation (Colorado, USA). *Geology*, 43, 691–694.

Baczynski, A.A., McInerney, F.A., Wing, S.L., Kraus, M.J., Bloch, J.I. and Secord, R. (2017) Constraining paleohydrologic change during the Paleocene-Eocene Thermal Maximum in the continental interior of North America. *Palaeogeography, Palaeoclimatology, Palaeoecology*, 465, 237–246.

Bergner, A.G.N., Strecker, M.R., Trauth, M.H., Deino, A., Gasse, F., Blisniuk, P. and Dühnforth, M. (2009) Tectonic and climatic control on evolution of rift lakes in

the Central Kenya Rift, East Africa. *Quaternary Science Reviews*, 28, 2804–2816.

Birgenheier, L.P., Berg, M.D.V., Plink-Björklund, P., Gall, R.D., Rosencrans, E., Rosenberg, M.J., Toms, L.C. and Morris, J. (2020) Climate impact on fluvial-lake system evolution, Eocene Green River Formation, Uinta Basin, Utah, USA. *GSA Bulletin*, 132, 562–587.

Bonde, J.W., Druschke, P.A., Hilton, R.P., Henrici, A.C. and Rowland, S.M. (2020) Preservation of latest Cretaceous (Maastrichtian)—Paleocene frogs (*Eorubeta nevadensis*) of the Sheep Pass Formation of east-central Nevada and implications for paleogeography of the Nevadaplano. *PeerJ*, 8, e9455.

Bowen, G.J., Beerling, D.J., Koch, P.L., Zachos, J.C. and Quattlebaum, T. (2004) A humid climate state during the Palaeocene/Eocene thermal maximum. *Nature*, 432, 495–499.

Bowen, G.J., Daniels, A.L. and Bowen, B.B. (2008) Paleoenvironmental Isotope Geochemistry and Paragenesis of Lacustrine and Palustrine Carbonates, Flagstaff Formation, Central Utah, U.S.A. *Journal of Sedimentary Research*, 78, 162–174.

Buchheim, H.P. and Surdam, R.C. (1977) Fossil catfish and the depositional environment of the Green River Formation, Wyoming. *Geol*, 5, 196.

Cantine, M.D., Knoll, A.H. and Bergmann, K.D. (2020) Carbonates before skeletons: A database approach. *Earth-Science Reviews*, 201, 103065.

Carmichael, M.J., Lunt, D.J., Huber, M., Heinemann, M., Kiehl, J., LeGrande, A., Loptson, C.A., Roberts, C.D., Sagoo, N., Shields, C., Valdes, P.J., Winguth, A., Winguth, C. and Pancost, R.D. (2016) A model–model and data–model comparison for the early Eocene hydrological cycle. *Clim. Past*, 12, 455–481.

Carroll, A.R. and Bohacs, K.M. (1999) Stratigraphic classification of ancient lakes: Balancing tectonic and climatic controls. *Geol*, 27, 99.

Casado, A.I., Alonso-Zarza, A.M. and La Iglesia, Á. (2014) Morphology and origin of dolomite in paleosols and lacustrine sequences. Examples from the Miocene of the Madrid Basin. *Sedimentary Geology*, 312, 50–62.

Caumartin, J., Benzerara, K., Havas, R., Thomazo, C., Lòpez-García, P. and Duprat, E. (2023) The chemical conditions necessary for the formation of microbialites. *Geochem. Persp. Let.*, 25, 30–35.

Chagas, A.A.P., Webb, G.E., Burne, R.V. and Southam, G. (2016) Modern lacustrine microbialites: Towards a synthesis of aqueous and carbonate geochemistry and mineralogy. *Earth-Science Reviews*, 162, 338–363.

Chen, J. and Lee, J. (2014) Current Progress on the Geological Record of Microbialites and Microbial Carbonates. *Acta Geologica Sinica (Eng)*, 88, 260–275.

Choquette, P.W. and Pray, L.C. (1970) Geologic Nomenclature and Classification of Porosity in Sedimentary Carbonates. *Bulletin*, 54, 207–250.

Clyde, W.C. and Gingerich, P.D. (1998) Mammalian community response to the latest Paleocene thermal maximum: An isotaphonomic study in the northern Bighorn Basin, Wyoming. *Geol*, 26, 1011.

Coney, P.J. and Harms, T.A. (1984) Cordilleran metamorphic core complexes: Cenozoic extensional relics of Mesozoic compression. *Geol*, 12, 550.

De Deckker, P. and Last, W.M. (1989) Modern, non-marine dolomite in evaporitic playas of western Victoria, Australia. *Sedimentary Geology*, 64, 223–238.

De Deckker, P. and Last, W.M. (1988) Modern dolomite deposition in continental, saline lakes, western Victoria, Australia. *Geology*, 16, 29–32.

DeCelles, P.G. (2004) Late Jurassic to Eocene evolution of the Cordilleran thrust belt and foreland basin system, western U.S.A. *American Journal of Science*, 304, 105–168.

DeCelles, P.G. and Coogan, J.C. (2006) Regional structure and kinematic history of the Sevier fold-and-thrust belt, central Utah.

Dickinson, W.R. (2004) Evolution of the North American Cordillera. *Annu. Rev. Earth Planet. Sci.*, 32, 13–45.

Dickinson, W.R. and Gehrels, G.E. (2009) Use of U–Pb ages of detrital zircons to infer maximum depositional ages of strata: A test against a Colorado Plateau Mesozoic database. *Earth and Planetary Science Letters*, 288, 115–125.

Drummond, C.N., Wilkinson, B.H. and Lohmann, K.C. (1996) Climatic control of fluvial-lacustrine cyclicity in the Cretaceous Cordilleran Foreland Basin, western United States. *Sedimentology*, 43, 677–689.

Druschke, P., Hanson, A.D. and Wells, M.L. (2009a) Structural, stratigraphic, and geochronologic evidence for extension predating Palaeogene volcanism in the Sevier hinterland, east-central Nevada. *International Geology Review*, 51, 743–775.

Druschke, P., Hanson, A.D., Wells, M.L., Gehrels, G.E. and Stockli, D. (2011) Paleogeographic isolation of the Cretaceous to Eocene Sevier hinterland, east-central Nevada: Insights from U-Pb and (U-Th)/He detrital zircon ages of hinterland strata. *Geological Society of America Bulletin*, 123, 1141–1160.

Druschke, P., Hanson, A.D., Wells, M.L., Rasbury, T., Stockli, D.F. and Gehrels, G. (2009b) Synconvergent surface-breaking normal faults of Late Cretaceous age within the Sevier hinterland, east-central Nevada. *Geology*, 37, 447–450.

Dunagan, S.P. and Turner, C.E. (2004) Regional paleohydrologic and paleoclimatic settings of wetland/lacustrine depositional systems in the Morrison Formation (Upper Jurassic), Western Interior, USA. *Sedimentary Geology*, 167, 269–296.

Dunham, R.J. (1962) Classification of carbonate rocks according to depositional texture. *in Classification of carbonate rocks; a symposium*, 108–121.

Dupraz, C., Reid, R.P., Braissant, O., Decho, A.W., Norman, R.S. and Visscher, P.T. (2009) Processes of carbonate precipitation in modern microbial mats. *Earth-Science Reviews*, 96, 141–162.

Eljalafi, A. and Sarg, J.F. (2021) Depositional system and lake-stage control on microbialite morphology, Green River Formation, eastern Uinta Basin, Colorado and Utah, U.S.A. *Journal of Sedimentary Research*, 91, 636–661.

Emry, R.J. (1990) Mammals of the Bridgerian (middle Eocene) Elderberry Canyon Local Fauna of eastern Nevada. In: *Geological Society of America Special Papers*, *Geological Society of America*, 243, 187–210.

Emry, R.J. and Korth, W.W. (1989) Rodents of the Bridgerian (Middle Eocene) Elderberry Canyon Local Fauna of Eastern Nevada. *Smithsonian Contributions to Paleobiology*, 1–14.

Fahraeus, L.E., Slatt, R.M. and Nowlan, G.S. (1974) Origin of Carbonate Pseudopellets. *Journal of Sedimentary Petrology*, 44, 27–29.

Feldmann, M. and Mckenzie, J.A. (1998) Stromatolite-Thrombolite associations in a modern environment, Lee Stocking island. *Bahamas Palaios*, 201–212.

Fischer, A.G. and Roberts, L.T. (1991) Cyclicity in the Green River Formation (Lacustrine Eocene) of Wyoming. *Journal of Sedimentary Petrology*, 61, 1146–1154.

Folk, R.L. and Land, L.S. (1975) Mg/Ca Ratio and Salinity: Two Controls over Crystallization of Dolomite. Bulletin. doi: 10.1306/83D91C0E-16C7-11D7-8645000102C1865D

Fouch, T.D. (1979) Character and paleogeographic distribution of Upper Cretaceous (?) and Paleogene nonmarine sedimentary rocks in East-central Nevada. In: Armentrout, J.M., Cole, M.R., and Terbest, H., eds., Cenozoic Paleogeography of the Western United States: Pacific Coast Paleogeographic Symposium 3: Los Angeles, Pacific Section, Society for Economic and Petroleum Mineralogists, pp. 97–111.

Fouch, T.D., Lund, K., Schmitt, J.G., Good, S.C. and Hanley, J.H. (1991) Late Cretaceous(?) and Paleogene sedimentary rocks and extensional(?) basins in the region of the Egan and Grant ranges, and White River adn Railroad valleys, Nevada: their relation to Sevier and Laramide contractional basins in the southern Rocky Mountains and Colorado Plateau. *Nevada Petroleum Society Fieldtrip Guidebook*, 15–23.

Frantz, C.M., Gibby, C., Nilson, R., Nguyen, M., Ellsworth, C., Stern, C.J., Dolan, H., Sihapanya, A. and Baxter, B.K. (2023) Desiccation of ecosystem-critical microbialites in the shrinking Great Salt Lake, Utah (USA). *Environmental Sciences*.

Frantz, C.M., Petryshyn, V.A., Marenco, P.J., Tripati, A., Berelson, W.M. and Corsetti, F.A. (2014) Dramatic local environmental change during the Early Eocene Climatic Optimum detected using high resolution chemical analyses of Green River Formation stromatolites. *Palaeogeography, Palaeoclimatology, Palaeoecology*, 405, 1–15.

Freytet, P. (1965) Sedimentation microcyclothemique avec croutes zonaires a algues dans le calcaire de Beauce de Chauffour-Etrechy (Seine-et-Oise). *Bulletin de la Société Géologique de France*, 7, 309–313.

Freytet, P. (1973) Petrography and paleo-environment of continental carbonate deposits with particular reference to the upper cretaceous and lower eocene of languedoc (Southern France). *Sedimentary Geology*, 10, 25–60.

Freytet, P. and Plaziat, J.-C. (1982) Continental carbonate sedimentation and pedogenesis - Late Cretaceous and early Cainozoic of southern France. In: *Contributions to sedimentology*, *Stuttgart: Schweizerbart'sche Verlag*, 12, 217.

Freytet, P. and Verrecchia, E.P. (2002) Lacustrine and palustrine carbonate petrography: an overview. *Journal of Paleolimnology*, 27, 221–237.

García, A. (1994) Charophyta: their use in paleolimnology. *Journal of Paleolimnology*, 10, 43–52.

García Del Cura, M.A., Calvo, J.P., Ordóñez, S., Jones, B.F. and Cañaveras, J.C. (2001) Petrographic and geochemical evidence for the formation of primary, bacterially induced lacustrine dolomite: La Roda 'white earth' (Pliocene, central Spain). *Sedimentology*, 48, 897–915.

Gehrels, G., Valencia, V. and Pullen, A. (2006) Detrital zircon geochronology by laser-ablation multicollector ICPMS at the Arizona LaserChron Center. *The Paleontological Society Papers*, 12, 67–76.

Gehrels, G.E., Valencia, V.A. and Ruiz, J. (2008) Enhanced precision, accuracy, efficiency, and spatial resolution of U-Pb ages by laser ablation–multicollector–inductively coupled plasma–mass spectrometry.

Gierlowski-Kordesch, E.H. (2010) Chapter 1 Lacustrine Carbonates. In: *Developments in Sedimentology*, *Elsevier*, 61, 1–101.

Gingras, M.K., Pemberton, S.G. and Smith, M. (2015) Bioturbation: Reworking Sediments for Better or Worse. *Oilfield Review*, 26, 46–58.

Gischler, E., Gibson, M.A. and Oschmann, W. (2008) Giant Holocene Freshwater Microbialites, Laguna Bacalar, Quintana Roo, Mexico. *Sedimentology*, 55, 1293–1309.

Good, S.C. (1987) Mollusc-Based Interpretations of Lacustrine Paleoenvironments of the Sheep Pass Formation (Latest Cretaceous to Eocene) of East Central Nevada. *PALAIOS*, 2, 467.

Greenwood, D.R. and Wing, S.L. (1995) Eocene continental climates and latitudinal temperature gradients. *Geol*, 23, 1044.

Guo, P., Wen, H., Li, C., He, H. and Sánchez-Román, M. (2023) Lacustrine dolomite in deep time: What really matters in early dolomite formation and accumulation? *Earth-Science Reviews*, 104575.

Hanley, J.H. (1976) Paleosynecology of nonmarine Mollusca from the Green River and Wasatch Formations (Eocene), southwestern Wyoming and northwestern Colorado. *in Scott, R.W. and West, R.R., eds., Structure and classification of paleocommunities: Stroudsburg, Dowdin, Hutchinson and Ross, Inc., 291p*, 235–261.

Harman, W.N. and Jackson, D.F. (1967) A late winter survey of the macroscopic invertebrates in Green Lake, Fayetteville, New York. *in Jackson, D.F., ed., Some aspects of meromixis: Dept. of Civil Engineering, Syracuse University, Syracuse, New York*, 188–214.

Harwood Theisen, C. and Sumner, D.Y. (2016) Thrombolite fabrics and origins: Influences of diverse microbial and metazoan processes on Cambrian thrombolite variability in the Great Basin, California and Nevada. *Sedimentology*, 63, 2217–2252.

Heller, P.L., Komar, P.D. and Pevear, D.R. (1980) Transport Processes in Ooid Genesis. *SEPM JSR*, 50, 943–952.

Henrici, A.C., Druschke, P., Hilton, R.P. and Bonde, J.W. (2018) Redescription and phylogenetic reassessment of the enigmatic anuran *Eorubeta nevadensis* (Amphibia) based on new specimens from ?latest Cretaceous–Paleocene beds of the Sheep Pass Formation, Nevada. *Journal of Vertebrate Paleontology*, 38, e1510413.

Ingalls, M., Fetrow, A.C., Snell, K.E., Frantz, C.M. and Trower, E.J. (2022) Lake level controls the recurrence of giant stromatolite facies. *Sedimentology*, 69, 1649–1674.

Iniesto, M., Moreira, D., Reboul, G., Deschamps, P., Benzerara, K., Bertolino, P., Saghaï, A., Tavera, R. and López-García, P. (2021) Core microbial communities of lacustrine microbialites sampled along an alkalinity gradient. *Environmental Microbiology*, 23, 51–68.

Jones, C.H., Sonder, L.J. and Unruh, J.R. (1998) Lithospheric gravitational potential energy and past orogenesis: Implications for conditions of initial Basin and Range and Laramide deformation. *Geol*, 26, 639.

Keighley, D., Flint, S., Howell, J. and Moscariello, A. (2003) Sequence Stratigraphy in Lacustrine Basins: A Model for Part of the Green River Formation (Eocene), Southwest Uinta Basin, Utah, U.S.A. *Journal of Sedimentary Research*, 73, 987–1006.

Kellogg, H.E. (1964) Cenozoic Stratigraphy and Structure of the Southern Egan Range, Nevada. *Geol Soc America Bull*, 75, 949.

Kelts, K. and Hsü, K.J. (1978) Freshwater Carbonate Sedimentation. In: *Lakes: chemistry, geology, physics*, *Springer New York*, New York, NY, 295–323.

Kennard, J.M. and James, N.P. (1986) Thrombolites and Stromatolites: Two Distinct Types of Microbial Structures. *PALAIOS*, 1, 492.

Koch, P.L., Clyde, W.C., Hepple, R.P., Fogel, M.L., Wing, S.L. and Zachos, J.C. (2003) Carbon and oxygen isotope records from Paleosols spanning the Paleocene-Eocene boundary, Bighorn Basin, Wyoming. In: *Causes and consequences of globally warm climates in the early Paleogene*, *Geological Society of America*,

Kraus, M.J., McInerney, F.A., Wing, S.L., Secord, R., Baczynski, A.A. and Bloch, J.I. (2013) Paleohydrologic response to continental warming during the Paleocene–Eocene Thermal Maximum, Bighorn Basin, Wyoming. *Palaeogeography, Palaeoclimatology, Palaeoecology*, 370, 196–208.

Kraus, M.J. and Riggins, S. (2007) Transient drying during the Paleocene–Eocene Thermal Maximum (PETM): Analysis of paleosols in the bighorn basin, Wyoming. *Palaeogeography, Palaeoclimatology, Palaeoecology*, 245, 444–461.

Last, W.M. (1990) Lacustrine dolomite—an overview of modern, Holocene, and Pleistocene occurrences. *Earth-Science Reviews*, 27, 221–263.

Last, W.M. and De Deckker, P. (1990) Modern and Holocene carbonate sedimentology of two saline volcanic maar lakes, southern Australia. *Sedimentology*, 37, 967–981.

Lauretano, V., Littler, K., Polling, M., Zachos, J.C. and Lourens, L.J. (2015) Frequency, magnitude, and character of hyperthermal events at the onset of the Early Eocene Climatic Optimum. *Climate of the Past*, 11, 1313–1324.

Li, J., Zhu, L., Li, M., Wang, J. and Ma, Q. (2020) Origin of modern dolomite in surface lake sediments on the central and western Tibetan Plateau. *Quaternary International*, 544, 65–75.

Long, S.P. (2015) An upper-crustal fold province in the hinterland of the Sevier orogenic belt, eastern Nevada, U.S.A.: A Cordilleran Valley and Ridge in the Basin and Range. *Geosphere*, 11, 404–424.

Mata, S.A. and Bottjer, D.J. (2012) Microbes and mass extinctions: paleoenvironmental distribution of microbialites during times of biotic crisis. *Geobiology*, 10, 3–24.

Mather, C.C., Skrzypek, G., Dogramaci, S. and Grierson, P.F. (2018) Paleoenvironmental and paleohydrochemical conditions of dolomite formation within a saline wetland in arid northwest Australia. *Quaternary Science Reviews*, 185, 172–188.

McCormack, J., Baldermann, A., Bontognali, T.R.R., Wolf, A. and Kwiecien, O. (2024) Hydrochemical mixing-zones trigger dolomite formation in an alkaline lake. *Sedimentology*, 71, 871–886.

Mees, F., Casteneda, C., Herrero, J. and Van Ranst, E. (2012) The Nature and Significance of Variations In Gypsum Crystal Morphology In Dry Lake Basins. *Journal of Sedimentary Research*, 82, 37–52.

Mei, M., Latif, K., Mei, C., Gao, J. and Meng, Q. (2020) Thrombolitic clots dominated by filamentous cyanobacteria and crusts of radio-fibrous calcite in the Furongian Changshan Formation, North China. *Sedimentary Geology*, 395, 105540.

Meister, P., Reyes, C., Beaumont, W., Rincon, M., Collins, L., Berelson, W., Stott, L., Corsetti, F. and Nealson, K.H. (2011) Calcium and magnesium-limited dolomite precipitation at Deep Springs Lake, California. *Sedimentology*, 58, 1810–1830.

Nickel, E. (1983) Environmental Significance of Freshwater Oncoids, Eocene Guarga Formation, Southern Pyrenees, Spain. In: *Coated Grains* (Ed Peryt, T.M.), Springer, Berling Heidelberg, pp. 308-329.

Pagani, M., Huber, M. and Sageman, B. (2014) Greenhouse Climates. In: *Treatise on Geochemistry*, *Elsevier*, 281–304.

Palacios-Festa, M.R., Cohen, A.S. and Anadón, P. (1994) Use of ostracodes as paleoenvironmental tools in the interpretation of ancient lacustrine records. *Revista española de paleontología*, 9, 145–161.

Pentecost, A. (1978) Blue-Green Algae and Freshwater Carbonate Deposits. *Proceedings of the Royal Society of London. B.*, 200, 43–61.

Pepin, N., Bradley, R.S., Diaz, H.F., Baraer, M., Caceres, E.B., Forsythe, N., Fowler, H., Greenwood, G., Hashmi, M.Z., Liu, X.D., Miller, J.R., Ning, L., Ohmura, A., Palazzi, E., Rangwala, I., Schöner, W., Severskiy, I., Shahgedanova, M., Wang, M.B., Williamson, S.N. and Yang, D.Q. (2015) Elevation dependent warming in mountain regions of the world. *Nature Climate Change 5*, 424–430.

Platt, N.H. (1989) Lacustrine carbonates and pedogenesis: sedimentology and origin of palustrine deposits from the Early Cretaceous Rupelo Formation, W Cameros Basin, N Spain. *Sedimentology*, 36, 665–684.

Platt, N.H. and Wright, V.P. (1991) Lacustrine Carbonates: Facies Models, Facies Distributions and Hydrocarbon Aspects. In: *Lacustrine Facies Analysis*, 1st edn. (Ed. P. Anadón, Li. Cabrera, and K. Kelts), *Wiley*, 57–74.

Platt, N.H. and Wright, V.P. (2023) Flooding of a carbonate platform: The Sian Ka'an Wetlands, Yucatán, Mexico—A model for the formation and evolution of palustrine carbonate factories around the modern Caribbean Sea and in the depositional record. *The Depositional Record*, 9, 99–151.

Pommer, M., Sarg, J.F. and McFarlin, F. (2023) Environmental and microbial influence on chemistry and dolomite formation in an ancient lake, Green River Formation (Eocene), Uinta basin, Utah, U.S.A. *Journal of Sedimentary Research*, 93, 213–242.

Pruss, S.B. and Knoll, A.H. (2017) Environmental covariation of metazoans and microbialites in the Lower Ordovician Boat Harhour Formation, Newfoundland. *Paleogeography, Paleoclimatology, Paleoecology*, 489, 917–929.

Rangwala, I., Sinsky, E. and Miller, J.R. (2013) Amplified warming projections for high altitude regions of the northern hemisphere mid-latitudes from CMIP5 models. *Environ. Res. Lett.*, 8, 024040.

Riding, R. (2011) Microbialites, Stromatolites, and Thrombolites. *Encyclopedia of geobiology*, 635–654.

Riding, R. (2006) Microbial carbonate abundance compared with fluctuations in metazoan diversity over geological time. *Sedimentary Geology*, 185, 229–238.

Rodriguez-Aranda, J.P. and Calvo, J.P. (1998) Trace fossils and rhizoliths as a tool for sedimentological and paleoenvironmental analysis of ancient continental evaporite successions. *Palaeogeography, Palaeoclimatology, Palaeoecology*, 140, 383–399.

Roehler, H.W. (1993) Eocene climates, depositional environments, and geography, greater Green River basin, Wyoming, Utah, and Colorado. *US Geological Survey Professional Paper 1506-F*, 74 pp.

Rosen, M.R., Miser, D.E., Starcher, M.A. and Warren, J.K. (1989) Formation of dolomite in the Coorong region, South Australia. *Geochimica et Cosmochimica Acta*, 53, 661–669.

Sarg, J.F., Suriamin, N., TÌnavsuu-Milkeviciene, K. and Humphrey, J.D. (2013) Lithofacies, stable isotopic composition, and stratigraphic evolution of microbial and associated carbonates, Green River Formation (Eocene), Piceance Basin, Colorado. *Bulletin*, 97, 1937–1966.

Schieber, J. (2007) Benthic microbial mats as an oil shale component: Green River Formation (Eocene) of Wyoming and Utah. In: Atlas of microbial mat features preserved within the clastic rock record, Schieber, J., Bose, P.K., Eriksson, P.G., Banerjee, S., Sarkar, S. Altermann, W., and Catuneau, O., (Eds.), pp. 225–232. Elsevier, Amserdam, the Netherlands.

Seard, C., Camoin, G., Rouchy, J.-M. and Virgone, A. (2013) Composition, structure and evolution of a lacustrine carbonate margin dominated by microbialites: Case study from the Green River formation (Eocene; Wyoming, USA). *Palaeogeography, Palaeoclimatology, Palaeoecology*, 381–382, 128–144.

Shapiro, R. (2000) A Comment on the Systematic Confusion of Thrombolites. *PALAIOS*, 15, 166–169.

Shinn, E.A. (1983) Birdseyes, Fenestrae, Shrinkage Pores, and Loferites: A Reevaluation. *SEPM JSR*, 53, 619–628.

Smith, M.E. and Carroll, A.R. (eds) (2015) Stratigraphy and Paleolimnology of the Green River Formation, Western USA. *Springer Netherlands*, Dordrecht.

Smith, M.E., Carroll, A.R. and Singer, B.S. (2008) Synoptic reconstruction of a major ancient lake system: Eocene Green River Formation, western United States. *Geological Society of America Bulletin*, 120, 54–84.

Snell, K.E. (2011) Paleoclimate and Paleoelevation of the western Cordillera in the United States. *University of California Santa Cruz*, PhD Thesis.

Snell, K.E., Koch, P.L., Druschke, P., Foreman, B.Z. and Eiler, J.M. (2014) High elevation of the 'Nevadaplano' during the Late Cretaceous. *Earth and Planetary Science Letters*, 386, 52–63.

Snell, K.E., Thrasher, B.L., Eiler, J.M., Koch, P.L., Sloan, L.C. and Tabor, N.J. (2013) Hot summers in the Bighorn Basin during the early Paleogene. *Geology*, 41, 55–58.

Sundell, K.E., Gehrels, G.E. and Pecha, M.E. (2021) Rapid U-Pb Geochronology by Laser Ablation Multi-Collector ICP-MS. *Geostandard Geoanalytic Res*, 45, 37–57.

Surdam, R.C. and Stanley, K.O. (1979) Lacustrine sedimentation during the culminating phase of Eocene Lake Gosiute, Wyoming (Green River Formation). *Geol Soc America Bull*, 90, 93.

Swain, F.M. (1987) Late Cretaceous? and Paleogene freshwater ostracoda from central and eastern Nevada. *Review Espanola de Micropaleontologia*, 181–227.

Tänavsuu-Milkeviciene, K. and Sarg, J.F. (2012) Evolution of an organic-rich lake basin – stratigraphy, climate and tectonics: Piceance Creek basin, Eocene Green River Formation. *Sedimentology*, 59, 1735–1768.

Tänavsuu-Milkeviciene, K., Sarg, J.F. and Bartov, Y. (2017) Depositional Cycles and Sequences In An Organic-Rich Lake Basin: Eocene Green River Formation, Lake Uinta, Colorado and Utah, U.S.A. *Journal of Sedimentary Research*, 87, 210–229.

The Cenozoic CO Proxy Integration Project (CenCOPIP) Consortium*†, Hönisch, B., Royer, D.L., Breecker, D.O., Polissar, P.J., Bowen, G.J., Henehan, M.J., Cui, Y., Steinthorsdottir, M., McElwain, J.C., Kohn, M.J., Pearson, A., Phelps, S.R., Uno, K.T., Ridgwell, A., Anagnostou, E., Austermann, J., Badger, M.P.S., Barclay, R.S., Bijl, P.K., Chalk, T.B., Scotese, C.R., De La Vega, E., DeConto, R.M., Dyez, K.A., Ferrini, V., Franks, P.J., Giulivi, C.F., Gutjahr, M., Harper, D.T., Haynes, L.L., Huber, M., Snell, K.E., Keisling, B.A., Konrad, W., Lowenstein, T.K., Malinverno, A., Guillermic, M., Mejía, L.M., Milligan, J.N.,

Morton, J.J., Nordt, L., Whiteford, R., Roth-Nebelsick, A., Rugenstein, J.K.C., Schaller, M.F., Sheldon, N.D., Sosdian, S., Wilkes, E.B., Witkowski, C.R., Zhang, Y.G., Anderson, L., Beerling, D.J., Bolton, C., Cerling, T.E., Cotton, J.M., Da, J., Ekart, D.D., Foster, G.L., Greenwood, D.R., Hyland, E.G., Jagniecki, E.A., Jasper, J.P., Kowalczyk, J.B., Kunzmann, L., Kürschner, W.M., Lawrence, C.E., Lear, C.H., Martínez-Botí, M.A., Maxbauer, D.P., Montagna, P., Naafs, B.D.A., Rae, J.W.B., Raitzsch, M., Retallack, G.J., Ring, S.J., Seki, O., Sepúlveda, J., Sinha, A., Tesfamichael, T.F., Tripati, A., Van Der Burgh, J., Yu, J., Zachos, J.C. and Zhang, L. (2023) Toward a Cenozoic history of atmospheric CO_2. *Science*, 382, 5177.

Thompson, J.B. and Ferris, F.G. (1990) Cyanobacterial precipitation of gypsum, calcite, and magnesite from natural alkaline lake water. *Geology*, 18, 995.

Van Der Meulen, B., Gingerich, P.D., Lourens, L.J., Meijer, N., Van Broekhuizen, S., Van Ginneken, S. and Abels, H.A. (2020) Carbon isotope and mammal recovery from extreme greenhouse warming at the Paleocene–Eocene boundary in astronomically-calibrated fluvial strata, Bighorn Basin, Wyoming, USA. *Earth and Planetary Science Letters*, 534, 116044.

Vandervoort, D.S. and Schmitt, J.G. (1990) Cretaceous to early Tertiary paleogeography in the hinterland of the Sevier thrust belt, east-central Nevada. *Geol*, 18, 567.

Wanas, H.A. and Sallam, E. (2016) Abiotically-formed, primary dolomite in the mid-Eocene lacustrine succession at Gebel El-Goza El-Hamra, NE Egypt: An approach to the role of smectitic clays. *Sedimentary Geology*, 343, 132–140.

Warren, J.K. (1990) Sedimentology and Mineralogy of Dolomitic Coorong Lakes, South Australia. SEPM JSR. doi: 10.1306/212F929B-2B24-11D7-8648000102C1865D

Westerhold, T., Marwan, N., Drury, A.J., Liebrand, D., Agnini, C., Anagnostou, E., Barnet, J.S.K., Bohaty, S.M., De Vleeschouwer, D., Florindo, F., Frederichs, T., Hodell, D.A., Holbourn, A.E., Kroon, D., Lauretano, V., Littler, K., Lourens, L.J., Lyle, M., Pälike, H., Röhl, U., Tian, J., Wilkens, R.H., Wilson, P.A. and Zachos, J.C. (2020) An astronomically dated record of Earth's climate and its predictability over the last 66 million years. *Science*, 369, 1383–1387.

Widlansky, S.J., Secord, R., Snell, K.E., Chew, A.E. and Clyde, W.C. (2022) Terrestrial carbon isotope stratigraphy and mammal turnover during post-PETM hyperthermals in the Bighorn Basin, Wyoming, USA. *Clim. Past*, 18, 681–712.

Wilf, P. (2000) Late Paleocene–early Eocene climate changes in southwestern Wyoming: Paleobotanical analysis. *Geological Society of America Bulletin*, 112, 292–307.

Winfrey, W.M. (1960) Stratigraphy, Correlation, and Oil Potential of the Sheep Pass Formation, East-Central Nevada. 126–133.

Wing, S.L., Harrington, G.J., Smith, F.A., Bloch, J.I., Boyer, D.M. and Freeman, K.H. (2005) Transient Floral Change and Rapid Global Warming at the Paleocene-Eocene Boundary. *Science*, 310, 993–996.

Wolfbauer, C.A. and Surdam, R.C. (1974) Origin of Nonmarine Dolomite in Eocene Lake Gosiute, Green River Basin, Wyoming. *Geol Soc America Bull*, 85, 1733.
Woolway, R.I., Kraemer, B.M., Lenters, J.D., Merchant, C.J., O'Reilly, C.M. and Sharma, S. (2020) Global lake responses to climate change. *Nat Rev Earth Environ*, 1, 388–403.
Wright, D.T. and Wacey, D. (2004) Sedimentary dolomite: a reality check. *SP*, 235, 65–74.
Wright, V.P. (1986) The role of fungal biomineralization in the formation of Early Carboniferous soil fabrics. *Sedimentology*, 33, 831–838.
Wright, V.P. and Platt, N.H. (1995) Seasonal wetland carbonate sequences and dynamic catenas: a re-appraisal of palustrine limestones. *Sedimentary Geology*, 99, 65–71.
Wrona, F.J., Prowse, T.D., Reist, J.D., Hobbie, J.E., Lévesque, L.M.J. and Vincent, W.F. (2006) Climate Change Effects on Aquatic Biota, Ecosystem Structure and Function. *AMBIO: A Journal of the Human Environment*, 35, 359–369.
Zachos, J., Pagani, M., Sloan, L., Thomas, E. and Billups, K. (2001) Trends, Rhythms, and Aberrations in Global Climate 65 Ma to Present. *Science*, 292, 686–693.
Zachos, J.C., Dickens, G.R. and Zeebe, R.E. (2008) An early Cenozoic perspective on greenhouse warming and carbon-cycle dynamics. *Nature*, 451, 279–283.

2.11 Supplemental Materials

Information about the OSF repository:

This repository contains three folders in addition to this Supplemental Materials document. Those folders include 1) Detrital Zircon U-Pb Data (backscattered electron and reflected light sample images and raw data spreadsheets), 2) X-ray Diffraction Data (individual XRD spectra), and 3) Thin Section Mosaics (for all samples that have a corresponding thin section).

This Supplemental Materials document includes:

1) Figure S1
2) Figure S2
3) Tables S1 to S3
4) Additional methods for detrital zircon U-Pb analyses with field photos
5) Additional XRD methods and results
6) Additional methods for calculating composite stratigraphic level of select members in measured transects

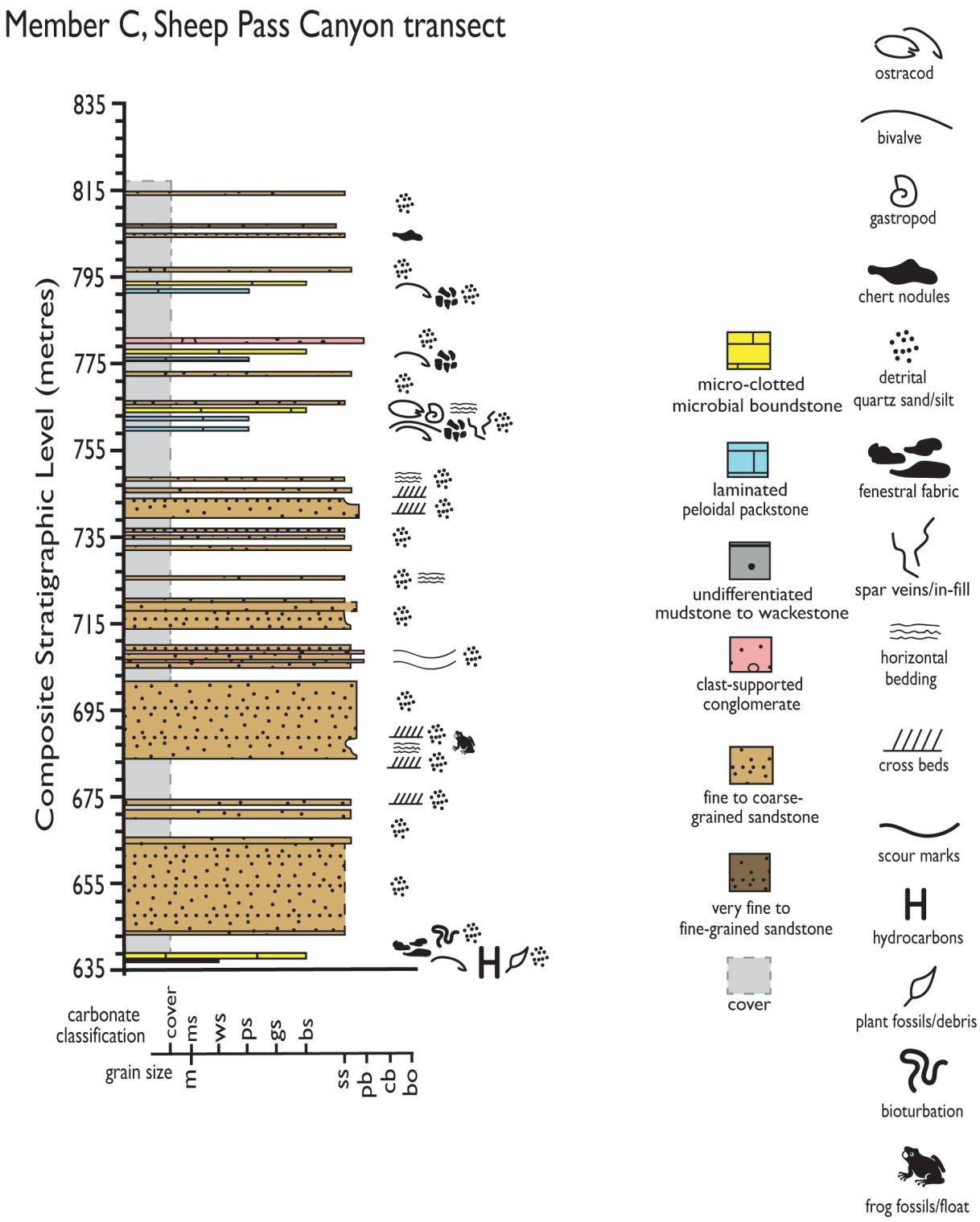

Figure 2-S1: Composite stratigraphic column for Member C, Sheep Pass Canyon measured transect.

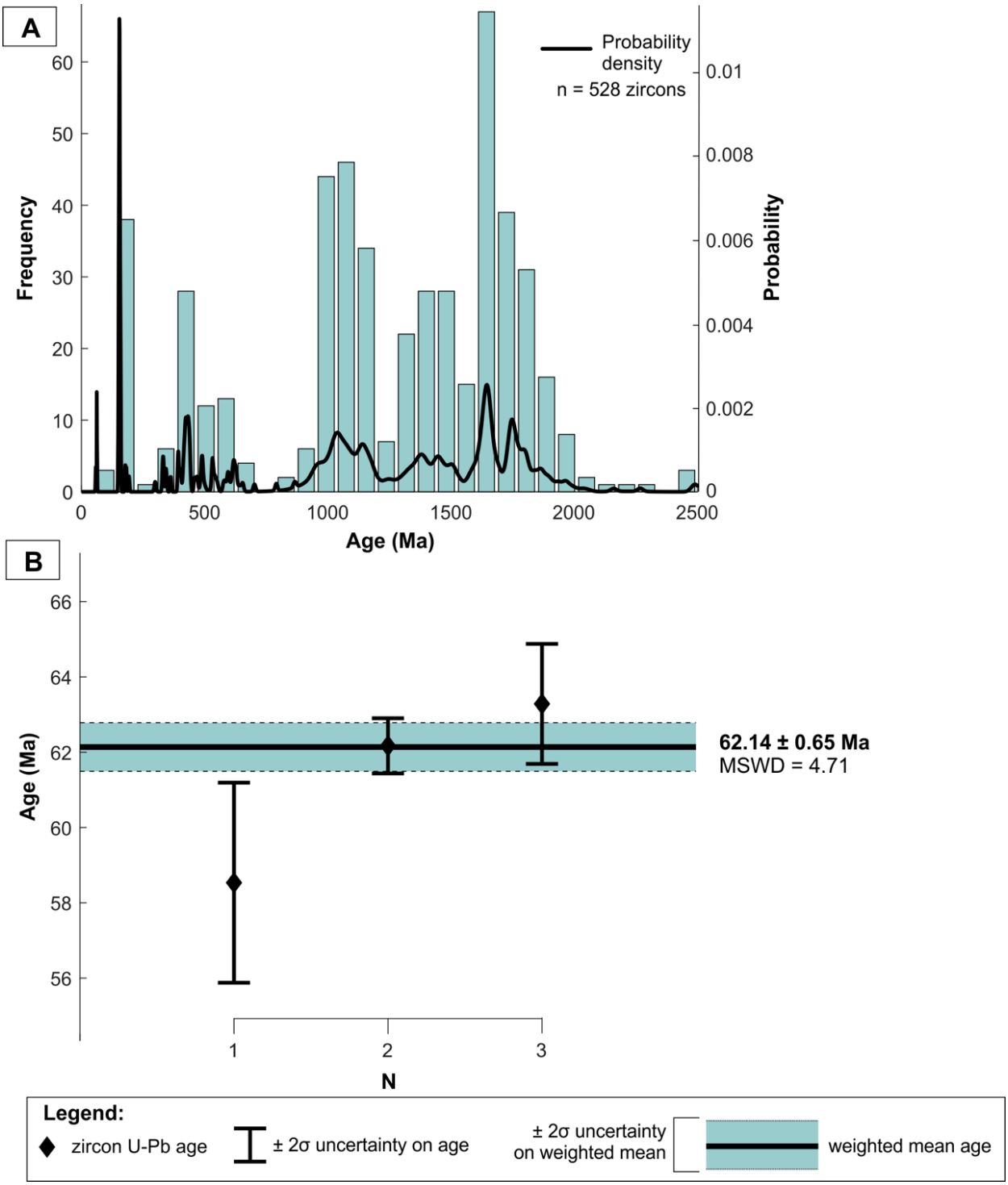

Figure 2-S2: A) Detrital zircon U-Pb age distribution from sandstone sample SP1986 (Member C, Mainline transect). Shaded bars are a histogram showing number of zircon grains and black curve shows the age probability normalized to the total number of analyses. B) Weighted mean age of the youngest population of grains (N = 3 grains) from sample SP1986.

Sample ID	Coordinates	Transect	Member	Composite Stratigraphic Level (m)	Facies	Thin Section
SPB19-SPC01	N 38.73812, W 114.96490	SPC	A	263.4	Fine-grained Sandstone	
SPB19-SPC02	N 38.73842, W 114.96391	SPC	A	292.4	Matrix-supported Conglomerate	X
SPB19-SPC03	N 38.73840, W 114.96370	SPC	A	300.5	Fine-grained Sandstone	
SPB19-SPC04	N 38.73898, W 114.96270	SPC	A	333	Fine-grained Sandstone	
SPB19-SPC05	N 38.73900, W 114.96254	SPC	A	336	Fine-grained Sandstone	
SPB19-SPC06	N 38.73851, W 114.96225	SPC	A	356.3	Very fine- to Fine-grained Sandstone	X
SPB19-SPC07	N 38.73853, W 114.96220	SPC	A	358.7	Very fine- to Fine-grained Sandstone	X
SPB19-ML01	N 38.72538, W 114.97237	ML	B	364.4	Bioclast-rich Wackestone to Packstone	X
SPB19-ML02	N 38.72536, W 114.97234	ML	B	365.7	Bioclast-rich Wackestone to Packstone	
SPB19-ML03	N 38.72526, W 114.97224	ML	B	368.4	Laminated Peloidal Packstone	
SPB19-ML04	N 38.72525, W 114.97224	ML	B	369.1	Micro-clotted Microbial Boundstone	X
SPB19-ML05	N 38.72527, W 114.97223	ML	B	369.7	Peloidal Grainstone	
SPB19-ML06	N 38.72527, W 114.97223	ML	B	370.7	Bioclast-rich Wackestone to Packstone	
SPB19-ML07	N 38.72527, W 114.97223	ML	B	371.7	Thrombolite Boundstone (small clots)	
SPB19-ML08	N 38.72528, W 114.97221	ML	B	372.9	Thrombolite Boundstone (framework of clots)	X
SPB19-ML09	N 38.72529, W 114.97217	ML	B	374.9	Bioclast-rich Wackestone to Packstone	X
SPB19-ML10	N 38.72529, W 114.97218	ML	B	375.8	Laminated Peloidal Packstone	
SPB19-ML11	N 38.72545, W 114.97222	ML	B	377.6	Thrombolite Boundstone (small clots)	X
SPB19-ML12	N 38.72546, W 114.97221	ML	B	378.9	Thrombolite Boundstone (large clots)	X
SPB19-ML13	N 38.72537, W 114.97208	ML	B	383.3	Micro-clotted Microbial Boundstone	X
SPB19-ML14	N 38.72549, W 114.97214	ML	B	385.1	Laminated Peloidal Packstone	
SPB19-ML15	N 38.72538, W 114.97206	ML	B	386.7	Laminated Peloidal Packstone	X
SPB19-ML16	N 38.72538, W 114.97205	ML	B	388.3	Micro-clotted Microbial Boundstone	
SPB19-ML17	N 38.72537, W 114.97198	ML	B	391.1	Micro-clotted Microbial Boundstone	X
SPB19-ML18	N 38.72537, W 114.97295	ML	B	394.1	Micro-clotted Microbial Boundstone	
SPB19-ML19	N 38.72541, W 114.97187	ML	B	400.7	Laminated Peloidal Packstone	
SPB19-ML20	N 38.72543, W 114.97185	ML	B	403.9	Bioclast-rich Wackestone to Packstone	
SPB19-ML21	N 38.72543, W 114.97182	ML	B	405.9	Micro-clotted Microbial Boundstone	
SPB19-ML22	N 38.72543, W 114.97179	ML	B	406.9	Bioturbated Peloidal Packstone	
SPB19-ML23	N 38.72546, W 114.97179	ML	B	408.8	Bioturbated Peloidal Packstone	X
SPB19-ML24	N 38.72547, W 114.97178	ML	B	409.9	Laminated Peloidal Packstone	
SPB19-ML25	N 38.72550, W 114.97177	ML	B	412.1	Bioturbated Peloidal Packstone	

SPB19-ML26	N 38.72551, W 114.97175	ML	B	414.1	Laminated Peloidal Packstone	
SPB19-ML27	N 38.72549, W 114.97173	ML	B	414.4	Ooid Grainstone	X
SPB19-ML28	N 38.72552, W 114.97174	ML	B	414.8	Bioturbated Peloidal Packstone	
SPB19-ML29	N 38.72551, W 114.97172	ML	B	416.7	Bioturbated Peloidal Packstone	
SPB19-ML30	N 38.72553, W 114.97172	ML	B	418.4	Bioturbated Peloidal Packstone	
SPB19-ML31	N 38.72558, W 114.97162	ML	B	425.9	Thrombolite Boundstone (small clots)	X, alizarin red-stained
SPB19-ML32	N 38.72561, W 114.97164	ML	B	427.9	Thrombolite Boundstone (large clots)	
SPB19-ML33	N 38.72570, W 114.97164	ML	B	428.6	Thrombolite Boundstone (framework of clots)	X
SPB19-ML34	N 38.72562, W 114.97160	ML	B	430.2	Micro-clotted Microbial Boundstone	
SPB19-ML35	N 38.72565, W 114.97157	ML	B	434.3	Thrombolite Boundstone (small clots)	
SPB19-ML36	N 38.72571, W 114.97152	ML	B	438.8	Thrombolite Boundstone (large clots)	X
SPB19-ML37	N 38.72576, W 114.97151	ML	B	442.6	Thrombolite Boundstone (small clots)	
SPB19-ML38	N 38.72580, W 114.97150	ML	B	445.9	Thrombolite Boundstone (small clots)	
SPB19-ML39	N 38.72586, W 114.97146	ML	B	451	Peloidal Grainstone	X
SPB19-ML40	N 38.72599, W 114.97142	ML	B	456.4	Vuggy Wackestone	
SPB19-ML41	N 38.72594, W 114.97118	ML	B	471.6	Peloidal Grainstone	
SPB19-ML42	N 38.72593, W 114.97118	ML	B	472.7	Undifferentiated Mudstone to Wackestone	
SPB19-ML43	N 38.72594, W 114.97115	ML	B	474.5	Laminated Peloidal Packstone	
SPB19-ML44	N 38.72578, W 114.97099	ML	B	484.5	Bioturbated Peloidal Packstone	
SPB19-ML45	N 38.72580, W 114.97096	ML	B	486.9	Bioturbated Peloidal Packstone	X
SPB19-ML46	N 38.72596, W 114.97095	ML	B	489.7	Bioturbated Peloidal Packstone	
SPB19-ML47	N 38.72588, W 114.97087	ML	B	493.8	Laminated Peloidal Packstone	
SPB19-ML48	N 38.72586, W 114.97073	ML	B	506.2	Laminated Peloidal Packstone	X, alizarin red-stained
SPB19-ML49	N 38.72584, W 114.97070	ML	B	507.9	Laminated Peloidal Packstone	
SPB19-ML50	N 38.72593, W 114.97069	ML	B	513.4	Micro-clotted Microbial Boundstone	
SPB19-ML51	N 38.72604, W 114.97030	ML	C	540.6	Very fine- to Fine-grained Sandstone	X
SPB19-ML52	N 38.72622, W 114.97016	ML	C	551.5	Micro-clotted Microbial Boundstone	X
SPB19-ML53	N 38.72596, W 114.96989	ML	C	566.9	Very fine- to Fine-grained Sandstone	
SPB19-ML54	N 38.72596, W 114.96989	ML	C	567.1	Very fine- to Fine-grained Sandstone	
SPB19-ML55	N 38.72581, W 114.96943	ML	C	582.5	Very fine- to Fine-grained Sandstone	
SPB19-ML56	N 38.72632, W 114.96912	ML	C	596.1	Very fine- to Fine-grained Sandstone	
SPB19-ML57	N 38.72640, W 114.96818	ML	C	623.6	Very fine- to Fine-grained Sandstone	
SPB19-ML58	N 38.72655, W 114.96786	ML	C	637.2	Oncoid Packstone to Grainstone	X
SPB19-ML59	N 38.72635, W 114.96743	ML	C	651.2	Very fine- to Fine-grained Sandstone	

SP1986 DZ	N 38.72612, W 114.96732	ML	C	653.5 – 658.5	Coarse-grained sands for U-Pb detrital zircon analyses	
SPB19-ML60	N 38.72639, W 114.96719	ML	C	660.9	Laminated Peloidal Packstone	
SPB19-ML61	N 38.72660, W 114.96694	ML	C	679.5	Micro-clotted Microbial Boundstone	X
SPB19-ML62	N 38.72672, W 114.96684	ML	C	684.2	Peloidal Grainstone	
SPB19-ML63	N 38.72671, W 114.96682	ML	C	685	Bioturbated Peloidal Packstone	
SPB19-ML64	N 38.72668, W 114.96678	ML	C	688	Micro-clotted Microbial Boundstone	
SPB19-ML65	N 38.72726, W 114.96618	ML	C	693.5	Bioclast-rich Wackestone to Packstone	X, alizarin red-stained
SPB19-ML66	N 38.72711, W 114.96600	ML	C	698	Very fine- to Fine-grained Sandstone	X
SPB19-ML67	N 38.72658, W 114.96470	ML	C	743.5	Very fine- to Fine-grained Sandstone	
SPB19-ML68	N 38.72664, W 114.96432	ML	D	753	Undifferentiated Mudstone to Wackestone	
SPB19-ML69	N 38.72664, W 114.96432	ML	D	754	Vuggy Wackestone	X
SPB19-ML70	N 38.72660, W 114.96422	ML	D	760.9	Vuggy Wackestone	
SPB19-ML71	N 38.72649, W 114.96410	ML	D	771.7	Spar	
SPB19-ML72	N 38.72652, W 114.96391	ML	D	784.5	Undifferentiated Mudstone to Wackestone	
SPB19-ML73	N 38.72661, W 114.96350	ML	D	805.5	Undifferentiated Mudstone to Wackestone	
SPB19-ML74	N 38.72666, W 114.96325	ML	D	811	Undifferentiated Mudstone to Wackestone	X
SPB19-ML75	N 38.72658, W 114.96286	ML	D	819.8	Vuggy Wackestone	
SPB19-ML76	N 38.72657, W 114.96287	ML	D	821	Vuggy Wackestone	
SPB19-ML77	N 38.72657, W 114.96275	ML	D	825.2	Vuggy Wackestone	
SPB19-ML78	N 38.72654, W 114.96267	ML	D	827	Bioclast-rich Wackestone to Packstone	X
SPB19-ML79	N 38.72651, W 114.96253	ML	D	827.2	Bioturbated Peloidal Packstone	
SPB19-ML80	N 38.72657, W 114.96237	ML	D	827.5	Vuggy Wackestone	
SPB19-ML81	N 38.72665, W 114.96209	ML	D	827.5	Vuggy Wackestone	
SPB19-ML82	N 38.72661, W 114.96191	ML	D	827.5	Vuggy Wackestone	
SPB19-ML83	N 38.72639, W 114.96146	ML	D	834.8	Vuggy Wackestone	X, alizarin red-stained
SPB19-ML84	N 38.72627, W 114.96095	ML	D	842	Vuggy Wackestone	
SPB19-ML85	N 38.72617, W 114.96068	ML	D	854.5	Undifferentiated Mudstone to Wackestone	X
SPB19-ML86	N 38.72599, W 114.96053	ML	D	862.4	Undifferentiated Mudstone to Wackestone	
SPB19-ML87	N 38.72580, W 114.96051	ML	D	877	Undifferentiated Mudstone to Wackestone	
SPB19-ML88	N 38.72548, W 114.96003	ML	D	915.4	Undifferentiated Mudstone to Wackestone	
SPB19-ML89	N 38.72566, W 114.95900	ML	D	944.1	Undifferentiated Mudstone to Wackestone	
SPB19-ML90	N 38.72564, W 114.95930	ML	D	953.7	Undifferentiated Mudstone to Wackestone	
SPB19-ML91	N 38.72556, W 114.95905	ML	D	965.2	Undifferentiated Mudstone to Wackestone	X, alizarin red-stained
SPB19-ML92	N 38.72550, W 114.95899	ML	D	970.2	Undifferentiated Mudstone to Wackestone	

SPB19-ML93	N 38.72546, W 114.95892	ML	D	974.2	Undifferentiated Mudstone to Wackestone	X
SPB19-ML94	N 38.72542, W 114.95885	ML	D	979.2	Undifferentiated Mudstone to Wackestone	
SPB19-ML95	N 38.72536, W 114.95877	ML	E	985.2	Bioclast-rich Wackestone to Packstone	
SPB19-ML96	N 38.72533, W 114.95873	ML	E	988.9	Bioclast-rich Wackestone to Packstone	
SPB19-ML97	N 38.72544, W 114.95823	ML	E	1014.5	Bioclast-rich Wackestone to Packstone	X
SPB20-SPC00	N 38.73849, W 114.96086	SPC	B	413.35	Laminated Peloidal Packstone	X, alizarin red-stained
SPB20-SPC01	N 38.73856, W 114.96074	SPC	B	418.4	Laminated Peloidal Packstone	
SPB20-SPC02	N 38.73862, W 114.96075	SPC	B	420.20	Laminated Peloidal Packstone	
SPB20-SPC03	N 38.73860, W 114.96069	SPC	B	423.95	Very fine- to Fine-grained Sandstone	
SPB20-SPC04	N 38.73859, W 114.96064	SPC	B	425.4	Very fine- to Fine-grained Sandstone	X
SPB20-SPC05	N 38.73865, W 114.96067	SPC	B	426.6	Very fine- to Fine-grained Sandstone	
SPB20-SPC06	N 38.73862, W 114.96062	SPC	B	427.7	Laminated Peloidal Packstone	X, alizarin red-stained
SPB20-SPC07	N 38.73862, W 114.96055	SPC	B	428.9	Bioclast-rich Wackestone to Packstone	
SPB20-SPC08	N 38.73864, W 114.96053	SPC	B	431.6	Laminated Peloidal Packstone	
SPB20-SPC09	N 38.73864, W 114.96054	SPC	B	432.85	Bioclast-rich Wackestone to Packstone	X
SPB20-SPC10	N 38.73864, W 114.96054	SPC	B	433.65	Very fine- to Fine-grained Sandstone	
SPB20-SPC11	N 38.73867, W 114.96049	SPC	B	435.25	Laminated Peloidal Packstone	X
SPB20-SPC12	N 38.73873, W 114.96050	SPC	B	438.25	Laminated Peloidal Packstone	
SPB20-SPC13	N 38.73871, W 114.96046	SPC	B	440.35	Laminated Peloidal Packstone	
SPB20-SPC14	N 38.73870, W 114.96036	SPC	B	446.7	Laminated Peloidal Packstone	
SPB20-SPC15	N 38.73869, W 114.96030	SPC	B	448	Laminated Peloidal Packstone	
SPB20-SPC16	N 38.73869, W 114.96032	SPC	B	449	Clast-supported Conglomerate	X
SPB20-SPC17	N 38.73869, W 114.96032	SPC	B	449.65	Laminated Peloidal Packstone	X, alizarin red-stained
SPB20-SPC18	N 38.73869, W 114.96032	SPC	B	449.9	Fine-grained Sandstone	
SPB20-SPC19	N 38.73857, W 114.96021	SPC	B	452.45	Bioclast-rich Wackestone to Packstone	
SPB20-SPC20	N 38.73857, W 114.96021	SPC	B	453	Laminated Peloidal Packstone	
SPB20-SPC21	N 38.73857, W 114.96021	SPC	B	454.5	Oncoid Packstone to Grainstone	X
SPB20-SPC22	N 38.73857, W 114.96021	SPC	B	455.1	Oncoid Packstone to Grainstone	X
SPB20-SPC23	N 38.74002, W 114.95521	SPC	B	459.1	Laminated Peloidal Packstone	
SPB20-SPC24	N 38.74002, W 114.95521	SPC	B	459.3	Oncoid Packstone to Grainstone	
SPB20-SPC25	N 38.74002, W 114.95521	SPC	B	459.6	Oncoid Packstone to Grainstone	
SPB20-SPC26	N 38.74002, W 114.95521	SPC	B	459.9	Bioturbated Peloidal Packstone	X, alizarin red-stained
SPB20-SPC27	N 38.73827, W 114.95988	SPC	B	473.9	Laminated Peloidal Packstone	
SPB20-SPC28	N 38.73827,	SPC	B	489.2	Bioturbated Peloidal Packstone	X

	W 114.95976					
SPB20-SPC29	N 38.73824, W 114.95955	SPC	B	500	Bioturbated Peloidal Packstone	
SPB20-SPC30	N 38.73810, W 114.95878	SPC	B	540.2	Micro-clotted Microbial Boundstone	X
SPB20-SPC31	N 38.73809, W 114.95866	SPC	B	546	Thrombolite Boundstone (large clots)	X, alizarin red-stained
SPB20-SPC32	N 38.73809, W 114.95829	SPC	B	558	Vuggy Wackestone	
SPB20-SPC33	N 38.73830, W 114.95789	SPC	B	573.7	Bioturbated Peloidal Packstone	
SPB20-SPC34	N 38.73846, W 114.95649	SPC	B	611.75	Micro-clotted Microbial Boundstone	X
SPB20-SPC35	N 38.73824, W 114.95605	SPC	B	622.2	Micro-clotted Microbial Boundstone	
SPB20-SPC45	N 38.73952, W 114.95514	SPC	B	637.25	Micro-clotted Microbial Boundstone	X
SPB20-SPC46	N 38.73962, W 114.95516	SPC	C	638.15	Undifferentiated Mudstone to Wackestone	
SPB20-SPC47	N 38.73962, W 114.95516	SPC	C	638.55	Micro-clotted Microbial Boundstone	
SPB20-SPC51	N 38.73947, W 114.95055	SPC	C	762.4	Laminated Peloidal Packstone	X
SPB20-SPC50	N 38.73947, W 114.95055	SPC	C	763.9	Micro-clotted Microbial Boundstone	X, alizarin red-stained
SPB20-SPC49	N 38.73952, W 114.95010	SPC	C	780.95	Clast-supported Conglomerate	
SPB20-SPC48	N 38.73947, W 114.94976	SPC	C	793.25	Micro-clotted Microbial Boundstone	X, alizarin red-stained
				Measured Level (m)		
SPB20-SPC36	N 38.73737, W 114.95876	Lower B	B	0.70	Thrombolite Boundstone (large clots)	X, alizarin red-stained
SPB20-SPC37	N 38.73735, W 114.95866	Lower B	B	3.70	Laminated Peloidal Packstone	
SPB20-SPC38	N 38.73733, W 114.95847	Lower B	B	8.70	Thrombolite Boundstone (large clots)	X
SPB20-SPC39	N 38.73716, W 114.95786	Lower B	B	22.75	Thrombolite Boundstone (small clots)	
SPB20-SPC40	N 38.73716, W 114.95786	Lower B	B	24.75	Thrombolite Boundstone (large clots)	
SPB20-SPC41	N 38.73721, W 114.95785	Lower B	B	27.40	Thrombolite Boundstone (large clots)	X
SPB20-SPC42	N 38.73739, W 114.95784	Lower B	B	30.40	Clast-supported Conglomerate	
SPB20-SPC43	N 38.73727, W 114.95781	Lower B	B	31.65	Peloidal Grainstone	X, alizarin red-stained
SPB20-SPC44	N 38.73733, W 114.95754	Lower B	B	38.90	Laminated Peloidal Packstone	

Table 2-S1: Summary of ID, GPS coordinates, measured transect, member, stratigraphic level in meters (composite or measured), and facies characterization for all SPF samples. Samples with a corresponding thin section are denoted with an "X" in the "Thin Section" column, including a note if stained with alizarin red for the identification of calcite. Note that the U-Pb detrital zircon sample is also included in this table.

Sample ID	**Transect**	**Member**	**Facies Name**	**XRD Dominant Mineralogy**		
				1st	**2nd**	**3rd**
SPB19-ML01	ML	B	Bioclast-rich WS/PS	Calcite, magnesian	Calcite	
SPB19-ML13	ML	B	Micro-clotted Microbial BS	Calcite	Calcite, magnesian	

SPB19-ML28	ML	B	Bioturbated PS	Magnesium Calcite	Calcite	
SPB19-ML33	ML	B	Thrombolite BS (framework)	Magnesium Calcite	Calcite	
SPB19-ML39	ML	B	Peloidal GS	Quartz	Dolomite (stoichiometrically ordered)	
SPB19-ML40	ML	B	Vuggy WS	Dolomite (stoichiometrically ordered and disordered)		
SPB19-ML43	ML	B	Laminated PS	Magnesium Calcite	Dolomite (stoichiometrically disordered)	Quartz low
SPB19-ML45	ML	B	Bioturbated PS	Dolomite (stoichiometrically ordered and disordered)	Quartz low	
SPB19-ML48	ML	B	Laminated PS	Dolomite (stoichiometrically ordered and disordered)	Quartz low	
SPB19-ML50	ML	B	Micro-clotted Microbial BS	Magnesium Calcite	Calcite	
SPB19-ML58	ML	C	Oncoid GS	Calcite, magnesian	Calcite	
SPB19-ML62	ML	C	Peloidal GS	Calcite	Magnesium Calcite	
SPB19-ML64	ML	C	Micro-clotted Microbial BS	Calcite	Magnesium Calcite	
SPB19-ML65	ML	C	Bioclast-rich WS/PS	Dolomite (stoichiometrically ordered)		
SPB19-ML66	ML	C	Very fine- to fine-grained SS	Dolomite (stoichiometrically ordered)	Quartz low	
SPB19-ML68	ML	D	Undifferentiated MS/WS	Dolomite (stoichiometrically ordered)		
SPB19-ML93	ML	D	Undifferentiated MS/WS	Dolomite (stoichiometrically ordered)		
SPB19-ML95	ML	E	Bioclast-rich WS/PS	Calcite		
SPB19-ML97	ML	E	Bioclast-rich WS/PS	Magnesium Calcite	Calcite	Calcite, magnesian
SPB20-SPC02	SPC	B	Laminated PS	Calcite	Calcite, magnesian	
SPB20-SPC22	SPC	B	Oncoid PS/GS	Calcite	Calcite, magnesian	Quartz low
SPB20-SPC28	SPC	B	Bioturbated PS	Magnesium Calcite	Calcite	
SPB20-SPC31	SPC	B	Thrombolite BS (large clots)	Calcite	Magnesium Calcite	
SPB20-SPC32	SPC	B	Vuggy WS	Dolomite (stoichiometrically ordered and disordered)		
SPB20-SPC34	SPC	B	Micro-clotted Microbial BS	Calcite	Quartz low	
SPB20-SPC45	SPC	B	Micro-clotted Microbial BS	Calcite		
SPB20-SPC47	SPC	B	Micro-clotted Microbial BS	Calcite	Calcite, magnesian	
SPB20-SPC49	SPC	B	Clast-Supported Congl	Calcite, magnesian	Calcite	
SPB20-SPC48	SPC	B	Micro-clotted Microbial BS	Calcite, magnesian	Calcite	Dolomite
SPB20-SPC40	Member B Slope	B	Thrombolite BS (large clots)	Calcite, magnesian	Calcite	
SPB20-SPC43	Member B Slope	B	Peloidal GS	Dolomite (stoichiometrically ordered and disordered)	Calcite, magnesian	

Table 2-S2: Summary of dominant mineralogy for the subset of samples analyzed with X-ray diffractometry mineralogy. When present, dolomite is noted as being stoichiometrically ordered and/or disordered.

Facies Plate	**Figure Panel ID**	**Sample ID**
Fig 4. – Boundstone Facies Plate	Fig. 4A	SPB20-SPC40
	Fig. 4B	SPB19-ML31
	Fig. 4C	Above SPB19-ML33

	Fig. 4D	Above SPB19-ML33
	Fig. 4E	SPB19-ML31
	Fig. 4F	SPB19-ML37
	Fig. 4G	SPB20-SPC31
	Fig. 4H	SPB19-ML33
	Fig. 4I	SPB20-SPC31
	Fig. 4J	SPB20-SPC31
	Fig. 4K	SPB19-ML33
	Fig. 4L	SPB19-ML04
	Fig. 4M	SPB19-ML04
	Fig. 4N	SPB19-ML04
Fig. 5 – Grainstone Facies Plate	Fig. 5A	SPB19-ML05
	Fig. 5B	SPB19-ML05
	Fig. 5C	SPB20-SPC43
	Fig. 5D	SPB19-ML39
	Fig. 5E	SPB19-ML39
	Fig. 5F	SPB19-ML39
	Fig. 5G	SPB19-ML27
	Fig. 5H	SPB19-ML27
	Fig. 5I	SPB19-ML27
	Fig. 5J	SPB19-ML27
	Fig. 5K	SPB20-SPC22
	Fig. 5L	SPB20-SPC24
	Fig. 5M	SPB20-SPC22
	Fig. 5N	SPB20-SPC22
	Fig. 5O	SPB19-ML58
Fig. 6 – Packstone Facies Plate	Fig. 6A	SPB20-SPC11
	Fig. 6B	SPB19-ML47
	Fig. 6C	SPB19-ML19
	Fig. 6D	SPB20-SPC17
	Fig. 6E	SPB20-SPC11
	Fig. 6F	SPB20-SPC11
	Fig. 6G	SPB19-ML22
	Fig. 6H	SPB19-ML23
	Fig. 6I	SPB19-ML23
	Fig. 6J	SPB19-ML01
	Fig. 6K	SPB19-ML97
	Fig. 6L	SPB19-ML65
Fig. 7 – Mudstone and Wackestone Facies Plate	Fig. 7A	SPB19-ML46
	Fig. 7B	SPB19-ML85
	Fig. 7C	SPB19-ML93
	Fig. 7D	SPB19-ML74
	Fig. 7E	SPB19-ML74
	Fig. 7F	SPB20-SPC32
	Fig. 7G	SPB19-ML83
	Fig. 7H	SPB19-ML83
	Fig. 7I	SPB19-ML69
	Fig. 7J	SPB19-ML69
Fig. 8 – Siliciclastic Facies Plate	Fig. 8A	SPB19-SPC04 and above
	Fig. 8B	SPB19-SPC07 and above
	Fig. 8C	Member C, ML transect ~658 m
	Fig. 8D	SPB19-ML61 and above
	Fig. 8E	Member C, ML transect ~621 m
	Fig. 8F	SPB19-ML59
	Fig. 8G	SPB19-ML51
	Fig. 8H	SPB19-ML51
	Fig. 8I	SPB19-ML51

Table 2-S3: Sample IDs associated with images in facies plate figures.

S.2.1 Extended methods for detrital zircon U-Pb analyses with field photos

The U-Pb detrital zircon sample was collected from coarse-sand layers within an ~5 m-thick channel deposit that consisted of clast-supported pebble conglomerates (some exhibiting trough cross-bedding) and various coarse-grained sands with planar cross-bedding between 653.5 and 658.5 meters in the Mainline transect (see Table S3 and field photos below). The sample was prepared using a jaw crusher, pulverizer, and water-table, followed by a heavy liquid mineral separation and Frantz magnetic separation. Backscattered electron (BSE) images were then created for grain mounts of the isolated crystals from the sample. The Arizona LaserChron Center used a Photon Machines Analyte G2 excimer laser (Teledyne Photon Machines, Bozeman, MT, USA) with a spot diameter of 25 or 30 μm, and subsequent analysis with a Nu Plasma high resolution MC-ICPMS (Nu Instruments, Wrexham, United Kingdom). An initial mount of 300 zircons was analyzed from the sample to determine suitability for the method. This was followed by a second mount for a total of 600 spot analyses. Results that were >20% discordant (by comparison of $^{206}Pb/^{238}U$ and $^{206}Pb/^{207}Pb$ ages) or >5% reverse discordant were not considered, as they likely experienced some degree of Pb-loss, initial disequilibrium, common Pb inclusion, or a combination of factors (Schoene, 2014).

Reference:

Schoene, B. (2014) U–Th–Pb Geochronology. In: *Treatise on Geochemistry*, *Elsevier*, 341–378.

Above: Select field photos of coarse-grained sand layers that contributed to the U-Pb detrital zircon sample from Member C (SP1986 DZ). Note that some field photos show different sample names (e.g., SP1951 (DZ)) because various detrital zircon samples from this ~5 m-thick channel deposit interval were sampled separately and then subsequently combined prior to preparation and analysis.

S.2.2. Additional XRD methods and results

For this study, calcite mineralogy corresponds to calcite, magnesian calcite, or magnesium calcite peaks identified by the spectral matching software (provided as unique mineral phase information only in Table S2). Dolomite is both stoichiometrically ordered and disordered (see individual XRD spectra).

S.2.3 Calculating composite stratigraphic level of select members in measured transects

Stratigraphic level corrections were completed in order create a composite stratigraphic level for all members within Sheep Pass Formation type section measured transects. Note that here "composite" does not refer to lateral stratigraphic correlation of parallel or overlapping sections, but rather to the extrapolation of known measurements (i.e., GPS coordinates, elevation, and/or strike and dip) to estimate stratigraphic positions of samples or member contacts within the same measured transect. In several cases, using a Jacob's staff to continuously measure stratigraphic level across all members was not possible. Thus, it was necessary to employ GPS coordinates, strike and dip measurements, and elevation to calculate the thickness between various intervals not measured with a Jacob's staff. This method was used for the following intervals:

1) In the Sheep Pass Canyon transect there was extensive cover between the base of member A and the first outcropping beds (base of measured section) in member A, which led us to collect a GPS coordinate and elevation at the base of member A and calculate the thickness to the base of the section.
2) In the Mainline transect, poor exposure and rugged surface conditions in member D led us to use elevation and strike and dip measurements to calculate the thickness between certain outcropping beds

3) In the Mainline transect, poor exposure in member E led us to use elevation and strike and dip measurements to calculate the thickness between certain outcropping beds

S.2.3.1 Summary of Methods

GPS coordinates were entered into Google Earth Pro and a path was drawn between waypoints. Google Earth defined the distance and the elevation difference between the two points (this can be found when viewing a path created in "see elevation profile" view). GPS coordinate units (in degrees) were converted to meters, and the azimuth (strike or bearing of the line that connects the two coordinate points) was found using the online application from Moveable Type Scripts, "Calculate the bearing between two Latitude/Longitude points" (https://www.movable-type.co.uk/scripts/latlong.html). Equations to calculate map-angle thickness were used from Groshong (2006) and are summarized below:

The equation for the map-angle thickness of a bed dipping in the same direction as the topographic slope is:

$$t=[h\cos(A)*\sin(d)-v\cos(d)]$$, note that [ ] denotes an absolute value

The equation for the map-angle thickness of a bed dipping in the opposite direction as the topographic slope is:

$$t=h\cos(A)*\sin(d) + v\cos(d)$$

where,
t=true thickness of bed
h=horizontal length between the two coordinates (this is the same as the horizontal distance between waypoints found in Google Earth Pro)

A=difference between the angle measure of the azimuth and the dip direction angle (note: dip direction angle is not the strike, but rather 90 degrees from strike, as it points in the exact direction that the bed dips)
d=dip angle of the beds (based off of the strike and dip measurements used when measuring the section with the Jacob staff)
v=the elevation difference (determined from Google Earth Pro)

S.2.3.2 Interval Map-Thickness Calculations

1) Base of member A to base of measured section in member A:

*Note that bedding dips in same direction as topographic slope

Waypoint for SPC-Abase (base of member A):
N 38.73999, W -114.96858

Waypoint for SPC-BOS (base of measured section in member A):
N 38.73816, W -114.96450

"Calculate the bearing between two Latitude/Longitude points" results:
Bearing: 119°

Google Earth Pro results from "elevation profile":
Distance between coordinate points, h: 403m
Difference in elevation, v: 26.8m

Strike and Dip of beds:
Strike: 035°
Dip Direction (Strike + 90 degrees): 125°
Dip Angle, d: 44°

Angle A (difference between the dip angle, d, and the azimuth): 125°- 119° = 6°

Calculation:
t=[hcos(A)*sin(d)-vcos(d)]
t=[(403m)cos(6°)*sin(44°) - (26.8m)cos(44°)] = **259m**

2) Thickness between SPB19-ML88 and SPB19-ML89 and SPB19-ML89 to "0 meter level" in member D:

*Note that bedding dips in opposite direction as topographic slope

-SPB19-ML88 to SPB19-ML89:

Waypoint for SPB19-ML88:
N 38.72548, W -114.96003

Waypoint for SPB19-ML89:
N 38.72566, W -114.95950

“Calculate the bearing between two Latitude/Longitude points” results:
Bearing: 66°

Google Earth Pro results from “elevation profile”:
Distance between coordinate points, h: 68.7m
Difference in elevation, v: 21.6m

Strike and Dip of beds:
Strike: 050°
Dip Direction (Strike + 90 degrees): 140°
Dip Angle, d: 40°

Angle A (difference between the dip angle, d, and the azimuth): 140° - 66° = 74°

Calculation:
t=hcos(A)*sin(d) + vcos(d)
t=(68.7m)cos(74°)*sin(40°) + (21.6m)cos(40°) = **28.7m**

-SPB19-ML89 to “0 meter level”

*Note “0 meter level” marked where we were able to start measuring with a Jacob’s staff in member D

Waypoint for SPB19-ML89:
N 38.72566, W -114.95950

Waypoint for ML “0 meter level”:
N 38.72569, W -114.95945

“Calculate the bearing between two Latitude/Longitude points” results:
Bearing: 52°

Google Earth Pro results from “elevation profile”:
Distance between coordinate points, h: 8.04m
Difference in elevation, v: 2.56m

Strike and Dip of beds:

Strike: 050°
Dip Direction (Strike + 90 degrees): 140°
Dip Angle, d: 40°

Angle A (difference between the dip angle, d, and the): 140° - 52° = 88°

Calculation:
t=hcos(A)*sin(d) + vcos(d)
t=(8.04m)cos(88°)*sin(40°) + (2.56m)cos(40°) = **2.1m**

3) Thickness between SPB19-ML96 and SPB19-ML97 in member E:

*Note that bedding dips in opposite direction as topographic slope

Waypoint for ML96:
N 38.72533, W -114. 95873

Waypoint for ML97
N 38.72544, W -114.95823

"Calculate the bearing between two Latitude/Longitude points" results:
Bearing: 74°

Google Earth Pro results from "elevation profile":
Distance between coordinate points, h: 56.9m
Difference in elevation, v: 14m

Strike and Dip of beds:
Strike: 050°
Dip Direction (Strike + 90 degrees): 140°
Dip Angle, d: 40°

Angle A (difference between the dip angle, d, and the): 140°- 74° = 66°

Calculation:
t=hcos(A)*sin(d) + vcos(d)
t=(56.9m)cos(66°)*sin(40°) + (14m)cos(40°) = **25.6m**

Reference:

Groshong, R.H. (2006) 3-D Structural Geology: A Practical Guide to Quantitative Surface and Subsurface Map Interpretation, 2nd edn. *Springer Netherlands*, 411 pp.

Chapter III: A geochemical record of environmental change in response to latest Cretaceous and early Paleogene climate in the Sheep Pass Formation, Nevada, USA

Juliana Olsen-Valdez[1], Sarah Widlansky[2], Elizabeth Trower[1], Kathryn Snell[1], William Clyde[3]

[1]Department of Geological Sciences, University of Colorado Boulder, Benson Earth Sciences Building, 2200 Colorado Ave., Boulder, Colorado 80309, USA

[2]Department of Earth Sciences, University of New Hampshire, 56 College Road, 214 James Hall, Durham, New Hampshire 03824, USA. Now at: Woods Hole Coastal and Marine Science Center, U.S. Geological Survey, 360 Woods Hole Road, Woods Hole, Massachusetts 02543, USA

[3]Department of Earth Sciences, University of New Hampshire, 56 College Road, 214 James Hall, Durham, New Hampshire 03824, USA

3.1 Abstract

Understanding the environmental response of ancient terrestrial lacustrine archives to global greenhouse climate expands our understanding of past environmental change beyond the marine realm and has the potential to provide key insights into the settings most threatened by future anthropogenic warming. The Sheep Pass Formation in east-central Nevada, USA preserves lacustrine, palustrine, and microbialite carbonates deposited from the latest Cretaceous to middle Eocene time, an interval characterized by both regional tectonic activity, as well as a

greenhouse climate with major global climate events. This study developed a new geochemical and paleotemperature record in the Sheep Pass Formation using stable carbon, oxygen, and carbonate clumped isotopes paired with transmitted light and cathodoluminescence microscopy. It also applied a dynamic time warping algorithm to better temporally correlate the Sheep Pass Formation type section record to global marine records from this time. Following careful screening techniques, we find that the Sheep Pass Basin preserves geochemical evidence for the possible preservation of both long-term and short-term global climate trends. The gradual warming and transition to higher $\delta^{13}C$ throughout much of the Sheep Pass Formation type section record is most representative of the long-term warming that characterized the later Paleocene and early Eocene. Sedimentological and geochemical evidence also signifies that the height of warming was marked by drier conditions in the Sheep Pass Basin, as is observed in other western USA records from this time. The dynamic time warping alignment suggests that some of these observed trends may also be the expression of short-term global climate transitions (e.g., the Paleocene-Eocene Thermal Maximum or an early Eocene hyperthermal). Further, the character of $\delta^{13}C$ and temperature shifts in the lower Sheep Pass Formation type section corresponds well to trends observed around the Cretaceous-Paleogene boundary in the global marine record and may be supported by the dynamic time warping alignment as well. Ultimately, this work highlights the promise of the Sheep Pass Formation type section in providing a new paleoclimate record during a pivotal climate interval.

3.2 Introduction

The Sheep Pass Formation type section in east-central Nevada, USA preserves lacustrine and palustrine carbonates deposited in a syn-tectonic, high-elevation lake basin between the latest Cretaceous and middle Eocene time (~70 Ma to ~45 Ma; Winfrey, 1960; Kellogg, 1964; Fouch, 1979; Olsen-Valdez et al., 2025; Druschke et al., 2009a; Snell et al., 2014). This depositional timeframe encompasses a pivotal past greenhouse climate interval, with applications as analogs for near-future anthropogenic climate change (Burke et al., 2018; Westerhold et al., 2020). In addition, developing geochemically and sedimentologically informed paleoclimate record in the Sheep Pass Formation type section has the potential to improve our understanding of how high-elevation terrestrial environments respond to greenhouse climate. This has implications for providing constraints on the expression of global climate signals in continental settings, which are known to be more climatically variable, often respond differently than the marine realm, and are usually poorly captured in global climate models (Thrasher and Sloan, 2009; Byrne and O'Gorman, 2015; Carmichael et al., 2016). Given that warming is amplified at higher elevations (Rangwala et al., 2013; Pepin et al., 2015), the results of this study may also provide timely nuance to current constraints on high-altitude environmental change under an Anthropocene climate.

Detailed sedimentological analyses in Chapter II (Olsen-Valdez et al., 2025) determined that the Sheep Pass Formation type section records a dynamic and highly sensitive high-elevation lake basin. Other sedimentary basins in the western USA

have been extensively studied and are coeval to the Sheep Pass Formation; they preserve evidence for paleobiological, paleohydrological, and/or paleotemperature variations in response to major global climate change during this time (e.g., Wilf et al., 2003; Kraus et al., 2013; Frantz et al., 2014). These records serve as an important comparative framework for the Sheep Pass Formation, especially with respect to stratigraphic intervals previously recognized as valuable targets for future paleoclimatic study (Olsen-Valdez et al., 2025). Despite the promise of the Sheep Pass Formation type section, only one geochemical study has been completed in this section to date (Snell et al., 2014).

In this study, we bridged this knowledge gap using transmitted light and cathodoluminescence microscopy, X-ray diffraction (XRD), and stable isotope geochemistry ($\delta^{13}C$, $\delta^{18}O_{carb}$, $\delta^{18}O_{water}$, and carbonate clumped isotope thermometry – $T(\Delta_{47})$) to investigate the paleoclimatic and paleoenvironmental conditions that characterized this dynamic, high-elevation lake basin during a past greenhouse climate interval.

3.3 Background

3.3.1 Overview of Latest Cretaceous to Early Paleogene Climate

The latest Cretaceous and early Paleogene periods encompass a greenhouse climate interval, which include both warmhouse and hothouse climate states in an ice-free world characterized by warmer mean global temperatures and elevated atmospheric pCO_2 concentrations compared to today (Zachos et al., 2008; Pagani et

al., 2014; Westerhold et al., 2020; The Cenozoic CO Proxy Integration Project (CenCOPIP) Consortium et al., 2023). The Late Cretaceous is characterized by gradual, long-term cooling following hothouse conditions in the mid-Cretaceous (Pagani et al., 2014; Huber et al., 2018; Scotese et al., 2025). Deccan Trap volcanism, which began in the latest Cretaceous, contributed to warming and climate instability leading up to the Cretaceous-Paleogene (K-Pg) boundary (Wilf et al., 2003; Petersen et al., 2016; Barnet et al., 2018; Keller et al., 2018).

The Cretaceous period culminated with a drop in global temperatures (~2-7°C; Wilf et al., 2003; Dennis et al., 2013; Tobin et al., 2014; Scotese et al., 2025), as well as a catastrophic bolide impact. This impact event is hypothesized to have resulted in the suspension of thousands of tons of vaporized rock material into the atmosphere, blocking sunlight and leading to a transient (<10s yrs) cooling event termed the 'impact winter', which is associated with up to 7°C of cooling and ultimately resulted in the major K-Pg mass extinction (~66 Ma; Alvarez et al., 1980; Vellekoop et al., 2014, 2016; Scotese et al., 2025). It is also argued that much of the volcanic activity associated with the Deccan Traps occurred at and closely following (<100 thousand years after) the K-Pg boundary (Renne et al., 2015; Richards et al., 2015; Petersen et al., 2016; Sprain et al., 2019); the increase in pCO_2 associated with these eruptions likely contributed to a warmer climate by the later Paleocene (Barnet et al., 2018; Scotese et al., 2025). Floral and faunal analyses also suggest at least two early Paleocene warming intervals in the first ~1 million years following the K-Pg boundary, associated with 2-5°C of warming during each interval (Lyson et al., 2019).

The relatively cooler temperatures in the Late Cretaceous and early Paleogene gave way to warming that started in the later Paleocene and culminated with the Early Eocene Climatic Optimum (EECO, ~49-53 Ma), which was the apex of extreme global warmth for the entire Cenozoic era with mean global temperatures >10°C warmer than today (Zachos et al., 2001, 2008; Pagani et al., 2014; Westerhold et al., 2020). Superimposed on this long-term warming were abrupt and transient (10s-100s kyr) global hyperthermal climate events associated with negative carbon isotope excursions (CIEs) related to the addition of 1,000s of gigatons of ^{13}C-depeleted carbon into the ocean-atmosphere system and CO_2-induced global warming (Zachos et al., 2001, 2008; Koch et al., 2003; Pagani et al., 2014; Lauretano et al., 2015; Abels et al., 2016; Westerhold et al., 2020; The Cenozoic CO Proxy Integration Project (CenCOPIP) Consortium et al., 2023). This includes the Paleocene-Eocene Thermal Maximum (PETM, ~56 Ma), which affected both the marine and terrestrial realm, and led to at least 5°C of global warming (Koch et al., 2003; Zachos et al., 2008; Pagani et al., 2014). The early Eocene is also characterized by several more hyperthermal climate events (Lauretano et al., 2015; Abels et al., 2016; Widlansky et al., 2022). The Eocene Thermal Maximum 2 (ETM2) and H2, both around 54 Ma, were the most immediate post-PETM hyperthermals and have also been associated with negative carbon isotope excursions and faunal turnover in the marine and terrestrial realm (Widlansky et al., 2022).

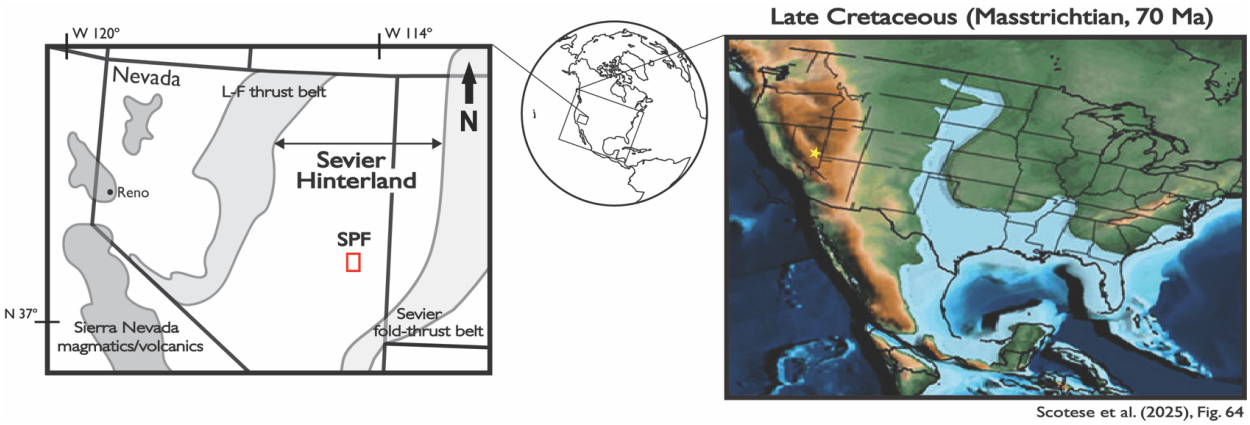

Figure 3-1: The Sheep Pass Formation (SPF) type section (red box) in the context of prevalent western USA tectonic features during its formation (modified from Druschke et al., 2009a) with present-day city of Reno, Nevada and paleogeography of the western USA in the Maastrichtian (70 Ma), towards the beginning of the SPF (yellow star) depositional timeframe (from Scotese et al., 2025). LF = Luning-Fencemaker.

3.3.2 Sheep Pass Formation Geologic Background and Existing Age Framework

The latest Cretaceous to middle Eocene Sheep Pass Formation (SPF) type section comprises an approximately 1 km thick mixed succession of lacustrine and palustrine carbonates (including microbialites – carbonate facies interpreted to have formed in association with microbial mats), as well as alluvial and fluvio-deltaic deposits in east central Nevada, USA (Fig. 1; Winfrey, 1960; Kellogg, 1964; Fouch, 1979; Fouch et al., 1991; Olsen-Valdez et al., 2025; Druschke et al., 2009a). The SPF type section is unconformably bound by underlying upper Paleozoic limestones, sandstones, and shales, and overlying upper Eocene to Oligocene volcaniclastics (Winfrey, 1960; Kellogg, 1964; Fouch, 1979; Fouch et al., 1991; Druschke et al., 2009a). Six lithologically distinct members (A to F) characterize the Sheep Pass Formation type section (Winfrey, 1960; Kellogg, 1964; Fouch, 1979; Good, 1987).

Member B, which is primarily composed of carbonate rocks, reflects the major lacustrine phase of this paleo-lake basin and has been the focus of past geochemical and sedimentological studies (Olsen-Valdez et al., in review; Snell et al., 2014).

The age framework of the SPF type section is based on a combination of biostratigraphy, palynology, and more recent U-Pb dating (Winfrey, 1960; Kellogg, 1964; Fouch, 1979; Good, 1987; Druschke et al., 2009b, 2009a, 2011; Olsen-Valdez et al., 2025). The top of Member A yielded U-Pb detrital zircon dates with a maximum depositional age between ~68-70 Ma ± 1 Ma (Druschke et al., 2009b). A calcite U-Pb age from near the base of Member B constrains the depositional age to 66.1 ± 5.4 Ma for that interval (Druschke et al., 2009b). A U-Pb detrital zircon sample from upper Member C has a maximum depositional age of 62.14 ± 0.65 Ma (Olsen-Valdez et al., 2025). These dates confirm biostratigraphic and palynological interpretations that Members A and B, and at least most of Member C were deposited between the Maastrichtian and Paleocene (Fouch, 1979; Good, 1987). Though no recent dating has been completed on Member E, molluscan associations constrain the member to middle Eocene (Bridgerian, 50.5-45.4 Ma; Good, 1987). Lastly, $^{40}Ar/^{39}Ar$ dates and detrital zircon age peaks suggest that overlying ash-flow tuffs and siliciclastic beds were deposited in late Eocene time (Druschke et al., 2009a, 35-38 Ma; 2011).

3.3.2.1 Tectonic Setting

The SPF type section was deposited in an extensional half-graben basin with locally high-relief (Vandervoort and Schmitt, 1990; Druschke et al., 2009b, 2011).

This topography was a product of compressional tectonics in the western USA during this time, related to the subduction of the Farallon Plate under North America (DeCelles, 2004; Dickinson, 2004; DeCelles and Coogan, 2006; Druschke et al., 2011; Long, 2015). This long-term plate convergence led to the development of a high-elevation orogenic plateau in present-day Nevada by the Late Cretaceous (Fig. 1; Coney and Harms, 1984; Jones et al., 1998; DeCelles, 2004; Dickinson, 2004; Druschke et al., 2011; Snell et al., 2014; Long, 2015).

Multiple lines of evidence suggest syn-depositional tectonic activity at the onset and throughout much of the SPF type section depositional timeframe (Winfrey, 1960; Kellogg, 1964; Fouch, 1979; Fouch et al., 1991; Druschke et al., 2009a). Specifically, Members A, B, and C preserve sedimentological features (e.g., megabreccia and gravity slide deposits in Member A, soft-sediment deformation structures and overturned bedding in Members B and C) supporting syn-depositional tectonic activity (Druschke et al., 2009a). Notably, Druschke et al. (2009a) suggested that Members D, E, and F time were marked by little to no syn-depositional tectonic activity, and that the basin-bounding fault in the SPF type section did not reactivate until middle to late Eocene time.

Facies Name	**Facies Name Abbreviation**	**Depositional Setting**	**Member(s)**	**Analyzed for T(Δ_{47})?**
Thombolite Boundstone	Thrombolite BS	Shallow Lacustrine	Member B: Interval II	Yes
Micro-clotted Microbial Boundstone	Micro-clotted Microbial BS	Shallow Lacustrine	Member B	Yes

Oncoid Packstone to Grainstone	Oncoid PS/GS	Shallow Lacustrine	Member B: Interval I and Member C	Yes
Ooid Grainstone	Ooid GS	Shallow Lacustrine	Member B: Interval I	Yes
Peloidal Grainstone	Peloidal GS	Transitional Shoreline (Shallow Lacustrine/Palustrine)	Member B: Interval III	Yes
Laminated Peloidal Packstone	Laminated Peloidal PS	Shallow Lacustrine	Member B	Yes
Bioturbated Peloidal Packstone	Bioturbated Peloidal PS	Shallow Lacustrine	Member B: Interval I	Yes
Bioclast-rich Wackestone to Packstone	Bioclast-rich WS/PS	Lacustrine to Palustrine	Members B and E	Yes
Undifferentiated Mudstone to Wackestone	Undiff. MS/WS	Palustrine	Member D	Yes
Vuggy Wackestone	Vuggy WS	Palustrine	Member D	Yes
Matrix-supported Conglomerate	Matrix-supported Congl.	Alluvio-fluvial	Member A	No
Clast-supported Conglomerate	Clast-supported Congl.	Alluvio-fluvial	Members A and C	No
Fine-grained Sandstone	Fine-grained SS	Alluvio-fluvial	Members A and C	No
Fine to Coarse-grained Sandstone	Fine to Coarse-grained SS	Alluvio-fluvial	Members A and C	No
Very fine to Fine-grained Sandstone	Very fine to Fine-grained SS	Fluvio-deltaic	Members A and C	Yes

Table 3-1: Summary of SPF facies and their depositional settings, including the member(s) in which they are most prevalent. See Olsen-Valdez et al. (2025) for more detailed sedimentological facies characterizations.

3.3.2.2 Depositional Environments of the Sheep Pass Formation

Key facies and their interpreted depositional environments in the SPF type section are summarized from Olsen-Valdez et al. (2025) in Table 1. Broadly, the Sheep Pass Basin went through an environmental evolution that included: (i) basin initiation and an alluvio-fluvial stage represented by Member A; (ii) a major lacustrine stage represented by Member B; (ii) a fluvio-deltaic stage represented by Member C; (iv) a major palustrine stage represented by Member D; and (v) an ephemeral lacustrine stage represented by Member E (Olsen-Valdez et al., 2025).

The major lacustrine stage (Member B) preserves three distinct environmental intervals (Olsen-Valdez et al., 2025). Interval I reflects a freshwater, high-energy shoreline with few microbialites in a hydrologically open, balanced-fill lake basin. Interval II reflects an alkaline, microbialite-dominated setting with low invertebrate abundance. Interval III reflects an evaporitic, marginal shoreline setting with varying lake level and periodically evaporative conditions that led to the formation of dolomite in more alkaline or saline water within a hydrologically closed, underfilled lake basin (Olsen-Valdez et al., 2025). Member C is also sub-divided based on the lower portion being calcitic and upper Member C being dolomitic (Olsen-Valdez et al., 2025). The transition to dolomitic mineralogy in upper Member C may also be stratigraphically associated with a previously identified frog fossil death bed horizon (Henrici et al., 2018; Olsen-Valdez et al., in review; Bonde et al., 2020).

Ultimately, Olsen-Valdez et al. (2025) interpreted that the Sheep Pass Basin environmental evolution was driven by both tectonics and climate over time. However, specific stratigraphic intervals (Member B – Interval II, Member B –

Interval III, upper Member C, and Member D) were hypothesized to have been largely influenced by climate-related change (Olsen-Valdez et al., 2025). Member B – Interval II (the alkaline, microbialite-dominated lake) was hypothesized to reflect unique physicochemical conditions following the K-Pg mass extinction, where microbialites may have thrived in response to environmental exclusion or the complete absence of competitor organism abundance (Riding, 2006; Mata and Bottjer, 2012; Olsen-Valdez et al., in review; Chen and Lee, 2014).

Further, Member B – Interval III, upper Member C, and Member D all share characteristics associated with evaporative conditions and a shift to more saline or alkaline water chemistry (Olsen-Valdez et al., 2025). They also share other sedimentological features indicative of, for example, subaerial exposure, evaporite deposition, and/or fluctuations in water level (Olsen-Valdez et al., 2025). These characteristics have also been associated with drier conditions in response to early Paleogene climate, the PETM, and/or early Eocene hothouse climate in either the Bighorn Basin, Flagstaff Formation, or Green River Formation (Kraus and Riggins, 2007; Smith et al., 2008; Bowen et al., 2008; Tänavsuu-Milkeviciene and Sarg, 2012; Kraus et al., 2013; Frantz et al., 2014; Birgenheier et al., 2020; Pommer et al., 2023).

3.3.3 Seasonality of Carbonate Precipitation in Lacustrine and Palustrine Archives

Leveraging carbonates as paleoclimate archives requires consideration of when in the year they precipitated. Lacustrine carbonates are typically interpreted as preserving a warm season bias due to the favorability of carbonate formation (carbonate supersaturation and lower CO_2 solubility) under warm and evaporative

conditions (Zeebe and Wolf-Gladrow, 2001; Leng and Marshall, 2004; Huntington et al., 2010). Other factors (e.g., the influence of biological activity) can also play a role in the timing of carbonate precipitation (Huntington et al., 2010; Ingalls et al., 2020). Lacustrine carbonates from Member B in the SPF type section have been previously interpreted to reflect summer formation (Snell, 2011; Snell et al., 2014). Though less characterized, palustrine carbonates most likely also reflect warm season carbonate precipitation (Fetrow et al., 2022).

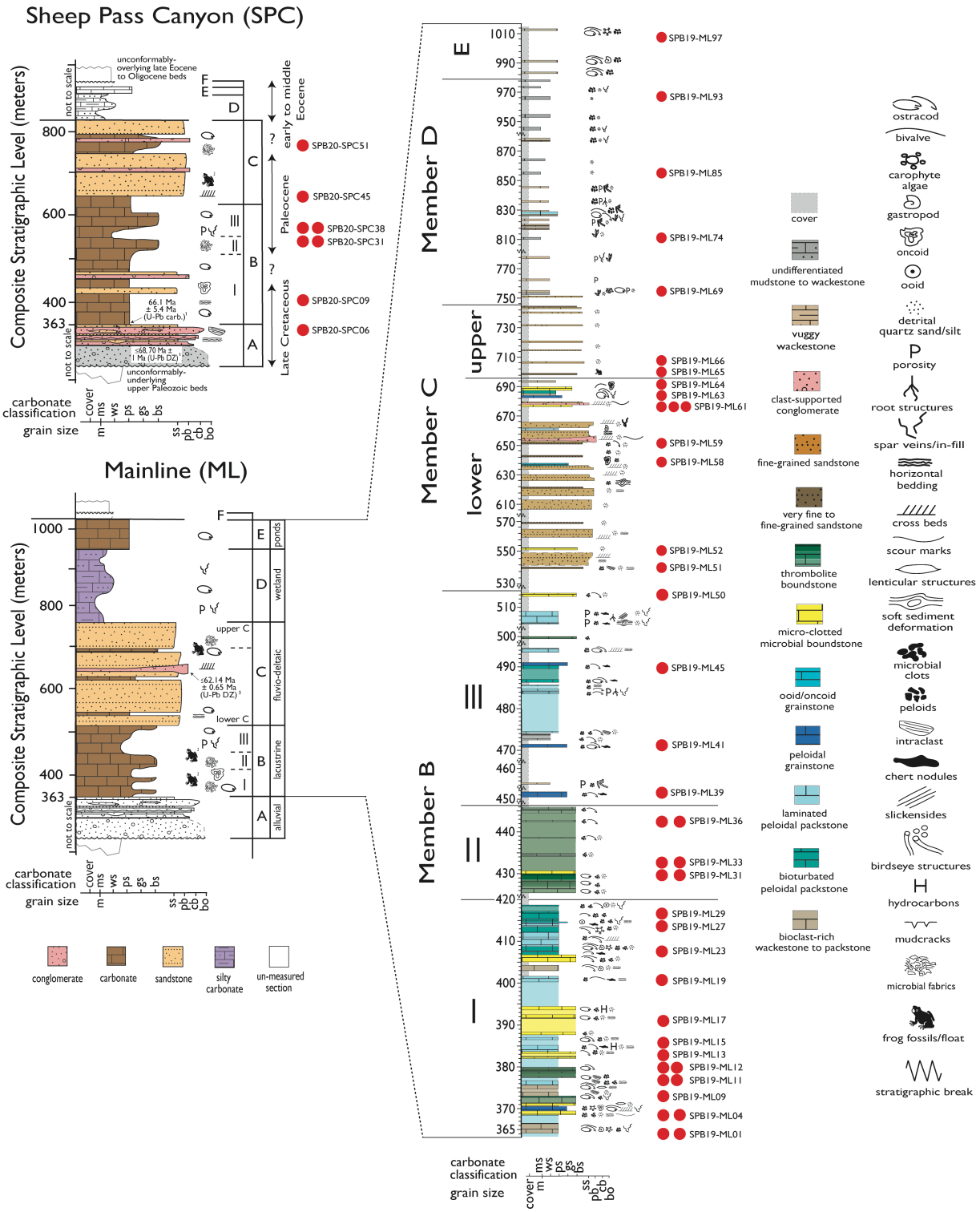

Figure 3-2: Overview and detailed stratigraphic columns with published age constraints from [1]Drushcke et al. (2009a) and [3]Olsen-Valdez et al. (2025). Stratigraphic levels of frog fossils/float from [2]Henrici et al. (2018). Δ_{47} samples labeled at their stratigraphic level (multiple dots indicates multiple fabrics sampled).

3.4 Materials and Methods

3.4.1 Field Methods and Hand Sample Preparation

We measured, described, and sampled two laterally adjacent stratigraphic transects – the Mainline and the Sheep Pass Canyon – within the Sheep Pass Formation type section area during field seasons in 2019 and 2020 (Fig. 2). A smaller (~40 m thick) stratigraphic transect – the Member B Slope – was measured, described, and sampled just south of the Sheep Pass Canyon transect. Carbonate beds were sampled from outcrops or shallow trenches at a resolution of <1 m in Member B, and ~5 m in Members A, C, D, and E. Member F was not sampled due to limited outcrop exposures (Winfrey, 1960; Fouch, 1979). Detailed field methods and resulting sedimentological facies characterizations are described in Olsen-Valdez et al. (2025). A total of 135 hand samples were collected from carbonate beds across all transects and a subset of 23 hand samples were collected from carbonate-cemented siliciclastic beds across all transects.

Hand samples were cut into billets and polished. Thin sections (n=56), prepared by Spectrum Petrographics and Grindstone Laboratory, were used for petrographic analysis, including preliminary determination of carbonate mineralogy (e.g., alizarin stain denoting calcite). Dominant mineralogy was also determined through the analysis of a subset of powdered carbonate samples on a Bruker D8 Advance X-Ray Diffractometer (Table S2 and see Olsen-Valdez et al., 2025). Analyses were completed at 40 kV power and a 40 mA current; resulting spectra reflected scans from $2\theta = 10°$ to 50° with 0.01° increments. For mineral identification, we used the DIFFRAC.EVA

software (Bruker, V.5.0) to match the unknown spectra to known spectra based on the International Centre for Diffraction Data PDF-4/Minerals database. For samples not directly analyzed for their dominant mineralogy, we labeled samples as either calcitic or dolomitic based on the mineralogical framework developed in Olsen-Valdez et al. (2025).

Cut and polished hand sample faces or polished sample billets (the mirrored faces to paired thin sections) were used to drill sample powder for geochemical analyses. When multiple fabrics were drilled from the same sample, they were considered discrete sample powders. For preliminary $\delta^{13}C$ and $\delta^{18}O_{carb}$ analyses, <5 mg aliquots of powder were generated using a fine, diamond-coated bit attached to a Dremel tool. For carbonate clumped isotope analyses, between 50-150 mg of powder was generated. Due to limited surface area, and to ensure powders reflected specific regions or textural components of a given sample based on previous petrographic characterization, billets were polished and then subsequently drilled up to six times and homogenized prior to carbonate clumped isotope analysis (e.g., clot and matrix components in sample SPB19-ML31).

Geochemical analyses were completed on samples comprising the full range of carbonate-bearing facies characterized by Olsen-Valdez et al. (2025) in the Sheep Pass Formation type section (Table 1 and Fig. 2). Additionally, a through-going crystalline spar vein was analyzed from a bioclast-rich wackestone to packstone sample to investigate the difference between the vein carbonate versus carbonate matrix in this sample.

3.4.2 Transmitted Light and Cathodoluminescence Microscopy

Transmitted light and cathodoluminescence (CL) microscopy techniques were used to determine both primary depositional and diagenetic (e.g., dissolution/reprecipitation) fabrics within Sheep Pass Formation type section samples. CL imaging allows for the visual identification of distinct generations of cement to help characterize primary versus diagenetic fabrics. In calcite and dolomite, luminescence mostly varies between red, orange, and yellow, as well as dull to non-luminescent (Machel and Burton, 1991). CL luminescence is a product of the spatial distribution of trace elements (primarily Mn or Fe) in a sample, as well as mineralogy (Pagel et al., 2000; Boggs and Krinsley, 2006). Luminescence can also be affected by several processes, including, for example, changes in precipitation rate, redox potential, and fluid evolution (Machel, 2000).

For this work, optical petrography was conducted on a Zeiss Axio Imager M2 microscope, while paired transmitted light and CL microscopy was conducted on a Technosyn Cathode Luminescence Model 8200 Mk II microscope. Petrography was completed for every sample in which there was a corresponding thin section (approximately one third of all samples collected). For samples with no corresponding thin section, fabric interpretations were applied from representative hand samples of the same facies.

3.4.3 Stable Carbon and Oxygen Isotopes

Carbonate sample powders (n=232; mostly from cut and polished hand sample faces) were weighed into ~120-150-μg-sized aliquots and placed into 12mL Labco

Exetainer vials with screw-top septa caps. The vials were purged with ultra-high purity Helium gas for 10 minutes to remove air from the vials. Powders were then digested in 70°C, 105%-110% orthophosphoric acid to release CO_2 for analysis. Carbonate standards that span a broad range of isotope values were weighed out and prepared identically to sample powders. Reacted sample and standard gases were analyzed for $\delta^{13}C$ and $\delta^{18}O_{carb}$ on a Thermo Fisher Scientific Gasbench II coupled to a Thermo Fisher Scientific Delta V continuous flow isotope ratio mass spectrometer in the University of Colorado Boulder Stable Isotope Laboratory (CUBES-SIL; RRID:SCR_019300).

Stable isotope values are reported in delta notation as permil values (parts per thousand, ‰) relative to Vienna Pee Dee Belemnite (VPDB; $\delta = [(R_{sample}/R_{standard})] - 1) \times 1000$, where R is the ratio of the heavier mass to lighter mass isotope). The analytical precision for both $\delta^{13}C$ and $\delta^{18}O_{carb}$ analyses was ± 0.1‰ or better, based on multiple replicate carbonate standard measurements (USGS44, IAEA-603, NBS18, Icelandic Spar (HIS), and an in-house marble standard, CU YULE). Raw values of all analyses were corrected with in-house CUBES-SIL R scripts that used the Isoreader R (Kopf et al., 2021) and tidyverse R packages. Raw values were first evaluated for linearity and/or drift effects; corrections were applied if either or both of those effects were identified. Corrected standard values were then used to determine a scale correction that was applied to all data. Because $\delta^{13}C$ and $\delta^{18}O_{carb}$ values were also obtained from analyses for carbonate clumped isotopes (see below), mean $\delta^{13}C$ and $\delta^{18}O_{carb}$ sample values and their errors were calculated for all

replicates from an individual sample across both analytical techniques. $\delta^{13}C$ and $\delta^{18}O_{carb}$ errors reported in the text reflect two standard errors (i.e., 2 s.e.) of the mean.

Samples with dolomitic mineralogy required a dolomite-specific calculation of the $\delta^{18}O_{carb}$ compared to calcitic samples because of the different fractionation factor between the oxygen isotopes of the carbonate versus reacted CO_2 for these two minerals (Rosenbaum and Sheppard, 1986; Lloyd et al., 2018). For $\delta^{18}O_{carb}$ sample replicate values generated with 70°C acid, a CO_2-dolomite fractionation factor of 1.009656 was used. This alpha value was determined by applying a 2nd order polynomial fit to data from Rosenbaum and Sheppard (1986), just as Lloyd et al. (2018) did to determine the CO_2-dolomite fractionation factor at 90°C (1.009218). We used the CO_2-dolomite fractionation factor from Lloyd et al. (2018) to correct $\delta^{18}O_{carb}$ sample replicate values generated with 90°C acid (i.e., from carbonate clumped isotope analyses; see below).

3.4.4 Carbonate Clumped Isotopes (Δ_{47})

The formation of multiply-substituted carbonate isotopologues (e.g., $^{13}C^{18}O^{16}O_2$) is thermodynamically favorable under decreasing temperatures (Ghosh et al., 2006; Eiler, 2007, 2011). Thus, the degree of multiple substitutions, or "clumping" (i.e., the abundance of these isotopologues) of heavy isotopes in the CO_2 evolved from a reacted carbonate sample can be leveraged as a paleothermometer. Sheep Pass Formation type section sample fabrics (n=51) were analyzed for carbonate clumped isotopes across nine sessions between 2020 and 2025. Samples were

generally prioritized based on their representative facies attributes and stratigraphic distribution, as well as if they appeared to be well preserved following transmitted light and CL petrography. Several internationally accepted (ETH1-4, IAEA-C1 and C2, Merck, and NBS19) and in-house standards (CU YULE and CU_CORAL) were analyzed at a sample-to-standard ratio of 1:1.

Between 8 and 20 mg of sample and standard powder was weighed into 6x4-mm-sized silver capsules, depending on the weight percent carbonate of the sample. As a pre-treatment for trace contaminants, some sample powders were soaked in a 3% solution of high purity sodium hypochlorite (i.e., bleach), rinsed five times with Milli-Q water, and dried in a vacuum oven at 30°C. Powders were digested for 25 minutes in a 90°C acid bath and the evolved CO_2 was subsequently passed through several purification steps – including two liquid nitrogen-cooled water traps, a silver wool trap, and a gas chromatography column containing PoraPak™ mesh porous polymer – to strip the reacted gas of water, sulfur, and/or organic compounds on a custom-built, automated line connected to the mass spectrometer. Select samples believed to contain trace contaminants were collected after a preliminary purification and processed through this system a second time prior to analysis (i.e., double cleaned). Cleaned CO_2 was then analyzed on a Thermo Fisher Scientific 253 Plus dual-inlet isotope ratio mass spectrometer in the CUBES-SIL.

The measured abundance of masses 44-49 of CO_2 were used to determine $\delta^{13}C_{carb}$, $\delta^{18}O_{carb}$, δ^{47} and Δ_{47} values for each sample and standard analyzed. Carbonate standard (ETH1-4, IAEA-C1 and C2) analyses were used to scale correct $\delta^{13}C_{carb}$ and

$\delta^{18}O_{carb}$ values, as well as correct all data into the Intercarb-Carbon Dioxide Equilibrium Scale (ICDES; Bernasconi et al., 2021). Δ_{47} values (‰, ICDES) reflect the difference between the measured ratios of mass-47 CO_2 (the doubly-substituted isotopologue, $^{13}C^{18}O^{16}O$) versus mass-44 CO_2 ($^{12}C^{16}O_2$) compared to the R^{47} expected in a stochastic (i.e., random) isotopic distribution (Ghosh et al., 2006; Schauble et al., 2006; Eiler, 2007):

$$\Delta_{47}\ (‰) = ((R^{47}_{sample}/R^{47}_{stochastic})\ -1) \times 1000, \text{ where } R^{47}=M^{47}/M^{44}$$

Analytical error for each single replicate analysis – reported as two standard errors of the mean (i.e., 2 s.e.) – is inclusive of error for each measurement, as well as the error associated with correction to the ICDES (Daëron et al., 2019; Bernasconi et al., 2021). Each sample had between 1-7 replicates. Samples with more than one replicate had mean Δ_{47} values calculated as error weighted means of all replicates, with Δ_{47} error also weighted based on individual replicate standard errors (Huntington et al., 2009). Samples with only one replicate inherited the standard error associated with the individual replicate Δ_{47} value.

Temperature estimates ($T(\Delta_{47})$) were calculated using mean Δ_{47} values and the temperature calibration equation from Anderson et al. (2021). Mean Δ_{47} errors informed the final error associated with the Δ_{47} temperature calculation for each sample. Median Δ_{47} temperatures were also calculated for comparison purposes. Notably, recent studies have concluded that there is no need for a dolomite-specific

Δ_{47} temperature calibration so all sample temperatures were calculated the same way regardless of mineralogy (Anderson et al., 2024). $\delta^{18}O_{water}$ values were calculated from the Δ_{47} temperature and $\delta^{18}O_{carb}$ value for each calcite sample using the calcite fractionation equation from Daëron et al. (2019). $\delta^{18}O_{water}$ values for all dolomite samples were calculated using the dolomite fractionation equation from Müller et al. (2019). All $\delta^{18}O_{water}$ values are reported relative to Vienna Standard Mean Ocean Water (VSMOW). Data correction and sample averaging was completed with in-house R scripts available in the CUBESSIL GitHub repository (https://github.com/cubessil).

3.4.5 Stratigraphic Correlation to a Global $\delta^{13}C$ Record Using Align

Align is an application for the numerical stratigraphic correlation of time-series data developed by Hagen et al. (2024), which uses a dynamic time warping (DTW) algorithm to generate various best fit (i.e., least-squares) scenarios for the alignment of a candidate time-series of data to a target time-series data set. In this work, we used *Align* to generate multiple DTW alignments of the $\delta^{13}C$ record from the SPF Mainline transect to a combined target record of age-tuned, global benthic marine $\delta^{13}C$ data from the latest Cretaceous (~72 Ma; Huber et al., 2018) through middle Eocene time (38 Ma; Westerhold et al., 2020), based on the existing age constraints in the SPF (see Background).

In the target data set, age-tuned values were used in the 'height' column so that the algorithm would match SPF-specific $\delta^{13}C$ values to a best fit target age value. Mainline transect $\delta^{13}C$ values that were previously attributed to local-scale carbon

cycling processes (e.g., the clot components in thrombolite boundstone and micro-clotted microbial boundstone samples, including those with mixed clot-matrix fabrics like SPB19-ML08 and SPB19-ML38; n=19), spar veins (n=7), clasts (n=4), and any other outlier samples that were anomalously high or low compared to the rest of the data set (SPB19-ML21-C, SPB19-ML19-A, SPB19-ML40-A, SPB19-ML48-B) were excluded from the candidate data set (n=117 remaining samples) so as not to interfere with the DTW alignment of the SPF $\delta^{13}C$ record to the target global $\delta^{13}C$ record. The $\delta^{13}C$ records from Sheep Pass Canyon and Member B Slope sections were not correlated because of their lower sampling resolution and more limited stratigraphic extent.

We considered SPF-global $\delta^{13}C$ record DTW alignments that had more than 10% overlap between both records, and that had a Pearson correlation coefficient value between both records of greater than 0.8 (n=9; Fig. S1). An initial screening highlighted that seven out of the nine DTW alignments did not fit within existing SPF age end-members (e.g., one DTW alignment correlated the SPF $\delta^{13}C$ record so that all $\delta^{13}C$ values were older than 55 Ma). The remaining two DTW alignments were mostly identical except in their correlation of the uppermost SPF $\delta^{13}C$ values to ages between 36 Ma and 37 Ma in one (g:1, edge:0.02), versus 38 Ma or older in the other (g:1, edge:0.14). Because of their overall similarity, and because of the known end-member age constraint of unconformably overlying units (35-38 Ma; see Background), we moved forward with investigation of only the DTW alignment that correlated the uppermost SPF $\delta^{13}C$ values to 38 Ma or older (g:1, edge:0.14).

For this one remaining DTW alignment, we evaluated how well its generated DTW age framework fit within all existing SPF age constraints (not just the end-member constraints used in the initial screening process). We also compared the SPF Mainline transect T(Δ_{47}), $\delta^{18}O_{water}$, and $\delta^{13}C$ records within this DTW age framework, investigating whether the SPF temperature and hydroclimate record corresponded to long-term and short-term global and/or regional trends during the same time point, especially with respect to notable short-term global climate transitions like the K-Pg boundary, the PETM, and early Eocene hyperthermals (see Background). Lastly, we investigated variations in sedimentation rate across the Sheep Pass Formation type section, which were reflected in how the DTW algorithm stretched or shrank the Mainline transect $\delta^{13}C$ record.

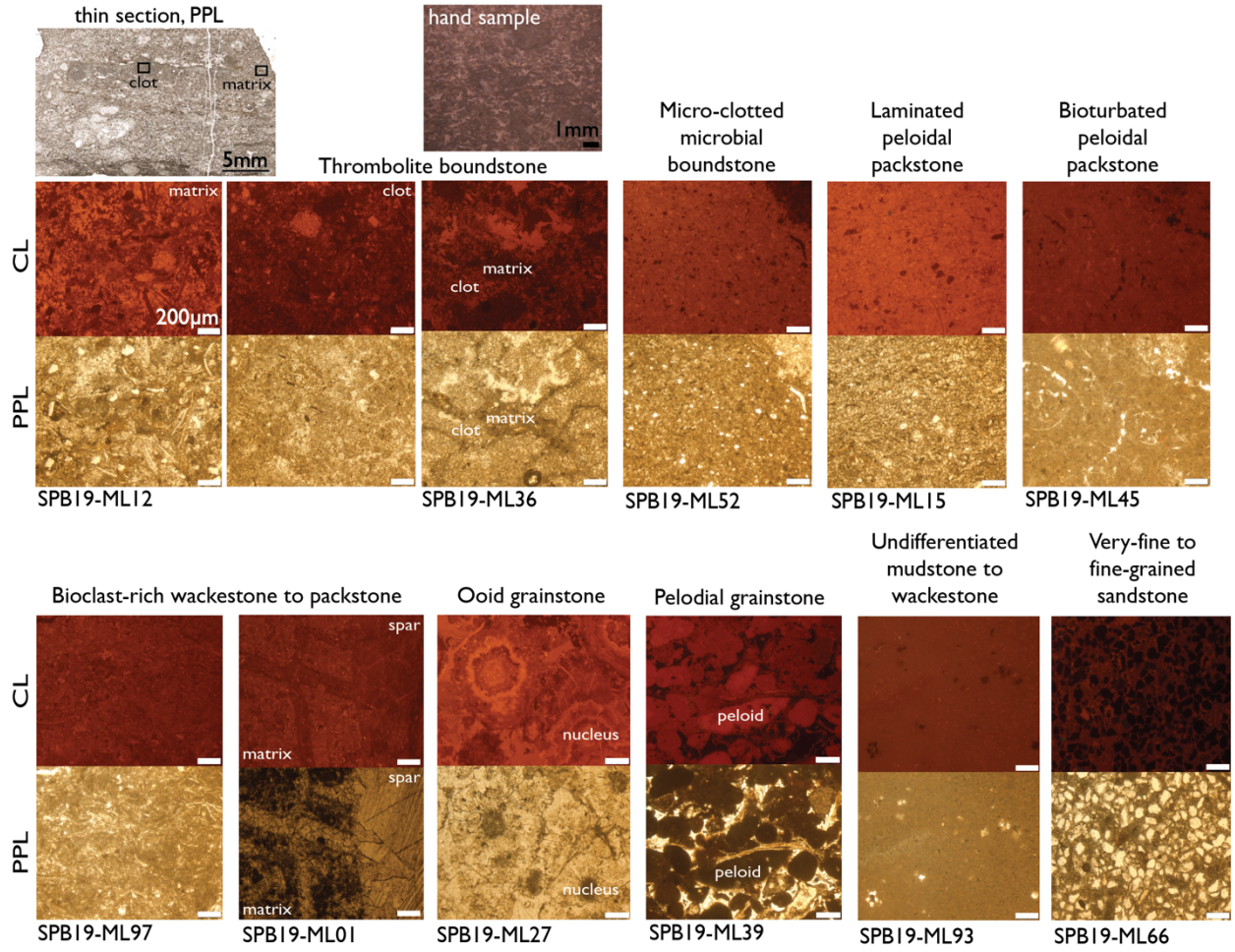

Figure 3-3: Representative cathodoluminescence (CL) and plane polarized light (PPL) images (4X) of facies analyzed for carbonate clumped isotopes (Δ_{47}). Note the oncoid packstone to grainstone and vuggy wackestone facies are not pictured (see Supplemental Material).

3.5 Results

3.5.1 Transmitted Light and Cathodoluminescence Microscopy

Transmitted light and cathodoluminescence microscopy highlight a range of fabrics and luminescence characteristics across all carbonate-bearing facies (Fig. 3). Because of previous detailed optical petrography on all SPF facies by Olsen-Valdez et al. (2025), we focus here on the CL characteristics of the carbonate-bearing facies.

The thrombolite (i.e., clotted microbialite) boundstone and micro-clotted microbial boundstone facies show the greatest range in luminescence, from no luminescence or dull, uniform dark orange luminescence up to patchy or mottled bright red and orange luminescence (see Fig. S2). The variation in luminescence often occurs at the <mm-scale and is associated with both the matrix and clot components (Fig. 3). In most cases, the matrix components exhibit brighter luminescence compared to the clots. Micro-clotted microbial boundstone samples preserve a similar range in luminescence and mottled texture as the thrombolite boundstone facies, but with less common bright orange to red luminescence (Figs. 3 and S2). Overall, luminescence is more homogeneous in the micro-clotted microbial boundstone facies compared to the thrombolite boundstone facies (Figs. 3 and S2).

The ooid grainstone facies also shows a similar range in luminescence compared to both boundstone facies. Variation in luminescence is most closely associated with distinct cortices or nuclei of ooid grains (Fig. 3, nucleus). The luminescence of the matrix ranges from non-luminescent to dull orange and its similarity in luminescence to some ooid cortices sometimes makes it hard to discern grain boundaries in CL (Fig. 3). The oncoid packstone to grainstone is largely comprised of smaller, <mm-scale coated grains, with a similar range in luminescence as the ooid grainstone facies (Fig. S4). The laminated peloidal packstone and bioturbated peloidal packstone preserve similar textures in CL, but with slightly different ranges in luminescence (Figs. 3 and S2). Both facies have a <mm-scale heterogeneous texture that varies between dull to bright orange luminescence, with the laminated peloidal packstone facies often

exhibiting a brighter orange luminescence (Fig. S2). Though some luminescence variation can be explained by the presence of bioclast fragments randomly distributed within the matrix of both facies, most of the subtle variation appears to be within the micritic matrix itself (Fig. 3 and S2).

The bioclast-rich wackestone to packstone facies shows a range in CL between non-luminescent to orange luminescence (Fig. 3). Most samples exhibit a uniform, dull orange luminescence within the micritic matrix. Bioclast fragments (translucent in PPL) are either non-luminescent or brighter orange in CL (Figs. 3 and S3). The representative spar vein, which crosscuts a bioclast-rich wackestone to packstone matrix, is characterized by a dull orange luminescence and is less luminescent than the surrounding matrix (SPB19-ML01; Fig. 3, see spar and matrix). The peloidal grainstone facies exhibits luminescence that ranges from non-luminescent to subtle bright orange luminescence (Fig. 3). The drusy mosaic cement between peloid grains is mostly non-luminescent, while peloids exhibit a uniform, subtle bright orange luminescence, with very little luminescence variation in any given peloid (Fig. 3, peloid).

Overall, the undifferentiated mudstone to wackestone facies exhibits a uniform, dull orange luminescence with only subtle regions of non-luminescence (associated with translucent microsparitic patches in PPL) or brighter orange luminescence (associated with darker patches randomly distributed throughout the micritic matrix in PPL; Figs. 3 and S4). The vuggy wackestone facies has similar CL characteristics as the undifferentiated mudstone to wackestone facies, though with

slightly brighter orange luminescence overall (Fig. S4). The very fine to fine-grained sandstone facies is carbonate-cemented and has a micritic matrix that luminesces dull to orange in CL (Figs. 3 and S4). Detrital quartz grains (translucent in PPL) are non-luminescent in CL (Fig. 3).

Clumped Isotope Sample ID	Facies/ Fabric	N	Mean $\delta^{13}C$ (‰, VPDB)	$\delta^{13}C$ 2 s.e. (‰, VPDB)	Mean $\delta^{18}O_{carb}$ (‰, VPDB)	$\delta^{18}O_{carb}$ 2 s.e. (‰, VPDB)	Mean $\delta^{18}O_{water}$ (‰, VPDB)	$\delta^{18}O_{water}$ 2 s.e. (‰, VPDB)	Mean Δ_{47} (‰)	Δ_{47} 2 s.e. (‰)	Mean $T(\Delta_{47})$ (°C)	Median $T(\Delta_{47})$ (°C)	$T(\Delta_{47})$ 2 s.e. (°C)	Primary (i.e., used for $T(\Delta_{47})$ record)?
SPB19-ML01-A	Bioclast-rich WS/PS	4	-1.9	0.14	-13.2	0.28	-10.0	1.0	0.56	0.02	39	36	6	No
SPB19-ML01-B	Spar	2	-2.6	0.03	-21.6	0.56	-15.4	1.2	0.51	0.003	57	57	6	No
SPB19-ML04-BC	Thrombolite BS - matrix	5	+1.3	0.12	-12.5	0.37	-10.8	1.2	0.58	0.02	30	32	6	Yes
SPB19-ML04-clot	Thrombolite BS - clot	2	+3.8	0.31	-12.4	0.12	-12.4	0.6	0.60	0.003	22	22	3	Yes
SPB19-ML09-B	Bioclast-rich WS/PS	7	-3.2	0.04	-13.8	0.45	-2.7	1.8	0.45	0.02	90	89	13	No
SPB19-ML11-C	Thrombolite BS - matrix	2	-4.7	0.09	-16.1	0.13	-6.6	1.2	0.47	0.0005	79	79	9	No
SPB19-ML11-clot	Thrombolite BS - clot	3	-3.5	0.38	-14.9	0.60	-0.9	5.2	0.42	0.08	113	113	44	No
SPB19-ML12-A	Thrombolite BS - matrix	3	-0.1	0.11	-12.7	0.11	-12.0	1.0	0.59	0.02	26	28	5	Yes
SPB19-ML12-B	Thrombolite BS - clot	4	+2.4	0.36	-12.6	0.51	-11.9	0.8	0.59	0.01	25	25	3	Yes
SPB19-ML13-B	Micro-clotted Microbial BS	4	-1.7	0.18	-12.3	0.18	-9.6	1.2	0.56	0.02	36	37	7	Yes
SPB19-ML15-A	Laminated Peloidal PS	3	-0.1	0.13	-13.4	0.27	-12.2	1.2	0.58	0.02	28	31	6	Yes
SPB19-ML17-B	Micro-clotted Microbial BS	5	+0.6	0.12	-8.6	0.17	-8.1	1.4	0.60	0.03	24	31	7	Yes
SPB19-ML19-A	Laminated Peloidal PS	3	+6.2	0.16	-12.6	0.25	-8.4	1.0	0.54	0.02	44	46	6	Yes
SPB19-ML23-A	Bioturbated Peloidal PS	3	-4.9	0.05	-13.4	0.44	-7.6	3.4	0.52	0.07	54	45	20	No
SPB19-ML27-B	Ooid GS	2	-0.8	0.16	-9.2	0.21	-9.2	1.8	0.60	0.04	21	20	9	Yes
SPB19-ML29-A	Bioturbated Peloidal PS	3	-4.6	0.11	-11.5	0.55	-10.9	1.6	0.59	0.03	25	22	7	Yes
SPB19-ML31-A	Thrombolite BS - matrix	2	+1.7	0.05	-5.7	0.19	-8.9	0.6	0.65	0.007	7	7	3	Yes
SPB19-ML31-B	Thrombolite BS - clot	3	+3.0	0.08	-4.6	0.20	-7.2	0.8	0.64	0.01	9	9	3	Yes
SPB19-ML33-AB	Thrombolite BS - clot	5	+4.6	0.16	-5.4	0.24	-7.0	0.8	0.63	0.01	14	16	3	Yes
SPB19-ML33-C	Thrombolite BS - matrix	2	+1.6	0.12	-8.1	0.23	-9.9	0.6	0.63	0.003	13	13	3	Yes
SPB19-ML36-A	Thrombolite BS - matrix	2	+2.7	0.04	-8.9	0.15	-8.8	0.8	0.60	0.02	22	22	4	Yes

SPB19-ML36-B	Thrombolite BS - clot	2	+4.1	0.02	-5.5	0.30	-6.6	0.6	0.62	0.003	16	16	3	Yes
SPB19-ML39-C	Peloidal GS	2	+3.0	0.06	-9.3	0.08	-2.5	1.0	0.49	0.004	66	66	7	No
SPB19-ML41-A	Peloidal GS	1	0.0	0.00	-7.5	0.00	-9.1	0.8	0.60	0.02	22	22	4	Yes
SPB19-ML45-B	Bioturbated Peloidal PS	4	-0.6	0.20	-9.1	0.15	-10.1	1.4	0.60	0.03	24	23	7	Yes
SPB19-ML50-A	Micro-clotted Microbial BS	3	+0.2	0.30	-8.5	0.61	-9.6	0.8	0.62	0.01	17	16	3	Yes
SPB19-ML51-A	Very fine to Fine-grained SS	2	-1.8	0.05	-18.4	0.05	-15.0	1.0	0.55	0.02	40	40	6	No
SPB19-ML52-A-matrix	Micro-clotted Microbial BS	3	+0.3	0.04	-4.9	0.02	-5.2	0.6	0.61	0.01	20	20	3	Yes
SPB19-ML58-B	Oncoid PS/GS	3	-1.4	0.22	-13.4	0.21	-11.2	0.8	0.57	0.01	33	34	4	Yes
SPB19-ML59-A	Very fine to Fine-grained SS	2	-1.7	0.07	-10.3	0.26	-7.7	0.8	0.56	0.01	36	35	4	Yes
SPB19-ML60-A	Laminated Peloidal PS	3	-3.3	0.10	-10.3	0.47	-6.9	1.0	0.55	0.01	40	39	4	Yes
SPB19-ML61-A	Micro-clotted Microbial BS	2	+1.6	0.08	-4.4	0.25	-2.9	1.4	0.58	0.03	29	29	7	Yes
SPB19-ML61-B	Micro-clotted Microbial BS	6	+1.5	0.22	-4.8	0.36	-4.6	0.8	0.60	0.01	23	25	3	Yes
SPB19-ML61-C	Micro-clotted Microbial BS	1	+1.8	0.12	-4.8	0.10	-7.5	0.8	0.65	0.02	9	9	4	No
SPB19-ML63-B	Bioturbated Peloidal PS	3	-3.9	0.16	-6.5	0.19	-6.0	0.8	0.60	0.01	24	25	3	Yes
SPB19-ML64-A	Micro-clotted Microbial BS	3	-1.7	0.13	-11.0	0.49	-7.4	1.0	0.55	0.01	41	41	5	Yes
SPB19-ML65-A	Bioclast-rich WS/PS	2	-2.9	0.10	-4.1	0.09	-7.4	1.5	0.63	0.07	15	11	14	No
SPB19-ML66-AB	Very fine to Fine-grained SS	1	-4.0	0.10	-9.0	0.78	-10.9	0.8	0.61	0.02	20	20	4	Yes
SPB19-ML69-A	Vuggy WS	1	-0.1	0.01	-4.1	0.44	-8.8	0.8	0.61	0.02	9	9	3	No
SPB19-ML74-A	Undiff. MS/WS	1	+1.0	0.20	-4.2	0.22	-6.1	0.8	0.61	0.02	20	20	4	Yes
SPB19-ML85-A	Undiff. MS/WS	1	+1.8	0.22	-4.4	0.37	-9.4	0.8	0.65	0.02	8	8	4	No
SPB19-ML93-A	Undiff. MS/WS	2	+0.9	0.04	-5.3	0.14	-6.1	0.6	0.59	0.01	25	26	3	Yes

SPB19-ML97-A	Bioclast-rich WS/PS	3	+1.3	0.03	-11.5	0.07	-10.8	1.2	0.59	0.02	25	29	6	Yes
SPB19-SPC06-A	Very fine to Fine-grained SS	3	-4.5	0.09	-12.3	0.12	-11.6	0.6	0.59	0.01	26	26	3	Yes
SPB20-SPC09-B	Bioclast-rich WS/PS	1	-1.6	0.13	-12.9	0.64	-9.0	1.0	0.55	0.02	43	43	6	No
SPB20-SPC31-A	Thrombolite BS - matrix	3	0.0	0.65	-8.3	0.20	-11.4	0.8	0.65	0.01	7	6	3	Yes
SPB20-SPC31-B	Thrombolite BS - clot	2	+7.6	0.05	-4.1	0.38	-6.5	0.8	0.64	0.01	10	10	3	Yes
SPB20-SPC38-A	Thrombolite BS - matrix	2	-1.2	0.18	-9.0	0.19	-11.6	1.4	0.64	0.03	9	8	7	Yes
SPB20-SPC38-B	Thrombolite BS - clot	2	+2.7	0.21	-7.1	0.65	-9.8	1.8	0.65	0.04	9	7	9	Yes
SPB20-SPC45-A	Micro-clotted Microbial BS	1	-0.5	0.27	-11.7	0.16	-6.0	1.0	0.52	0.01	53	53	6	No
SPB20-SPC51-A	Laminated Peloidal PS	3	-2.2	0.01	-11.0	0.11	-11.4	0.8	0.61	0.01	20	19	4	Yes

Table 3-2: Sample averages for $\delta^{13}C$, $\delta^{18}O_{carb}$, $\delta^{18}O_{water}$, and Δ_{47} values as well as mean and median $T(\Delta_{47})$ estimates with associated errors. Note that $\delta^{13}C$ and $\delta^{18}O_{carb}$ values reflect those analyzed for carbonate clumped isotopes on the 253 Plus instrument only.

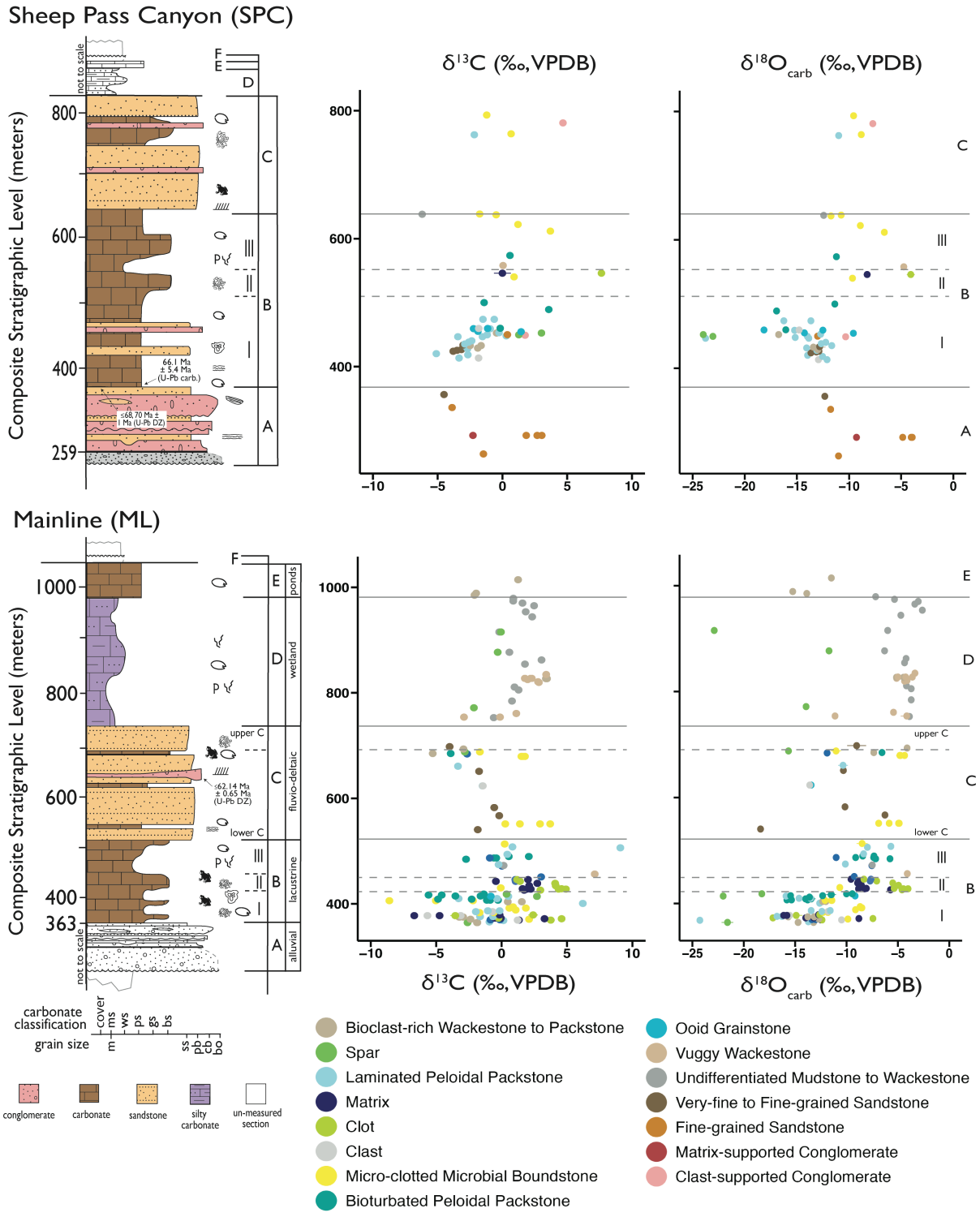

Figure 3-4: Mean $\delta^{13}C$ and $\delta^{18}O_{carb}$ values (‰, VPDB) versus composite stratigraphic meter level across the Sheep Pass Canyon and Mainline transects based on analyses compiled from data generated on both the Delta V and 253 Plus instruments (see

Materials and Methods). Error bars reflect 2 standard errors of the mean; most are not visible because they are smaller than the symbols. Note that composite meter level does not necessarily mean that the same meter levels across the Mainline and Sheep Pass Canyon transects are coeval.

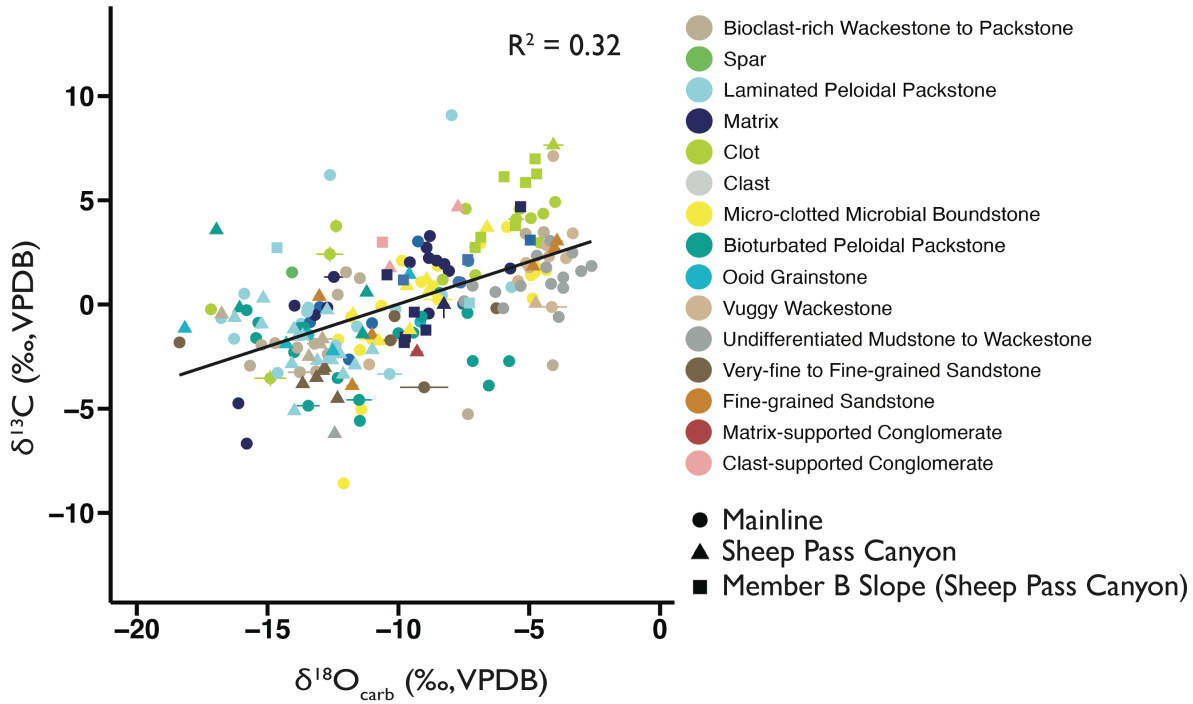

Figure 3-5: $\delta^{13}C$ versus $\delta^{18}O_{carb}$ values (‰, VPDB) for all samples in the Sheep Pass Formation. A linear regression of these data is associated with an R^2 value of 0.32.

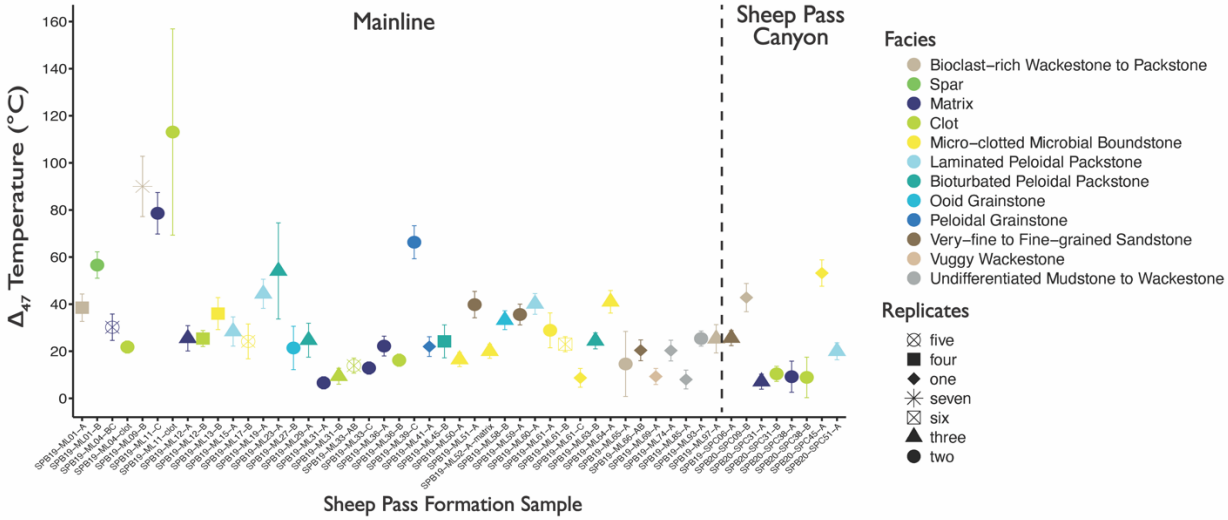

Figure 3-6: Sample mean Δ_{47} temperature estimates prior to screening for non-primary samples. Error bars reflect 2 standard errors of the mean.

3.5.2 Stable Isotope Geochemistry

Across all samples analyzed, $\delta^{13}C$, $\delta^{18}O_{carb}$, $\delta^{18}O_{water}$, Δ_{47} values and $T(\Delta_{47})$ estimates span large ranges (Table 2). $\delta^{13}C$ values range from -8.58‰ to +9.08‰ and $\delta^{18}O_{carb}$ values range from -24.28‰ to -2.76‰ (Mainline transect; Fig. 4). $\delta^{18}O_{water}$ values range from -15.4‰ to -0.1‰. Δ_{47} values are between 0.42‰ (± 0.08‰, 2 s.e.) and 0.65‰ (± 0.04‰, 2 s.e.) while $T(\Delta_{47})$ estimates range from 7°C to 113°C (Fig. 6).

3.5.2.1 Carbonate Carbon and Oxygen Isotopes Across the Sheep Pass Formation

In both the Mainline and Sheep Pass Canyon transects, Member B preserves the greatest variability in $\delta^{13}C$ and $\delta^{18}O_{carb}$ values (Fig. 4). In the Mainline transect, the lowest and highest $\delta^{13}C$ values across the entire SPF are recorded in Member B alone and $\delta^{18}O_{carb}$ values are between -24.28‰ and -4.00‰, accounting for almost the full range in observed SPF $\delta^{18}O_{carb}$ values as well. The greatest variability over rather small stratigraphic thicknesses (meter- to decameter-scale) occurs in Member B – Interval I (Fig. 4). Within Member B – Interval I, $\delta^{13}C$ and $\delta^{18}O_{carb}$ both abruptly shift from values around 0‰ for $\delta^{13}C$ and -12‰ for $\delta^{18}O_{carb}$ to lower values at ~378 m (-7‰ for $\delta^{13}C$ and -17‰ for $\delta^{18}O_{carb}$) and ~410 m (-6‰ for $\delta^{13}C$ and -16‰ for $\delta^{18}O_{carb}$) in the Mainline transect. These trends are not apparent in the Sheep Pass Canyon transect, though the Sheep Pass Canyon has a much lower sampling resolution. The Sheep Pass Canyon appears to preserve a shift to higher $\delta^{13}C$ (from -2‰ to +3‰) and lower $\delta^{18}O_{carb}$ (from -12‰ to -18‰) values at ~450 m.

In the SPF thrombolite boundstone samples, which comprise both matrix and clot components, the clot components consistently record higher $\delta^{13}C$ and $\delta^{18}O_{carb}$ values compared to the matrix component. Member B – Interval II, which is only composed of thrombolite boundstones in the Mainline transect, has less variability and exhibits higher $\delta^{13}C$ and $\delta^{18}O_{carb}$ values (+2‰ and -7‰, respectively) compared to Member B – Interval I averages (~0‰ and -11‰, respectively). Member B – Interval III also shows less variability in both $\delta^{13}C$ and $\delta^{18}O_{carb}$ values compared to Member B – Interval I. In Member B – Interval III, $\delta^{13}C$ values are similar to Member B – Interval I (~0‰), while $\delta^{18}O_{carb}$ values are higher (around -8‰), reflecting similar values as Member B – Interval II (Fig. 4).

In Member C, $\delta^{13}C$ values are between -5‰ and +4‰, while $\delta^{18}O_{carb}$ values are between -18‰ and -4‰ (Mainline transect; Fig. 4). Samples from Member C in the Sheep Pass Canyon transect exhibit a similar range in $\delta^{13}C$ and $\delta^{18}O_{carb}$ values, though sampling resolution is poor (n=6). In the Mainline transect, $\delta^{13}C$ values appear to get gradually lower before reaching the lowest value (-5‰) at ~685 m (upper Member C; Fig. 4). $\delta^{18}O_{carb}$ values have similar variability as in all of Member B, though this appears to be the artifact of individual samples recording more anomalous $\delta^{18}O_{carb}$ values, as well as a lower sampling resolution across Member C. The lowest $\delta^{13}C$ values in upper Member C are also associated with the highest $\delta^{18}O_{carb}$ values (around -4‰) in all of Member C (Fig. 4).

Member D preserves less variable $\delta^{13}C$ and $\delta^{18}O_{carb}$ values compared to the other SPF members. Excluding values from sampled spar veins, $\delta^{13}C$ values range from

around -3‰ to +3‰, while $\delta^{18}O_{carb}$ values range from around -11‰ to -3‰ (Fig. 4). These are the highest $\delta^{13}C$ and $\delta^{18}O_{carb}$ values across all members in the SPF. Three spar veins sampled in Member D record $\delta^{13}C$ values around 0% and $\delta^{18}O_{carb}$ values between -11 and -23% (Fig. 4). Member E records $\delta^{13}C$ values between -2‰ and +1‰ and $\delta^{18}O_{carb}$ values between -15‰ and -11‰ (n=3; Fig. 4). These values are most similar to average $\delta^{13}C$ and $\delta^{18}O_{carb}$ values in Member B – Interval I (~0‰ and -11‰, respectively). Plotting $\delta^{13}C$ versus $\delta^{18}O_{carb}$ values for all SPF samples shows a positive correlation, with an R^2 value of 0.32 (Fig. 5).

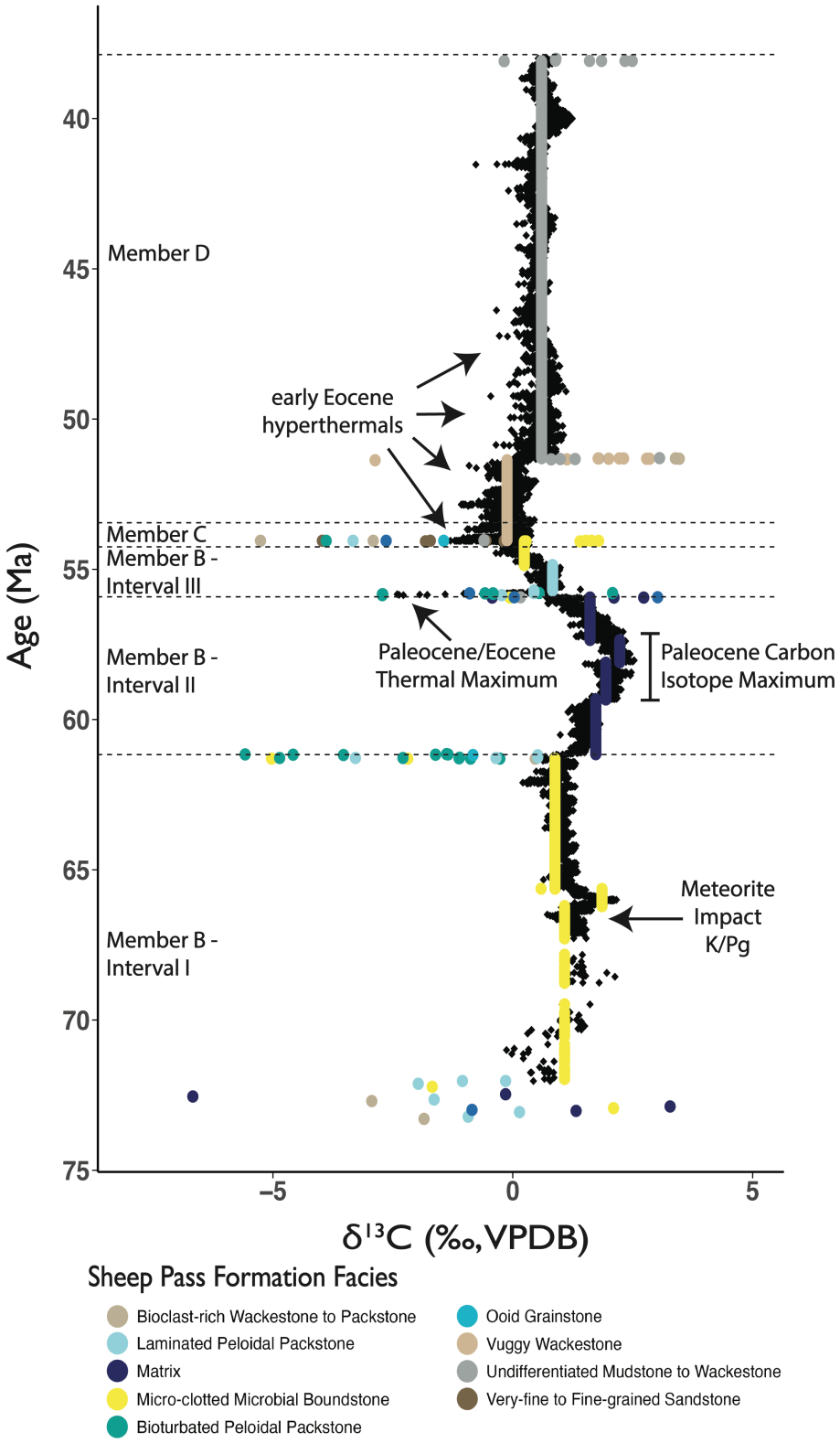

Figure 3-7: $\delta^{13}C$ (‰, VPDB) versus age (Ma) based on the dynamic time warping alignment of the SPF Mainline transect $\delta^{13}C$ values (color-coded to facies) to the

target benthic marine $\delta^{13}C$ values (black diamonds) from Huber et al. (2018) and Westerhold et al. (2020). Major global climate transitions are labelled following Westerhold et al. (2020). SPF member transitions (black-dashed lines) and labels are included for reference.

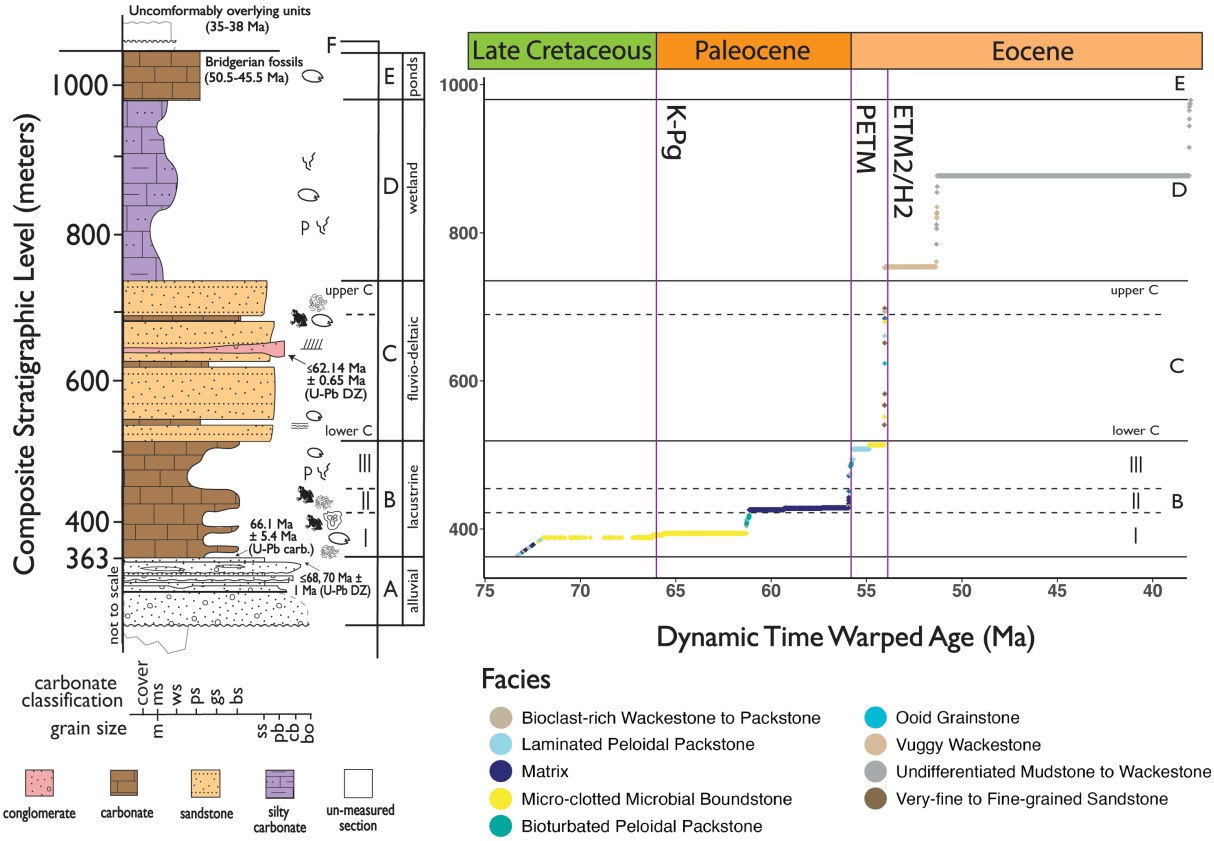

Figure 3-8: Mainline transect $\delta^{13}C$ record plotted relative to original composite stratigraphic level (meters) versus dynamic time warped age (Ma) with prominent global time intervals (K-Pg boundary, ~66 Ma; PETM, ~56 Ma; ETM2/H2, ~54 Ma) denoted by purple lines. Note that various SPF-wide age constraints are included in the stratigraphic column for reference. Data points are color-coded to facies type.

3.5.3 A Dynamic Time Warping Alignment of the Mainline Transect $\delta^{13}C$ Record

The DTW alignment of the SPF Mainline transect $\delta^{13}C$ record to the global benthic marine $\delta^{13}C$ record (Fig. 7; Huber et al., 2018; Westerhold et al., 2020) places the Cretaceous-Paleogene boundary (~66 Ma) within Member B – Interval I, the

Paleocene-Eocene boundary (~56 Ma) around the transition between Member B – Interval II and Member B – Interval III, and correlates Member C and lower Member D to the early Eocene (~50-54 Ma) within Member C and lower Member D. The DTW alignment also highlights the stretching and shrinking of the SPF Mainline $\delta^{13}C$ record during the correlation, with a notable stretching in parts of Member B and Member D, and a drastic shrinking of Member C compared to original stratigraphic height (Fig. 7).

3.5.3.1 Variations in Depositional Rate Across the Sheep Pass Formation

Comparing the original composite stratigraphic level (in meters) of the SPF Mainline $\delta^{13}C$ record to its DTW age (in Ma) suggests that the depositional rate varies significantly across the Sheep Pass Formation (Fig. 8). A constant depositional rate in the SPF would exhibit a positive, linear relationship between original composite stratigraphic level and DTW age. The very beginning of Member B – Interval I best exhibits this behavior.

The remainder of the SPF resembles a stair-step shape, reflecting either intervals of very low depositional rate (very little original composite stratigraphic level change over a long time) and/or erosion (leading to a stratigraphic disconformity), or very high depositional rate (a large change in original composite stratigraphic level over a very short time; Fig. 8). The middle of Member B – Interval I and the beginning of Member B – Interval II show long periods (~10 Ma and ~5 Ma, respectively) characterized by very little deposition (~6 meters and ~2.5 meters, respectively). Uppermost Member B has lower depositional rates as well, with around

20 meters of stratigraphic change over a 2-million-year interval. Parts of Member D also exhibit this behavior; lower Member D spans ~1 meter over a 3-million-year time interval and middle Member D has an interval of zero net deposition from around 38 Ma to 51 Ma (Fig. 8).

Intervals of very high depositional rate include the transition between Member B – Interval I to II (~22 meters of stratigraphic change aligned to roughly a single age, ~61 Ma) and Member B – Interval II to III (~47 meters of stratigraphic change aligned to roughly a single age, ~56 Ma). All of Member C is characterized by a very high depositional rate, with the full ~56-meter-thick member aligned to roughly a single age (~54 Ma). Member D also has two intervals characterized by 123 m and 137 m of net deposition over less than one million years, respectively.

3.6 Discussion

3.6.1 Assessing the Fidelity of Δ_{47} Temperatures

T(Δ_{47}) estimates span a range of values, including those typical of modern lakes, those associated with environments where surface temperatures are amplified compared to ambient air (e.g., mudflats), as well as those often associated with diagenetic fluids at high temperatures (Mildrexler et al., 2011; Quade et al., 2013; Fetrow et al., 2022). Diagenetic alteration, trace contaminants, solid state reordering, and disequilibrium carbonate precipitation processes can all lead to anomalous Δ_{47} values and, therefore, anomalous temperature estimates (e.g., Henkes et al., 2014; Ingalls et al., 2020, 2024; Fiebig et al., 2024). A careful screening for primary versus

anomalous T(Δ_{47}) estimates is required before leveraging these data for paleoclimatic interpretations.

3.6.1.1 Diagenetic Fabric Characterization with Cathodoluminescence Microscopy

Transmitted light and cathodoluminescence microscopy highlight textures associated with primary fabrics, as well as textures consistent with recrystallization and/or overprinting precipitation phases. The patchy to mottled luminescence observed in the thrombolite boundstone and micro-clotted microbial boundstone facies resembles the same characteristic mottling in CL that Hagen et al. (2025) interpreted as a primary, non-diagenetic cathodoluminescence feature in microbialite fabrics. Other ancient and modern microbialite fabrics exhibit these micro-scale changes in luminescence intensity as well (Eymard et al., 2020; Ingalls et al., 2022). This primary mottling likely reflects microbially-driven micro-scale differences in redox conditions in the microbialite micro-environment as carbonate precipitated (Hagen et al., 2025; Machel, 2000). Further the variations in luminescence between cortices and nuclei of ooid grains in the ooid grainstone facies likely reflect primary, distinct redox conditions during multiple generations of precipitation, rather than diagenetic overprinting or alteration (Boggs and Krinsley, 2006; Hagen et al., 2025; Paquette et al., 1993).

The peloidal grainstone facies – with clear differences in CL luminescence between the peloids and the drusy mosaic cement – appears to preserve two distinct phases of precipitation (Fig. 3). Olsen-Valdez et al. (2025) interpreted this facies as

reflecting deposition in a transitional lacustrine to palustrine setting, with evidence for re-working of muddy sediment and ephemeral subaerial exposure. It is difficult to constrain the timing of cementation in a depositional setting like this, but regardless, the two distinct phases suggest that each fabric may reflect unique fluid sources. Paired isotopic and petrographic analyses by Snell (2011) characterized non-luminescent spar veins in SPF samples as a product of later re-crystallization; the similar non-luminescence observed in this drusy mosaic cement may suggest a similar mechanism. One peloidal grainstone sample (SPB19-ML39) records a mean $T(\Delta_{47})$ estimate of 66°C (± 7°C, 2 s.e.) and a $\delta^{18}O_{water}$ value of -2.5‰ (± 1‰, 2 s.e.), which is one of the highest $\delta^{18}O_{water}$ values in the SPF (Table 2). Given the sedimentological evidence for subaerial exposure associated with this facies, high rates of evaporation (a kinetic process) may have led to a high $\delta^{18}O_{water}$ value and a high $T(\Delta_{47})$ estimate in this sample (Talbot, 1990; Leng and Marshall, 2004). Overall, this suggests that the peloidal grainstone sample may not be recording a primary Δ_{47} temperature, so we have excluded it from the primary $T(\Delta_{47})$ data set.

Overall, the laminated peloidal packstone, bioturbated peloidal packstone, and bioclast-rich wackestone to packstone facies appear to preserve primary fabrics given their relatively uniform CL characteristics across all samples (Fig. S3). In contrast, select samples (e.g., SPB19-ML23 and SPB20-SPC09) that appear to have been diagenetically altered exhibit adjacent non-luminescent and brightly luminescing regions that are not common in the other packstone samples (Fig. S3). The cross-cutting spar vein within a bioclast-rich wackestone to packstone sample (SPB19-

ML01) exhibited only subtle differences in luminescence between the micritic matrix and spar (Fig. 3). This suggests that the redox conditions that characterized re-crystallization associated with the cross-cutting spar vein may have also influenced the micritic matrix and its primary isotopic composition. SPB19-ML01 records a mean Δ_{47} temperature of 36°C (± 6°C, 2 s.e.) for the bioclast-rich wackestone to packstone matrix and 57°C (± 6°C, 2 s.e.) for the spar vein (Table 2). The $\delta^{18}O_{carb}$ values (matrix: -13%; vein: -21%) and $\delta^{18}O_{water}$ values (matrix: -10%; vein: -15%) between these two fabrics are very different, suggesting the matrix may not reflect the same diagenetic fluid source as the spar vein. However, out of caution, we remove both fabrics in SPB19-ML01 from the primary T(Δ_{47}) data set.

Despite the undifferentiated mudstone to wackestone facies and vuggy wackestone facies also reflecting palustrine deposition in the presence of pedogenic alteration, we interpret these fabrics as primary (Olsen-Valdez et al., 2025). The relatively uniform and dull luminescence in these samples suggests deposition occurred under relatively consistent redox conditions, likely when inorganic fine grained micrite was precipitating in the lacustrine setting prior to subaerial exposure and subsequent pedogenic modification (Olsen-Valdez et al., 2025; Wright & Platt, 1995; Alonso-Zarza & Wright, 2010). These facies textures also resemble other palustrine fabrics, including those deemed to preserve primary Δ_{47} temperatures in the mid-Cretaceous Newark Canyon Formation (Nevada, USA; Fetrow et al., 2022) Further, $\delta^{13}C$ and $\delta^{18}O_{carb}$ values are distinct between the undifferentiated mudstone to wackestone matrix and select spar samples (not analyzed for Δ_{47}) suggesting the

fluid phase associated with the few spar veins was different from the phase that characterized the matrix in these undifferentiated mudstone to wackestone samples (Fig. 4). One sample (SPB19-ML69, a vuggy wackestone at ~750 meters) exhibits brighter luminescence in CL and has a corresponding matrix $\delta^{18}O_{carb}$ value (-11%) that is most similar to the $\delta^{18}O_{carb}$ values of spar veins around this stratigraphic level (Fig. 4); this suggests it has been influenced by later alteration and is not primary.

3.6.1.2 Other Considerations and Screening Measures for Non-Primary Δ_{47} Temperatures

Some samples (e.g. SPB19-ML09 and SPB19-ML11) record extremely warm T(Δ_{47}) estimates that fall outside the range of reasonable earth surface temperatures (89°C ± 13°C; 79°C ± 13°C, and 113°C ± 22°C, respectively, 2 s.e.; Fig. 6). Solid-state reordering can change Δ_{47} values under high temperatures via the reordering of C-O bonds through solid state diffusion, but this process requires that temperatures greater than 100°C are sustained for at least one million years (Henkes et al., 2014). Though soft-sediment deformation features reflect syn-tectonic deposition during part of the Sheep Pass Formation depositional timeframe, work by Druschke et al. (2009a) highlights that evidence for more extensive tectonic alteration (e.g., contractional deformation or deep-thrust burial) is not present in the SPF. Thus, solid-state reordering cannot explain the higher T(Δ_{47}) estimates in these SPF samples.

The presence of trace contaminants (e.g., sulfur or organic compounds) can also lead to anomalous T(Δ_{47}) estimates by creating isobaric interference on masses 45, 46, or 47 (Eiler, 2007). We treated samples that had uncharacteristically low or high T(Δ_{47}) replicate values with a double cleaning procedure to strip reacted sample gas of isobars and also completed a sodium hypochlorite (i.e., bleach) rinse on a subset of samples (see Materials and Methods). For some samples, these treatment protocols resulted in Δ_{47} values that better resembled other samples in the data set, and that were different compared to their single-cleaned replicates. In others (e.g., SPB19-ML09 and SPB19-ML11), treatment protocols still resulted in uncharacteristically high temperature estimates.

An alternative mechanism for T(Δ_{47}) values that do not reflect deposition conditions is isotopic disequilibrium. Carbonate precipitation out of isotopic equilibrium can occur in association with microbial metabolisms (e.g., autotrophy and heterotrophy) and other kinetic isotope effects like CO_2 degassing (Guo, 2020; Ingalls et al., 2024). Additional screening of Δ_{47} versus Δ_{48} can help resolve if disequilibrium precipitation can explain anomalous T(Δ_{47}) estimates. The measurement of mass 48 for most samples in this data was at too low a precision to reliably calculate and apply Δ_{48} values for this purpose. Nevertheless, we suggest that samples like SPB19-ML09 and SPB19-ML11 may be recording disequilibrium precipitation but do not discuss this further.

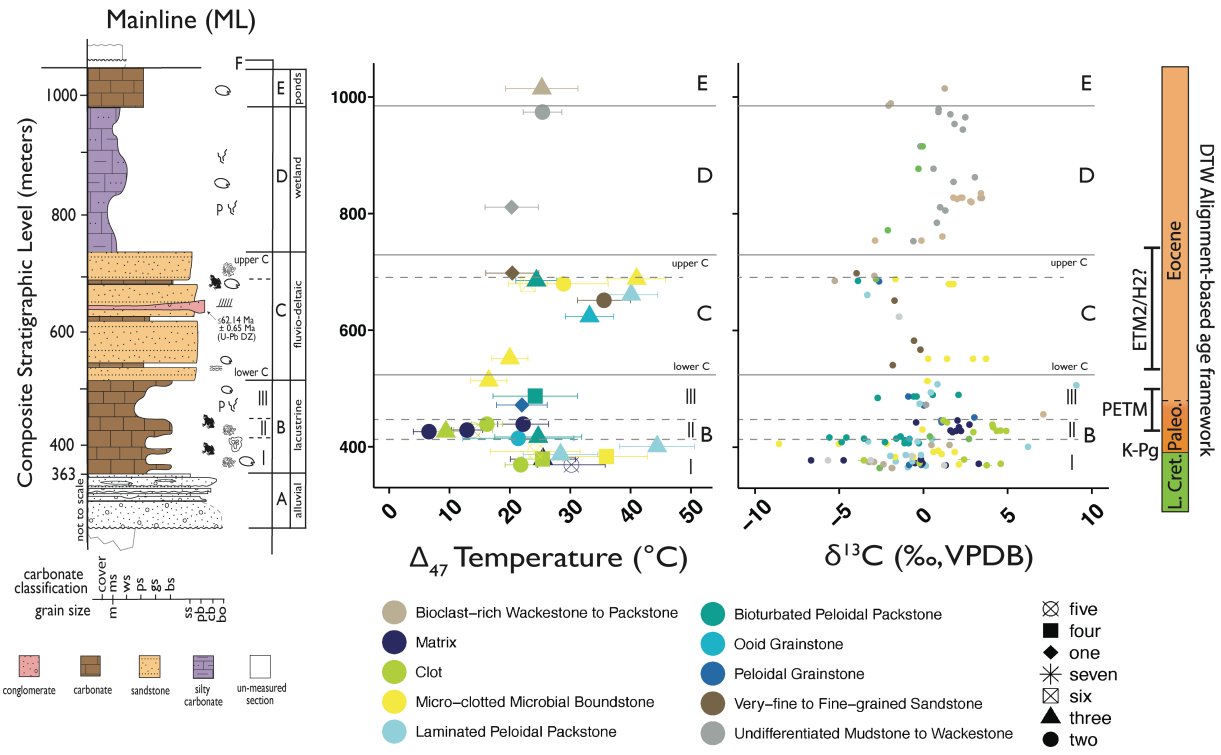

Figure 3-9: Sample mean Δ_{47} temperature estimates (°C) and $\delta^{13}C$ values (‰, VPDB) versus stratigraphic level for samples from the Mainline transect. Error bars reflect 2 standard errors of the mean; most $\delta^{13}C$ error bars are not visible because they are smaller than the symbols. Note that the $\delta^{13}C$ record is compiled from data generated on both the Delta V and 253 Plus instruments. The time scale on the right is based on the dynamic time warped age framework.

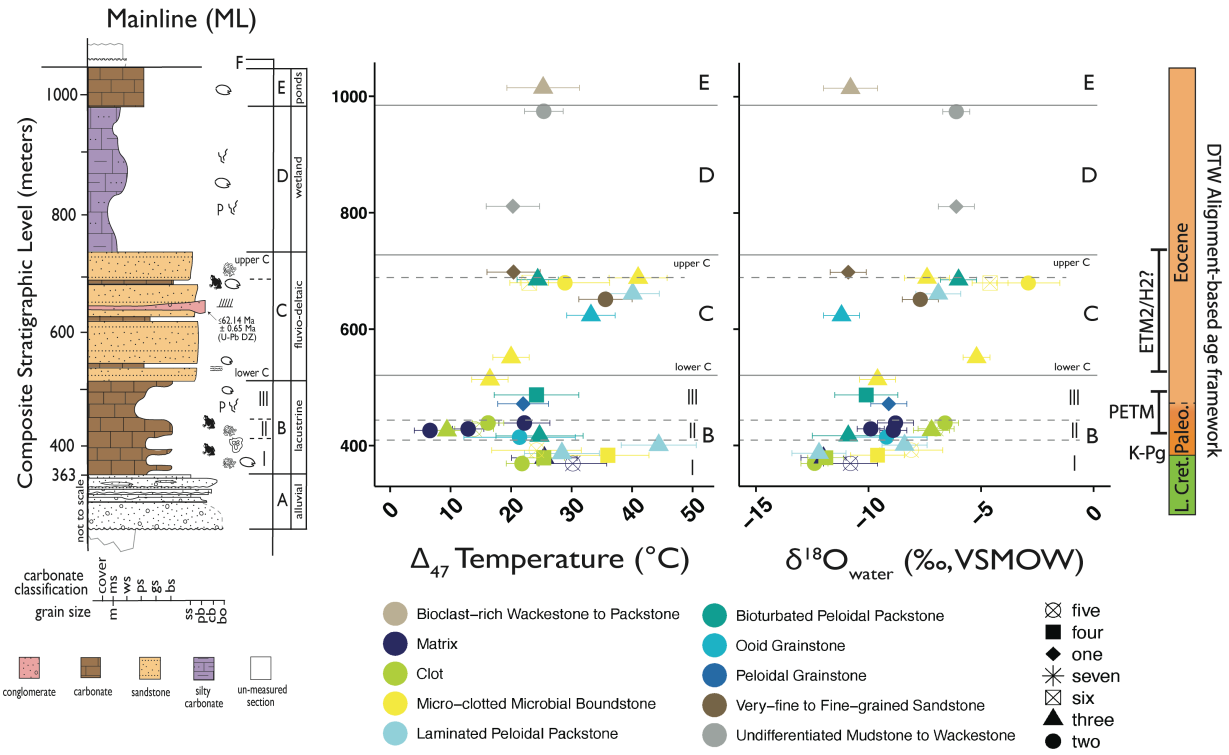

Figure 3-10: Sample mean Δ_{47} temperature estimates (°C) and calculated $\delta^{18}O_{water}$ values (‰, VSMOW) versus stratigraphic level for primary samples from the Mainline transect. Error bars reflect 2 standard errors of the mean. The time scale on the right is based on the dynamic time warped age framework.

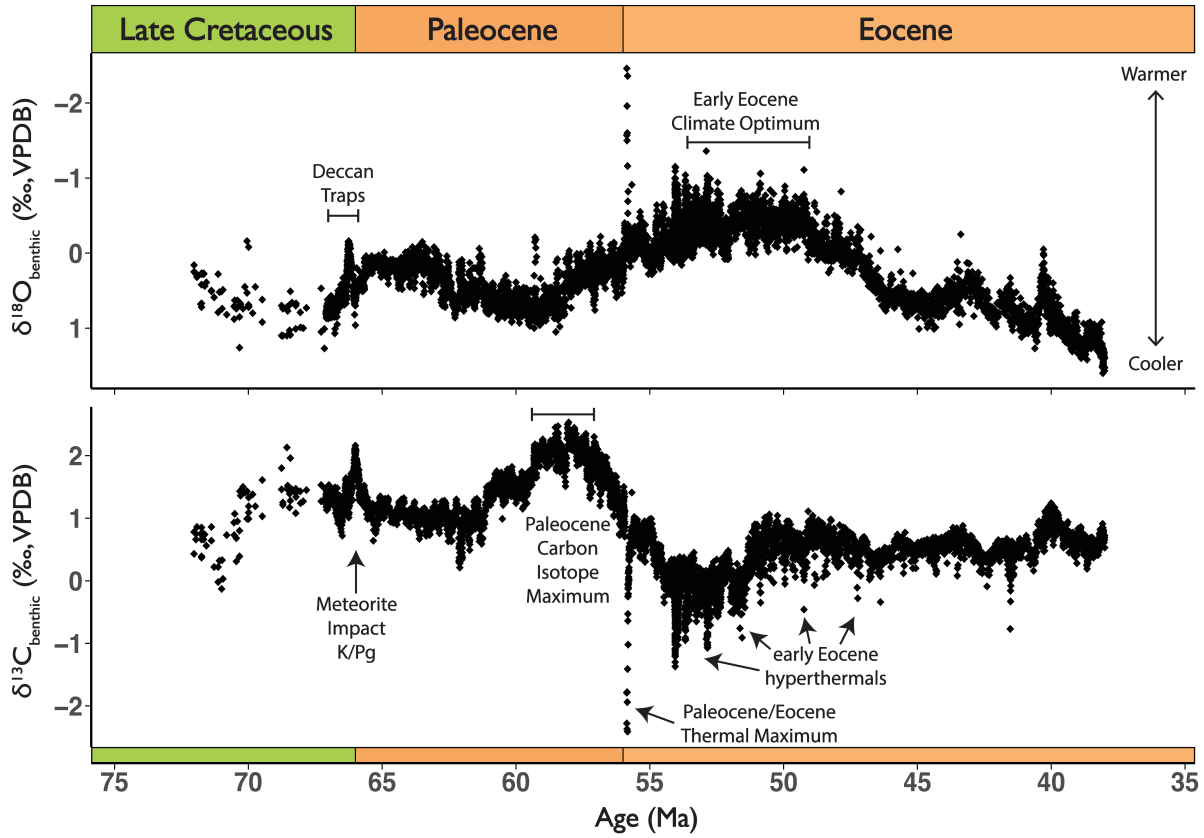

Figure 3-11: Benthic marine $\delta^{13}C$ and $\delta^{18}O$ (‰, VPDB) records from the Late Cretaceous through Eocene epochs based on combined data from Huber et al. (2018) and Westerhold et al. (2020). Major global climate transitions are labelled following Westerhold et al. (2020). Note that lower $\delta^{18}O$ values are associated with warmer temperatures and vice versa.

3.6.2 Paleoclimatic Trends Preserved in the Sheep Pass Formation

Following careful screening, the primary samples in the Sheep Pass Formation record $T(\Delta_{47})$ estimates between 7°C (± 3°C, 1 s.e.) to 44°C (± 6°C, 2 s.e.) and $\delta^{18}O_{water}$ values from -12.4‰ (± 0.6‰, 2 s.e.) to -2.9‰ (± 1.4‰, 2 s.e.; Figs. 9 and 10). We use primary $T(\Delta_{47})$ and $\delta^{18}O_{water}$ values, and the full $\delta^{13}C$ record to investigate the expression of paleoclimatic trends across the SPF Mainline transect. Using the refined age framework from the DTW alignment, we also compare the SPF-specific paleoclimatic trends within the temporal context of regional and global hydroclimatic

changes over this approximately 35-million-year time interval, with particular focus on major global climate transitions like the K-Pg boundary and both long-term and short-term warming in the early Paleogene.

3.6.2.1 An Initial Comparison of Sheep Pass Formation Trends to the Global Marine Record

Global marine $\delta^{13}C_{benthic}$ and $\delta^{18}O_{benthic}$ values from the latest Cretaceous through middle to late Eocene record both long-term and short-term changes over this approximately 35-million-year time interval (Fig. 11; Barnet et al., 2018; Huber et al., 2018; Westerhold et al., 2020). These global mean records can be leveraged as a comparison point for the expression of similar global trends within the Sheep Pass Formation. $\delta^{13}C_{benthic}$ values provide insight into global-scale carbon cycle changes. For example, abrupt perturbations related to the addition of CO_2 into the ocean-atmosphere system result in shifts to lower $\delta^{13}C_{benthic}$ values (negative carbon isotope excursions, CIEs; Zachos et al., 2001; Pagani et al., 2014). $\delta^{18}O_{benthic}$ has been leveraged as a temperature proxy because of its dominant control on $\delta^{18}O_{benthic}$ values in sea water during un-glaciated time periods (Urey, 1947; Dansgaard, 1964).

There are several Late Cretaceous through Eocene $\delta^{13}C_{benthic}$ and $\delta^{18}O_{benthic}$ trends to note. Long-term $\delta^{13}C_{benthic}$ values are relatively invariant from the Late Cretaceous to mid-Paleocene (except for during the K-Pg boundary), before reaching a maximum in the later Paleocene (Fig. 11). $\delta^{13}C_{benthic}$ values then decrease through the Eocene. More abrupt $\delta^{13}C_{benthic}$ shifts are superimposed on the record throughout

this time interval: higher $\delta^{13}C_{benthic}$ values mark the K-Pg boundary with lower $\delta^{13}C_{benthic}$ values before and after the K-Pg, while negative carbon isotope excursions define the PETM and other early Eocene hyperthermals (Fig. 11).

The $\delta^{18}O_{benthic}$ temperature record preserves the transition from cooler temperatures in the Late Cretaceous and much of the Paleocene, to warming from the later Paleocene to early Eocene (Fig. 11). The latest Cretaceous records an interval of relatively abrupt warming and then abrupt cooling at the K-Pg boundary. Carbon isotope excursions at the PETM and early Eocene correspond to abrupt warming in the $\delta^{18}O_{benthic}$ record (Fig. 11).

Does the SPF Mainline transect preserve similar long-term and short-term $\delta^{13}C$ and temperature trends? $\delta^{13}C$ values vary considerably in the lower portion of the SPF, particularly Member B – Interval I, which also reflects the highest sampling resolution (Fig. 9). The most notable smaller scale $\delta^{13}C$ shift in this part of the SPF record is an interval of lower (-7‰) to higher (1‰) to lower (-6‰) $\delta^{13}C$ values around 400 meters (Fig. 9). Member B – Interval II (between ~425 meters and 450 meters) records consistently higher $\delta^{13}C$ values (around 2‰) in thrombolite boundstone matrix components (not including the clot components, which reflect local-scale carbon cycling; see Chapter IV). SPF $\delta^{13}C$ values, though somewhat variable, get gradually lower between ~450 meters (Member B – Interval III) and 700 meters (Member C), before decreasing to a local minimum (-5‰) around the 700-meter-level (Fig. 9). Following that minimum, SPF $\delta^{13}C$ values record transitions to higher values that eventually remain relatively constant (around +2‰) through the top of the

section. The most notable similarities between SPF $\delta^{13}C$ values and global marine $\delta^{13}C_{benthic}$ values are: i) in the short-term transition from lower to higher to lower $\delta^{13}C$ values that occur in Member B – Interval I and around the K-Pg boundary in the global marine record; and ii) the gradual decrease in $\delta^{13}C$ values between ~450-700 meters, from Member B – Interval III to Member C in the SPF, which culminates in a local minimum in upper Member C, and resembles a similar long-term trend observed in the late Paleocene and into the early Eocene in the global marine record.

Like $\delta^{13}C$ values, Δ_{47} temperatures in the lower portion of Member B – Interval I are more variable, but with an average around 28°C (± 10°C, 2 s.d.; Fig. 9). The upper part of Member B – Interval I records an approximately 8°C temperature drop from warmer Δ_{47} temperatures (below 400 m; 36°C ± 7°C, 2 s.e.) to cooler Δ_{47} temperatures (around 400 m; 28°C ± 6°C, 2 s.e.), with the cooler temperatures persisting through the remainder of Member B – Interval I (21°C ± 8°C and 15°C ± 4°C, 2 s.e.; Fig. 9) Another drop in temperatures occurs at the Member B – Interval I and Interval II transition, where the coolest Δ_{47} temperature occurs in lowermost Member B – Interval II (~425 meters; 7°C ± 4°C, 2 s.e.; Fig. 9). The upper part of Member B – Interval II (~22°C ± 4°C, 2 s.e.), Member B – Interval III, and lowermost Member C appear to have more consistent Δ_{47} temperatures (mean: ~21°C ± 8°C, 2 s.d.; Fig. 9). The remainder of Member C is characterized by an approximately 13°C to 24°C increase in Δ_{47} temperatures up to ~700 meters, where they reach a local maximum in upper Member C (41°C ± 4°C, 2 s.e.). Δ_{47} temperatures are relatively consistent (mean: ~24°C ± 6°C, 2 s.d.) through Members D and E, though it should be

noted that sampling resolution is especially low in this part of the SPF section (n=3). The most notable similarities between SPF Δ_{47} temperatures and global marine $\delta^{18}O_{benthic}$ values are: i) in the short-term drop in Δ_{47} temperatures that occurs in upper Member B – Interval I, which has some resemblance to abrupt cooling observed in the latest Cretaceous and through the K-Pg boundary in the global marine record; and ii) the gradual increase in Δ_{47} temperatures from Member B – Interval III through Member C in the SPF, which culminates in a local maximum in upper Member C, and resembles a similar long-term trend observed in the late Paleocene and into the early Eocene in the global marine record.

3.6.3 Investigating the Expression of Short-Term and Long-Term Global Climate Trends in the Sheep Pass Basin Using the Dynamic Time Warping Alignment

Comparison of the $\delta^{13}C$ and temperature records between the SPF and global marine system suggests the possible preservation of both short-term and long-term trends in the Mainline transect. With our new DTW alignment, we can investigate if our hypotheses about the temporal correlation of the long-term and short-term climate transitions in the SPF are realistic within the context of the global marine record. However, we should first scrutinize how well the dynamic time warped SPF age framework agrees with all existing age constraints in the SPF.

3.6.3.1 Comparison of the Dynamic Time Warped Sheep Pass Formation Age Framework to Existing Age Constraints

A closer comparison of the DTW age framework for the Mainline transect suggests, overall, a good correlation to all existing age constraints in the Sheep Pass Formation (Fig. 8). All of Member C is aligned to a DTW age of around 54 Ma. In the Mainline transect, upper Member C is constrained to ≤62.14 ± 0.65 Ma (Olsen-Valdez et al., 2025), which would fit within the DTW age framework given that this is a maximum depositional age (i.e., could be younger).

Lower Member B is aligned to a DTW age between the latest Cretaceous and early Paleocene, with the base of Member B aligned to ~73 Ma (Fig. 8). In the Sheep Pass Canyon area, the base of Member B is constrained to an absolute depositional age of 66.1 ± 5.4 Ma, which suggests a latest Cretaceous (~71 Ma) to earliest Paleocene (~61 Ma) age when considering errors (Druschke et al., 2009b). Overall, this is in good agreement with the DTW age but may suggest that the DTW alignment has over stretched the lowermost part of the SPF record, especially given a maximum depositional age in uppermost Member A in the Sheep Pass Canyon of ~68-70 Ma ± 1 Ma (Druschke et al., 2009b). Conversely, it may be the case that there is simply variation in the age of the base of Member B in the Mainline transect versus the Sheep Pass Canyon, though more work is needed to thoroughly investigate this.

Lastly, the top of Member D is aligned to ~38 Ma, with the few samples from Member E excluded by the DTW alignment altogether (Fig. 8). Member E – which stratigraphically overlies Member D – is constrained to the Bridgerian (50.5-40.5 Ma) based on molluscan associations (Good, 1987). This suggests that the DTW alignment has over stretched the uppermost part of the SPF record to DTW ages in Member D

that are younger than existing age constraints. This may be a product of lower sampling resolution and poor outcrop exposure in Members D and E, which limited the amount of data available to the DTW algorithm for this part of the SPF section. Given that the major paleoclimatic trends we seek to investigate are within parts of the SPF where the alignment better agrees with existing age constraints (Members B and C), we move forward with investigation of the other parts of the SPF record based on this DTW age framework.

3.6.3.2 Assessing the Drivers of Depositional Rate Changes across the Sheep Pass Formation Based on the Dynamic Time Warping Alignment

Depositional rates are important to consider when generating terrestrial paleoclimate records because terrestrial systems can accumulate sediments at more variable rates than the marine records that they are often correlated to. To holistically evaluate SPF depositional rate variations based on the DTW alignment, a thorough investigation into sedimentological and stratigraphic evidence for depositional rate is required. Such a study is beyond the scope of this work; however, we put forward some hypotheses for the major drivers of varying depositional rate across the SPF Mainline transect.

First, Druschke et al. (2011) noted that a sharp sedimentological transition from Member C to Member D could represent a significant depositional hiatus. Based on the DTW alignment, the interval in lower Member D that spans approximately one meter over three million years may support this previous interpretation. Given a

similarly low depositional rate around the transition from Member B to Member C, it is possible that this contact is also marked by a significant depositional hiatus (around two million years if the alignment is accurate).

The DTW alignment suggests a high depositional rate across all of Member C, with the full ~56-meter-thick member aligned to roughly a single age (~54 Ma). Member C largely comprises siliciclastic facies beds, including sandstones and conglomerates, some of which resemble laterally traceable channel deposits with evidence of higher flow conditions (Olsen-Valdez et al., 2025). Relatively high siliciclastic sedimentation rates compared to lacustrine deposition would be expected in this high-relief setting and could explain the shorter duration of the majority-siliciclastic Member C compared to the majority non-siliciclastic Members B, D, and E in the Mainline transect.

Two intervals of high depositional rate occur within Member B, which marks the major lacustrine phase in the Sheep Pass Basin. Much of Member B – Interval III is characterized by high depositional rates based on the DTW alignment. Olsen-Valdez et al. (2025) interpreted Member B – Interval III to reflect a transitional lake shoreline to low-energy wetland setting. It was interpreted that the transition to a more marginal shoreline setting in Member B – Interval III was driven by either depositional rates eventually outpacing available accommodation space or by climate-driven evaporative conditions, the latter of which Olsen-Valdez et al. (2025) concluded was more of an influence on the culmination of the major lacustrine phase. Further, the intervals of high depositional rate in Member B do not appear to be

correlated with specific facies (e.g., more siliciclastic or detrital compositions) as in Member C. Parts of Member D – also interpreted to reflect a low-energy, evaporative wetland environment most influenced by climate – exhibit intervals of high depositional rate based on the DTW alignment. It is possible that lower sampling resolution in Member B – Interval III and much lower sampling resolution in Member D are influencing the robustness of the DTW alignment in these stratigraphic intervals.

Lastly, two intervals of low depositional rates observed in Member B are intriguing in that they correlate to an approximately 10-meter-thick interval of micro-clotted microbial boundstone in Member B – Interval I and a section that comprises the most well-developed microbialite boundstones in Member B – Interval II. Though other micro-clotted microbial boundstone and thrombolite boundstone facies beds were aligned to intervals of higher depositional rates, the association of these microbially-derived facies to intervals of low depositional rate suggests that microbial processes may have been directly influencing depositional rates at this time. In particular, the well-developed thrombolite boundstones in lowermost Member B – Interval II have fabrics that resemble an internal framework of clots and exhibit more developed, mound-like shapes in outcrop (Olsen-Valdez et al., 2025). Microbialite mounds can reflect long temporal durations; for example, radiocarbon dating of Great Salt Lake microbialites suggests they have been accumulating for over ten thousand years (e.g., Bouton et al., 2016). It is likely that the lower depositional rates implied for the well-developed thrombolite boundstone facies beds in Member B – Interval II

or the micro-clotted microbial boundstone facies beds in Member B – Interval I reflect the long-term accumulation of microbially-derived sediments rather than a depositional hiatus as was posited for the Member B-C or Member C-D transitions.

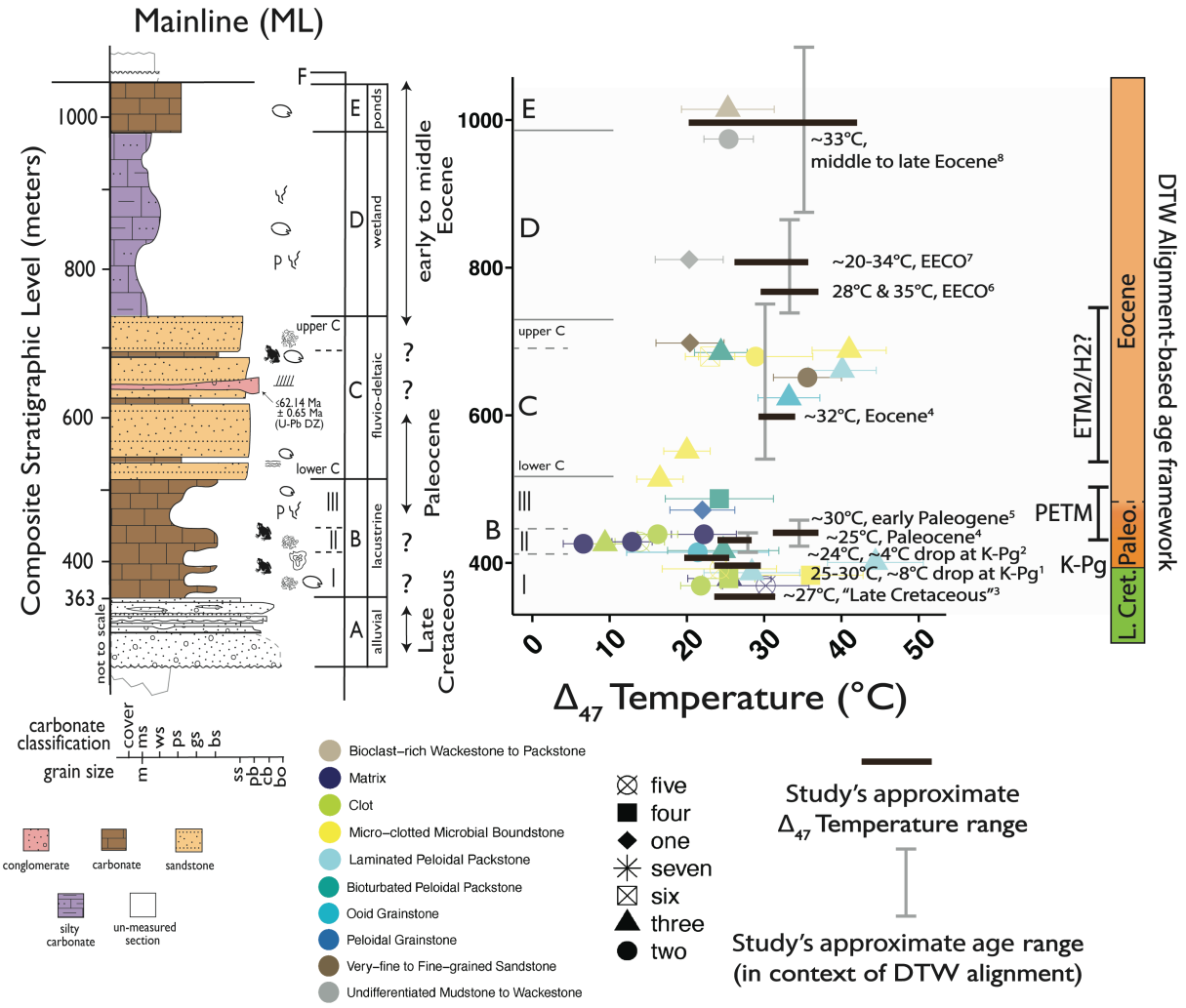

Figure 3-12: A comparison of Δ_{47} temperature estimates (°C) from the Sheep Pass Formation to other western USA records during this depositional time frame. Δ_{47} temperature ranges (black lines) from other records are paired with their approximate age range (grey bracket) within the context of the dynamic time warping alignment. Site locations and References: [1]Hell Creek Fm, Tobin et al. (2014); [2]Hell Creek Fm., Dennis et al. (2013); [3]Sheep Pass Formation, Snell et al. (2014); [4]Tornillo Basin, Kelson et al. (2018); [5]Bighorn Basin, Snell et al. (2013); [6]Green River Fm.,

Frantz et al. (2014); [7]Green River Fm., Ingalls et al. (2022); [8]Elko Fm., Ibarra et al. (2019).

3.6.3.3 Investigating the Expression of Long-Term Warming from the Paleocene through Eocene in the Sheep Pass Basin

T(Δ_{47}) estimates from several western USA sites reflect warm temperatures between the Paleocene and Eocene, including extreme warmth at the Early Eocene Climatic Optimum. Δ_{47} temperatures from the Tornillo Basin (Texas, USA) increase from ~25°C in the Paleocene to ~32°C in the early Eocene (Fig. 12; Kelson et al., 2018). Δ_{47} temperatures from the Bighorn Basin (Wyoming, USA) are around 30°C during the early Paleogene (Snell et al., 2013). And Δ_{47} temperatures from stromatolitic fabrics of the Green River Formation (Wyoming, Colorado, Utah, USA) suggest warm season temperatures of ~28 and 35°C at the height of the EECO (~51 Ma; Frantz et al., 2014), with temperatures between ~20-34°C just after (Fig. 12; Ingalls et al., 2022).

With respect to the SPF record, we hypothesized that the gradual ~5‰ decrease in $\delta^{13}C$ and associated ~13-24°C increase in Δ_{47} temperatures from Member B – Interval III through Member C, including a local $\delta^{13}C$ minimum (-5‰) and Δ_{47} temperature maximum (mean: ~30°C ± 16°C, 2 s.d.) in upper Member C of the Mainline transect resembled the expression of long-term warming from the later Paleocene through early Eocene (~53-58 Ma; Figs. 9 and 11). The other western USA records suggest ~7°C of warming between the Paleocene and Eocene (Kelson et al., 2018), and maximum temperatures associated with the EECO of up to ~35°C (Frantz

et al., 2014). These western USA records align well with the expression of global climate in the marine realm, where peak temperatures are recorded in association with the EECO (~49-53 Ma; Fig. 11).

Based on the DTW alignment, Member B – Interval III through Member C in the SPF are correlated to the Paleocene-Eocene boundary (~56 Ma) and the earliest Eocene (~54 Ma; Figs. 8 and 9), respectively. Overall, the timing of this correlation lines up with our hypothesis that decreasing $\delta^{13}C$ and associated warming in the SPF likely occurred across the later Paleocene and early Eocene. However, the DTW alignment suggests that the nature of this trend may also be recording short-term global climate transitions (e.g., the PETM or an early Eocene hyperthermal) rather than simply a long-term trend.

Over this SPF warming trend, $\delta^{18}O_{water}$ values increase from around -10‰ to as high as -3‰, with the highest $\delta^{18}O_{water}$ values corresponding to peak warming around 700 meters in upper Member C (Fig. 10). High $\delta^{18}O_{water}$ values can occur from evaporative concentration under warm climate; evaporation leads to an ^{18}O-enriched residual DIC pool from which carbonate minerals precipitate, resulting in high $\delta^{18}O_{water}$ of the carbonates themselves (Talbot, 1990; Leng and Marshall, 2004). These paired high $\delta^{18}O_{water}$ values and Δ_{47} temperatures in upper Member C suggest that the Sheep Pass Basin environment was characterized by drier conditions during this time. Interestingly, Olsen-Valdez et al. (2025) previously identified sedimentological and mineralogical evidence for a transition to more saline or highly alkaline waters around this same interval of peak warming and corresponding dry conditions (~700

meters; Fig. 10). This suggests that both the geochemical and sedimentological records in the SPF capture a notable shift to a warmer and drier paleoenvironment during the deposition of upper Member C, which may reflect early Eocene time based on the DTW alignment (Figs. 8 and 10).

These observations also share similarities to other western USA records from the early Eocene. Sedimentological evidence for progressive warming and drying, seasonally-driven runoff, and highly fluctuating lake levels are associated with early Eocene climate in the Green River Formation (Smith et al., 2008; Tänavsuu-Milkeviciene and Sarg, 2012; Frantz et al., 2014; Birgenheier et al., 2020; Ingalls et al., 2022) and Flagstaff Formation (Utah, USA) (Bowen et al., 2008). Evidence for increased evaporation between the Paleocene and Eocene is reflected in an ~2‰ shift to higher $\delta^{18}O_{water}$ values in the Tornillo Basin (Kelson et al., 2018).

Further, Member C in the Mainline transect is characterized by abundant siliciclastic facies beds deposited in a fluvio-deltaic setting (Olsen-Valdez et al., 2025). The Green River Formation also preserves evidence for more cyclic fluvial deposits associated with both precipitation and erosion under intensified hydroclimate conditions in the early Eocene (e.g., Tänavsuu-Milkeviciene et al., 2017; Birgenheier et al., 2020). These sedimentological attributes suggest that hydrological variability under an early Eocene climate may have driven both the deposition of thick siliciclastic facies beds and a transition to drier conditions in the Sheep Pass Basin during this time. Given that the DTW alignment correlated Member C to an age of approximately 54 Ma, it is possible that the geochemical and sedimentological trends

observed in the SPF are not just a reflection of early Eocene climate but may be the result of a specific hyperthermal climate event (e.g., the ETM2/H2 at ~54 Ma; see Background).

Though post-PETM hyperthermal climate events like the ETM2/H2 are generally less understood than the PETM in the western USA, newer work has highlighted that the ETM2/H2 hyperthermals are characterized by carbon isotope excursions of ~1-3‰ and distinct episodes of mammal turnover in the Bighorn Basin (Widlansky et al., 2022). In the SPF, the approximate stratigraphic position of the peak warming trend in upper Member C may also be associated with a previously recognized frog fossil deathbed horizon, suggesting a similar climatic expression as is observed in the Bighorn Basin during this time, though higher resolution sampling and chronostratigraphy would be required to test this (Bonde et al., 2020; Olsen-Valdez et al., 2025).

Lastly, the DTW alignment of much of Member B – Interval II and Member B – Interval III to the PETM (i.e., at the Paleocene-Eocene boundary) is notable because expression of this major hyperthermal climate event has been recognized in both the marine and terrestrial realm, including the western USA (see Background). In the Bighorn Basin, the PETM is associated with a negative carbon isotope excursion of ~4‰ (a larger magnitude than the global marine record), as well as abrupt warming (~3-10°C; Koch et al., 2003; Fricke and Wing, 2004; Wing et al., 2005) and evidence for transient drying (Kraus and Riggins, 2007). The parts of Member B – Interval II and III that are aligned to the PETM have $\delta^{13}C$ values around 0‰ (between -2.5‰

and 2.5‰, with the lower end-member defined by a single sample), fairly consistent $\delta^{18}O_{water}$ values around -10‰, and Δ_{47} temperatures that average 22°C (± 8°C, 2 s.d.; n=3), with a possible ~9°C increase from an underlying sample (13°C ± 6°C, 2 s.e.; Figs. 8, 9, and S5). Though the geochemical record suggests a weak shift to warmer temperatures, overall, the SPF signal differs from the prominent expression of the PETM in both the marine and terrestrial realm. This suggests that either the DTW alignment is incorrect, that sampling resolution is currently too low to fully discern the expression of this major hyperthermal event in the SPF record, or that expression of the PETM in the SPF record was fundamentally different than that of other basins in the western USA. More work will need to be completed in order to investigate this. Nonetheless, these results highlight that the Sheep Pass Formation type section shares many similarities in the expression of global climate during later Paleocene and early Eocene time and may even record the expression of short-term hyperthermal climate events in its record.

3.6.3.4 Investigating the Expression of Short-Term Cooling around the Cretaceous to Paleogene Boundary in the Sheep Pass Basin

The global marine benthic record highlights a prominent transition from a carbon isotope minimum at ~66.5 Ma that transitions to a carbon isotope maximum just prior to the K-Pg boundary, followed by a carbon isotope minimum at the K-Pg boundary around 66 Ma (Fig. 11). Marine and terrestrial paleobotanical archives also suggest that the very latest Cretaceous was characterized by warming and climate

instability from Deccan Trap volcanism (Wilf et al., 2003; Petersen et al., 2016; Barnet et al., 2018; Keller et al., 2018), along with an approximately 7°C cooling event just prior to the K-Pg boundary (Wilf et al., 2003). Δ_{47} temperatures from the western USA (Hell Creek Formation, Montana and North Dakota) corroborate this latter observation, estimating a drop in temperatures between ~4°C (Dennis et al., 2013) and ~8°C (Tobin et al., 2014) in the latest Cretaceous (Fig. 12). The K-Pg boundary is associated with additional cooling in response to the 'impact winter' in the <10s years following the bolide impact; this is what ultimately led to the major K-Pg mass extinction (Vellekoop et al., 2014, 2016; Scotese et al., 2025). It has been estimated that this transient cooling event led to a drop in temperatures between ~3°C (Vellekoop et al., 2016) and ~7°C (Vellekoop et al., 2014).

With respect to the SPF record, we hypothesized that the shift from lower (-7‰) to higher (1‰) to lower (-6‰) $\delta^{13}C$ values and associated ~8°C Δ_{47} temperature drop in upper Member B – Interval I resembled the expression of a short-term transition of carbon isotope and temperatures changes around the K-Pg boundary (~66 Ma; Figs. 9 and 11). The regional and global records suggest an approximately 3-8°C temperature drop when considering either cooling in the latest Cretaceous or cooling at the K-Pg boundary, suggesting that both the direction and the magnitude of latest Cretaceous $\delta^{13}C$ and temperature changes may be preserved in the SPF records.

Based on the DTW alignment, Member B – Interval I is correlated to the latest Cretaceous through earliest Paleocene time, with the K-Pg boundary placed just

below 400 meters (Figs. 8 and 9). Overall, this supports our hypothesis that shifting $\delta^{13}C$ values and a decrease in Δ_{47} temperatures in the upper part of Member B – Interval I likely occurred around the K-Pg boundary. Further, this alignment suggests that the warming trend observed in the global marine record may be preserved in the SPF record as well, where Δ_{47} temperatures in the lower part of Member B – Interval I have an average of ~28°C (n=4) before increasing to 36°C (n=1; Figs. 9 and 10).

Unfortunately, our current interpretations for these important Δ_{47} temperature transitions rely on two individual samples to define this change, highlighting the need for a higher sampling resolution in this stratigraphic interval before further interpretations can be made. This includes a more detailed investigation into if the observed cooling in the SPF Δ_{47} temperature record is best correlated to global cooling prior to the K-Pg boundary or abrupt cooling associated with the meteorite impact at the K-Pg boundary. Nonetheless, these results highlight that the Sheep Pass Formation type section may preserve short-term trends associated with the Cretaceous-Paleogene boundary and shares striking similarities to both global and regional records in the paleoclimatic expression of this major climate event.

3.7 Conclusions

Combined transmitted light and cathodoluminescence microscopy, X-ray diffractometry (XRD), and stable isotope geochemistry ($\delta^{13}C$, $\delta^{18}O_{carb}$, $\delta^{18}O_{water}$, and carbonate clumped isotope thermometry – $T(\Delta_{47})$) from carbonate-bearing facies

throughout the Sheep Pass Formation type section (east central Nevada, USA) suggest that processes like alteration through diagenesis or disequilibrium precipitation are present in the SPF. By leveraging a dynamic time warping algorithm to temporally correlate the SPF and global marine records, an investigation into environmental change in response to latest Cretaceous through Eocene climate among the primary samples reveals the possible expression of both long-term and short-term global climate signals. These include:

1) A gradual decrease in $\delta^{13}C$ values and increase in Δ_{47} temperatures through much of the Sheep Pass Formation type section. This trend is most similar to the long-term warming observed from the later Paleocene to early Eocene in the global marine record. Overall, the dynamic time warping alignment supports this proposed timing, but suggests that the nature of this signal may also reflect short-term global climate transitions (e.g., the PETM or an early Eocene hyperthermal) rather than only a long-term trend. The association of higher Δ_{47} temperatures and $\delta^{18}O_{water}$ values paired with previous sedimentological evidence for more evaporative conditions suggests that the height of warming was characterized by dry conditions in the Sheep Pass Basin, similar to other western USA records from this time.
2) Small-scale shifts in paired $\delta^{13}C$ values and a drop in Δ_{47} temperatures in the lower part of the Sheep Pass Formation type section. The similarity of the shifts in this interval to the global marine record, as well as its temporal

correlation based on the dynamic time warping alignment, suggests it may reflect paleoclimate changes around the Cretaceous-Paleogene boundary.

Ultimately, this initial geochemical study provides a unique high-elevation perspective compared to previous records of environmental change in response to Late Cretaceous and early Paleogene climate in the western USA. This new terrestrial paleoclimate record aids ongoing efforts to holistically characterize the response of continental settings to greenhouse climate.

3.8 Acknowledgements

Field work and sample collection, as well as subsequent laboratory analyses at the University of Colorado Boulder, were conducted on the ancestral homelands, including unceded territory, of the Western Shoshone, Goshute, Timpanogos, Arapaho, Ute, and Cheyenne peoples. We thank A. Fetrow, B. Davidheiser-Kroll, R. Havranek, and A. Maloney for their laboratory assistance. We also thank C. Hagen for technical assistance with *Align*. This work was funded by the National Science Foundation (EAR 1826850: Snell and Trower; EAR 1826769: Clyde; GRFP: Olsen-Valdez).

3.9 Works Cited

Abels, H.A., Lauretano, V., van Yperen, A.E., Hopman, T., Zachos, J.C., Lourens, L.J., Gingerich, P.D., and Bowen, G.J., 2016, Environmental impact and magnitude of paleosol carbonate carbon isotope excursions marking five early Eocene hyperthermals in the Bighorn Basin, Wyoming: Climate of the Past, v. 12, p. 1151–1163, doi:10.5194/cp-12-1151-2016.

Alvarez, L.W., Alvarez, W., Asaro, F., and Michel, H.V., 1980, Extraterrestrial Cause for the Cretaceous-Tertiary Extinction: Science, v. 208, p. 1095–1108, doi:10.1126/science.208.4448.1095.

Anderson, N.T., Bonifacie, M., Jost, A.B., Siebert, J., Bontognali, T., Horita, J., Müller, I.A., Bernasconi, S.M., and Bergmann, K.D., 2024, Re-Assessing the Need for Apatite- and Dolomite-Specific Calibrations of the Carbonate Clumped Isotope Thermometer: Geochemistry, Geophysics, Geosystems, v. 25, p. e2023GC011049, doi:10.1029/2023GC011049.

Barnet, J.S.K., Littler, K., Kroon, D., Leng, M.J., Westerhold, T., Röhl, U., and Zachos, J.C., 2018, A new high-resolution chronology for the late Maastrichtian warming event: Establishing robust temporal links with the onset of Deccan volcanism: Geology, v. 46, p. 147–150, doi:10.1130/G39771.1.

Bernasconi, S.M. et al., 2021, InterCarb: A Community Effort to Improve Interlaboratory Standardization of the Carbonate Clumped Isotope Thermometer Using Carbonate Standards: Geochemistry, Geophysics, Geosystems, v. 22, p. e2020GC009588, doi:10.1029/2020GC009588.

Birgenheier, L.P., Berg, M.D.V., Plink-Björklund, P., Gall, R.D., Rosencrans, E., Rosenberg, M.J., Toms, L.C., and Morris, J., 2020, Climate impact on fluvial-lake system evolution, Eocene Green River Formation, Uinta Basin, Utah, USA: GSA Bulletin, v. 132, p. 562–587, doi:10.1130/B31808.1.

Boggs, S., and Krinsley, D., 2006, Application of Cathodoluminescence Imaging to the Study of Sedimentary Rocks: Cambridge University Press, doi:10.1017/CBO9780511535475.

Bonde, J.W., Druschke, P.A., Hilton, R.P., Henrici, A.C., and Rowland, S.M., 2020, Preservation of latest Cretaceous (Maastrichtian)—Paleocene frogs (*Eorubeta nevadensis*) of the Sheep Pass Formation of east-central Nevada and implications for paleogeography of the Nevadaplano: PeerJ, v. 8, p. e9455, doi:10.7717/peerj.9455.

Bouton, A. et al., 2016, Linking the distribution of microbial deposits from the Great Salt Lake(Utah, USA) to tectonic and climatic processes: Biogeosciences, v. 13, p. 5511–5526, doi:10.5194/bg-13-5511-2016.

Bowen, G.J., Daniels, A.L., and Bowen, B.B., 2008, Paleoenvironmental Isotope Geochemistry and Paragenesis of Lacustrine and Palustrine Carbonates, Flagstaff Formation, Central Utah, U.S.A.: Journal of Sedimentary Research, v. 78, p. 162–174, doi:10.2110/jsr.2008.021.

Breecker, D.O., Sharp, Z.D., and McFadden, L.D., 2009, Seasonal bias in the formation and stable isotopic composition of pedogenic carbonate in modern soils from central New Mexico, USA: Geological Society of America Bulletin, v. 121, p. 630–640, doi:10.1130/B26413.1.

Burke, K.D., Williams, J.W., Chandler, M.A., Haywood, A.M., Lunt, D.J., and Otto-Bliesner, B.L., 2018, Pliocene and Eocene provide best analogs for near-future climates: Proceedings of the National Academy of Sciences, v. 115, p. 13288–13293, doi:10.1073/pnas.1809600115.

Byrne, M.P., and O'Gorman, P.A., 2015, The Response of Precipitation Minus Evapotranspiration to Climate Warming: Why the "Wet-Get-Wetter, Dry-Get-Drier" Scaling Does Not Hold over Land*: Journal of Climate, v. 28, p. 8078–8092, doi:10.1175/JCLI-D-15-0369.1.

Carmichael, M.J. et al., 2016, A model–model and data–model comparison for the early Eocene hydrological cycle: Climate of the Past, v. 12, p. 455–481, doi:10.5194/cp-12-455-2016.

Chen, J., and Lee, J., 2014, Current Progress on the Geological Record of Microbialites and Microbial Carbonates: Acta Geologica Sinica - English Edition, v. 88, p. 260–275, doi:10.1111/1755-6724.12196.

Coney, P.J., and Harms, T.A., 1984, Cordilleran metamorphic core complexes: Cenozoic extensional relics of Mesozoic compression: Geology, v. 12, p. 550, doi:10.1130/0091-7613(1984)12<550:CMCCCE>2.0.CO;2.

Daëron, M., Drysdale, R.N., Peral, M., Huyghe, D., Blamart, D., Coplen, T.B., Lartaud, F., and Zanchetta, G., 2019, Most Earth-surface calcites precipitate out of isotopic equilibrium: Nature Communications, v. 10, p. 429, doi:10.1038/s41467-019-08336-5.

Dansgaard, W., 1964, Stable isotopes in precipitation: Tellus, v. 16, p. 436–468, doi:10.1111/j.2153-3490.1964.tb00181.x.

DeCelles, P.G., 2004, Late Jurassic to Eocene evolution of the Cordilleran thrust belt and foreland basin system, western U.S.A.: American Journal of Science, v. 304, p. 105–168, doi:10.2475/ajs.304.2.105.

DeCelles, P.G., and Coogan, J.C., 2006, Regional structure and kinematic history of the Sevier fold-and-thrust belt, central Utah: Geological Society of America Bulletin,.

Dennis, K.J., Cochran, J.K., Landman, N.H., and Schrag, D.P., 2013, The climate of the Late Cretaceous: New insights from the application of the carbonate clumped isotope thermometer to Western Interior Seaway macrofossil: Earth and Planetary Science Letters, v. 362, p. 51–65, doi:10.1016/j.epsl.2012.11.036.

Dickinson, W.R., 2004, Evolution of the North American Cordillera: Annual Review of Earth and Planetary Sciences, v. 32, p. 13–45, doi:10.1146/annurev.earth.32.101802.120257.

Druschke, P., Hanson, A.D., and Wells, M.L., 2009a, Structural, stratigraphic, and geochronologic evidence for extension predating Palaeogene volcanism in the Sevier hinterland, east-central Nevada: International Geology Review, v. 51, p. 743–775, doi:10.1080/00206810902917941.

Druschke, P., Hanson, A.D., Wells, M.L., Gehrels, G.E., and Stockli, D., 2011, Paleogeographic isolation of the Cretaceous to Eocene Sevier hinterland, east-central Nevada: Insights from U-Pb and (U-Th)/He detrital zircon ages of hinterland strata: Geological Society of America Bulletin, v. 123, p. 1141–1160, doi:10.1130/B30029.1.

Druschke, P., Hanson, A.D., Wells, M.L., Rasbury, T., Stockli, D.F., and Gehrels, G., 2009b, Synconvergent surface-breaking normal faults of Late Cretaceous age

within the Sevier hinterland, east-central Nevada: Geology, v. 37, p. 447–450, doi:10.1130/G25546A.1.
Eiler, J.M., 2007, “Clumped-isotope” geochemistry—The study of naturally-occurring, multiply-substituted isotopologues: Earth and Planetary Science Letters, v. 262, p. 309–327, doi:10.1016/j.epsl.2007.08.020.
Eiler, J.M., 2011, Paleoclimate reconstruction using carbonate clumped isotope thermometry: Quaternary Science Reviews, v. 30, p. 3575–3588, doi:10.1016/j.quascirev.2011.09.001.
Eymard, I., Alvarez, M., Bilmes, A., Vasconcelos, C., and Ariztegui, D., 2020, Tracking Organomineralization Processes from Living Microbial Mats to Fossil Microbialites: Minerals, v. 10, p. 605, doi:10.3390/min10070605.
Fetrow, A.C., Snell, K.E., Di Fiori, R.V., Long, S.P., and Bonde, J.W., 2022, How Hot Is Too Hot? Disentangling Mid-Cretaceous Hothouse Paleoclimate From Diagenesis: Paleoceanography and Paleoclimatology, v. 37, p. e2022PA004517, doi:10.1029/2022PA004517.
Fiebig, J. et al., 2024, Carbonate clumped isotope values compromised by nitrate-derived NO2 interferent: Chemical Geology, v. 670, p. 122382, doi:10.1016/j.chemgeo.2024.122382.
Fouch, T.D. (1979) Character and paleogeographic distribution of Upper Cretaceous (?) and Paleogene nonmarine sedimentary rocks in East-central Nevada. In: Armentrout, J.M., Cole, M.R., and Terbest, H., eds., Cenozoic Paleogeography of the Western United States: Pacific Coast Paleogeographic Symposium 3: Los Angeles, Pacific Section, Society for Economic and Petroleum Mineralogists, pp. 97–111.
Fouch, T.D., Lund, K., Schmitt, J.G., Good, S.C. and Hanley, J.H. (1991) Late Cretaceous(?) and Paleogene sedimentary rocks and extensional(?) basins in the region of the Egan and Grant ranges, and White River adn Railroad valleys, Nevada: their relation to Sevier and Laramide contractional basins in the southern Rocky Mountains and Colorado Plateau. *Nevada Petroleum Society Fieldtrip Guidebook*, 15–23.
Frantz, C.M., Petryshyn, V.A., Marenco, P.J., Tripati, A., Berelson, W.M., and Corsetti, F.A., 2014, Dramatic local environmental change during the Early Eocene Climatic Optimum detected using high resolution chemical analyses of Green River Formation stromatolites: Palaeogeography, Palaeoclimatology, Palaeoecology, v. 405, p. 1–15, doi:10.1016/j.palaeo.2014.04.001.
Fricke, H.C., and Wing, S.L., 2004, Oxygen isotope and paleobotanical estimates of temperature and 18O-latitude gradients over North America during the early Eocene: American Journal of Science, v. 304, p. 612–635, doi:10.2475/ajs.304.7.612.
Ghosh, P., Adkins, J., Affek, H., Balta, B., Guo, W., Schauble, E.A., Schrag, D., and Eiler, J.M., 2006, 13C–18O bonds in carbonate minerals: A new kind of paleothermometer: Geochimica et Cosmochimica Acta, v. 70, p. 1439–1456, doi:10.1016/j.gca.2005.11.014.

Good, S.C., 1987, Mollusc-Based Interpretations of Lacustrine Paleoenvironments of the Sheep Pass Formation (Latest Cretaceous to Eocene) of East Central Nevada: PALAIOS, v. 2, p. 467, doi:10.2307/3514618.

Guo, W., 2020, Kinetic clumped isotope fractionation in the DIC-H2O-CO2 system: Patterns, controls, and implications: Geochimica et Cosmochimica Acta, v. 268, p. 230–257, doi:10.1016/j.gca.2019.07.055.

Hagen, C.J., Hibner, B., Olsen-Valdez, J., Brumberger, H., Fontana, C.G., Gutoski, J.R., Hankins, J.C., Kashyap, S., Lincoln, T.A., Mizrahi, N., Snell, K.E., and Trower, L.J., 2025, Microbialite cathodoluminescence: A tool for investigating paleoredox conditions, alteration histories, and primary textures across time. *The Depositional Record*, 00, 1-19, doi: 10.1002/dep2.70008.

Hagen, C., Creveling, J., and Huybers, P., 2024, Align: A User-Friendly App for Numerical Stratigraphic Correlation: GSA Today, v. 34, p. 4–9, doi:10.1130/GSATG575A.1.

Henkes, G.A., Passey, B.H., Grossman, E.L., Shenton, B.J., Pérez-Huerta, A., and Yancey, T.E., 2014, Temperature limits for preservation of primary calcite clumped isotope paleotemperatures: Geochimica et Cosmochimica Acta, v. 139, p. 362–382, doi:10.1016/j.gca.2014.04.040.

Henrici, A.C., Druschke, P., Hilton, R.P., and Bonde, J.W., 2018, Redescription and phylogenetic reassessment of the enigmatic anuran *Eorubeta nevadensis* (Amphibia) based on new specimens from ?latest Cretaceous–Paleocene beds of the Sheep Pass Formation, Nevada: Journal of Vertebrate Paleontology, v. 38, p. e1510413, doi:10.1080/02724634.2018.1510413.

Huber, B.T., MacLeod, K.G., Watkins, D.K., and Coffin, M.F., 2018, The rise and fall of the Cretaceous Hot Greenhouse climate: Global and Planetary Change, v. 167, p. 1–23, doi:10.1016/j.gloplacha.2018.04.004.

Huntington, K.W. et al., 2009, Methods and limitations of 'clumped' CO_2 isotope (Δ_{47}) analysis by gas-source isotope ratio mass spectrometry: Journal of Mass Spectrometry, v. 44, p. 1318–1329, doi:10.1002/jms.1614.

Huntington, K.W., Wernicke, B.P., and Eiler, J.M., 2010, Influence of climate change and uplift on Colorado Plateau paleotemperatures from carbonate clumped isotope thermometry: Tectonics, v. 29, p. 2009TC002449, doi:10.1029/2009TC002449.

Ingalls, M., Fetrow, A.C., Snell, K.E., Frantz, C.M., and Trower, E.J., 2022, Lake level controls the recurrence of giant stromatolite facies (M. Rogerson, Ed.): Sedimentology, v. 69, p. 1649–1674, doi:10.1111/sed.12967.

Ingalls, M., Frantz, C.M., Snell, K.E., and Trower, E.J., 2020, Carbonate facies-specific stable isotope data record climate, hydrology, and microbial communities in Great Salt Lake, UT: Geobiology, v. 18, p. 566–593, doi:10.1111/gbi.12386.

Ingalls, M., Leapaldt, H.C., and Lloyd, M.K., 2024, Microbial Autotrophy Recorded by Carbonate Dual Clumped Isotope Disequilibrium: Geochemistry, Geophysics, Geosystems, v. 25, p. e2024GC011590, doi:10.1029/2024GC011590.

Jones, C.H., Sonder, L.J., and Unruh, J.R., 1998, Lithospheric gravitational potential energy and past orogenesis: Implications for conditions of initial Basin and Range and Laramide deformation: Geology, v. 26, p. 639, doi:10.1130/0091-7613(1998)026<0639:LGPEAP>2.3.CO;2.

Keller, G., Mateo, P., Punekar, J., Khozyem, H., Gertsch, B., Spangenberg, J., Bitchong, A.M., and Adatte, T., 2018, Environmental changes during the Cretaceous-Paleogene mass extinction and Paleocene-Eocene Thermal Maximum: Implications for the Anthropocene: Gondwana Research, v. 56, p. 69–89, doi:10.1016/j.gr.2017.12.002.

Kellogg, H.E., 1964, Cenozoic Stratigraphy and Structure of the Southern Egan Range, Nevada: Geological Society of America Bulletin, v. 75, p. 949, doi:10.1130/0016-7606(1964)75[949:CSASOT]2.0.CO;2.

Kelson, J.R., Watford, D., Bataille, C., Huntington, K.W., Hyland, E., and Bowen, G.J., 2018, Warm Terrestrial Subtropics During the Paleocene and Eocene: Carbonate Clumped Isotope (Δ_{47}) Evidence From the Tornillo Basin, Texas (USA): Paleoceanography and Paleoclimatology, v. 33, p. 1230–1249, doi:10.1029/2018PA003391.

Koch, P.L., Clyde, W.C., Hepple, R.P., Fogel, M.L., Wing, S.L., and Zachos, J.C., 2003, Carbon and oxygen isotope records from Paleosols spanning the Paleocene-Eocene boundary, Bighorn Basin, Wyoming, *in* Causes and consequences of globally warm climates in the early Paleogene, Geological Society of America, doi:10.1130/0-8137-2369-8.49.

Kraus, M.J., McInerney, F.A., Wing, S.L., Secord, R., Baczynski, A.A., and Bloch, J.I., 2013, Paleohydrologic response to continental warming during the Paleocene–Eocene Thermal Maximum, Bighorn Basin, Wyoming: Palaeogeography, Palaeoclimatology, Palaeoecology, v. 370, p. 196–208, doi:10.1016/j.palaeo.2012.12.008.

Kraus, M.J., and Riggins, S., 2007, Transient drying during the Paleocene–Eocene Thermal Maximum (PETM): Analysis of paleosols in the bighorn basin, Wyoming: Palaeogeography, Palaeoclimatology, Palaeoecology, v. 245, p. 444–461, doi:10.1016/j.palaeo.2006.09.011.

Lauretano, V., Littler, K., Polling, M., Zachos, J.C., and Lourens, L.J., 2015, Frequency, magnitude, and character of hyperthermal events at the onset of the Early Eocene Climatic Optimum: Climate of the Past, v. 11, p. 1313–1324.

Leng, M.J., and Marshall, J.D., 2004, Palaeoclimate interpretation of stable isotope data from lake sediment archives: Quaternary Science Reviews, v. 23, p. 811–831, doi:10.1016/j.quascirev.2003.06.012.

Lloyd, M.K., Ryb, U., and Eiler, J.M., 2018, Experimental calibration of clumped isotope reordering in dolomite: Geochimica et Cosmochimica Acta, v. 242, p. 1–20, doi:10.1016/j.gca.2018.08.036.

Long, S.P., 2015, An upper-crustal fold province in the hinterland of the Sevier orogenic belt, eastern Nevada, U.S.A.: A Cordilleran Valley and Ridge in the Basin and Range: Geosphere, v. 11, p. 404–424, doi:10.1130/GES01102.1.

Lyson, T.R. et al., 2019, Exceptional continental record of biotic recovery after the Cretaceous–Paleogene mass extinction: Science, v. 366, p. 977–983, doi:10.1126/science.aay2268.

Machel, H., 2000, Application of cathodoluminescence to carbonate diagenesis, *in* Cathodoluminescence in Geosciences, Springer Berlin Heidelberg, p. 271–302.

Machel, H., and Burton, E., 1991, Factors governing cathodoluminescence in calcite and dolomite, and their implications for studies of carbonate diagenesis: Geoscience Canada, v. 12, p. 139–147.

Mata, S.A., and Bottjer, D.J., 2012, Microbes and mass extinctions: paleoenvironmental distribution of microbialites during times of biotic crisis: Geobiology, v. 10, p. 3–24, doi:10.1111/j.1472-4669.2011.00305.x.

Mildrexler, D.J., Zhao, M., and Running, S.W., 2011, Satellite Finds Highest Land Skin Temperatures on Earth: Bulletin of the American Meteorological Society, v. 92, p. 855–860, doi:10.1175/2011BAMS3067.1.

Olsen-Valdez, J., Widlansky, S., Trower, E., Snell, K., and Clyde, W., 2025, Carbonates and microbialites record a dynamic lake basin evolution in the Late Cretaceous to Eocene Sheep Pass Formation, Nevada, USA: Sedimentology, p. sed.13264, doi:10.1111/sed.13264.

Pagani, M., Huber, M., and Sageman, B., 2014, Greenhouse Climates, *in* Treatise on Geochemistry, Elsevier, p. 281–304, doi:10.1016/B978-0-08-095975-7.01314-0.

Pagel, M., Barbin, V., Blanc, P., and Ohnenstetter, D. (Eds.), 2000, Cathodoluminescence in Geosciences: Berlin, Heidelberg, Springer Berlin Heidelberg, doi:10.1007/978-3-662-04086-7.

Pepin, N. et al., 2015, Elevation dependent warming in mountain regions of the world.: Nature Climate Change 5, p. 424–430, doi:10.1038/nclimate2563.

Petersen, S.V., Dutton, A., and Lohmann, K.C., 2016, End-Cretaceous extinction in Antarctica linked to both Deccan volcanism and meteorite impact via climate change: Nature Communications, v. 7, p. 12079, doi:10.1038/ncomms12079.

Pommer, M., Sarg, J.F., and McFarlin, F., 2023, Environmental and microbial influence on chemistry and dolomite formation in an ancient lake, Green River Formation (Eocene), Uinta basin, Utah, U.S.A.: Journal of Sedimentary Research, v. 93, p. 213–242, doi:10.2110/jsr.2022.016.

Quade, J., Eiler, J., Daëron, M., and Achyuthan, H., 2013, The clumped isotope geothermometer in soil and paleosol carbonate: Geochimica et Cosmochimica Acta, v. 105, p. 92–107, doi:10.1016/j.gca.2012.11.031.

Rangwala, I., Sinsky, E., and Miller, J.R., 2013, Amplified warming projections for high altitude regions of the northern hemisphere mid-latitudes from CMIP5 models: Environmental Research Letters, v. 8, p. 024040, doi:10.1088/1748-9326/8/2/024040.

Renne, P.R., Sprain, C.J., Richards, M.A., Self, S., Vanderkluysen, L., and Pande, K., 2015, State shift in Deccan volcanism at the Cretaceous-Paleogene boundary, possibly induced by impact: Science, v. 350, p. 76–78, doi:10.1126/science.aac7549.

Richards, M.A., Alvarez, W., Self, S., Karlstrom, L., Renne, P.R., Manga, M., Sprain, C.J., Smit, J., Vanderkluysen, L., and Gibson, S.A., 2015, Triggering of the largest Deccan eruptions by the Chicxulub impact: Geological Society of America Bulletin, v. 127, p. 1507–1520, doi:10.1130/B31167.1.

Riding, R., 2006, Microbial carbonate abundance compared with fluctuations in metazoan diversity over geological time: Sedimentary Geology, v. 185, p. 229–238, doi:10.1016/j.sedgeo.2005.12.015.

Rosenbaum, J., and Sheppard, S.M.F., 1986, An isotopic study of siderites, dolomites and ankerites at high temperatures: Geochimica et Cosmochimica Acta, v. 50, p. 1147–1150, doi:10.1016/0016-7037(86)90396-0.

Schauble, E.A., Ghosh, P., and Eiler, J.M., 2006, Preferential formation of 13C–18O bonds in carbonate minerals, estimated using first-principles lattice dynamics: Geochimica et Cosmochimica Acta, v. 70, p. 2510–2529, doi:10.1016/j.gca.2006.02.011.

Scotese, C.R., Vérard, C., Burgener, L., Elling, R.P., and Kocsis, A.T., 2025, The Cretaceous world: plate tectonics, palaeogeography and palaeoclimate: Geological Society, London, Special Publications, v. 544, p. SP544-2024–28, doi:10.1144/SP544-2024-28.

Smith, M.E., Carroll, A.R., and Singer, B.S., 2008, Synoptic reconstruction of a major ancient lake system: Eocene Green River Formation, western United States: Geological Society of America Bulletin, v. 120, p. 54–84, doi:10.1130/B26073.1.

Snell, K.E., 2011, Paleoclimate and Paleoelevation of the western Cordillera in the United States: University of California Santa Cruz, p. PhD Thesis.

Snell, K.E., Koch, P.L., Druschke, P., Foreman, B.Z., and Eiler, J.M., 2014, High elevation of the 'Nevadaplano' during the Late Cretaceous: Earth and Planetary Science Letters, v. 386, p. 52–63, doi:10.1016/j.epsl.2013.10.046.

Snell, K.E., Thrasher, B.L., Eiler, J.M., Koch, P.L., Sloan, L.C., and Tabor, N.J., 2013, Hot summers in the Bighorn Basin during the early Paleogene: Geology, v. 41, p. 55–58, doi:10.1130/G33567.1.

Sprain, C.J., Renne, P.R., Vanderkluysen, L., Pande, K., Self, S., and Mittal, T., 2019, The eruptive tempo of Deccan volcanism in relation to the Cretaceous-Paleogene boundary: Science, v. 363, p. 866–870, doi:10.1126/science.aav1446.

Talbot, M.R., 1990, A review of the palaeohydrological interpretation of carbon and oxygen isotopic ratios in primary lacustrine carbonates: Chemical Geology: Isotope Geoscience section, v. 80, p. 261–279, doi:10.1016/0168-9622(90)90009-2.

Tänavsuu-Milkeviciene, K., and Sarg, J.F., 2012, Evolution of an organic-rich lake basin – stratigraphy, climate and tectonics: Piceance Creek basin, Eocene Green River Formation: Sedimentology, v. 59, p. 1735–1768, doi:10.1111/j.1365-3091.2012.01324.x.

Tänavsuu-Milkeviciene, K., Sarg, J.F., and Bartov, Y., 2017, Depositional Cycles and Sequences In An Organic-Rich Lake Basin: Eocene Green River Formation, Lake Uinta, Colorado and Utah, U.S.A.: Journal of Sedimentary Research, v. 87, p. 210–229, doi:10.2110/jsr.2017.11.

The Cenozoic CO Proxy Integration Project (CenCOPIP) Consortium et al., 2023, Toward a Cenozoic history of atmospheric CO_2: Science, v. 382, p. 5177, doi:10.1126/science.adi5177.

Thrasher, B.L., and Sloan, L.C., 2009, Carbon dioxide and the early Eocene climate of western North America: Geology, v. 37, p. 807–810, doi:10.1130/G30090A.1.

Tobin, T.S., Wilson, G.P., Eiler, J.M., and Hartman, J.H., 2014, Environmental change across a terrestrial Cretaceous-Paleogene boundary section in eastern Montana, USA, constrained by carbonate clumped isotope paleothermometry: Geology, v. 42, p. 351–354, doi:10.1130/G35262.1.

Urey, H., 1947, The Thermodynamic Properties of Isotopic Substances: Journal of the Chemical Society (Resumed), p. 562–581.

Vandervoort, D.S., and Schmitt, J.G., 1990, Cretaceous to early Tertiary paleogeography in the hinterland of the Sevier thrust belt, east-central Nevada: Geology, v. 18, p. 567, doi:10.1130/0091-7613(1990)018<0567:CTETPI>2.3.CO;2.

Vellekoop, J., Esmeray-Senlet, S., Miller, K.G., Browning, J.V., Sluijs, A., Van De Schootbrugge, B., Sinninghe Damsté, J.S., and Brinkhuis, H., 2016, Evidence for Cretaceous-Paleogene boundary bolide "impact winter" conditions from New Jersey, USA: Geology, v. 44, p. 619–622, doi:10.1130/G37961.1.

Vellekoop, J., Sluijs, A., Smit, J., Schouten, S., Weijers, J.W.H., Sinninghe Damsté, J.S., and Brinkhuis, H., 2014, Rapid short-term cooling following the Chicxulub impact at the Cretaceous–Paleogene boundary: Proceedings of the National Academy of Sciences, v. 111, p. 7537–7541, doi:10.1073/pnas.1319253111.

Westerhold, T. et al., 2020, An astronomically dated record of Earth's climate and its predictability over the last 66 million years: Science, v. 369, p. 1383–1387, doi:10.1126/science.aba6853.

Widlansky, S.J., Secord, R., Snell, K.E., Chew, A.E., and Clyde, W.C., 2022, Terrestrial carbon isotope stratigraphy and mammal turnover during post-PETM hyperthermals in the Bighorn Basin, Wyoming, USA: Climate of the Past, v. 18, p. 681–712, doi:10.5194/cp-18-681-2022.

Wilf, P., Johnson, K.R., and Huber, B.T., 2003, Correlated terrestrial and marine evidence for global climate changes before mass extinction at the Cretaceous–Paleogene boundary: Proceedings of the National Academy of Sciences, v. 100, p. 599–604, doi:10.1073/pnas.0234701100.

Winfrey, W.M., 1960, Stratigraphy, Correlation, and Oil Potential of the Sheep Pass Formation, East-Central Nevada: , p. 126–133.

Wing, S.L., Harrington, G.J., Smith, F.A., Bloch, J.I., Boyer, D.M., and Freeman, K.H., 2005, Transient Floral Change and Rapid Global Warming at the Paleocene-Eocene Boundary: Science, v. 310, p. 993–996, doi:10.1126/science.1116913.

Zachos, J.C., Dickens, G.R., and Zeebe, R.E., 2008, An early Cenozoic perspective on greenhouse warming and carbon-cycle dynamics: Nature, v. 451, p. 279–283, doi:10.1038/nature06588.

Zachos, J., Pagani, M., Sloan, L., Thomas, E., and Billups, K., 2001, Trends, Rhythms, and Aberrations in Global Climate 65 Ma to Present: Science, v. 292, p. 686–693, doi:10.1126/science.1059412.

Zeebe, R.E., and Wolf-Gladrow, D., 2001, CO2 in Seawater: Equilibrium, Kinetics, Isotopes: Elsevier, Elsevier Oceanography Series 65.

3.10 Supplemental Materials

Sample ID	Coordinates	Transect	Member	Composite Stratigraphic Level (m)	Facies	Thin Section
SPB19-SPC06	N 38.73851, W 114.96225	SPC	A	356.3	Very fine to Fine-grained Sandstone	X
SPB19-ML01	N 38.72538, W 114.97237	ML	B	364.4	Bioclast-rich Wackestone to Packstone	X
SPB19-ML04	N 38.72525, W 114.97224	ML	B	369.1	Micro-clotted Microbial Boundstone	X
SPB19-ML09	N 38.72529, W 114.97217	ML	B	374.9	Bioclast-rich Wackestone to Packstone	X
SPB19-ML11	N 38.72545, W 114.97222	ML	B	377.6	Thrombolite Boundstone (small clots)	X
SPB19-ML12	N 38.72546, W 114.97221	ML	B	378.9	Thrombolite Boundstone (large clots)	X
SPB19-ML13	N 38.72537, W 114.97208	ML	B	383.3	Micro-clotted Microbial Boundstone	X
SPB19-ML15	N 38.72538, W 114.97206	ML	B	386.7	Laminated Peloidal Packstone	X
SPB19-ML17	N 38.72537, W 114.97198	ML	B	391.1	Micro-clotted Microbial Boundstone	X
SPB19-ML19	N 38.72541, W 114.97187	ML	B	400.7	Laminated Peloidal Packstone	
SPB19-ML23	N 38.72546, W 114.97179	ML	B	408.8	Bioturbated Peloidal Packstone	X
SPB19-ML27	N 38.72549, W 114.97173	ML	B	414.4	Ooid Grainstone	X
SPB19-ML29	N 38.72551, W 114.97172	ML	B	416.7	Bioturbated Peloidal Packstone	
SPB19-ML31	N 38.72558, W 114.97162	ML	B	425.9	Thrombolite Boundstone (small clots)	X, alizarin red-stained
SPB19-ML33	N 38.72570, W 114.97164	ML	B	428.6	Thrombolite Boundstone (framework of clots)	X
SPB19-ML36	N 38.72571, W 114.97152	ML	B	438.8	Thrombolite Boundstone (large clots)	X
SPB19-ML39	N 38.72586, W 114.97146	ML	B	451	Peloidal Grainstone	X
SPB19-ML41	N 38.72594, W 114.97118	ML	B	471.6	Peloidal Grainstone	
SPB19-ML45	N 38.72580, W 114.97096	ML	B	486.9	Bioturbated Peloidal Packstone	X
SPB19-ML50	N 38.72593, W 114.97069	ML	B	513.4	Micro-clotted Microbial Boundstone	
SPB19-ML51	N 38.72604, W 114.97030	ML	C	540.6	Very fine to Fine-grained Sandstone	X
SPB19-ML52	N 38.72622, W 114.97016	ML	C	551.5	Micro-clotted Microbial Boundstone	X
SPB19-ML58	N 38.72655, W 114.96786	ML	C	637.2	Oncoid Packstone to Grainstone	X
SPB19-ML59	N 38.72635, W 114.96743	ML	C	651.2	Very fine to Fine-grained Sandstone	
SPB19-ML60	N 38.72639, W 114.96719	ML	C	660.9	Laminated Peloidal Packstone	
SPB19-ML61	N 38.72660, W 114.96694	ML	C	679.5	Micro-clotted Microbial Boundstone	X
SPB19-ML63	N 38.72671, W 114.96682	ML	C	685	Bioturbated Peloidal Packstone	
SPB19-ML64	N 38.72668, W 114.96678	ML	C	688	Micro-clotted Microbial Boundstone	
SPB19-ML65	N 38.72726, W 114.96618	ML	C	693.5	Bioclast-rich Wackestone to Packstone	X, alizarin red-stained
SPB19-ML66	N 38.72711, W 114.96600	ML	C	698	Very fine to Fine-grained Sandstone	X
SPB19-ML69	N 38.72664,	ML	D	754	Vuggy Wackestone	X

	W 114.96432					
SPB19-ML74	N 38.72666, W 114.96325	ML	D	811	Undifferentiated Mudstone to Wackestone	X
SPB19-ML85	N 38.72617, W 114.96068	ML	D	854.5	Undifferentiated Mudstone to Wackestone	X
SPB19-ML93	N 38.72546, W 114.95892	ML	D	974.2	Undifferentiated Mudstone to Wackestone	X
SPB19-ML97	N 38.72544, W 114.95823	ML	E	1014.5	Bioclast-rich Wackestone to Packstone	X
SPB20-SPC09	N 38.73864, W 114.96054	SPC	B	432.85	Bioclast-rich Wackestone to Packstone	X
SPB20-SPC31	N 38.73809, W 114.95866	SPC	B	546	Thrombolite Boundstone (large clots)	X, alizarin red-stained
SPB20-SPC45	N 38.73952, W 114.95514	SPC	B	637.25	Micro-clotted Microbial Boundstone	X
SPB20-SPC51	N 38.73947, W 114.95055	SPC	C	762.4	Laminated Peloidal Packstone	X
				Measured Level (m)		
SPB20-SPC38	N 38.73733, W 114.95847	Lower B	B	8.70	Thrombolite Boundstone (large clots)	X

Table S3-1: Summary of ID, GPS coordinates, measured transect, member, stratigraphic level in meters (composite or measured), and facies characterization for all SPF samples. Samples with a corresponding thin section are denoted with an "X" in the "Thin Section" column, including a note if stained with alizarin red for the identification of calcite.

Sample ID	**Transect**	**Member**	**Facies Name**	**XRD Dominant Mineralogy**		
				1st	**2nd**	**3rd**
SPB19-ML01	ML	B	Bioclast-rich WS/PS	Calcite, magnesian	Calcite	
SPB19-ML13	ML	B	Micro-clotted Microbial BS	Calcite	Calcite, magnesian	
SPB19-ML33	ML	B	Thrombolite BS (framework)	Magnesium Calcite	Calcite	
SPB19-ML39	ML	B	Peloidal GS	Quartz	Dolomite (stoichiometrically ordered)	
SPB19-ML41	ML	B	Peloidal GS	Dolomite (stoichiometrically ordered and disordered)	Quartz low	
SPB19-ML45	ML	B	Bioturbated PS	Dolomite (stoichiometrically ordered and disordered)	Quartz low	
SPB19-ML50	ML	B	Micro-clotted Microbial BS	Magnesium Calcite	Calcite	
SPB19-ML58	ML	C	Oncoid GS	Calcite, magnesian	Calcite	
SPB19-ML64	ML	C	Micro-clotted Microbial BS	Calcite	Magnesium Calcite	
SPB19-ML65	ML	C	Bioclast-rich WS/PS	Dolomite (stoichiometrically ordered)		
SPB19-ML66	ML	C	Very fine to fine-grained SS	Dolomite (stoichiometrically ordered)	Quartz low	
SPB19-ML93	ML	D	Undifferentiated MS/WS	Dolomite (stoichiometrically ordered)		
SPB19-ML97	ML	E	Bioclast-rich WS/PS	Magnesium Calcite	Calcite	Calcite, magnesian
SPB20-SPC31	SPC	B	Thrombolite BS (large clots)	Calcite	Magnesium Calcite	
SPB20-SPC45	SPC	B	Micro-clotted Microbial BS	Calcite		

Table S3-2: Summary of dominant mineralogy for the subset of samples analyzed with X-ray diffractometry mineralogy. When present, dolomite is noted as being stoichiometrically ordered and/or disordered.

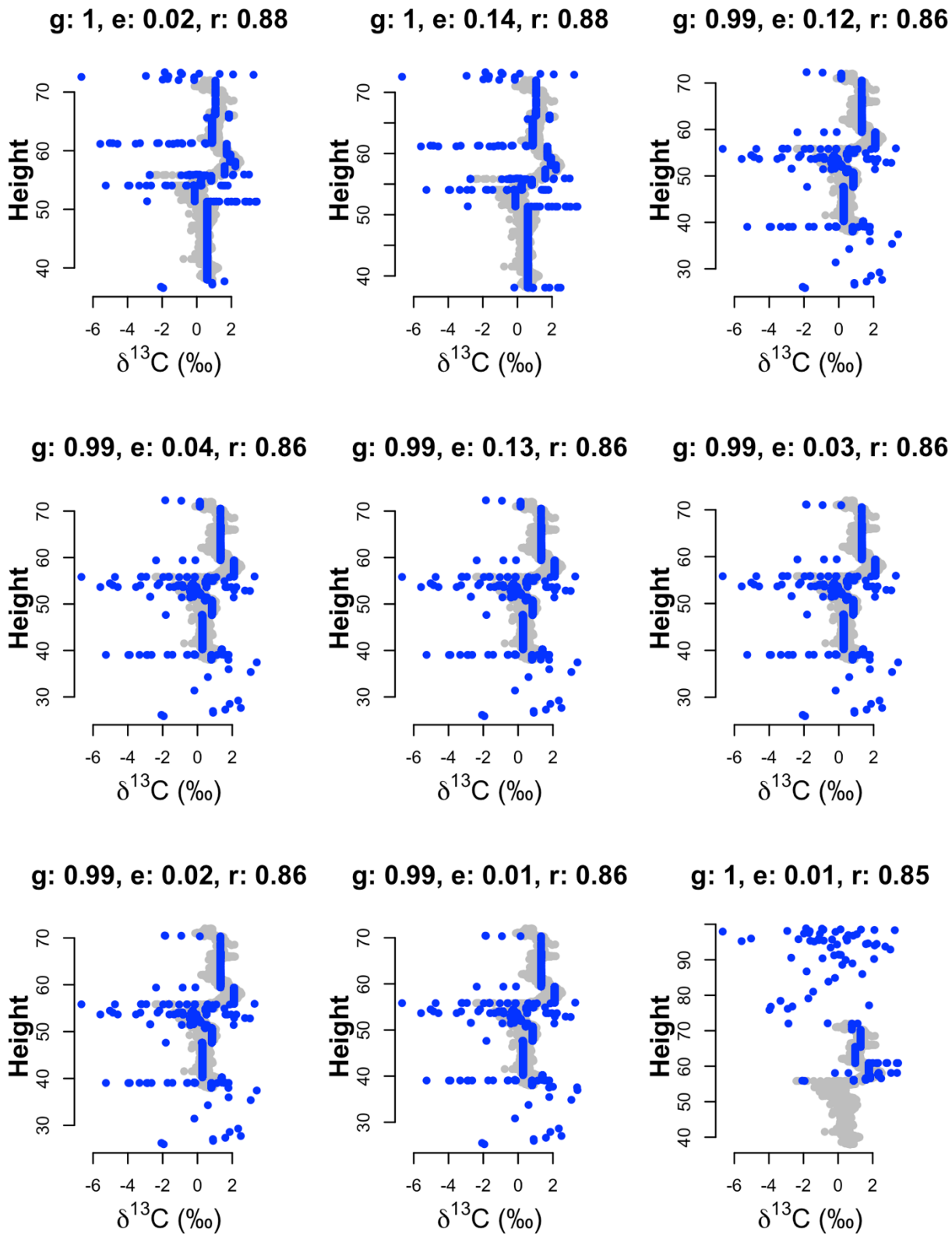

Figure S3-1: All possible dynamic time warping (DTW) alignments of the SPF Mainline transect $\delta^{13}C$ (‰, VPDB) candidate record (blue) to the target global $\delta^{13}C$

(‰, VPDB) record (gray) compiled from Huber et al. (2018) and Westerhold et al. (2020). These DTW alignments reflect those that had more than 10% overlap between both records, and that had a Pearson correlation coefficient value between both records of greater than 0.8 (see Materials and Methods). Note that the y-axis (labelled Height) is the age scale from the target time-series data set where, for example, "40" reflects 40 Ma. Also note that only the first two DTW alignments (g:1, e:0.02; g:1, e:0.14) fit within existing SPF age constraints, and only the second one was investigated in the Discussion (g:1, e:0.14; see Materials and Methods).

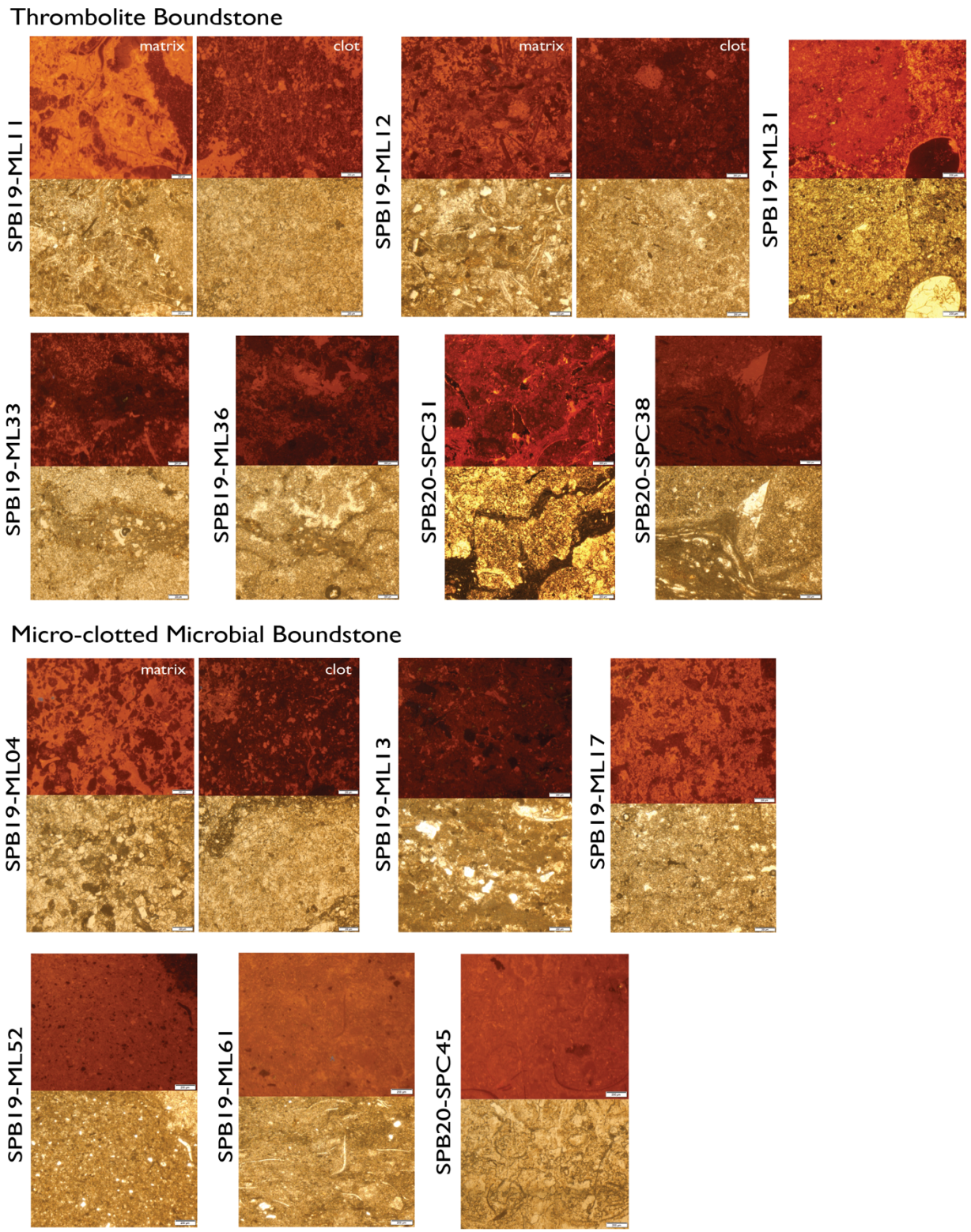

Figure S3-2: Cathodoluminescence and plane polarized light images for the thrombolite boundstone and micro-clotted microbial boundstone facies. Samples pictured were run for carbonate clumped isotopes (Δ_{47}).

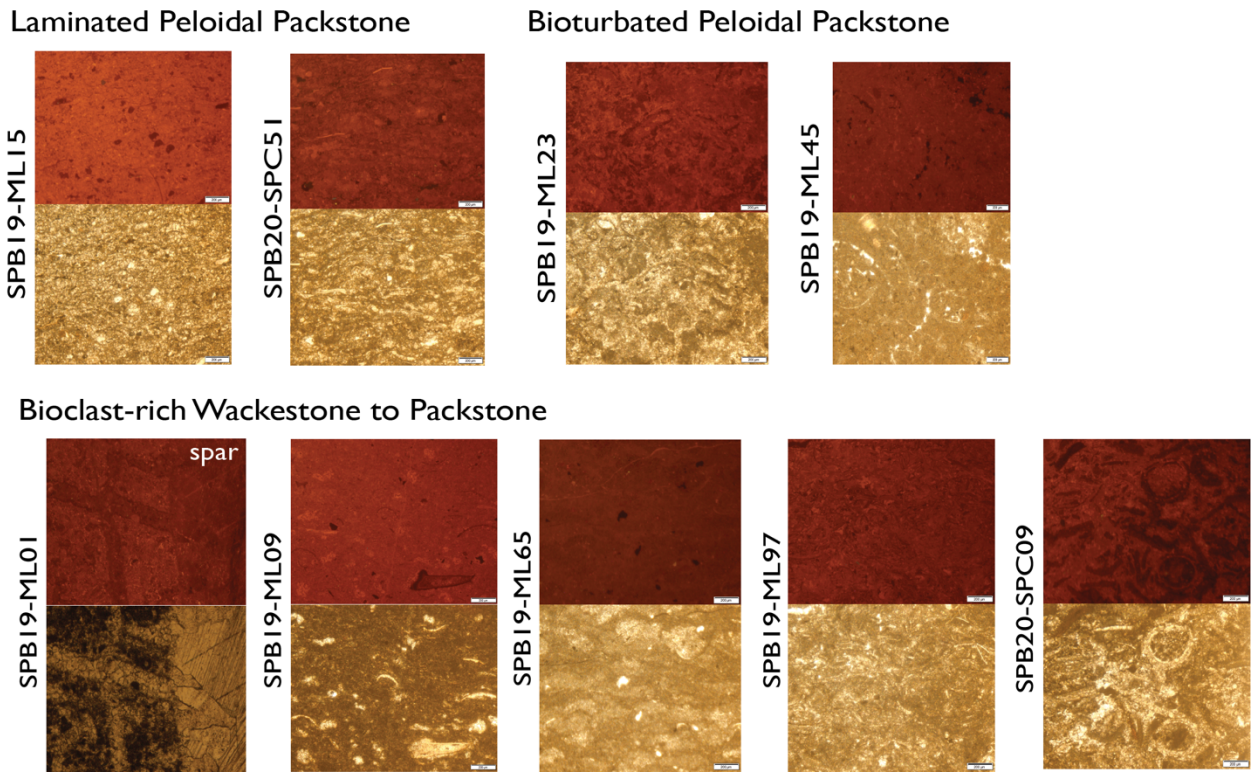

Figure S3-3: Cathodoluminescence and plane polarized light images for the laminated peloidal packstone and bioturbated peloidal packstone facies. Samples pictured were run for carbonate clumped isotopes (Δ_{47}). SPB19-ML01 is at the same scale as all other images (4X magnification).

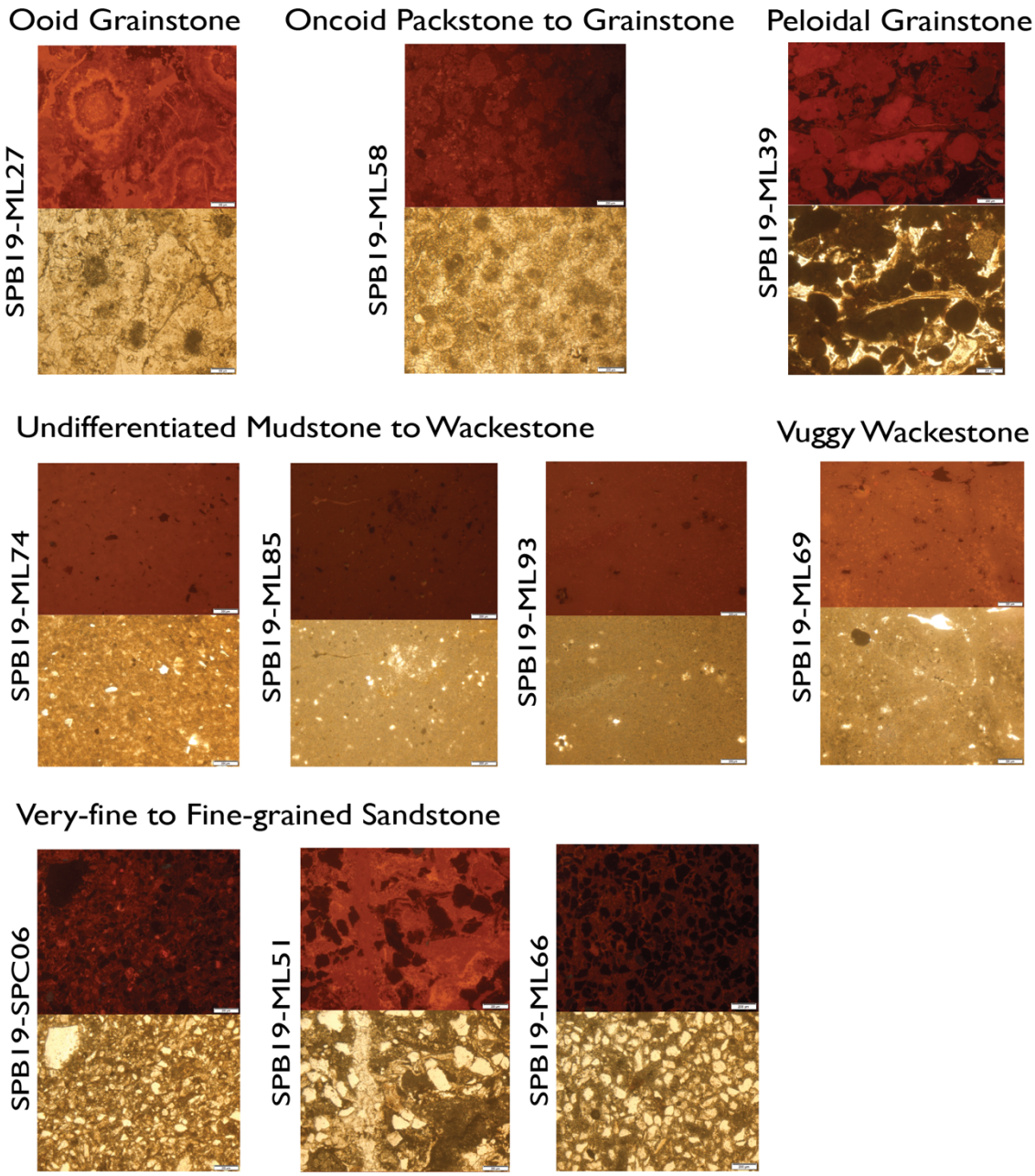

Figure S3-4: Cathodoluminescence and plane polarized light images for the ooid grainstone, oncoid packstone to grainstone, peloidal grainstone, undifferentiated mudstone to wackestone, vuggy wackestone, and very-fine to fine-grained sandstone facies. Samples pictured were run for carbonate clumped isotopes (Δ_{47}).

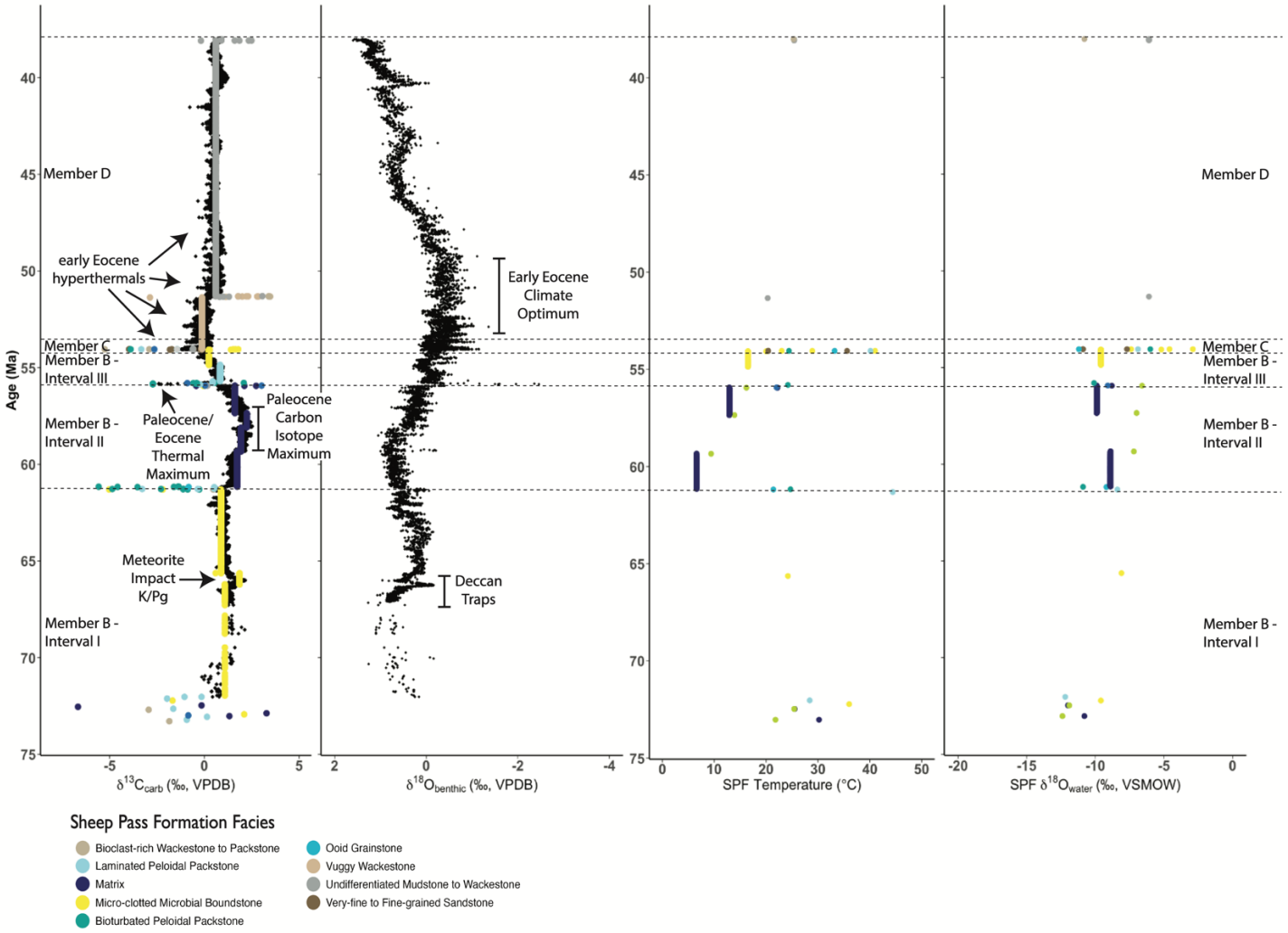

Figure S3-5: Global benthic marine and Sheep Pass Formation $\delta^{13}C$ (‰, VPDB), global benthic marine $\delta^{18}O$ (‰, VPDB), and $T(\Delta_{47})$ estimates (°C) and calculated $\delta^{18}O_{water}$ (‰, VSMOW) values from primary Mainline transect samples versus age (Ma), based on the dynamic time warping alignment. All SPF samples are color-coded by facies type.

Chapter IV: Photosynthetic carbon cycling signal preserved in carbonate $\delta^{13}C$ values of ancient thrombolites

Juliana Olsen-Valdez[1], Cedric J. Hagen[1,2], Sarah J. Widlansky[3], Elizabeth J. Trower[1], Kathryn E. Snell[1], and William C. Clyde[4]

[1]Department of Geological Sciences, University of Colorado Boulder, Benson Earth Sciences Building, 2200 Colorado Ave., Boulder, Colorado 80309, USA

[2]National Ecological Observatory Network, Battelle, Boulder, CO 80301, USA

[3]Department of Earth Sciences, University of New Hampshire, 56 College Road, 214 James Hall, Durham, New Hampshire 03824, USA. Now at: Woods Hole Coastal and Marine Science Center, U.S. Geological Survey, 360 Woods Hole Road, Woods Hole, Massachusetts 02543, USA

[4]Department of Earth Sciences, University of New Hampshire, 56 College Road, 214 James Hall, Durham, New Hampshire 03824, USA

4.1 Abstract

Thrombolites–clotted organo-sedimentary deposits–forming today preserve carbonate carbon isotope ($\delta^{13}C_{carb}$) values that suggest photosynthesis shifts the $\delta^{13}C$ of the local dissolved inorganic carbon pool 1-6‰ higher than that expected for carbonate minerals precipitated in equilibrium with ambient lake water. However, no study has documented similar $\delta^{13}C_{carb}$ signals in fossil thrombolites. To test whether these signals are preserved in the geologic record, we analyzed the $\delta^{13}C_{carb}$

This chapter version is currently in review with *Geology*

values of thrombolites from the Cretaceous to Eocene Sheep Pass Formation (NV, USA). We performed fabric-specific analyses of both the clot component–interpreted to reflect microbially-influenced precipitation–and adjacent matrix carbonate–interpreted to reflect abiotic precipitation. We find that the $\delta^{13}C_{carb}$ values of clot components are consistently offset to higher values than adjacent matrix, with a mean offset ($\Delta^{13}C$) between the clots and matrix of +2.77‰ (± 0.94, 2 s.e.). These $\Delta^{13}C$ values are consistent with predictions by a model of diurnal carbon cycling driven by photosynthesis. Modeled $\Delta^{13}C$ values also match the documented $\Delta^{13}C$ values in modern lacustrine thrombolites and suggest that the concentration of dissolved inorganic carbon serves as a major control for the magnitude of $\Delta^{13}C$ values. Together, the model results and measurements of $\Delta^{13}C$ values offer a new tool for reconstructing water chemistry changes in ancient lake systems. The Sheep Pass Formation $\Delta^{13}C$ values preserve signals related to both local and external influences on the dissolved inorganic carbon pool. Fabric-informed sampling can disentangle these two signals, allowing for more robust chemostratigraphy from microbialite archives.

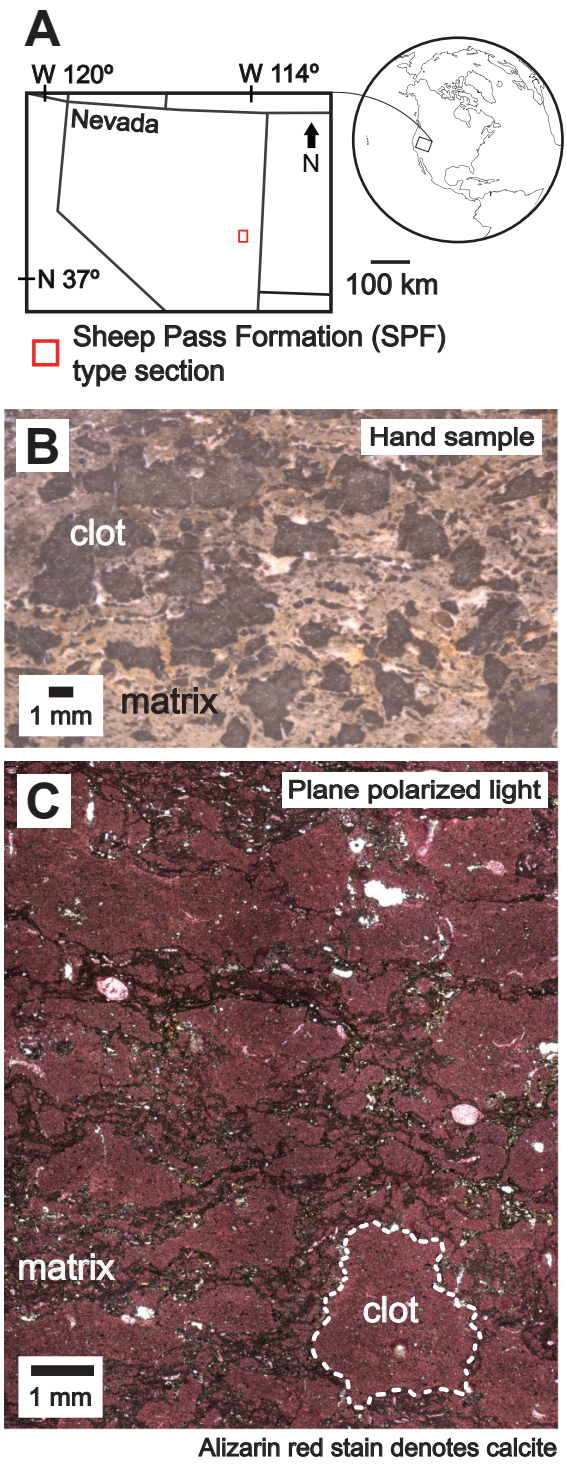

Figure 4-1: A) Sheep Pass Formation type section (red box) in the context of North America and the western United States, B) representative hand sample of thrombolite, and C) representative thin section image of thrombolitic fabric comprising clot and matrix components.

4.2 Introduction

Microbialites are organo-sedimentary deposits that form through microbial trapping and binding of detrital sediment and/or microbially-influenced *in situ* mineral precipitation (Burne and Moore, 1987). Thrombolites are a type of microbialite with a clotted texture comprising distinct polymorphic clots surrounded by micritic and sparry carbonate (Aitken, 1967; Kennard and James, 1986). Carbonate microbialites are useful paleoenvironmental archives because they are common throughout the geological record and their carbonate carbon isotope values ($\delta^{13}C_{carb}$) can preserve information about short-term, local-scale microbial carbon cycling (Sumner, 2001; Andres et al., 2006; Breitbart et al., 2009) and long-term changes to the global carbon cycle over 10s-100s kyrs or more (Buongiorno et al., 2019; Huang et al., 2022; Fogret et al., 2024).

Present-day lacustrine thrombolites preserve $\delta^{13}C_{carb}$ values up to 6.8‰ higher than the $\delta^{13}C_{carb}$ values expected for precipitation of carbonate minerals in equilibrium with the measured $\delta^{13}C$ values of the dissolved inorganic carbon (DIC) pool ($\delta^{13}C_{DIC}$) in these respective systems ([1]Table S1; Moore and Burne, 1994; Ferris et al., 1997; Kempe and Kaźmierczak, 2007; Brady et al., 2010, 2014; Kaźmierczak et al., 2011; Warden et al., 2016; Belan et al., 2019; White et al., 2020). This offset between the expected versus observed thrombolite $\delta^{13}C_{carb}$ values in these modern settings–hereafter referred to as $\Delta^{13}C_{modern}$–has been interpreted as an isotopic biosignature of photosynthesis, whereby preferential uptake and conversion of $^{12}CO_2$ into organic matter results in ^{13}C-enrichment of the residual DIC pool. This effect can

be preserved in the $\delta^{13}C$ values of carbonate precipitated in the immediate vicinity and has been well documented in the literature (Merz, 1992; McConnaughey et al., 1997; Sumner, 2001; White et al., 2020).

$\Delta^{13}C$ values analogous to $\Delta^{13}C_{modern}$ values have not been documented in ancient samples. Such data could provide a new geochemical fingerprint of photosynthesis in microbialite archives. This study presents fabric-specific $\delta^{13}C_{carb}$ values measured from clot and matrix components of thrombolites from the type section of the latest Cretaceous to middle Eocene (~70 Ma to ~45 Ma) Sheep Pass Formation (SPF) in east-central Nevada (Fig. 1; Fouch, 1979; Druschke et al., 2009). SPF thrombolites formed in a shallow, freshwater lake basin (Olsen-Valdez et al., 2025). Clots range from the μm- to cm-scale, are irregularly shaped, and are composed of micrite and microsparite (Fig. 1; Olsen-Valdez et al., 2025). The interstitial matrix is largely composed of micrite with detrital quartz grains and bioclast fragments. The clots and matrix reflect contemporaneous authigenic deposition, at least at the timescale relevant to this work. Clots reflect *in situ* calcification in the microbially-influenced DIC pool, while the interstitial matrix reflects precipitation in pore spaces around clots from a DIC pool more representative of the broader lake water (Kennard and James, 1986; Mei et al., 2020; Olsen-Valdez et al., 2025).

4.3 Methods

4.3.1 Carbon Isotopes of Thrombolite Carbonate

Thrombolite samples (n=18) were collected from two stratigraphic sections within the SPF: the Sheep Pass Canyon and the Mainline (Table S2; see Olsen-Valdez et al., 2025). To obtain $\delta^{13}C_{carb}$ values, we prepared and analyzed both the matrix and clot components of the carbonate samples using the methods outlined in the Supplemental Material. $\delta^{13}C_{carb}$ values are reported relative to Vienna Pee Dee Belemnite (VPDB) in delta notation (parts per thousand, ‰) and reflect standard corrected sample means ± two standard deviations (i.e., 2 s.d.). $\delta^{13}C_{carb}$ precision for individual sample analyses is ± 0.1‰ or better (1 sigma).

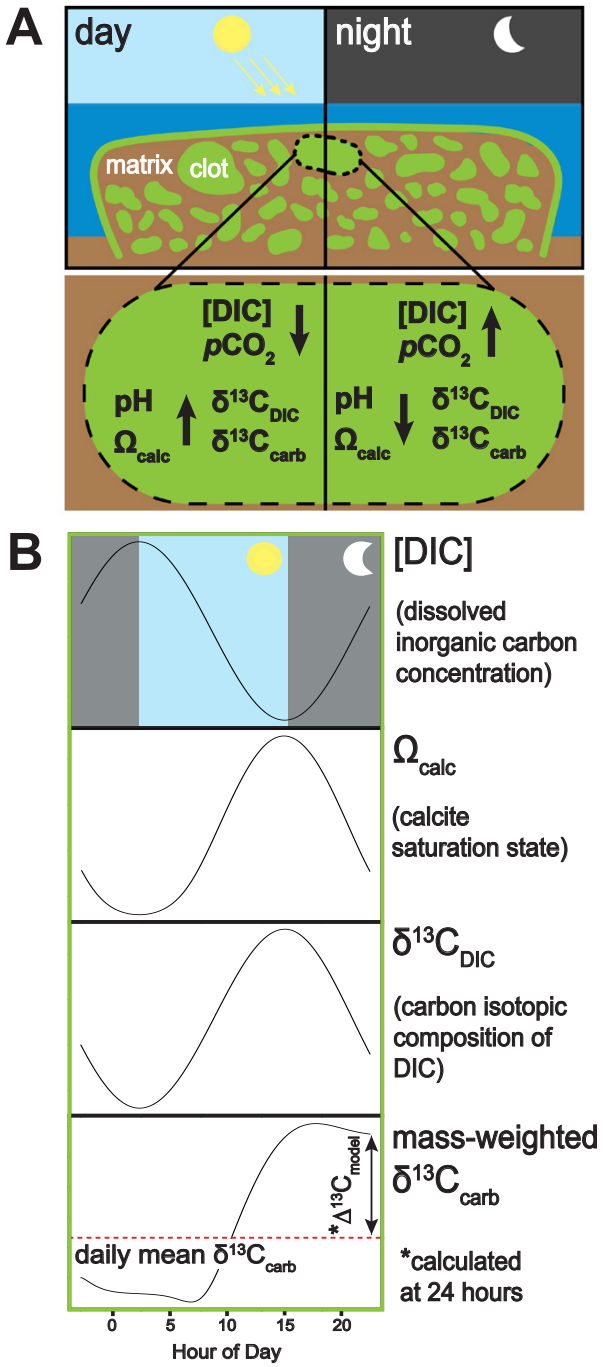

Figure 4-2: A) Schematic of the photosynthesis-driven diurnal carbon engine, and its effect on major model variables within a clot during the day versus night, B) example model output highlighting the relative changes in [DIC], Ω_{calc}, $\delta^{13}C_{DIC}$, and mass-weighted $\delta^{13}C_{carb}$ over the course of a day. $\Delta^{13}C_{model}$ is the difference between daily mean $\delta^{13}C_{DIC}$ and the mass-weighted $\delta^{13}C_{carb}$ value for carbonate accumulated throughout the 24-hour interval.

4.3.2 Diurnal Carbon Cycling Model

To aid in our interpretation of SPF $\delta^{13}C_{carb}$ data, we compared our data with $\delta^{13}C$ values generated by a diurnal carbon cycling model. According to the diurnal carbon engine hypothesis described by Geyman and Maloof (2019), daytime photosynthesis consumes DIC and drives increases in $\delta^{13}C_{DIC}$, $\delta^{13}C_{carb}$, and Ω_{calc} (calcite saturation state), while heterotrophy at night reverses daytime trends (e.g., decreases $\delta^{13}C_{DIC}$). Together, these processes result in diurnal carbon cycling (Fig. 2). Here, we adapted the marine-specific diurnal carbon cycling model of Trower et al. (2024) to the lacustrine data presented herein. This includes: precipitation of calcite rather than aragonite; the use of PHREEQC (Parkhurst and Appelo, 2013) rather than seawater-specific CO2SYS (Lewis and Wallace, 1998) for equilibrium chemistry calculations; and major ion concentrations based on representative modern lake systems. This diurnal carbon cycling model version has also been translated into R, making the code free and open source.

We determined carbon isotope values of bulk organic matter ($\delta^{13}C_{org}$) from acidified carbonate and total lipid extracts for a subset of SPF thrombolites (n=5) using the methods outlined in the Supplemental Material. All $\delta^{13}C_{org}$ values (‰) are reported relative to VPDB and reflect corrected triplicate sample means ± two standard errors (i.e., s.e.) with an analytical precision of ± 0.2‰ or better (1 sigma). $\delta^{13}C_{org}$ values are -28.39‰ (± 0.14‰) to -31.49‰ (± 0.19‰) for total lipid extracts and -24.40‰ (± 0.02‰) to -27.81‰ (± 0.12‰) for acidified carbonate. These values imply isotopic fractionations typical of photoautotrophic bacteria fixing inorganic carbon

using the Calvin cycle (Preuß et al., 1989; Sumner, 2001). The mean difference between the carbonate $\delta^{13}C_{matrix}$ and the acidified carbonate $\delta^{13}C_{org}$ across all samples is 28.23‰ (± 2.74‰, 2 s.e.; Table S4). We used this mean difference to determine the $\delta^{13}C_{DIC}$– $\delta^{13}C_{org}$ photosynthetic fractionation (ε_P) as 27.23‰ in the diurnal carbon cycling model.

We used water chemistry data from three modern lakes: Fayetteville Green Lake (NY, USA; Leapaldt et al., 2024), Great Salt Lake (UT, USA; Ingalls et al., 2020), and Pavilion Lake (BC, Canada; Lim et al., 2009) (Table S5). We also modeled a fourth scenario ("Synthetic") that uses Pavilion Lake values but a decreased alkalinity as a point of comparison. In all modeling scenarios, we computed the difference between the mass-weighted $\delta^{13}C_{carb}$ value of all carbonate accumulated throughout the 24-hour interval and the $\delta^{13}C_{carb}$ value predicted from the mean $\delta^{13}C_{DIC}$ value over the same 24-hour interval with an assumed +1‰ fractionation between DIC and calcite; we refer to this difference as $\Delta^{13}C_{model}$ (Fig. 2). We conducted sensitivity analyses for these $\Delta^{13}C_{model}$ values across a range of productivity (κ_p, the magnitude of photosynthetic forcing = 0–800 μmol/kg; see Trower et al., 2024), pCO_2 (200–1200 ppm), and temperature values (20–30°C) for the four lake scenarios.

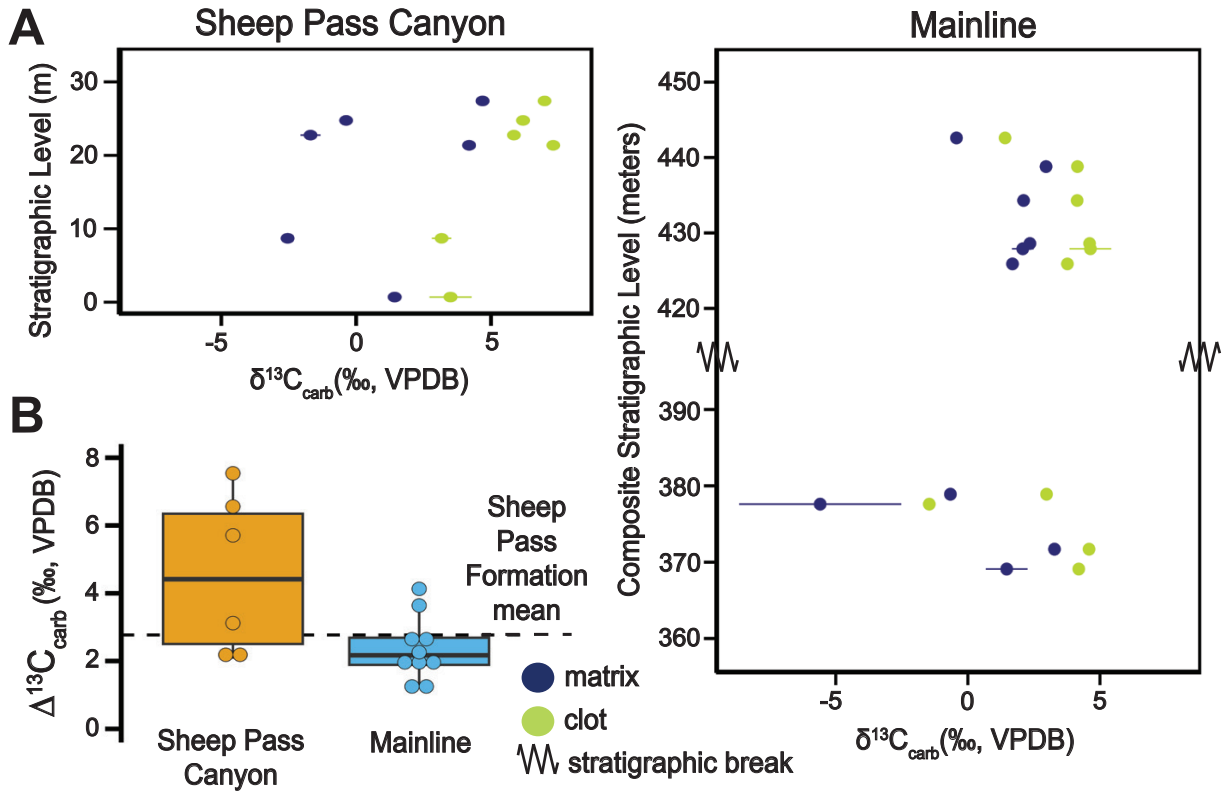

Figure 4-3: A) $\delta^{13}C_{carb}$ values (± two standard deviations) versus stratigraphic level for matrix and clot components in thrombolites and B) box plots of $\Delta^{13}C_{carb}$ ($\delta^{13}C_{matrix-clot}$) in the Sheep Pass Canyon versus Mainline. Plots in (A) are aligned to the same approximate stratigraphic level.

4.4 Results and Interpretation

4.4.1 Consistent $\Delta^{13}C_{carb}$ Values in Ancient Thrombolites

The clots in SPF thrombolites consistently have higher $\delta^{13}C_{carb}$ values than the adjacent matrix; $\Delta^{13}C_{carb}$ values (i.e., the difference between $\delta^{13}C_{matrix}$ and $\delta^{13}C_{clot}$, ± 2 s.d.) range from +1.19‰ (± 0.25) to +7.54‰ (± 0.38) across all samples, with a weighted mean of +2.77‰ (± 0.94, 2 s.e., n=16; Fig. 3; Tables S6 and S7). Following initial data quality control, a Welch's *t*-test confirms that matrix and clot components have statistically different $\delta^{13}C_{carb}$ values (p = 0.0008).

Could these $\Delta^{13}C_{carb}$ values result from two different carbonate pools: the matrix reflecting an older, detrital pool and the clot reflecting the authigenic pool? We examined the stratigraphic variability of $\Delta^{13}C_{carb}$ values to assess this possibility. If the matrix pool represents an older detrital carbonate signal, it should be relatively invariant compared to the authigenic signal preserved in the clots; this scenario would result in $\delta^{13}C_{matrix}$ and $\delta^{13}C_{clot}$ values that do not correlate. In contrast, the $\delta^{13}C_{matrix}$ and $\delta^{13}C_{clot}$ values are highly correlated (Pearson correlation coefficient; r = 0.72) over a > 75 m stratigraphic interval, consistent with both components recording relatively contemporaneous authigenic carbonate precipitation (Fig. S3). Thus, we infer that concurrent shifts in the paired $\delta^{13}C_{matrix}$ and $\delta^{13}C_{clot}$ values record changes in the lake water DIC in response to external forcings (e.g., changes in $\delta^{13}C$ of atmospheric CO_2 over time).

The magnitude of $\Delta^{13}C_{carb}$ values closely resembles $\Delta^{13}C_{modern}$ values from across the globe, including in Pavilion Lake (Canada; Brady et al., 2010, 2014; Belan et al., 2019), Kelly Lake (Canada; Ferris et al., 1997; White et al., 2020), Lake Clifton (Australia; Moore and Burne, 1994; Warden et al., 2016), Lake Van (Turkey; Kempe and Kaźmierczak, 2007), and Lake Alchichica (Mexico; Kaźmierczak et al., 2011). We interpret that SPF $\Delta^{13}C_{carb}$ values preserve a photosynthetic carbon cycling mechanism similar to these modern lakes, whereby $\delta^{13}C_{clot}$ values reflect carbonate precipitation from a microbially-associated, residual ^{13}C-enriched DIC pool compared to carbonate precipitation out of the broader lake water DIC pool ($\delta^{13}C_{matrix}$).

When investigated as two separate sample populations, the range of $\Delta^{13}C_{carb}$ values (± 2 s.d.) in the Sheep Pass Canyon is +2.07‰ (± 0.79) to +7.54‰ (± 0.38) with a weighted mean of 4.39‰ (± 1.92, 2 s.e., n=6), while the Mainline has a $\Delta^{13}C_{carb}$ range between +1.19‰ (± 0.25) and +4.13‰ (± 3.06) and a weighted mean of +2.10‰ (± 0.59, 2 s.e., n=10; Fig. 3). A one-way ANOVA test confirms that Sheep Pass Canyon and Mainline $\Delta^{13}C_{carb}$ values are statistically different (F = 6.989, p = 0.019). The Sheep Pass Canyon section represents a more shoreline-proximal lacustrine setting compared to the Mainline section (Olsen-Valdez et al., 2025). We would expect a shallower setting to be associated with greater photosynthetic carbon cycling within the thrombolite micro-environment. Our observation of higher $\Delta^{13}C_{carb}$ values associated with thrombolites from the shallower portion of the Sheep Pass Basin aligns with this expectation.

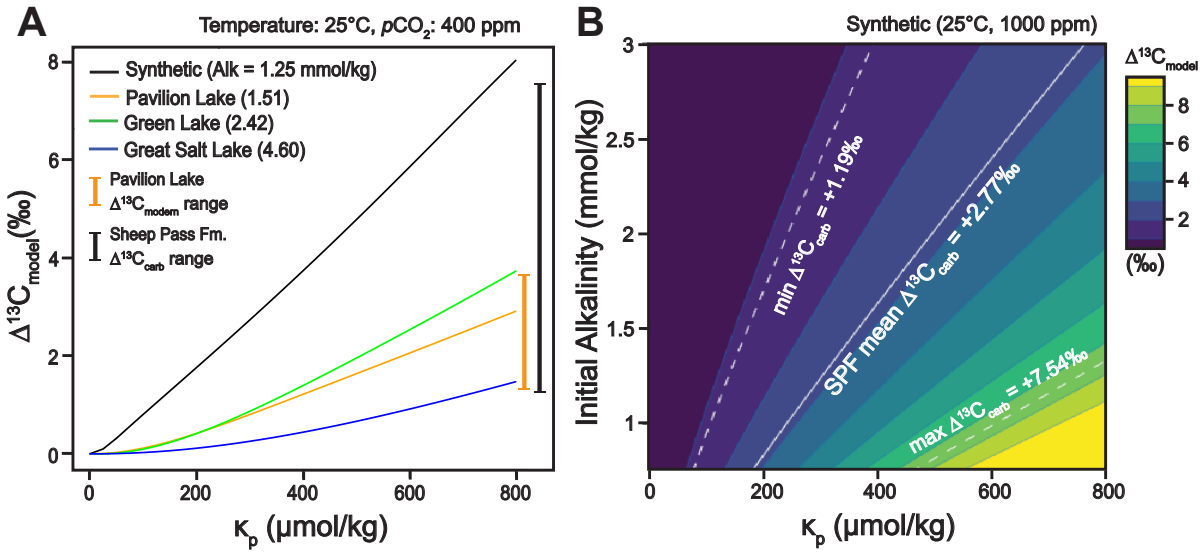

Figure 4-4: A) The effect of productivity (κ_p) on $\Delta^{13}C_{model}$ across the four lake scenarios (alkalinity in parentheses) compared to the $\Delta^{13}C$ range for Pavilion Lake and SPF and B) $\Delta^{13}C_{model}$ over a range of alkalinity and productivity for the Synthetic model scenario, with overlaid mean, minimum, and maximum SPF $\Delta^{13}C_{carb}$ values.

4.4.2 Key Controls on Modeled $\Delta^{13}C$ Values

Each lake had a different range in $\Delta^{13}C_{model}$ values, but for all lakes, the range of $\Delta^{13}C_{model}$ values depended more strongly on productivity and initial lake water chemistry than pCO_2 or temperature (Fig. S4).

Pavilion Lake $\Delta^{13}C_{model}$ values were in good agreement with observed $\Delta^{13}C$ values in Pavilion Lake thrombolites (Fig. 4A; Brady et al., 2010, 2014; Belan et al., 2019). The Pavilion Lake model results overlapped with the range of $\Delta^{13}C_{carb}$ from SPF thrombolites, but could not explain the larger SPF $\Delta^{13}C_{carb}$ values. When we decreased the Pavilion Lake initial alkalinity value ("Synthetic" scenario; Table S5), $\Delta^{13}C_{model}$ values encompassed the full range of SPF $\Delta^{13}C_{carb}$ (Fig. 4A). A sensitivity test exploring the impact of alkalinity and κ_p values on the resulting $\Delta^{13}C_{model}$ values demonstrated that decreasing alkalinity and increasing κ_p led to larger $\Delta^{13}C_{model}$ values (Fig. 4B). Mechanistically, lower [DIC] drives the sensitivity to alkalinity because a smaller DIC pool will experience a greater magnitude of change in both concentration and $\delta^{13}C$ value for a given κ_p value than a larger DIC pool. In most carbonate-producing lakes, total alkalinity primarily comprises carbonate alkalinity. Therefore, the magnitudes of alkalinity and [DIC] are similar and co-vary, and decreasing alkalinity is equivalent to decreasing [DIC]. Using the mean and range of SPF $\Delta^{13}C_{carb}$ values, we constrained the combination of possible alkalinity and κ_p values that likely characterized the Sheep Pass Basin (Fig. 4B).

These results suggest that changes in the magnitude of measured $\Delta^{13}C_{carb}$ values could be leveraged as a proxy for tracking shifts in [DIC] or alkalinity in other ancient

lakes, assuming productivity is relatively constant—an assumption that could be supported by facies analysis. For the SPF thrombolites, we assume a relatively constant productivity within each section given that this facies reflects the same microbial mat depositional process. However, our observation of larger $\Delta^{13}C_{carb}$ values in the Sheep Pass Canyon (Fig. 3) is consistent with higher productivity in a shallower part of the lake (Olsen-Valdez et al., 2025).

4.4.3 Summary and Implications

Fabric-specific sampling of matrix and clot components in ancient SPF thrombolites reveals $\Delta^{13}C$ values similar to those associated with photosynthesis in modern lacustrine thrombolites. Our diurnal carbon cycling model accurately reproduces modern $\Delta^{13}C$ values and, when paired with measured $\Delta^{13}C$ values and informed by detailed facies analysis, can be leveraged as a tool for tracking changes in alkalinity and [DIC], and/or microbialite productivity in ancient systems.

The $\Delta^{13}C_{carb}$ values within some SPF thrombolites are +5‰ or more, highlighting that the full range of $\delta^{13}C_{matrix}$ and $\delta^{13}C_{clot}$ values in a single sample is on par with the range of global marine $\delta^{13}C_{carb}$ across the entire Cenozoic Era (Westerhold et al., 2020). Random or bulk sampling for $\delta^{13}C_{carb}$ that comprises an unknown mix of $\delta^{13}C_{matrix}$ and $\delta^{13}C_{clot}$ values could dampen the local-scale photosynthetic carbon cycling signal, while also skewing the magnitude and significantly increasing the variability of $\delta^{13}C_{carb}$ values ascribed to global-scale carbon cycling.

The characteristics of SPF $\Delta^{13}C_{carb}$ values suggest that, in addition to preservation of a local-scale photosynthetic carbon cycling signal, externally driven, long-term changes in the DIC pool can be resolved using the fabric-specific sampling approach in this study. Changes in the external carbon pool propagate through the lake system, affecting the lake water DIC pool ($\delta^{13}C_{matrix}$ values) and, subsequently, the photosynthetically influenced residual DIC pool in the thrombolite micro-environment ($\delta^{13}C_{clot}$ values).

4.5 Acknowledgements

Sample collection in Nevada and analyses at the University of Colorado Boulder were conducted on the unceded territory of the Western Shoshone, Goshute, Timpanogos, Arapaho, Ute, and Cheyenne peoples. We thank J. Sepúlveda for insight on organic carbon methodology and S. Kashyap, W. Roth, L. van Maldegem, and A. Maloney (CUBES-SIL Core Facility RRID:SCR_019300) for lab assistance. Funding was provided by the National Science Foundation under EAR 1826850 (Snell and Trower) and a Graduate Research Fellowship (Olsen-Valdez).

4.6 Works Cited

Aitken, J.D., 1967, Classification and Environmental Significance of Cryptalgal Limestones and Dolomites, with Illustrations from the Cambrian and Ordovician of Southwestern Alberta: SEPM Journal of Sedimentary Research, v. Vol. 37, doi:10.1306/74D7185C-2B21-11D7-8648000102C1865D.

Andres, M.S., Sumner, D.Y., Reid, R.P., and Swart, P.K., 2006, Isotopic fingerprints of microbial respiration in aragonite from Bahamian stromatolites: Geology, v. 34, p. 973, doi:10.1130/G22859A.1.

Belan, M.A., Brady, A.L., Kim, S.-T., Lim, D.S.S., and Slater, G.F., 2019, Spatial Distribution and Preservation of Carbon Isotope Biosignatures in Freshwater Microbialite Carbonate: ACS Earth and Space Chemistry, v. 3, p. 335–343, doi:10.1021/acsearthspacechem.8b00182.

Brady, A.L., Laval, B., Lim, D.S.S., and Slater, G.F., 2014, Autotrophic and heterotrophic associated biosignatures in modern freshwater microbialites over seasonal and spatial gradients: Organic Geochemistry, v. 67, p. 8–18, doi:10.1016/j.orggeochem.2013.11.013.

Brady, A.L., Slater, G.F., Omelon, C.R., Southam, G., Druschel, G., Andersen, D.T., Hawes, I., Laval, B., and Lim, D.S.S., 2010, Photosynthetic isotope biosignatures in laminated micro-stromatolitic and non-laminated nodules associated with modern, freshwater microbialites in Pavilion Lake, B.C.: Chemical Geology, v. 274, p. 56–67, doi:10.1016/j.chemgeo.2010.03.016.

Breitbart, M., Hoare, A., Nitti, A., Siefert, J., Haynes, M., Dinsdale, E., Edwards, R., Souza, V., Rohwer, F., and Hollander, D., 2009, Metagenomic and stable isotopic analyses of modern freshwater microbialites in Cuatro Ciénegas, Mexico: Environmental Microbiology, v. 11, p. 16–34, doi:10.1111/j.1462-2920.2008.01725.x.

Buongiorno, J., Gomez, F.J., Fike, D.A., and Kah, L.C., 2019, Mineralized microbialites as archives of environmental evolution, Laguna Negra, Catamarca Province, Argentina: Geobiology, v. 17, p. 199–222, doi:10.1111/gbi.12327.

Burne, R.V., and Moore, L.S., 1987, Microbialites: Organosedimentary Deposits of Benthic Microbial Communities: PALAIOS, v. 2, p. 241, doi:10.2307/3514674.

Druschke, P., Hanson, A.D., and Wells, M.L., 2009, Structural, stratigraphic, and geochronologic evidence for extension predating Palaeogene volcanism in the Sevier hinterland, east-central Nevada: International Geology Review, v. 51, p. 743–775, doi:10.1080/00206810902917941.

Ferris, F.G., Thompson, J.B., and Beveridge, T.J., 1997, Modern Freshwater Microbialites from Kelly Lake, British Columbia, Canada: PALAIOS, v. 12, p. 213, doi:10.2307/3515423.

Fogret, L., Sansjofre, P., and Lalonde, S.V., 2024, Geochemistry of carbonate microbialites through time and space: Insights from the microbialite collection of the Muséum National d'Histoire Naturelle (MNHN), France: Chemical Geology, v. 662, p. 122239, doi:10.1016/j.chemgeo.2024.122239.

Fouch, T.D., 1979, Character and paleogeographic distribution of Upper Cretaceous (?) and Paleogene nonmarine sedimentary rocks in East-central Nevada: in Pacific Coast Paleogeography Symposium 3: Cenozoic Paleogeography of the Western United States, p. 97–111.

Geyman, E.C., and Maloof, A.C., 2019, A diurnal carbon engine explains ^{13}C-enriched carbonates without increasing the global production of oxygen: Proceedings of the National Academy of Sciences, v. 116, p. 24433–24439, doi:10.1073/pnas.1908783116.

Huang, X., Li, D., Zhang, X., Xu, Y., Sun, L., Li, M., and Shen, Y., 2022, High resolution C-isotopic data from microbialites in the aftermath of the end-Permian mass extinction in South China: Frontiers in Earth Science, v. 10, p. 914432, doi:10.3389/feart.2022.914432.

Ingalls, M., Frantz, C.M., Snell, K.E., and Trower, E.J., 2020, Carbonate facies-specific stable isotope data record climate, hydrology, and microbial communities in Great Salt Lake, UT: Geobiology, v. 18, p. 566–593, doi:10.1111/gbi.12386.

Kaźmierczak, J., Kempe, S., Kremer, B., López-García, P., Moreira, D., and Tavera, R., 2011, Hydrochemistry and microbialites of the alkaline crater lake Alchichica, Mexico: Facies, v. 57, p. 543–570, doi:10.1007/s10347-010-0255-8.

Kempe, S., and Kaźmierczak, J., 2007, Hydrochemical Key to the Genesis of Calcareous Nonlaminated and Laminated Cyanobacterial Microbialites, *in* Seckbach, J. ed., Algae and Cyanobacteria in Extreme Environments, Dordrecht, Springer Netherlands, Cellular Origin, Life in Extreme Habitats and Astrobiology, v. 11, p. 239–264, doi:10.1007/978-1-4020-6112-7_13.

Kennard, J.M., and James, N.P., 1986, Thrombolites and Stromatolites: Two Distinct Types of Microbial Structures: PALAIOS, v. 1, p. 492, doi:10.2307/3514631.

Leapaldt, H.C., Frantz, C.M., Olsen-Valdez, J., Snell, K.E., Trower, E.J., and Ingalls, M., 2024, Primary to post-depositional microbial controls on the stable and clumped isotope record of shoreline sediments at Fayetteville Green Lake: Geobiology, v. 22, p. e12609, doi:10.1111/gbi.12609.

Lewis, E., and Wallace, D.W.R., 1998, Basic program for CO2 system in seawater: Oak Ridge National Laboratory ORNL/CDIAC-105.

Lim, D.S.S. et al., 2009, Limnology of Pavilion Lake, B. C., Canada Characterization of a microbialite forming environment: Fundamental and Applied Limnology, v. 173, p. 329–351, doi:10.1127/1863-9135/2009/0173-0329.

McConnaughey, T.A., Burdett, J., Whelan, J.F., and Paull, C.K., 1997, Carbon isotopes in biological carbonates: Respiration and photosynthesis: Geochimica et Cosmochimica Acta, v. 61, p. 611–622, doi:10.1016/S0016-7037(96)00361-4.

Mei, M., Latif, K., Mei, C., Gao, J., and Meng, Q., 2020, Thrombolitic clots dominated by filamentous cyanobacteria and crusts of radio-fibrous calcite in the Furongian Changshan Formation, North China: Sedimentary Geology, v. 395, p. 105540, doi:10.1016/j.sedgeo.2019.105540.

Merz, M.U.E., 1992, The biology of carbonate precipitation by cyanobacteria: Facies, v. 26, p. 81–101, doi:10.1007/BF02539795.

Moore, L.S., and Burne, R.V., 1994, The Modern Thrombolites of Lake Clifton, Western Australia, *in* Bertrand-Sarfati, J. and Monty, C. eds., Phanerozoic Stromatolites II, Dordrecht, Springer Netherlands, p. 3–29, doi:10.1007/978-94-011-1124-9_1.

Olsen-Valdez, J., Widlansky, S., Trower, E., Snell, K., and Clyde, W., 2025, Carbonates and microbialites record a dynamic lake basin evolution in the Late Cretaceous to Eocene Sheep Pass Formation, Nevada, USA: Sedimentology, p. sed.13264, doi:10.1111/sed.13264.

Parkhurst, D.L., and Appelo, C.A., 2013, Description of input and examples for PHREEQC version 3—a computer program for speciation, batch-reaction, one-dimensional transport, and inverse geochemical calculations: US Geological Survey Techniques and Methods 6-A43, 497 p., https://pubs.usgs.gov/tm/06/a43/.

Preuß, A., Schauder, R., Fuchs, G., and Stichler, W., 1989, Carbon Isotope Fractionation by Autotrophic Bacteria with Three Different C0 $_2$ Fixation Pathways: Zeitschrift für Naturforschung C, v. 44, p. 397–402, doi:10.1515/znc-1989-5-610.

Sumner, D.Y., 2001, Microbial Influences on Local Carbon Isotopic Ratios and Their Preservation in Carbonate: Astrobiology, v. 1, p. 57–70, doi:10.1089/153110701750137431.

Trower, E.J., Hibner, B.M., Lincoln, T.A., Dodd, J.E., Hagen, C.J., Cantine, M.D., and Gomes, M.L., 2024, Revisiting Elevated δ^{13}C Values of Sediment on Modern Carbonate Platforms: Geophysical Research Letters, v. 51, p. e2023GL107703, doi:10.1029/2023GL107703.

Warden, J.G., Casaburi, G., Omelon, C.R., Bennett, P.C., Breecker, D.O., and Foster, J.S., 2016, Characterization of Microbial Mat Microbiomes in the Modern Thrombolite Ecosystem of Lake Clifton, Western Australia Using Shotgun Metagenomics: Frontiers in Microbiology, v. 7, doi:10.3389/fmicb.2016.01064.

Westerhold, T. et al., 2020, An astronomically dated record of Earth's climate and its predictability over the last 66 million years: Science, v. 369, p. 1383–1387, doi:10.1126/science.aba6853.

White, R.A., Soles, S.A., Brady, A.L., Southam, G., Lim, D.S.S., and Slater, G.F., 2020, Biosignatures Associated with Freshwater Microbialites: Life, v. 10, p. 66, doi:10.3390/life10050066.

4.7 Supplemental Materials

This supplemental material document includes:
1) Summary of modern thrombolite environments with documented $\delta^{13}C_{carb}$ offsets (i.e., $\Delta^{13}C_{modern}$) (Table S1)
2) Additional sample information and data (Tables S2-S8)
3) Figures S1-S4, including:
    -All hand-sample images, including those culled after data quality control (Figure S1)
    -$\delta^{13}C_{carb}$ values by section for matrix, clot, and "mixed" component (Figure S2)
    -Covariation of matrix $\delta^{13}C_{carb}$ values vs clot $\delta^{13}C_{carb}$ values (Figure S3)
    -Model sensitivity test plots for $\Delta^{13}C_{model}$ values given a range of productivity, pCO2, and temperatures across all three modern analog initial water chemistry scenarios (Figure S4)
4) Extended methods, including:
    -Carbonate $\delta^{13}C$ analyses and averaging
    -Organic $\delta^{13}C$ sample preparation
    -Organic $\delta^{13}C$ analyses
    -Diurnal carbon cycling model parameterization
    -Stratigraphic level corrections in the Sheep Pass Canyon
5) Extended results, including:
    -Data quality control in carbonate $\delta^{13}C$ values

In addition to this document, other supplemental information within the Open Science Framework repository (https://doi.org/10.17605/OSF.IO/U2687) includes:
1) Data spreadsheets, an R Project, and an R markdown file for all $\delta^{13}C_{carb}$, $\Delta^{13}C_{carb}$, and $\delta^{13}C_{org}$ averaging and plotting
2) An R Project and R script to run the diurnal carbon cycling model version used in this study
    1) Tables S1 to S7
    2) Figure S1 and S2
    3) Extended methods
    4) Extended results

Site	Microbialite Type	Magnitude of carbonate ^{13}C-enrichment compared to predicted equilibrium value based on measured $\delta^{13}C_{DIC}$ (‰)	Water depth (meters)	Citation
Pavilion Lake, British Columbia	Porous and denser microbialites	Up to +2.4‰	6m, 11m, 20m, and 26m	Brady et al., 2014; Organic Geochemistry
Pavilion Lake, British Columbia	Carbonate nodules on microbialite surfaces	+1.3‰ to +3.6‰	10m, 18m, and 21m	Brady et al.., 2010; Chemical Geology
Pavilion Lake, British Columbia	Microbialite surface nodules	Up to +2.6‰	10m, 18m, 21m, 26m, and 27m	Belan et al., 2019; American Chemical Society
Kelly Lake, British Columbia	Microbialites	0‰ up to +3.6‰	11m, 14m, 20m, and 26m	White et al., 2020; Life MDPI
Kelly Lake, British Columbia	Thrombolitic crusts and stromatolites	+3.6‰ to +4.2‰	0.5 m, up to 20 m	Ferris et al., 1997; PALAIOS
Lake Clifton, Western Australia	Thrombolites	+3.5‰ to +6.8‰ (relative to max equilibrium value rather than mean)	<0.5m	Warden et al., 2016; Frontiers in Microbiology
Lake Clifton, Western Australia	Thrombolites	Measured $\delta^{13}C_{DIC}$ value of -7.0‰ versus measured $\delta^{13}C_{carb}$ of +7.1‰	<0.5m	Moore and Burne, 1994; *Phanerozoic Stromatolites*
Lake Van, Turkey	Microbialite crust, thrombolitic and micritic	+2.5‰ to +4‰ (relative to mean $\delta^{13}C_{DIC}$ value of +2.70‰ rather than predicted equilibrium value)	Shallow water	Kempe and Kazmierczak, 2007; *Algae and Cyanobacteria in Extreme Environments*
Lake Alchichica, Mexico	Microbialites, thrombolitic microfabrics	+3.5‰ to +4.5‰ (relative to measured $\delta^{13}C_{DIC}$ values)	4m, 8m, 14m	Kazmierczak et al., 2011; *Facies*

Table 4-S1: Compiled data of modern microbialite-forming environments with documented microbialite carbonate ^{13}C-enriched values compared to those predicted for abiotic precipitation in equilibrium with the dissolved inorganic carbon pool. See bibliography for full references.

Sample ID	Coordinates	Transect	Member	Composite Stratigraphic Level (m)	Facies	Thin Section
SPB19-ML04	N 38.72525, W 114.97224	ML	B	369.1	Micro-clotted Microbial Boundstone	X
SPB19-ML07	N 38.72527, W 114.97223	ML	B	371.7	Thrombolite Boundstone (small clots)	
SPB19-ML08	N 38.72528, W 114.97221	ML	B	372.9	Thrombolite Boundstone (framework of clots)	X
SPB19-ML11	N 38.72545, W 114.97222	ML	B	377.6	Thrombolite Boundstone (small clots)	X
SPB19-ML12	N 38.72546, W 114.97221	ML	B	378.9	Thrombolite Boundstone (large clots)	X
SPB19-ML31	N 38.72558, W 114.97162	ML	B	425.9	Thrombolite Boundstone (small clots)	X
SPB19-ML32	N 38.72561,	ML	B	427.9	Thrombolite Boundstone (large clots)	

	W 114.97164					
SPB19-ML33	N 38.72570, W 114.97164	ML	B	428.6	Thrombolite Boundstone (framework of clots)	X
SPB19-ML35	N 38.72565, W 114.97157	ML	B	434.3	Thrombolite Boundstone (small clots)	
SPB19-ML36	N 38.72571, W 114.97152	ML	B	438.8	Thrombolite Boundstone (large clots)	X
SPB19-ML37	N 38.72576, W 114.97151	ML	B	442.6	Thrombolite Boundstone (small clots)	
SPB19-ML38	N 38.72580, W 114.97150	ML	B	445.9	Thrombolite Boundstone (small clots)	
SPB20-SPC31	N 38.73809, W 114.95866	SPC	B	546	Thrombolite Boundstone (large clots)	X
				Measured Level (m)		
SPB20-SPC36	N 38.73737, W 114.95876	SPC (Member B Slope)	B	0.70	Thrombolite Boundstone (large clots)	X
SPB20-SPC38	N 38.73733, W 114.95847	SPC (Member B Slope)	B	8.70	Thrombolite Boundstone (large clots)	X
SPB20-SPC39	N 38.73716, W 114.95786	SPC (Member B Slope)	B	22.75	Thrombolite Boundstone (small clots)	
SPB20-SPC40	N 38.73716, W 114.95786	SPC (Member B Slope)	B	24.75	Thrombolite Boundstone (large clots)	
SPB20-SPC41	N 38.73721, W 114.95785	SPC (Member B Slope)	B	27.40	Thrombolite Boundstone (large clots)	X

Table 4-S2: Summary of sample ID, GPS coordinates, measured transect, member, stratigraphic level in meters (composite or measured), and facies characterization for SPF thrombolite samples included in this study. Note that SPC and SPC-Member B Slope samples were all collected from the Sheep Pass Canyon section. The corrected meter level for SPB20-SPC31 is discussed in the methods text below.

Sample ID	Bulk weight percent organic carbon (%)	Bulk weight percent carbonate (%)
SPB19-ML04	2.28	37.34
SPB19-ML07	2.34	38.69
SPB19-ML33	1.65	40.76
SPB20-SPC31	1.67	40.56
SPB20-SPC38	1.52	39.76

Table 4-S3: Bulk weight percent organic carbon and bulk weight percent carbonate compositions of all samples analyzed for $\delta^{13}C_{org}$.

Sample ID	Average $\delta^{13}C_{org}$ (total lipid extract, brick blank corrected, ‰, VPDB ± 2 s.e.)	Average $\delta^{13}C_{org}$ (acidified carbonate, ‰, VPDB ± 2 s.e.)	$\delta^{13}C_{carb}$ (matrix, ‰, VPDB ± 2 s.d.)	Absolute difference between $\delta^{13}C_{carb}$ (matrix) and acidified carbonate $\delta^{13}C_{org}$ values (‰, VPDB ± 2 s.d.)
SPB19-ML04	-28.39 ± 0.14	-24.40 ± 0.02	+1.47 ± 0.79	25.87 ± 0.80
SPB19-ML07	-31.49 ± 0.19	-27.81 ± 0.12	+3.28 ± 0.09	31.09 ± 0.23
SPB19-ML33	-30.03 ± 0.13	-26.81 ± 0.07	+2.35 ± 0.17	29.16 ± 0.21
SPB20-SPC31	-28.69 ± 0.15	-26.62 ± 0.09	+4.19 ± 0.14	30.81 ± 0.22
SPB20-SPC38	-29.17 ± 0.20	-26.74 ± 0.05	-2.54 ± 0.14	24.20 ± 0.17
			Average Value	**28.23 ‰ ± 2.74 (2 s.e.)**

Table 4-S4: Organic carbon $\delta^{13}C$ for total lipid extracts and acidified carbonates for the sample subset. $\delta^{13}C_{carb}$ values for matrix components of each sample in the subset are included and used for calculation of $\Delta^{13}C$, the absolute difference between the $\delta^{13}C$ of the acidified carbonate and the carbonate matrix component, which also has a calculated mean across all samples.

Lake	Location	$\delta^{13}C_{DIC}$ (‰)	$\delta^{13}C_{carb}$ (‰)	Alkalinity (mmol/kg)	Ca (mmol/kg)	Mg (mmol/kg)	Na (mmol/kg)	K (mmol/kg)	Cl (mmol/kg)	SO4 (mmol/kg)	Water density (kg/m³)	Reference
Fayetteville Green Lake	NY, USA	-7.0	-2.4	2.42	9.8	2.5	1.2	0.1	0.6	9.8	1000	Leapaldt et al., 2024; Geobiology
Great Salt Lake	UT, USA	-0.7	4.0	4.60	4.5	156	1433	58	1659	78	1080	Ingalls et al., 2020; Geobiology
Pavilion Lake	British Columbia, Canada	0*	0.8^	1.51	1.1	0.8	0.3	0.1	0.1	0.1	1000	Lim et al., 2019; Fundamental and Applied Limnology
Synthetic Lake	NA	0*	0.8^	1.25	1.1	0.8	0.3	0.1	0.1	0.1	1000	See Methods

Table 4-S5: Initial water chemistry inputs used in the diurnal carbon cycling model scenarios. * Indicates that the $\delta^{13}C_{DIC}$ value was not reported, thus 0‰ was chosen for simplicity. ^ indicates that the $\delta^{13}C_{carb}$ value was not reported, thus we chose the average $\delta^{13}C_{carb}$ (0.8‰) between those reported from Fayetteville Green Lake (-2.4‰) and Great Salt Lake (4.0‰).

Transect	Sample ID	Mean $\delta^{13}C_{clot}$	Mean $\delta^{13}C_{matrix}$	$\delta^{13}C_{clot}$ 1 s.d.	$\delta^{13}C_{clot}$ 2 s.d.	$\delta^{13}C_{matrix}$ 1 s.d.	$\delta^{13}C_{matrix}$ 2 s.d.	Clot N	Matrix N	$\Delta^{13}C_{carb}$ ($\delta^{13}C_{matrix-clot}$)	$\Delta^{13}C_{carb}$ 1 s.d.	$\Delta^{13}C_{carb}$ 2 s.d.
ML	SPB19-ML04	+4.20	+1.47	0.05	0.09	0.40	0.79	1	2	+2.73	0.40	0.81
ML	SPB19-ML07	+4.59	+3.28	0.05	0.09	0.05	0.09	1	1	+1.31	0.07	0.14
ML	*SPB19-ML08*	-0.23	-0.28	0.04	0.08	0.31	0.63	1	2	+0.05	0.31	0.63
ML	SPB19-ML11	-1.46	-5.59	0.05	0.09	1.53	3.07	1	2	+4.13	1.53	3.06
ML	SPB19-ML12	+2.98	-0.66	0.05	0.09	0.05	0.09	1	1	+3.64	0.07	0.14
ML	SPB19-ML31	+3.77	+1.69	0.09	0.17	0.09	0.17	1	1	+2.08	0.13	0.25
ML	SPB19-ML32	+4.64	+2.08	0.40	0.79	0.20	0.41	2	2	+2.56	0.45	0.89
ML	SPB19-ML33	+4.61	+2.35	0.01	0.02	0.09	0.17	2	1	+2.26	0.09	0.18
ML	SPB19-ML35	+4.14	+2.11	0.06	0.12	0.09	0.17	1	1	+2.03	0.11	0.22
ML	SPB19-ML36	+4.15	+2.96	0.09	0.17	0.09	0.17	1	1	+1.19	0.13	0.25
ML	SPB19-ML37	+1.41	-0.43	0.01	0.02	0.03	0.06	1	1	+1.84	0.03	0.06
ML	*SPB19-ML38*	+1.19	+2.02	0.07	0.15	0.07	0.15	1	1	-0.83	0.10	0.20
SPC	SPB20-SPC31	+7.31	+4.19	0.07	0.14	0.07	0.14	1	1	+3.12	0.10	0.20
SPC	SPB20-SPC36	+3.50	+1.43	0.39	0.78	0.07	0.14	2	1	+2.07	0.40	0.79
SPC	SPB20-SPC38	+3.17	-2.54	0.18	0.36	0.07	0.14	1	1	+5.71	0.19	0.39
SPC	SPB20-SPC39	+5.85	-1.69	0.06	0.12	0.18	0.37	1	2	+7.54	0.19	0.38
SPC	SPB20-SPC40	+6.19	-0.37	0.10	0.19	0.07	0.15	2	1	+6.56	0.12	0.24
SPC	SPB20-SPC41	+6.99	+4.69	0.05	0.11	0.07	0.14	1	1	+2.30	0.09	0.17

Table 4-S6: Mean carbonate $\delta^{13}C$ values for matrix and clot components, and calculated $\Delta^{13}C_{carb}$ values between $\delta^{13}C_{matrix}$ and $\delta^{13}C_{clot}$ for all samples in this study. Note that samples SPB19-ML08 and SPB19-ML38 (italicized) are excluded from calculations and discussion in the main manuscript; see explanation in the extended methods below. All isotope values are reported as permil values, relative to VPDB (‰, VPDB).

Section	Mainline (ML)	Sheep Pass Canyon (SPC)	Sheep Pass Formation (SPF)
N	10	6	16
Min $\delta^{13}C_{clot}$	-1.46	+3.17	-1.46
Max $\delta^{13}C_{clot}$	+4.64	+7.31	+7.31
Med $\delta^{13}C_{clot}$	+4.14	+6.02	+4.18
Mean $\delta^{13}C_{clot}$	+3.30	+5.50	+4.13
Weighted Mean $\delta^{13}C_{clot}$	+3.04	+6.23	+3.60
$\delta^{13}C_{clot}$ 2 s.e.	1.23	1.44	1.06
Min $\delta^{13}C_{matrix}$	-5.59	-2.54	-5.59
Max $\delta^{13}C_{matrix}$	+3.28	+4.69	+4.69
Med $\delta^{13}C_{matrix}$	+1.89	+0.53	+1.58
Mean $\delta^{13}C_{matrix}$	+0.93	+0.95	+0.94
Weighted Mean $\delta^{13}C_{matrix}$	+1.19	+1.25	+1.21
$\delta 13C_{matrix}$ 2 s.e.	1.66	2.47	1.34
Mean $\Delta^{13}C_{carb}$ ($\delta^{13}C_{matrix-clot}$)	+2.38	+4.55	+3.19
Weighted Mean $\Delta^{13}C_{carb}$	+2.10	+4.39	+2.77
$\Delta^{13}C_{carb}$ 2 s.e.	0.59	1.92	0.94

Table 4-S7: Mean carbonate $\delta^{13}C$ values for the Mainline, Sheep Pass Canyon, and across the whole Sheep Pass Formation type section. All isotope values are reported as permil values, relative to VPDB (‰, VPDB). Note that values reflect means after excluding SPB19-ML08 and SPB19-ML38 in the data quality control step.

Section	Sample ID	Component	N	Mean $\delta^{13}C_{carb}$	$\delta^{13}C_{carb}$ s.e.	$\delta^{13}C_{carb}$ 2 s.e.
ML	SPB19-ML37	Mixed	1	+1.08	0.09	0.17
ML	SPB19-ML38	Mixed	1	+1.05	0.09	0.17
SPC	SPB20-SPC39	Mixed	1	+1.17	0.07	0.14
SPC	SPB20-SPC40	Mixed	1	+2.15	0.07	0.14

Table 4-S8: Mean carbonate $\delta^{13}C$ values for samples in which the mixed component was analyzed. Note that mixed components are not discussed in the main manuscript. All isotope values are reported as permil values, relative to VPDB (‰, VPDB).

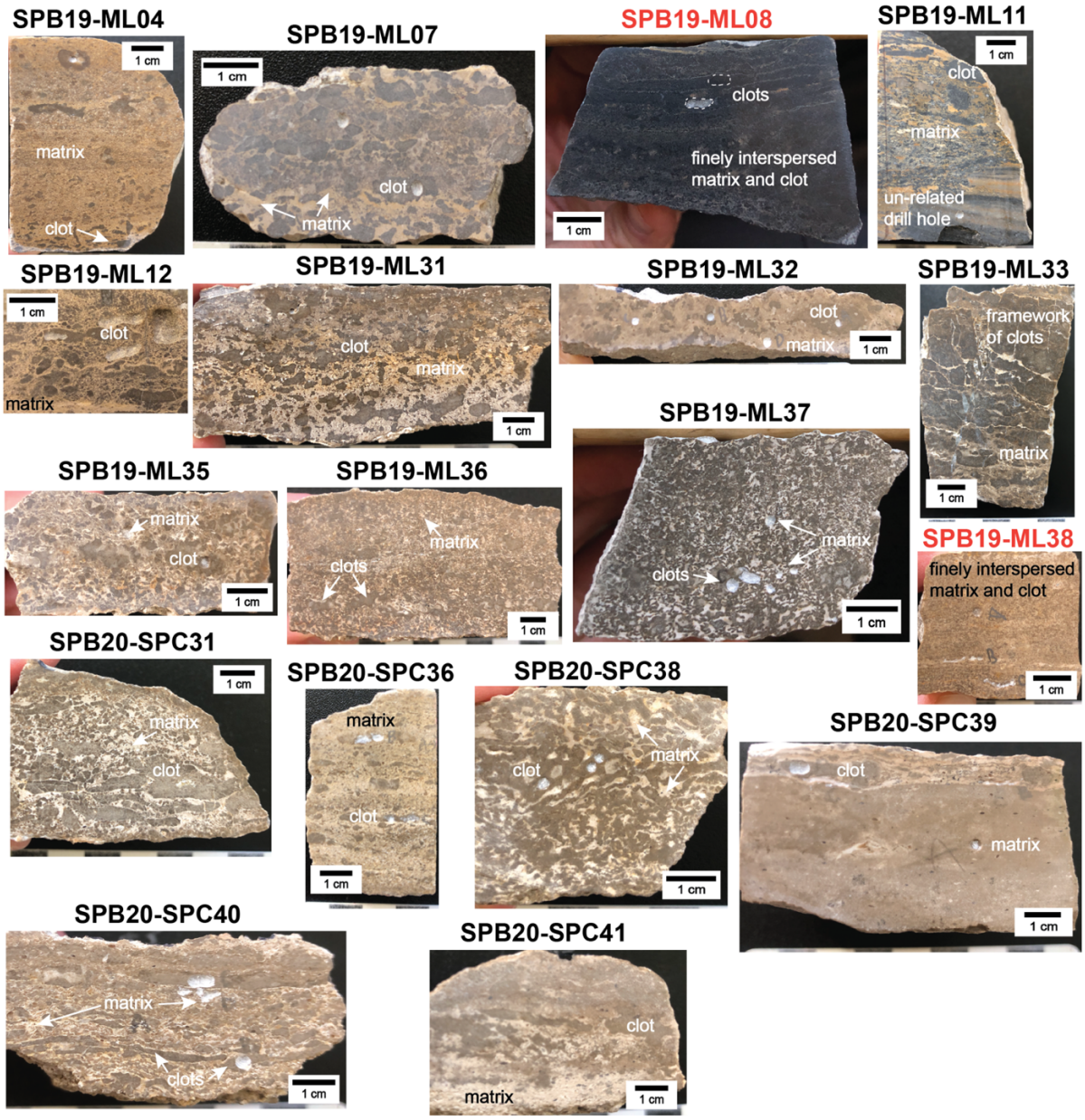

Figure 4-S1: Polished hand sample surfaces for all thrombolite boundstones included in the main data set. Note that SPB19-ML08 and SPB19-ML38 (red labels) have finely interspersed matrix and clot textures that did not allow for discrete sampling of the endmember components.

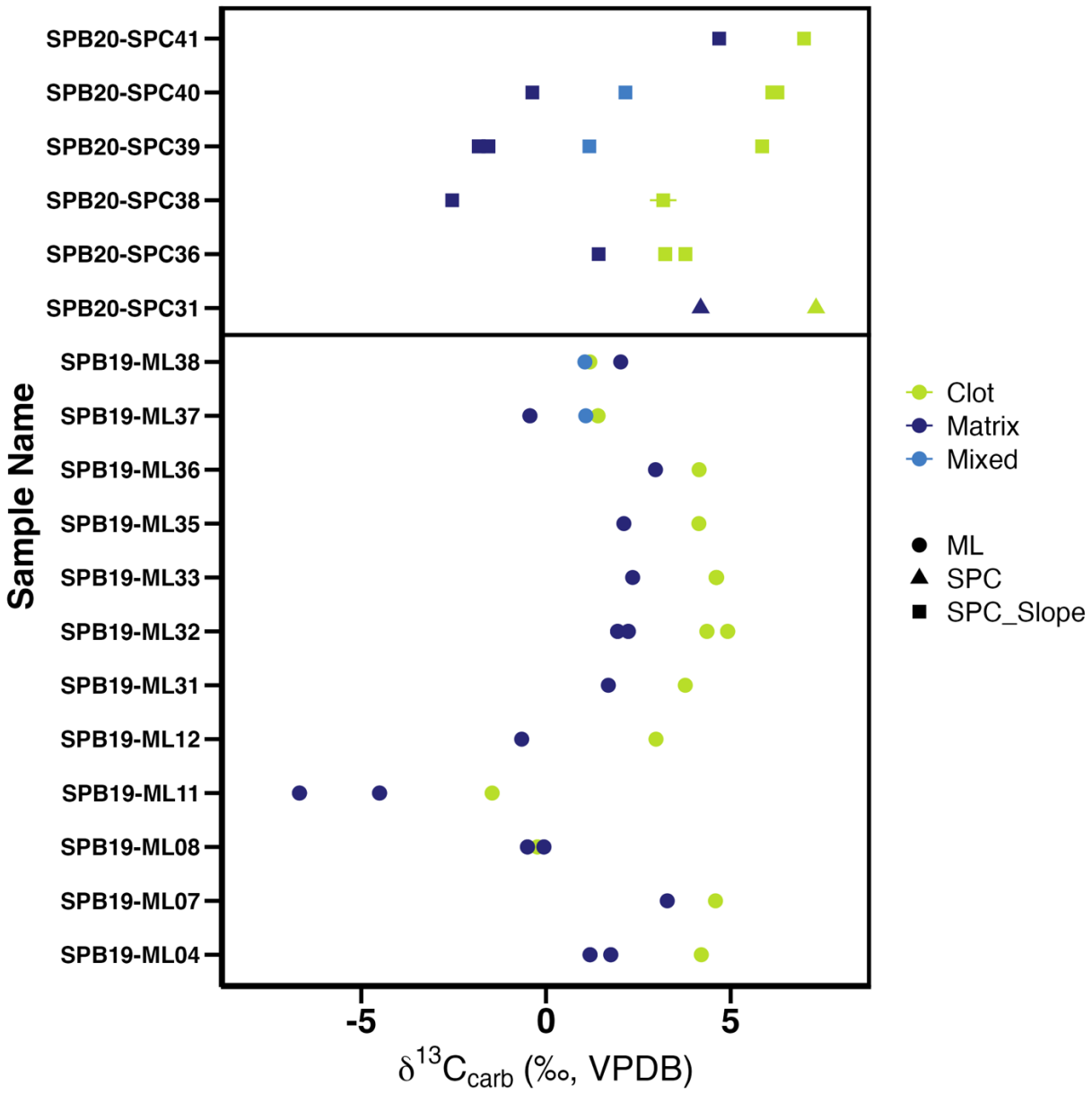

Figure 4-S2: $\delta^{13}C_{carb}$ values of matrix and clot components for each sample. Note that some samples have mixed components as well. Data point shapes reflect measured section; SPC and SPC_Slope samples are both from the Sheep Pass Canyon measured section. Horizontal black line separates Mainline data (below) from Sheep Pass Canyon data (above). Data point error bars reflect two standard deviations (symbols without visible error bars have uncertainties smaller than the size of data points). Note that the y-axis is not necessarily correlated to stratigraphic level.

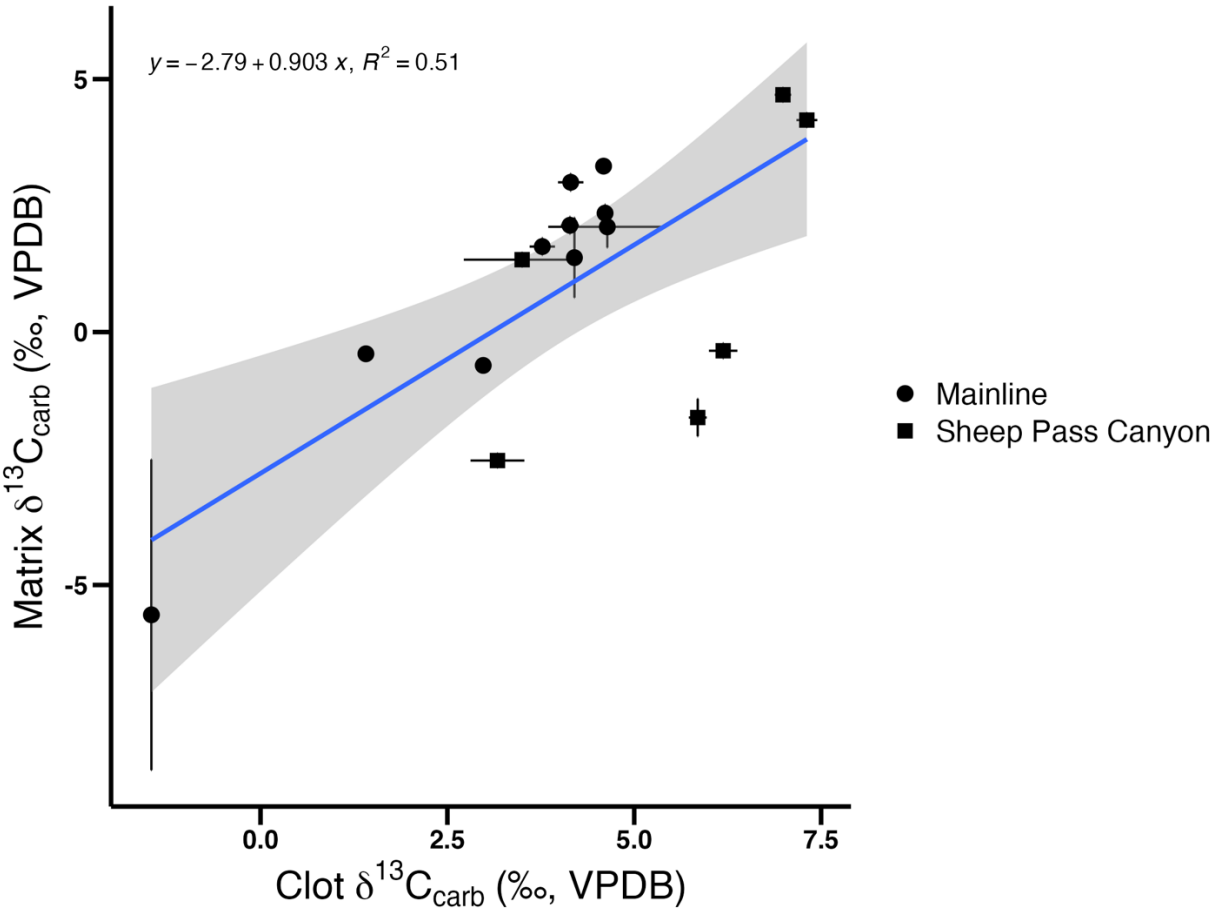

Figure 4-S3: Covariation of matrix $\delta^{13}C_{carb}$ values versus clot $\delta^{13}C_{carb}$ values across all Sheep Pass Formation samples. Data point shape reflects stratigraphic section (note that SPC and SPC_Slope samples were both included in the Sheep Pass Canyon section). Data point error bars reflect two standard deviations (symbols without visible error bars have uncertainties smaller than size of data points). In the top right corner are the equation and R^2 value of the best fit line (blue) with 95% confidence interval (gray).

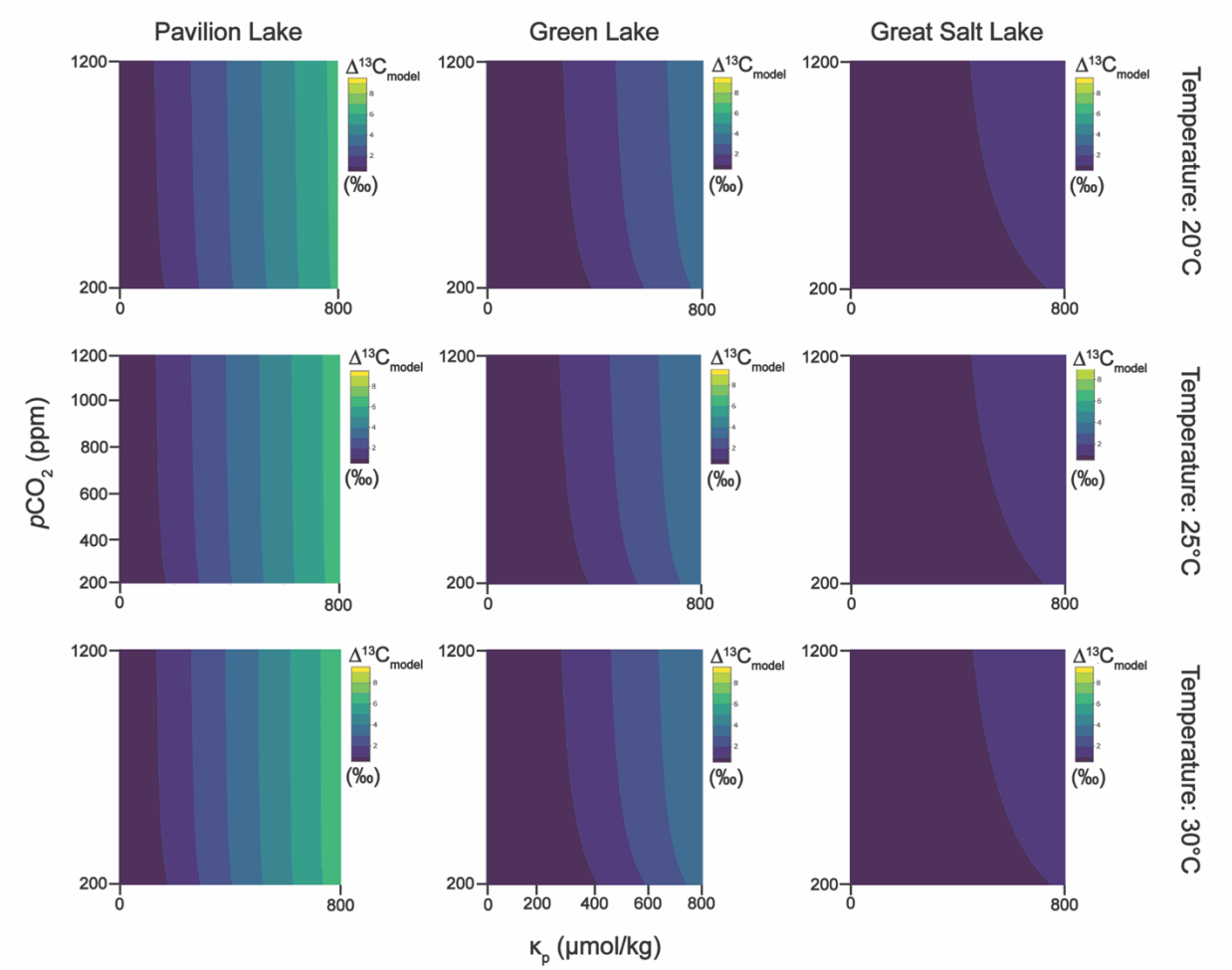

Figure 4-S4: Contour plots of $\Delta^{13}C_{model}$ across a range of pCO_2 (200-1200 ppm), productivity (κ_p, 0–800 µmol/kg) and temperature (20°C, 25°C, and 30°C) for the Pavilion Lake, Green Lake, and Great Salt Lake initial water chemistry scenarios. Note that $\Delta^{13}C_{model}$ depends most strongly on productivity, while pCO_2 and temperature played a more minimal role.

S.4.1 Extended Methods

S.4.1.1 Carbonate $\delta^{13}C$ Analyses and Averaging

Thrombolite boundstone samples were powdered for both matrix and clot components on cut and polished sample surfaces with a fine, diamond-coated bit attached to a Dremel tool. Approximately 120-150-µg-sized carbonate sample and

standard aliquots were placed in 12mL Labco Exetainer vials with screw-top septa caps. The vials were purged with ultra-high purity Helium gas for 10 minutes to displace atmosphere. Powders were then digested in 70°C, 105%-110% orthophosphoric acid to release CO_2 for analysis on a Thermo Scientific Gasbench II coupled to a Thermo Delta V continuous flow isotope ratio mass spectrometer at the University of Colorado Boulder Stable Isotope Laboratory (CUBES-SIL; RRID:SCR_019300). Several replicate carbonate standard measurements (USGS44, IAEA-603, NBS18, Icelandic Spar (HIS), and an in-house marble standard, CU YULE) yielded an analytical precision of ± 0.1‰ or better. Raw values of all analyses were corrected using in-house CUBES-SIL R scripts that employed the Isoreader (Kopf et al., 2021) and Tidyverse R packages; the data reduction and quality control process included first evaluating and then correcting standard values for linearity and drift effects, if present. Corrected standard values were then used in a scale correction applied to all data using CU YULE, HIS, and either IAEA-603 or NBS18 (two runs also included USGS44), following the recommendations of Qi et al. (2020).

A subset of samples had replicates run to investigate the analytical reproducibility of $\delta^{13}C_{carb}$ values from the same aliquot of sample powder. These replicates reproduced within 0.06‰ (1 s.d.) of each other, which is within the long-term analytical reproducibility of the instrument. For this subset of samples, standard deviations were calculated based on all analytical replicates. Samples without analytical replicates inherited the run-specific uncertainty based on the scale correction for each run.

Another subset of samples was used to investigate the range of $\delta^{13}C_{matrix}$ and $\delta^{13}C_{clot}$ values preserved across a samples' surface. These replicates were kept separate in the analytical replicate averaging step (because they reflect distinct sample powder aliquots) but were averaged together when calculating mean $\delta^{13}C_{matrix}$ and $\delta^{13}C_{clot}$ values by sample (Table S6). Because some samples had average $\delta^{13}C_{matrix}$ and $\delta^{13}C_{clot}$ values based on single replicates, sample-specific $\Delta^{13}C_{carb}$ values, as well as all sample-specific uncertainties were calculated with respect to two standard deviations. Conversely, uncertainty associated with mean and weighted mean $\delta^{13}C_{matrix}$, $\delta^{13}C_{clot}$, and $\Delta^{13}C_{carb}$ values across the Mainline section (n=10), Sheep Pass Canyon section (n=6), and whole Sheep Pass Formation type-section (n=16) were calculated with respect to two standard errors of the mean.

S.4.1.2 Organic $\delta^{13}C$ Sample Preparation

Sample preparation techniques were modified from French et al. (2015) and in-house methods developed by Kaitlin Rempfert, with additional modification through guidance from Srishti Kashyap. Sample exteriors were first rinsed in 70% ethanol (EtOH) and Milli-Q water and then left to air dry. Prior to first use and between each sample cutting, the saw blade was solvent cleaned using 1-2x rinses of methanol (MeOH; Fisher Chemical Methylene Chloride Optima ®) followed by dicholormethane (DCM; Fisher Chemical Optima ® LC/MS). All surfaces around the saw apparatus were sprayed with ethanol, and then wiped with alcohol wipes and kimwipes. The top surface of the saw apparatus (surrounding the blade slit) was

covered in combusted (450°C, 8 hrs) aluminum foil. The saw apparatus was filled with fresh Milli-Q water before each sample was cut. Unanalyzed combusted (450°C, 8 hrs) clay brick pieces were sawed into to remove contaminating particles from the blade as the last step in the cleaning protocol.

Between 3mm and 1cm was pared off each exterior side of the samples using a Hi-Tech Diamond thin notched diamond saw blade (Product ID: SB06-015) on a Hi-Tech Diamond 6" Trim saw (SKU: 22-319). The interior sample pieces were approximately 2cm-by-1cm-by-1cm (equivalent to about 25-50g) and were stored in combusted aluminum foil before powdering. The sample pieces were then powdered using a Tungsten mortar and pestle that was cleaned with Milli-Q water and ethanol prior to and between each sample. Small pieces of unanalyzed combusted clay brick were ground and disposed of between each sample; the mortar and pestle were then wiped down once more with ethanol as the last step in the cleaning protocol. Sample powders were stored in combusted and/or ethanol-rinsed glass vials wrapped in combusted aluminum foil before analysis.

Between 300 to 400 grams of the sample powders were used to determine the bulk weight percent composition from loss on ignition following the methods of Summons et al. (2013). Loss on ignition analyses were completed with a Thermolyne 30400 Furnace in the University of Colorado Institute for Arctic and Alpine Research Sedimentology Lab. The powders were placed in small ceramic crucibles and heated in the muffle furnace for 4 hours at 550°C. Once cool, the crucibles were placed in a desiccator for 30 minutes and then weighed to determine bulk weight percent organic

matter (Table S3). The crucibles were then heated for 2 hours at 950°C. Mass loss following the second heating reflected the bulk weight percent carbonate (Table S3).

Based on the bulk weight percent organic matter results from the loss on ignition analyses, between 10-20 grams of each sample powder was prepared for a Soxhlet solvent extraction in the University of Colorado Boulder Institute for Arctic and Alpine Research Organic Geochemistry Lab. Weighed sample powders were transferred to a combusted glass microfiber extraction filter before being placed within the Soxhlet apparatus. The extractions used ~300 mL of a 9:1 DCM:MeOH solvent mixture kept at ~70°C, which cycled through the filters over an ~24 hour period.

Following the extraction period, filters were removed from the apparatus to dry before residual sample powders from the extractions were weighed post-extraction. Total lipid extracts were transferred to 40 mL combusted glass vials before being placed in a TurboVap (R) LV Evaporator with an ~5 psi Nitrogen stream and an ~25°C water bath. Once almost all solvent was evaporated, the total lipid extract component was transferred to combusted 4 mL vials using a combusted glass pipet by completing a 3x rinse with <1 mL of DCM. The total lipid extract and solvent mixture went through a second evaporation procedure before being transferred to 2 mL vials through the same solvent rinse procedure. Total lipid extract and solvent mixtures were then evaporated until only the total lipid extract remained.

A ~2 g aliquot of sample powder was also acidified with hydrochloric acid (HCl) to remove all carbonate from the samples. First, powders were weighed into

combusted 50 mL glass centrifuge tubes and then treated with 5x10 mL volumes of HCl. Samples were left to sit until no bubbling persisted, then vortexed and centrifuged on Thermo Fisher Sorvall Legend XTR Centrifuge for 5 minutes at 1400 rpm. Acid was decanted off between each treatment. Once the sample powders no longer bubbled following addition of HCl and a pH test strip showed the liquid in each vial as ~3 or lower, the samples were rinsed with 5 x 10 mL Milli-Q water rinses. For the rinses, centrifuge settings were increased to 8 minutes and 1600 rpm and water was pipetted off in ~1-2 mL volume-rounds using a plastic pipette tip. Once the pH of the liquid in each vial was ~5-6 (pH of Milli-Q water), the liquid in the samples was pipetted off and the samples were placed in a drying oven at ~ 35°C until dry. Acidified sample powders were then re-weighed and each homogenized in an ethanol-rinsed mortar and pestle.

A combusted (800°C, 8 hrs) clay brick blank was subjected to the entire sample preparation and extraction protocols summarized above (except for determination of bulk composition from loss on ignition) to test if these methods introduced any additional contamination during this process. Approximately 20 grams of the brick blank was used for the solvent extraction.

S.4.1.3 Organic $\delta^{13}C$ Analyses

40-60 μg-sized aliquots of total lipid extracts (re-suspended with ~100-300 mL of DCM and then pipetted into a pre-weighed tin capsule which was re-weighed to determine the sample mass after the solvent had evaporated), approximately 2000

μg-sized aliquots of the acidified sample powders, and a suite of both organic (act1, pugel, EDTA2, L_glut) and sediment (HOS, LOS) standards were weighed out to between ~5-5,500 μg into tin capsules, folded/crushed into cubes, and then analyzed on a Flash 2000 Elemental Analyzer coupled to a Thermo Delta V continuous flow isotope ratio mass spectrometer at the CUBESSIL. All acidified carbonate and total lipid extract samples were run as analytical triplicates (i.e., from the same sample aliquot). Six tin capsule blanks (empty tin capsules) and three solvent blanks (pre-weighed tin capsules with ~25 mL of DCM added to them before being re-weighed following evaporation) were included in the run.

Total lipid extract and acidified carbonate replicates were corrected separately, but with the full standard suite (organic and sediment standards) applied to both data sets for analytical corrections (e.g., linearity or drift). Several replicate organic and sediment standard measurements yielded an analytical precision of ± 0.1‰ (1 sigma) or better when the sediment standards were excluded (for total lipid extract data corrections), and ± 0.2‰ (1 sigma) or better when the sediment standards were included (for sediment data corrections). Raw values of all analyses were corrected using in-house CUBES-SIL R data correction scripts that first evaluated and then corrected standard values for a blank effect, and then linearity and drift effects, if present. Corrected standard values were then used in a scale correction applied to all data. For the total lipid extract scale correction, act1, pugel, EDTA2, and L_glut were used; the sediment scale correction used the same standards as in the total lipid extract scale correction, with the addition of LOS and HOS.

The brick blanks showed a possible minor contribution of contaminated organic carbon in the total lipid extract sample values (the average area of the carbon peaks for brick blanks was ~30). Thus, all total lipid extract replicates were brick blank-corrected using a simple mass balance equation to calculate the blank-removed $\delta^{13}C_{org}$ of each sample, assuming the $\delta^{13}C_{org}$ of each analysis included the sample value and a consistent, minor contribution of organic carbon contaminant reflected by the brick blank:

$$areaC_{analysis} * \delta^{13}C_{analysis} = areaC_{brick\ blank} * \delta^{13}C_{brick\ blank} + areaC_{sample} * \delta^{13}C_{sample},$$

rearranged to solve for $\delta^{13}C_{sample}$:

$$\delta^{13}C_{sample} = [(areaC_{analysis} * \delta^{13}C_{analysis}) - (areaC_{brick\ blank} * \delta^{13}C_{brick\ blank})] / areaC_{sample},$$

where all $\delta^{13}C$ values reflect the scale-corrected values, $areaC_{brick\ blank}$ and $\delta^{13}C_{brick\ blank}$ values reflect averages between the three brick blank replicates, and the $areaC_{sample}$ was calculated by subtracting the areaC of each analysis from the $areaC_{brick\ blank}$ average value. Brick blank corrected total lipid extract $\delta^{13}C_{org}$ values are reported in Table S4. Because all samples were analyzed in triplicates, sample $\delta^{13}C_{org}$ uncertainties were calculated with respect to two standard errors of the mean.

S.4.1.4 Diurnal Carbon Cycling Model Parameterization

Details about the mechanics of the diurnal carbon cycling model can be found in Trower et al. (2024), with modifications required for this work described in the main text. Briefly, the model tracks changes in lake water carbonate chemistry (alkalinity, [DIC], pH, $\Omega_{calcite}$) across a diurnal cycle. This diurnal cycle is driven by a sinusoid photosynthetic forcing function; at each time step, the model calculates

changes in alkalinity and [DIC] resulting from the combination of photosynthetic forcing, gas (CO_2) exchange, and $CaCO_3$ precipitation or dissolution. We then use PHREEQC to solve for the other carbonate chemistry parameters (pH and $\Omega_{calcite}$). At each time step, the model also tracks changes in $\delta^{13}C_{DIC}$ that result from the photosynthetic forcing (i.e., increases when photosynthesis dominates during the day, decreases when heterotrophy dominates at night). From this combination of values, the model calculates an instantaneous $\delta^{13}C_{carb}$ value (calcite forming in equilibrium from lake water with the $\delta^{13}C_{DIC}$ value for that time step) and an instantaneous carbonate precipitation rate (a function of $\Omega_{calcite}$ for that time step). After the model has iterated through a full 24-hour cycle, we can then calculate a mass-weighted $\delta^{13}C_{carb}$ value of all the carbonate that has accumulated throughout that 24-hour interval. Finally, we calculate the difference between this value and the mean $\delta^{13}C_{DIC}$ value over the same 24-hour interval (with an assumed +1‰ fractionation between DIC and calcite); this difference is reported in the text as $\Delta^{13}C_{model}$.

Because it is not possible to obtain unique water chemistry information from the ~60-million-year-old Sheep Pass Basin, we compared the $\Delta^{13}C_{model}$ resulting from the initial water chemistries of three modern analog lake sites: Fayetteville Green Lake in New York (USA), the Great Salt Lake in Utah (USA), and Pavilion Lake in British Columbia (Canada). Fayetteville Green Lake is a temperate, freshwater lake with thrombolite bioherms forming along the shoreline of the lake, ~150 meters above sea level (Leapaldt et al., 2024 and references therein). The Great Salt Lake is a shallow, hypersaline lake with thrombolitic microbialites in a dry, semi-arid climate,

~1000 meters above sea level (Ingalls et al., 2020; Frantz et al., 2023). Pavilion Lake is a freshwater lake at a higher latitude than the other two lakes, with thrombolites forming along the shore and at depth, ~800 meters above sea level (Lim et al., 2009).

Initial water chemistry data was adopted from Leapaldt et al. (2024) for Fayetteville Green Lake, Ingalls et al. (2020) for the Great Salt Lake, and Lim et al. (2009) for Pavilion Lake. We also ran a model simulation where we decreased the initial alkalinity from 1.51 mmol/kg to 1.25 mmol/kg (but otherwise adopted all other Pavilion Lake initial water chemistry values) to drive larger $\Delta^{13}C_{model}$ values, as a point for comparison. This is referred to as the fourth initial water chemistry in the Methods and as "Synthetic Lake" in Table S5 and Figure 4 in the main manuscript. Note that an initial $\delta^{13}C_{DIC}$ value was not reported for Pavilion Lake; thus, we chose a $\delta^{13}C_{DIC}$ value of 0‰ for simplicity. An average $\delta^{13}C_{carb}$ value is also required to run the model because carbonate dissolution ($\Omega_{calcite} < 1$) affects carbonate from a bigger, time-averaged pool rather than just the newly formed carbonate in the model. For Pavilion Lake, we chose a $\delta^{13}C_{carb}$ of 0.8‰ based on an average between the reported $\delta^{13}C_{carb}$ for Fayetteville Green Lake (-2.4‰) and Great Salt Lake (4.0‰) (Table S5). These Pavilion Lake $\delta^{13}C_{DIC}$ and $\delta^{13}C_{carb}$ values were also adopted in the "Synthetic Lake" scenario.

PHREEQC was used for calculating carbonate chemistry in the model (https://doi.org/10.32614/CRAN.package.phreeqc). Following sensitivity tests where we investigated $\Delta^{13}C_{model}$ values across a range of productivity (κ_p = 0–800 μmol/kg), pCO_2 (200–1200 ppm), and temperature values (20–30°C), we determined that

$\Delta^{13}C_{model}$ values depended most strongly on productivity, while pCO_2 and temperature played a more minimal role (Fig. S4). Thus, subsequent model investigations (e.g., varying initial alkalinity across a range of productivity values) for each scenario were all completed at constant pCO_2 (400 ppm) and temperature (25°C) unless otherwise noted.

The $\delta^{13}C_{DIC}$– $\delta^{13}C_{org}$ photosynthetic fractionation (ε_P) used in the diurnal carbon cycling model was informed by the absolute difference between the carbonate $\delta^{13}C_{matrix}$ and the acidified carbonate $\delta^{13}C_{org}$ for Sheep Pass Formation samples (Table S4). Because the mean absolute difference between the carbonate $\delta^{13}C_{matrix}$ and the acidified carbonate $\delta^{13}C_{org}$ (28.23‰) reflects a $\delta^{13}C_{carb}$ - $\delta^{13}C_{org}$ fractionation, we subtracted 1‰ from this value to account for the fractionation between DIC and calcite, resulting in a $\delta^{13}C_{DIC}$– $\delta^{13}C_{org}$ photosynthetic fractionation of 27.23‰ for the model. We used this value in all model scenarios to avoid introducing variability in modeled $\delta^{13}C_{carb}$ offset simply due to differences in the ε_P value.

When modeling $\Delta^{13}C_{model}$ values for the "Synthetic Lake" scenario over a range of initial alkalinities (0-3 mmol/kg), we ran the model at a constant temperature of 25°C and a pCO_2 of 1000 ppm (see main text Fig. 4B). We used a pCO_2 value of 1000 ppm versus 400 ppm (the value used when modeling all scenarios in main text Fig. 4A) in order to best constrain the initial alkalinity and productivity values required for the observed range of $\Delta^{13}C_{carb}$ values that we measured from the SPF thrombolite boundstone samples. Given previous work, the most likely age of the SPF thrombolite boundstones samples in this study is Late Cretaceous to Paleocene (Druschke et al.,

2009; Olsen-Valdez et al., 2025). A value of 1000 ppm is a fair estimate of the pCO_2 for this time (The Cenozoic CO Proxy Integration Project (CenCOPIP) Consortium et al., 2023). In addition, considering our sensitivity tests highlighted that pCO_2 plays a minimal role on $\Delta^{13}C_{model}$ values, uncertainty in this estimate of pCO_2 has little impact on our interpretations.

S.4.1.5 Stratigraphic Level Corrections in the Sheep Pass Canyon

Samples from within the Sheep Pass Canyon were collected along two measured transects: the main Sheep Pass Canyon (SPC) transect and a sub-transect called the Member B Slope (SPC_Slope). Almost all thrombolite boundstone samples from within the Sheep Pass Canyon were collected from the Member B Slope, which has a stratigraphic level not corrected to composite stratigraphic level as in the Mainline transect or the main Sheep Pass Canyon transect. Because only one sample (SPB20-SPC31) came from the main Sheep Pass Canyon transect, we estimated the stratigraphic position of this sample within the Member B Slope transect so that all samples from the Sheep Pass Canyon could be plotted against a single stratigraphic level framework.

SPB20-SPC31 and all of the thrombolite boundstone samples in the Member B Slope transect come from a previously characterized microbialite-dominated interval (Member B – Interval II) within the Sheep Pass Formation type section; this interval is laterally continuous across all measured transects in the SPF type section and its upper stratigraphic limit is characterized by a transition from calcitic to dolomitic mineralogy (see Olsen-Valdez et al., 2025). Member B – Interval II is ~25.9

meters thick in the Sheep Pass Canyon transect and ~30.4 meters thick in the Member B Slope transect. Based on the known stratigraphic position of SPB20-SPC31 within Interval II of the Sheep Pass Canyon transect (18.2 meters from the base), we calculated the relative (i.e., proportionally consistent) stratigraphic position of SPB29-SPC31 within Interval II of the Member B Slope transect (X meters from the base):

$$\begin{array}{lccc} \text{Transect} & \text{Sheep Pass Canyon} & & \text{Member B Slope} \\ \dfrac{\text{meter level}}{\text{thickness}} & = \dfrac{\text{18.2 meters}}{\text{25.9 meters}} & = \dfrac{\text{X}}{\text{30.4 meters}}, & \text{X} = 21.36 \text{ meters} \end{array}$$

The relative stratigraphic level for SPB20-SPC31 was updated to 21.36 meters and all samples from the Sheep Pass Canyon were given the section label of "SPC" (where the Member B Slope samples were originally labeled "SPC_Slope").

S.4.2 Extended Results

S.4.2.1 Data Quality Control in Carbonate $\delta^{13}C$ Values

Sampling for fabric-specific $\delta^{13}C_{carb}$ measurements was complicated in SPF thrombolite samples where the clots were small (sub-millimeter), the matrix component was rare, or the clot and matrix components were interspersed at a very fine scale, as is common in thrombolitic textures (Kennard and James, 1986; Shapiro, 2000; Riding, 2011). A "mixed" component was analyzed in some samples and reflected sample powder containing both endmember matrix and clot components (Fig. S2). In most cases, $\delta^{13}C_{mixed}$ values fell between $\delta^{13}C_{clot}$ and $\delta^{13}C_{matrix}$ values in

samples where all three textural components were analyzed (e.g., SPB19-ML37 and SPB20-SPC40; Fig. S2).

Samples SPB19-ML08 and SPB19-ML38 had $\delta^{13}C_{clot}$ and $\delta^{13}C_{matrix}$ values (and for SPB19-ML38, also a $\delta^{13}C_{mixed}$ value) that were largely indistinguishable from each other (Fig. S2; Tables S6 and S8). Their textures –predominantly finely interspersed matrix and clot – indicated that drill powders originally labeled as distinct matrix and clot components in SPB19-ML08 and SPB19-ML38 were ultimately not reflective of these endmember components (Fig. S1, red labels). Thus, sample SPB19-ML08 and SPB19-ML38 were removed from the data set before calculating the mean $\delta^{13}C_{matrix}$ and $\delta^{13}C_{clot}$, and $\Delta^{13}C_{carb}$ values presented in the main manuscript (Table S7).

References:

Belan, M.A., Brady, A.L., Kim, S.-T., Lim, D.S.S., and Slater, G.F., 2019, Spatial Distribution and Preservation of Carbon Isotope Biosignatures in Freshwater Microbialite Carbonate: ACS Earth and Space Chemistry, v. 3, p. 335–343, doi:10.1021/acsearthspacechem.8b00182.

Brady, A.L., Laval, B., Lim, D.S.S., and Slater, G.F., 2014, Autotrophic and heterotrophic associated biosignatures in modern freshwater microbialites over seasonal and spatial gradients: Organic Geochemistry, v. 67, p. 8–18, doi:10.1016/j.orggeochem.2013.11.013.

Brady, A.L., Slater, G.F., Omelon, C.R., Southam, G., Druschel, G., Andersen, D.T., Hawes, I., Laval, B., and Lim, D.S.S., 2010, Photosynthetic isotope biosignatures in laminated micro-stromatolitic and non-laminated nodules associated with modern, freshwater microbialites in Pavilion Lake, B.C.: Chemical Geology, v. 274, p. 56–67, doi:10.1016/j.chemgeo.2010.03.016.

Druschke, P., Hanson, A.D., and Wells, M.L., 2009, Structural, stratigraphic, and geochronologic evidence for extension predating Palaeogene volcanism in the Sevier hinterland, east-central Nevada: International Geology Review, v. 51, p. 743–775, doi:10.1080/00206810902917941.

Ferris, F.G., Thompson, J.B., and Beveridge, T.J., 1997, Modern Freshwater Microbialites from Kelly Lake, British Columbia, Canada: PALAIOS, v. 12, p. 213, doi:10.2307/3515423.

Frantz, C.M., Gibby, C., Nilson, R., Nguyen, M., Ellsworth, C., Stern, C.J., Dolan, H., Sihapanya, A., and Baxter, B.K., 2023, Desiccation of ecosystem-critical microbialites in the shrinking Great Salt Lake, Utah (USA): Environmental Sciences preprint, doi:10.31223/X5BH2F.

French, K.L. et al., 2015, Reappraisal of hydrocarbon biomarkers in Archean rocks: Proceedings of the National Academy of Sciences, v. 112, p. 5915–5920, doi:10.1073/pnas.1419563112.

Ingalls, M., Frantz, C.M., Snell, K.E., and Trower, E.J., 2020, Carbonate facies-specific stable isotope data record climate, hydrology, and microbial communities in Great Salt Lake, UT: Geobiology, v. 18, p. 566–593, doi:10.1111/gbi.12386.

Kaźmierczak, J., Kempe, S., Kremer, B., López-García, P., Moreira, D., and Tavera, R., 2011, Hydrochemistry and microbialites of the alkaline crater lake Alchichica, Mexico: Facies, v. 57, p. 543–570, doi:10.1007/s10347-010-0255-8.

Kempe, S., and Kaźmierczak, J., 2007, Hydrochemical Key to the Genesis of Calcareous Nonlaminated and Laminated Cyanobacterial Microbialites, *in* Seckbach, J. ed., Algae and Cyanobacteria in Extreme Environments, Dordrecht, Springer Netherlands, Cellular Origin, Life in Extreme Habitats and Astrobiology, v. 11, p. 239–264, doi:10.1007/978-1-4020-6112-7_13.

Kennard, J.M., and James, N.P., 1986, Thrombolites and Stromatolites: Two Distinct Types of Microbial Structures: PALAIOS, v. 1, p. 492, doi:10.2307/3514631.

Kopf, S., Davidheiser-Kroll, B., and Kocken, I., 2021, Isoreader: An R package to read stable isotope data files for reproducible research: Journal of Open Source Software, v. 6, p. 2878, doi:10.21105/joss.02878.

Leapaldt, H.C., Frantz, C.M., Olsen-Valdez, J., Snell, K.E., Trower, E.J., and Ingalls, M., 2024, Primary to post-depositional microbial controls on the stable and clumped isotope record of shoreline sediments at Fayetteville Green Lake: Geobiology, v. 22, p. e12609, doi:10.1111/gbi.12609.

Lim, D.S.S. et al., 2009, Limnology of Pavilion Lake, B. C., Canada Characterization of a microbialite forming environment: Fundamental and Applied Limnology, v. 173, p. 329–351, doi:10.1127/1863-9135/2009/0173-0329.

Moore, L.S., and Burne, R.V., 1994, The Modern Thrombolites of Lake Clifton, Western Australia, *in* Bertrand-Sarfati, J. and Monty, C. eds., Phanerozoic Stromatolites II, Dordrecht, Springer Netherlands, p. 3–29, doi:10.1007/978-94-011-1124-9_1.

Olsen-Valdez, J., Widlansky, S., Trower, E., Snell, K., and Clyde, W., 2025, Carbonates and microbialites record a dynamic lake basin evolution in the Late Cretaceous to Eocene Sheep Pass Formation, Nevada, USA: Sedimentology, p. sed.13264, doi:10.1111/sed.13264.

Qi, H. et al., 2021, USGS44, a new high-purity calcium carbonate reference material for δ^{13} C measurements: Rapid Communications in Mass Spectrometry, v. 35, p. e9006, doi:10.1002/rcm.9006.

Riding, R., 2011, Microbialites, Stromatolites, and Thrombolites: Encyclopedia of geobiology, p. 635–654.

Shapiro, R., 2000, A Comment on the Systematic Confusion of Thrombolites: PALAIOS, v. 15, p. 166–169.

The Cenozoic CO Proxy Integration Project (CenCOPIP) Consortium et al., 2023, Toward a Cenozoic history of atmospheric CO $_2$: Science, v. 382, p. 5177, doi:10.1126/science.adi5177.

Trower, E.J., Hibner, B.M., Lincoln, T.A., Dodd, J.E., Hagen, C.J., Cantine, M.D., and Gomes, M.L., 2024, Revisiting Elevated δ^{13} C Values of Sediment on Modern Carbonate Platforms: Geophysical Research Letters, v. 51, p. e2023GL107703, doi:10.1029/2023GL107703.

Warden, J.G., Casaburi, G., Omelon, C.R., Bennett, P.C., Breecker, D.O., and Foster, J.S., 2016, Characterization of Microbial Mat Microbiomes in the Modern Thrombolite Ecosystem of Lake Clifton, Western Australia Using Shotgun Metagenomics: Frontiers in Microbiology, v. 7, doi:10.3389/fmicb.2016.01064.

White, R.A., Soles, S.A., Brady, A.L., Southam, G., Lim, D.S.S., and Slater, G.F., 2020, Biosignatures Associated with Freshwater Microbialites: Life, v. 10, p. 66, doi:10.3390/life10050066.

Chapter V: Conclusions

The goal of this dissertation was to holistically characterize the sedimentology and geochemistry of the Sheep Pass Formation type section in order to investigate the potential expression of early Paleogene climatic trends in this ancient high-elevation lake basin. Below, I briefly summarize the results, broader implications, and future directions of this research.

In Chapter 2, I combine sedimentological, stratigraphic, and mineralogical methods to describe the environmental evolution of the Sheep Pass Basin, finding that it reflects a dynamic and hydrologically sensitive setting due to its small size. I also conclude that environmental change was driven by both tectonics and climate, though particular stratigraphic intervals appear to be more associated with a climatic forcing, highlighting promising focus areas for future chemo- and chronostratigraphic studies.

In Chapter 3, I leverage this detailed sedimentological framework to develop stable carbon and oxygen, as well as carbonate clumped isotope, records throughout the Sheep Pass Formation type section. These records confirm the environmental variability observed in the sedimentological results from Chapter 2. Careful comparison to both the global marine and terrestrial records from this time, aided by a refined stratigraphic correlation based on the application of a dynamic time warping algorithm, suggests that the Sheep Pass Formation type section preserves evidence for both long-term and short-term climate change. In particular, I investigate the expression of long-term warming from the later Paleocene to early

Eocene, with the possible preservation of short-term hyperthermal climate events during this time, as well as short-term climate change associated with the K-Pg boundary in the Sheep Pass Basin. These results are the first to investigate the correlation of a comprehensive Sheep Pass Formation type section geochemical record to global climate signals throughout the latest Cretaceous and early Paleogene.

In Chapter 4, I focus on the local-scale processes preserved in the geochemical records of the Sheep Pass Formation type section. I leverage carbon isotopic compositions of textural components from the carbonate microbialites in this section. Comparing these results to both modern observations and modeled values suggests that the carbon isotopic trends in the thrombolitic fabrics of the Sheep Pass Formation type section are the result of photosynthetic carbon cycling metabolisms that were present as these carbonate minerals were precipitated. This finding reflects what is likely the first study to date to identify this isotopic biosignature in ancient microbialites. It has broad implications for the ways that microbialite archives can be leveraged in paleoenvironmental and paleobiological reconstructions and provides a strong argument for the importance of facies-specific investigations when developing geochemical paleoclimate records.

The results of this dissertation highlight that the Sheep Pass Formation preserves the expression of paleoenvironmental and paleoclimatic change over several spatial (global and local) and temporal (long-term and short-term) scales. There are several implications for this research. First, the development of a new sedimentological and geochemical framework sets the groundwork for any future

study in the Sheep Pass Formation type section. This includes desperately needed chronostratigraphic work to place the promising paleoenvironmental and paleoclimatic interpretations made in this research into a more robust age framework. For example, the Sheep Pass Formation type section, with its variety of carbonate-bearing facies, would be a great place to continue to apply *in situ* U-Pb dating of carbonate rocks.

Continental settings are variable on small spatial and temporal scales and hard to accurately capture in models; high-elevation continental ecosystems are also some of the settings most sensitive to global warming, requiring that they be well-understood in the face of anthropogenic climate change. The results of this current work suggest that the Sheep Pass Formation type section reflects a dynamic setting, sensitive to subtle shifts in basin hydrology. However, it is still unclear to what extent this was driven by its higher elevation. A careful investigation into the paleoaltimetry of the Sheep Pass Formation type section over its full depositional time frame would help constrain the expression of greenhouse climate in high altitude settings during the early Paleogene. Paleoaltimetry results would likely also add nuance to ongoing debates about the nature and timing of complex orogenic events in the western USA during this time.

Lastly, the geochemical results from this work also highlight new directions for the application of novel microscopy and isotopic methods in the Sheep Pass Formation type section carbonates, specifically the microbialites. For example, high precision dual Δ_{47}-Δ_{48} thermometry would help resolve the potential role of

disequilibrium precipitation in Sheep Pass Formation type section samples, including microbially-influenced carbonate fabrics. Further, high-resolution scanning electron microscopy and other paired techniques would aid in characterizing the micron scale textures in the Sheep Pass Formation type section thrombolites, which could provide new insights into how microbialites form and the processes that influence their fabrics over time.

References

Abels, H.A., Lauretano, V., van Yperen, A.E., Hopman, T., Zachos, J.C., Lourens, L.J., Gingerich, P.D. and Bowen, G.J. (2016) Environmental impact and magnitude of paleosol carbonate carbon isotope excursions marking five early Eocene hyperthermals in the Bighorn Basin, Wyoming. *Clim. Past*, 12, 1151–1163.

Aitken, J.D. (1967) Classification and Environmental Significance of Cryptalgal Limestones and Dolomites, with Illustrations from the Cambrian and Ordovician of Southwestern Alberta. SEPM JSR. doi: 10.1306/74D7185C-2B21-11D7-8648000102C1865D

Alonso Zarza, A.M., Calvo, J.P. and García Del Cura, M.A. (1992) Palustrine sedimentation and associated features—grainification and pseudo-microkarst—in the Middle Miocene (intermediate unit) of the Madrid Basin, Spain. *Sedimentary Geology*, 76, 43–61.

Alonso-Zarza, A.M. (2003) Palaeoenvironmental significance of palustrine carbonates and calcretes in the geological record. *Earth-Science Reviews*, 60, 261–298.

Alonso-Zarza, A.M. and Wright, V.P. (2010) Palustrine Carbonates. In: *Developments in Sedimentology - Carbonates in Continental Settings: Facies, Environments, and Processes*, *Elsevier*, 61, 103–131.

Alvarez, L.W., Alvarez, W., Asaro, F., and Michel, H.V., 1980, Extraterrestrial Cause for the Cretaceous-Tertiary Extinction: Science, v. 208, p. 1095–1108, doi:10.1126/science.208.4448.1095.

Anderson, N.T., Bonifacie, M., Jost, A.B., Siebert, J., Bontognali, T., Horita, J., Müller, I.A., Bernasconi, S.M., and Bergmann, K.D., 2024, Re-Assessing the Need for Apatite- and Dolomite-Specific Calibrations of the Carbonate Clumped Isotope Thermometer: Geochemistry, Geophysics, Geosystems, v. 25, p. e2023GC011049, doi:10.1029/2023GC011049.

Andres, M.S., Sumner, D.Y., Reid, R.P., and Swart, P.K., 2006, Isotopic fingerprints of microbial respiration in aragonite from Bahamian stromatolites: Geology, v. 34, p. 973, doi:10.1130/G22859A.1.

Arenas, C., Casanova, J. and Pardo, G. (1997) Stable-isotope characterization of the Miocene lacustrine systems of Los Monegros (Ebro Basin, Spain): palaeogeographic and palaeoclimatic implications. *Palaeogeography, Palaeoclimatology, Palaeoecology*, 128, 133–155.

Arribas, M.E., Bustillo, A. and Tsige, M. (2004) Lacustrine chalky carbonates: origin, physical properties and diagenesis (Palaeogene of the Madrid Basin, Spain). *Sedimentary Geology*, 166, 335–351.

Awramik, S.M. and Buchheim, H.P. (2015) Giant stromatolites of the Eocene Green River Formation (Colorado, USA). *Geology*, 43, 691–694.

Baczynski, A.A., McInerney, F.A., Wing, S.L., Kraus, M.J., Bloch, J.I. and Secord, R. (2017) Constraining paleohydrologic change during the Paleocene-Eocene Thermal Maximum in the continental interior of North America. *Palaeogeography, Palaeoclimatology, Palaeoecology*, 465, 237–246.

Barnet, J.S.K., Littler, K., Kroon, D., Leng, M.J., Westerhold, T., Röhl, U., and Zachos, J.C., 2018, A new high-resolution chronology for the late Maastrichtian warming event: Establishing robust temporal links with the onset of Deccan volcanism: Geology, v. 46, p. 147–150, doi:10.1130/G39771.1.

Belan, M.A., Brady, A.L., Kim, S.-T., Lim, D.S.S., and Slater, G.F., 2019, Spatial Distribution and Preservation of Carbon Isotope Biosignatures in Freshwater Microbialite Carbonate: ACS Earth and Space Chemistry, v. 3, p. 335–343, doi:10.1021/acsearthspacechem.8b00182.

Bergner, A.G.N., Strecker, M.R., Trauth, M.H., Deino, A., Gasse, F., Blisniuk, P. and Dühnforth, M. (2009) Tectonic and climatic control on evolution of rift lakes in the Central Kenya Rift, East Africa. *Quaternary Science Reviews*, 28, 2804–2816.

Bernasconi, S.M. et al., 2021, InterCarb: A Community Effort to Improve Interlaboratory Standardization of the Carbonate Clumped Isotope Thermometer Using Carbonate Standards: Geochemistry, Geophysics, Geosystems, v. 22, p. e2020GC009588, doi:10.1029/2020GC009588.

Birgenheier, L.P., Berg, M.D.V., Plink-Björklund, P., Gall, R.D., Rosencrans, E., Rosenberg, M.J., Toms, L.C. and Morris, J. (2020) Climate impact on fluvial-lake system evolution, Eocene Green River Formation, Uinta Basin, Utah, USA. *GSA Bulletin*, 132, 562–587.

Boggs, S., and Krinsley, D., 2006, Application of Cathodoluminescence Imaging to the Study of Sedimentary Rocks: Cambridge University Press, doi:10.1017/CBO9780511535475.

Bonde, J.W., Druschke, P.A., Hilton, R.P., Henrici, A.C. and Rowland, S.M. (2020) Preservation of latest Cretaceous (Maastrichtian)—Paleocene frogs (*Eorubeta nevadensis*) of the Sheep Pass Formation of east-central Nevada and implications for paleogeography of the Nevadaplano. *PeerJ*, 8, e9455.

Bouton, A. et al., 2016, Linking the distribution of microbial deposits from the Great Salt Lake(Utah, USA) to tectonic and climatic processes: Biogeosciences, v. 13, p. 5511–5526, doi:10.5194/bg-13-5511-2016.

Bowen, G.J., Beerling, D.J., Koch, P.L., Zachos, J.C. and Quattlebaum, T. (2004) A humid climate state during the Palaeocene/Eocene thermal maximum. *Nature*, 432, 495–499.

Bowen, G.J., Daniels, A.L. and Bowen, B.B. (2008) Paleoenvironmental Isotope Geochemistry and Paragenesis of Lacustrine and Palustrine Carbonates, Flagstaff Formation, Central Utah, U.S.A. *Journal of Sedimentary Research*, 78, 162–174.

Brady, A.L., Laval, B., Lim, D.S.S., and Slater, G.F., 2014, Autotrophic and heterotrophic associated biosignatures in modern freshwater microbialites over seasonal and spatial gradients: Organic Geochemistry, v. 67, p. 8–18, doi:10.1016/j.orggeochem.2013.11.013.

Brady, A.L., Slater, G.F., Omelon, C.R., Southam, G., Druschel, G., Andersen, D.T., Hawes, I., Laval, B., and Lim, D.S.S., 2010, Photosynthetic isotope biosignatures in laminated micro-stromatolitic and non-laminated nodules

associated with modern, freshwater microbialites in Pavilion Lake, B.C.: Chemical Geology, v. 274, p. 56–67, doi:10.1016/j.chemgeo.2010.03.016.

Breecker, D.O., Sharp, Z.D., and McFadden, L.D., 2009, Seasonal bias in the formation and stable isotopic composition of pedogenic carbonate in modern soils from central New Mexico, USA: Geological Society of America Bulletin, v. 121, p. 630–640, doi:10.1130/B26413.1.

Breitbart, M., Hoare, A., Nitti, A., Siefert, J., Haynes, M., Dinsdale, E., Edwards, R., Souza, V., Rohwer, F., and Hollander, D., 2009, Metagenomic and stable isotopic analyses of modern freshwater microbialites in Cuatro Ciénegas, Mexico: Environmental Microbiology, v. 11, p. 16–34, doi:10.1111/j.1462-2920.2008.01725.x.

Buchheim, H.P. and Surdam, R.C. (1977) Fossil catfish and the depositional environment of the Green River Formation, Wyoming. *Geol*, 5, 196.

Buongiorno, J., Gomez, F.J., Fike, D.A., and Kah, L.C., 2019, Mineralized microbialites as archives of environmental evolution, Laguna Negra, Catamarca Province, Argentina: Geobiology, v. 17, p. 199–222, doi:10.1111/gbi.12327.

Burke, K.D., Williams, J.W., Chandler, M.A., Haywood, A.M., Lunt, D.J., and Otto-Bliesner, B.L., 2018, Pliocene and Eocene provide best analogs for near-future climates: Proceedings of the National Academy of Sciences, v. 115, p. 13288–13293, doi:10.1073/pnas.1809600115.

Burne, R.V., and Moore, L.S., 1987, Microbialites: Organosedimentary Deposits of Benthic Microbial Communities: PALAIOS, v. 2, p. 241, doi:10.2307/3514674.

Byrne, M.P., and O'Gorman, P.A., 2015, The Response of Precipitation Minus Evapotranspiration to Climate Warming: Why the "Wet-Get-Wetter, Dry-Get-Drier" Scaling Does Not Hold over Land*: Journal of Climate, v. 28, p. 8078–8092, doi:10.1175/JCLI-D-15-0369.1.

Cantine, M.D., Knoll, A.H. and Bergmann, K.D. (2020) Carbonates before skeletons: A database approach. *Earth-Science Reviews*, 201, 103065.

Carmichael, M.J., Lunt, D.J., Huber, M., Heinemann, M., Kiehl, J., LeGrande, A., Loptson, C.A., Roberts, C.D., Sagoo, N., Shields, C., Valdes, P.J., Winguth, A., Winguth, C. and Pancost, R.D. (2016) A model–model and data–model comparison for the early Eocene hydrological cycle. *Clim. Past*, 12, 455–481.

Carroll, A.R. and Bohacs, K.M. (1999) Stratigraphic classification of ancient lakes: Balancing tectonic and climatic controls. *Geol*, 27, 99.

Casado, A.I., Alonso-Zarza, A.M. and La Iglesia, Á. (2014) Morphology and origin of dolomite in paleosols and lacustrine sequences. Examples from the Miocene of the Madrid Basin. *Sedimentary Geology*, 312, 50–62.

Caumartin, J., Benzerara, K., Havas, R., Thomazo, C., Lòpez-García, P. and Duprat, E. (2023) The chemical conditions necessary for the formation of microbialites. *Geochem. Persp. Let.*, 25, 30–35.

Chagas, A.A.P., Webb, G.E., Burne, R.V. and Southam, G. (2016) Modern lacustrine microbialites: Towards a synthesis of aqueous and carbonate geochemistry and mineralogy. *Earth-Science Reviews*, 162, 338–363.

Chen, J. and Lee, J. (2014) Current Progress on the Geological Record of Microbialites and Microbial Carbonates. *Acta Geologica Sinica (Eng)*, 88, 260–275.

Choquette, P.W. and Pray, L.C. (1970) Geologic Nomenclature and Classification of Porosity in Sedimentary Carbonates. *Bulletin*, 54, 207–250.

Clyde, W.C. and Gingerich, P.D. (1998) Mammalian community response to the latest Paleocene thermal maximum: An isotaphonomic study in the northern Bighorn Basin, Wyoming. *Geol*, 26, 1011.

Coney, P.J. and Harms, T.A. (1984) Cordilleran metamorphic core complexes: Cenozoic extensional relics of Mesozoic compression. *Geol*, 12, 550.

Daëron, M., Drysdale, R.N., Peral, M., Huyghe, D., Blamart, D., Coplen, T.B., Lartaud, F., and Zanchetta, G., 2019, Most Earth-surface calcites precipitate out of isotopic equilibrium: Nature Communications, v. 10, p. 429, doi:10.1038/s41467-019-08336-5.

Dansgaard, W., 1964, Stable isotopes in precipitation: Tellus, v. 16, p. 436–468, doi:10.1111/j.2153-3490.1964.tb00181.x.

De Deckker, P. and Last, W.M. (1989) Modern, non-marine dolomite in evaporitic playas of western Victoria, Australia. *Sedimentary Geology*, 64, 223–238.

De Deckker, P. and Last, W.M. (1988) Modern dolomite deposition in continental, saline lakes, western Victoria, Australia. *Geology*, 16, 29–32.

DeCelles, P.G. (2004) Late Jurassic to Eocene evolution of the Cordilleran thrust belt and foreland basin system, western U.S.A. *American Journal of Science*, 304, 105–168.

DeCelles, P.G. and Coogan, J.C. (2006) Regional structure and kinematic history of the Sevier fold-and-thrust belt, central Utah.

Dennis, K.J., Cochran, J.K., Landman, N.H., and Schrag, D.P., 2013, The climate of the Late Cretaceous: New insights from the application of the carbonate clumped isotope thermometer to Western Interior Seaway macrofossil: Earth and Planetary Science Letters, v. 362, p. 51–65, doi:10.1016/j.epsl.2012.11.036.

Dickinson, W.R. (2004) Evolution of the North American Cordillera. *Annu. Rev. Earth Planet. Sci.*, 32, 13–45.

Dickinson, W.R. and Gehrels, G.E. (2009) Use of U–Pb ages of detrital zircons to infer maximum depositional ages of strata: A test against a Colorado Plateau Mesozoic database. *Earth and Planetary Science Letters*, 288, 115–125.

Drummond, C.N., Wilkinson, B.H. and Lohmann, K.C. (1996) Climatic control of fluvial-lacustrine cyclicity in the Cretaceous Cordilleran Foreland Basin, western United States. *Sedimentology*, 43, 677–689.

Druschke, P., Hanson, A.D. and Wells, M.L. (2009a) Structural, stratigraphic, and geochronologic evidence for extension predating Palaeogene volcanism in the Sevier hinterland, east-central Nevada. *International Geology Review*, 51, 743–775.

Druschke, P., Hanson, A.D., Wells, M.L., Gehrels, G.E. and Stockli, D. (2011) Paleogeographic isolation of the Cretaceous to Eocene Sevier hinterland, east-central Nevada: Insights from U-Pb and (U-Th)/He detrital zircon ages of hinterland strata. *Geological Society of America Bulletin*, 123, 1141–1160.

Druschke, P., Hanson, A.D., Wells, M.L., Rasbury, T., Stockli, D.F. and Gehrels, G. (2009b) Synconvergent surface-breaking normal faults of Late Cretaceous age within the Sevier hinterland, east-central Nevada. *Geology*, 37, 447–450.

Dunagan, S.P. and Turner, C.E. (2004) Regional paleohydrologic and paleoclimatic settings of wetland/lacustrine depositional systems in the Morrison Formation (Upper Jurassic), Western Interior, USA. *Sedimentary Geology*, 167, 269–296.

Dunham, R.J. (1962) Classification of carbonate rocks according to depositional texture. *in Classification of carbonate rocks; a symposium*, 108–121.

Dupraz, C., Reid, R.P., Braissant, O., Decho, A.W., Norman, R.S. and Visscher, P.T. (2009) Processes of carbonate precipitation in modern microbial mats. *Earth-Science Reviews*, 96, 141–162.

Eiler, J.M., 2007, "Clumped-isotope" geochemistry—The study of naturally-occurring, multiply-substituted isotopologues: Earth and Planetary Science Letters, v. 262, p. 309–327, doi:10.1016/j.epsl.2007.08.020.

Eiler, J.M., 2011, Paleoclimate reconstruction using carbonate clumped isotope thermometry: Quaternary Science Reviews, v. 30, p. 3575–3588, doi:10.1016/j.quascirev.2011.09.001.

Eljalafi, A. and Sarg, J.F. (2021) Depositional system and lake-stage control on microbialite morphology, Green River Formation, eastern Uinta Basin, Colorado and Utah, U.S.A. *Journal of Sedimentary Research*, 91, 636–661.

Emry, R.J. (1990) Mammals of the Bridgerian (middle Eocene) Elderberry Canyon Local Fauna of eastern Nevada. In: *Geological Society of America Special Papers*, *Geological Society of America*, 243, 187–210.

Emry, R.J. and Korth, W.W. (1989) Rodents of the Bridgerian (Middle Eocene) Elderberry Canyon Local Fauna of Eastern Nevada. *Smithsonian Contributions to Paleobiology*, 1–14.

Eymard, I., Alvarez, M., Bilmes, A., Vasconcelos, C., and Ariztegui, D., 2020, Tracking Organomineralization Processes from Living Microbial Mats to Fossil Microbialites: Minerals, v. 10, p. 605, doi:10.3390/min10070605.

Fahraeus, L.E., Slatt, R.M. and Nowlan, G.S. (1974) Origin of Carbonate Pseudopellets. *Journal of Sedimentary Petrology*, 44, 27–29.

Feldmann, M. and Mckenzie, J.A. (1998) Stromatolite-Thrombolite associations in a modern environment, Lee Stocking island. *Bahamas Palaios*, 201–212.

Ferris, F.G., Thompson, J.B., and Beveridge, T.J., 1997, Modern Freshwater Microbialites from Kelly Lake, British Columbia, Canada: PALAIOS, v. 12, p. 213, doi:10.2307/3515423.

Fetrow, A.C., Snell, K.E., Di Fiori, R.V., Long, S.P., and Bonde, J.W., 2022, How Hot Is Too Hot? Disentangling Mid-Cretaceous Hothouse Paleoclimate From Diagenesis: Paleoceanography and Paleoclimatology, v. 37, p. e2022PA004517, doi:10.1029/2022PA004517.

Fiebig, J. et al., 2024, Carbonate clumped isotope values compromised by nitrate-derived NO2 interferent: Chemical Geology, v. 670, p. 122382, doi:10.1016/j.chemgeo.2024.122382.

Fischer, A.G. and Roberts, L.T. (1991) Cyclicity in the Green River Formation (Lacustrine Eocene) of Wyoming. *Journal of Sedimentary Petrology*, 61, 1146–1154.

Fogret, L., Sansjofre, P., and Lalonde, S.V., 2024, Geochemistry of carbonate microbialites through time and space: Insights from the microbialite collection of the Muséum National d'Histoire Naturelle (MNHN), France: Chemical Geology, v. 662, p. 122239, doi:10.1016/j.chemgeo.2024.122239.

Folk, R.L. and Land, L.S. (1975) Mg/Ca Ratio and Salinity: Two Controls over Crystallization of Dolomite. Bulletin. doi: 10.1306/83D91C0E-16C7-11D7-8645000102C1865D

Fouch, T.D. (1979) Character and paleogeographic distribution of Upper Cretaceous (?) and Paleogene nonmarine sedimentary rocks in East-central Nevada. In: Armentrout, J.M., Cole, M.R., and Terbest, H., eds., Cenozoic Paleogeography of the Western United States: Pacific Coast Paleogeographic Symposium 3: Los Angeles, Pacific Section, Society for Economic and Petroleum Mineralogists, pp. 97–111.

Fouch, T.D., Lund, K., Schmitt, J.G., Good, S.C. and Hanley, J.H. (1991) Late Cretaceous(?) and Paleogene sedimentary rocks and extensional(?) basins in the region of the Egan and Grant ranges, and White River adn Railroad valleys, Nevada: their relation to Sevier and Laramide contractional basins in the southern Rocky Mountains and Colorado Plateau. *Nevada Petroleum Society Fieldtrip Guidebook*, 15–23.

Frantz, C.M., Gibby, C., Nilson, R., Nguyen, M., Ellsworth, C., Stern, C.J., Dolan, H., Sihapanya, A. and Baxter, B.K. (2023) Desiccation of ecosystem-critical microbialites in the shrinking Great Salt Lake, Utah (USA). *Environmental Sciences*.

Frantz, C.M., Petryshyn, V.A., Marenco, P.J., Tripati, A., Berelson, W.M. and Corsetti, F.A. (2014) Dramatic local environmental change during the Early Eocene Climatic Optimum detected using high resolution chemical analyses of Green River Formation stromatolites. *Palaeogeography, Palaeoclimatology, Palaeoecology*, 405, 1–15.

French, K.L. et al., 2015, Reappraisal of hydrocarbon biomarkers in Archean rocks: Proceedings of the National Academy of Sciences, v. 112, p. 5915–5920, doi:10.1073/pnas.1419563112.

Freytet, P. (1965) Sedimentation microcyclothemique avec croutes zonaires a algues dans le calcaire de Beauce de Chauffour-Etrechy (Seine-et-Oise). *Bulletin de la Société Géologique de France*, 7, 309–313.

Freytet, P. (1973) Petrography and paleo-environment of continental carbonate deposits with particular reference to the upper cretaceous and lower eocene of languedoc (Southern France). *Sedimentary Geology*, 10, 25–60.

Freytet, P. and Plaziat, J.-C. (1982) Continental carbonate sedimentation and pedogenesis - Late Cretaceous and early Cainozoic of southern France. In: *Contributions to sedimentology*, *Stuttgart: Schweizerbart'sche Verlag*, 12, 217.

Freytet, P. and Verrecchia, E.P. (2002) Lacustrine and palustrine carbonate petrography: an overview. *Journal of Paleolimnology*, 27, 221–237.

Fricke, H.C., and Wing, S.L., 2004, Oxygen isotope and paleobotanical estimates of temperature and 18O-latitude gradients over North America during the early Eocene: American Journal of Science, v. 304, p. 612–635, doi:10.2475/ajs.304.7.612.

García, A. (1994) Charophyta: their use in paleolimnology. *Journal of Paleolimnology*, 10, 43–52.

García Del Cura, M.A., Calvo, J.P., Ordóñez, S., Jones, B.F. and Cañaveras, J.C. (2001) Petrographic and geochemical evidence for the formation of primary, bacterially induced lacustrine dolomite: La Roda 'white earth' (Pliocene, central Spain). *Sedimentology*, 48, 897–915.

Gehrels, G., Valencia, V. and Pullen, A. (2006) Detrital zircon geochronology by laser-ablation multicollector ICPMS at the Arizona LaserChron Center. *The Paleontological Society Papers*, 12, 67–76.

Gehrels, G.E., Valencia, V.A. and Ruiz, J. (2008) Enhanced precision, accuracy, efficiency, and spatial resolution of U-Pb ages by laser ablation–multicollector–inductively coupled plasma–mass spectrometry.

Geyman, E.C., and Maloof, A.C., 2019, A diurnal carbon engine explains ^{13}C-enriched carbonates without increasing the global production of oxygen: Proceedings of the National Academy of Sciences, v. 116, p. 24433–24439, doi:10.1073/pnas.1908783116.

Ghosh, P., Adkins, J., Affek, H., Balta, B., Guo, W., Schauble, E.A., Schrag, D., and Eiler, J.M., 2006, 13C–18O bonds in carbonate minerals: A new kind of paleothermometer: Geochimica et Cosmochimica Acta, v. 70, p. 1439–1456, doi:10.1016/j.gca.2005.11.014.

Gierlowski-Kordesch, E.H. (2010) Chapter 1 Lacustrine Carbonates. In: *Developments in Sedimentology*, *Elsevier*, 61, 1–101.

Gingras, M.K., Pemberton, S.G. and Smith, M. (2015) Bioturbation: Reworking Sediments for Better or Worse. *Oilfield Review*, 26, 46–58.

Gischler, E., Gibson, M.A. and Oschmann, W. (2008) Giant Holocene Freshwater Microbialites, Laguna Bacalar, Quintana Roo, Mexico. *Sedimentology*, 55, 1293–1309.

Good, S.C. (1987) Mollusc-Based Interpretations of Lacustrine Paleoenvironments of the Sheep Pass Formation (Latest Cretaceous to Eocene) of East Central Nevada. *PALAIOS*, 2, 467.

Greenwood, D.R. and Wing, S.L. (1995) Eocene continental climates and latitudinal temperature gradients. *Geol*, 23, 1044.

Guo, P., Wen, H., Li, C., He, H. and Sánchez-Román, M. (2023) Lacustrine dolomite in deep time: What really matters in early dolomite formation and accumulation? *Earth-Science Reviews*, 104575.

Guo, W., 2020, Kinetic clumped isotope fractionation in the DIC-H2O-CO2 system: Patterns, controls, and implications: Geochimica et Cosmochimica Acta, v. 268, p. 230–257, doi:10.1016/j.gca.2019.07.055.

Hagen, C.J., Hibner, B., Olsen-Valdez, J., Brumberger, H., Fontana, C.G., Gutoski, J.R., Hankins, J.C., Kashyap, S., Lincoln, T.A., Mizrahi, N., Snell, K.E., and Trower, L.J., 2025, Microbialite cathodoluminescence: A tool for investigating paleoredox conditions, alteration histories, and primary textures across time. *The Depositional Record*, 00, 1-19, doi: 10.1002/dep2.70008.

Hagen, C., Creveling, J., and Huybers, P., 2024, Align: A User-Friendly App for Numerical Stratigraphic Correlation: GSA Today, v. 34, p. 4–9, doi:10.1130/GSATG575A.1.

Hanley, J.H. (1976) Paleosynecology of nonmarine Mollusca from the Green River and Wasatch Formations (Eocene), southwestern Wyoming and northwestern Colorado. *in Scott, R.W. and West, R.R., eds., Structure and classification of paleocommunities: Stroudsburg, Dowdin, Hutchinson and Ross, Inc., 291p*, 235–261.

Harman, W.N. and Jackson, D.F. (1967) A late winter survey of the macroscopic invertebrates in Green Lake, Fayetteville, New York. *in Jackson, D.F., ed., Some aspects of meromixis: Dept. of Civil Engineering, Syracuse University, Syracuse, New York*, 188–214.

Harwood Theisen, C. and Sumner, D.Y. (2016) Thrombolite fabrics and origins: Influences of diverse microbial and metazoan processes on Cambrian thrombolite variability in the Great Basin, California and Nevada. *Sedimentology*, 63, 2217–2252.

Heller, P.L., Komar, P.D. and Pevear, D.R. (1980) Transport Processes in Ooid Genesis. *SEPM JSR*, 50, 943–952.

Henkes, G.A., Passey, B.H., Grossman, E.L., Shenton, B.J., Pérez-Huerta, A., and Yancey, T.E., 2014, Temperature limits for preservation of primary calcite clumped isotope paleotemperatures: Geochimica et Cosmochimica Acta, v. 139, p. 362–382, doi:10.1016/j.gca.2014.04.040.

Henrici, A.C., Druschke, P., Hilton, R.P. and Bonde, J.W. (2018) Redescription and phylogenetic reassessment of the enigmatic anuran *Eorubeta nevadensis* (Amphibia) based on new specimens from ?latest Cretaceous–Paleocene beds of the Sheep Pass Formation, Nevada. *Journal of Vertebrate Paleontology*, 38, e1510413.

Huang, X., Li, D., Zhang, X., Xu, Y., Sun, L., Li, M., and Shen, Y., 2022, High resolution C-isotopic data from microbialites in the aftermath of the end-Permian mass extinction in South China: Frontiers in Earth Science, v. 10, p. 914432, doi:10.3389/feart.2022.914432.

Huber, B.T., MacLeod, K.G., Watkins, D.K., and Coffin, M.F., 2018, The rise and fall of the Cretaceous Hot Greenhouse climate: Global and Planetary Change, v. 167, p. 1–23, doi:10.1016/j.gloplacha.2018.04.004.

Huntington, K.W. et al., 2009, Methods and limitations of 'clumped' CO_2 isotope (Δ_{47}) analysis by gas-source isotope ratio mass spectrometry: Journal of Mass Spectrometry, v. 44, p. 1318–1329, doi:10.1002/jms.1614.

Huntington, K.W., Wernicke, B.P., and Eiler, J.M., 2010, Influence of climate change and uplift on Colorado Plateau paleotemperatures from carbonate clumped

isotope thermometry: Tectonics, v. 29, p. 2009TC002449, doi:10.1029/2009TC002449.

Ingalls, M., Leapaldt, H.C., and Lloyd, M.K., 2024, Microbial Autotrophy Recorded by Carbonate Dual Clumped Isotope Disequilibrium: Geochemistry, Geophysics, Geosystems, v. 25, p. e2024GC011590, doi:10.1029/2024GC011590.

Ingalls, M., Fetrow, A.C., Snell, K.E., Frantz, C.M. and Trower, E.J. (2022) Lake level controls the recurrence of giant stromatolite facies. *Sedimentology*, 69, 1649–1674.

Ingalls, M., Frantz, C.M., Snell, K.E., and Trower, E.J., 2020, Carbonate facies-specific stable isotope data record climate, hydrology, and microbial communities in Great Salt Lake, UT: Geobiology, v. 18, p. 566–593, doi:10.1111/gbi.12386.

Iniesto, M., Moreira, D., Reboul, G., Deschamps, P., Benzerara, K., Bertolino, P., Saghaï, A., Tavera, R. and López-García, P. (2021) Core microbial communities of lacustrine microbialites sampled along an alkalinity gradient. *Environmental Microbiology*, 23, 51–68.

Jones, C.H., Sonder, L.J. and Unruh, J.R. (1998) Lithospheric gravitational potential energy and past orogenesis: Implications for conditions of initial Basin and Range and Laramide deformation. *Geol*, 26, 639.

Kaźmierczak, J., Kempe, S., Kremer, B., López-García, P., Moreira, D., and Tavera, R., 2011, Hydrochemistry and microbialites of the alkaline crater lake Alchichica, Mexico: Facies, v. 57, p. 543–570, doi:10.1007/s10347-010-0255-8.

Keighley, D., Flint, S., Howell, J. and Moscariello, A. (2003) Sequence Stratigraphy in Lacustrine Basins: A Model for Part of the Green River Formation (Eocene), Southwest Uinta Basin, Utah, U.S.A. *Journal of Sedimentary Research*, 73, 987–1006.

Keller, G., Mateo, P., Punekar, J., Khozyem, H., Gertsch, B., Spangenberg, J., Bitchong, A.M., and Adatte, T., 2018, Environmental changes during the Cretaceous-Paleogene mass extinction and Paleocene-Eocene Thermal Maximum: Implications for the Anthropocene: Gondwana Research, v. 56, p. 69–89, doi:10.1016/j.gr.2017.12.002.

Kellogg, H.E. (1964) Cenozoic Stratigraphy and Structure of the Southern Egan Range, Nevada. *Geol Soc America Bull*, 75, 949.

Kelson, J.R., Watford, D., Bataille, C., Huntington, K.W., Hyland, E., and Bowen, G.J., 2018, Warm Terrestrial Subtropics During the Paleocene and Eocene: Carbonate Clumped Isotope (Δ_{47}) Evidence From the Tornillo Basin, Texas (USA): Paleoceanography and Paleoclimatology, v. 33, p. 1230–1249, doi:10.1029/2018PA003391.

Kelts, K. and Hsü, K.J. (1978) Freshwater Carbonate Sedimentation. In: *Lakes: chemistry, geology, physics*, *Springer New York*, New York, NY, 295–323.

Kempe, S., and Kaźmierczak, J., 2007, Hydrochemical Key to the Genesis of Calcareous Nonlaminated and Laminated Cyanobacterial Microbialites, *in* Seckbach, J. ed., Algae and Cyanobacteria in Extreme Environments,

Dordrecht, Springer Netherlands, Cellular Origin, Life in Extreme Habitats and Astrobiology, v. 11, p. 239–264, doi:10.1007/978-1-4020-6112-7_13.
Kennard, J.M. and James, N.P. (1986) Thrombolites and Stromatolites: Two Distinct Types of Microbial Structures. *PALAIOS*, 1, 492.
Koch, P.L., Clyde, W.C., Hepple, R.P., Fogel, M.L., Wing, S.L., and Zachos, J.C., 2003, Carbon and oxygen isotope records from Paleosols spanning the Paleocene-Eocene boundary, Bighorn Basin, Wyoming, *in* Causes and consequences of globally warm climates in the early Paleogene, Geological Society of America, doi:10.1130/0-8137-2369-8.49.
Kopf, S., Davidheiser-Kroll, B., and Kocken, I., 2021, Isoreader: An R package to read stable isotope data files for reproducible research: Journal of Open Source Software, v. 6, p. 2878, doi:10.21105/joss.02878.
Kraus, M.J., McInerney, F.A., Wing, S.L., Secord, R., Baczynski, A.A. and Bloch, J.I. (2013) Paleohydrologic response to continental warming during the Paleocene–Eocene Thermal Maximum, Bighorn Basin, Wyoming. *Palaeogeography, Palaeoclimatology, Palaeoecology*, 370, 196–208.
Kraus, M.J. and Riggins, S. (2007) Transient drying during the Paleocene–Eocene Thermal Maximum (PETM): Analysis of paleosols in the bighorn basin, Wyoming. *Palaeogeography, Palaeoclimatology, Palaeoecology*, 245, 444–461.
Last, W.M. (1990) Lacustrine dolomite—an overview of modern, Holocene, and Pleistocene occurrences. *Earth-Science Reviews*, 27, 221–263.
Last, W.M. and De Deckker, P. (1990) Modern and Holocene carbonate sedimentology of two saline volcanic maar lakes, southern Australia. *Sedimentology*, 37, 967–981.
Lauretano, V., Littler, K., Polling, M., Zachos, J.C. and Lourens, L.J. (2015) Frequency, magnitude, and character of hyperthermal events at the onset of the Early Eocene Climatic Optimum. *Climate of the Past*, 11, 1313–1324.
Leapaldt, H.C., Frantz, C.M., Olsen-Valdez, J., Snell, K.E., Trower, E.J., and Ingalls, M., 2024, Primary to post-depositional microbial controls on the stable and clumped isotope record of shoreline sediments at Fayetteville Green Lake: Geobiology, v. 22, p. e12609, doi:10.1111/gbi.12609.
Leng, M.J., and Marshall, J.D., 2004, Palaeoclimate interpretation of stable isotope data from lake sediment archives: Quaternary Science Reviews, v. 23, p. 811–831, doi:10.1016/j.quascirev.2003.06.012.
Lewis, E., and Wallace, D.W.R., 1998, Basic program for CO2 system in seawater: Oak Ridge National Laboratory ORNL/CDIAC-105.
Li, J., Zhu, L., Li, M., Wang, J. and Ma, Q. (2020) Origin of modern dolomite in surface lake sediments on the central and western Tibetan Plateau. *Quaternary International*, 544, 65–75.
Lim, D.S.S. et al., 2009, Limnology of Pavilion Lake, B. C., Canada Characterization of a microbialite forming environment: Fundamental and Applied Limnology, v. 173, p. 329–351, doi:10.1127/1863-9135/2009/0173-0329.

Lloyd, M.K., Ryb, U., and Eiler, J.M., 2018, Experimental calibration of clumped isotope reordering in dolomite: Geochimica et Cosmochimica Acta, v. 242, p. 1–20, doi:10.1016/j.gca.2018.08.036.

Long, S.P. (2015) An upper-crustal fold province in the hinterland of the Sevier orogenic belt, eastern Nevada, U.S.A.: A Cordilleran Valley and Ridge in the Basin and Range. *Geosphere*, 11, 404–424.

Lyson, T.R. et al., 2019, Exceptional continental record of biotic recovery after the Cretaceous–Paleogene mass extinction: Science, v. 366, p. 977–983, doi:10.1126/science.aay2268.

Machel, H., 2000, Application of cathodoluminescence to carbonate diagenesis, *in* Cathodoluminescence in Geosciences, Springer Berlin Heidelberg, p. 271–302.

Machel, H., and Burton, E., 1991, Factors governing cathodoluminescence in calcite and dolomite, and their implications for studies of carbonate diagenesis: Geoscience Canada, v. 12, p. 139–147.

Mata, S.A. and Bottjer, D.J. (2012) Microbes and mass extinctions: paleoenvironmental distribution of microbialites during times of biotic crisis. *Geobiology*, 10, 3–24.

Mather, C.C., Skrzypek, G., Dogramaci, S. and Grierson, P.F. (2018) Paleoenvironmental and paleohydrochemical conditions of dolomite formation within a saline wetland in arid northwest Australia. *Quaternary Science Reviews*, 185, 172–188.

McConnaughey, T.A., Burdett, J., Whelan, J.F., and Paull, C.K., 1997, Carbon isotopes in biological carbonates: Respiration and photosynthesis: Geochimica et Cosmochimica Acta, v. 61, p. 611–622, doi:10.1016/S0016-7037(96)00361-4.

McCormack, J., Baldermann, A., Bontognali, T.R.R., Wolf, A. and Kwiecien, O. (2024) Hydrochemical mixing-zones trigger dolomite formation in an alkaline lake. *Sedimentology*, 71, 871–886.

Mees, F., Casteneda, C., Herrero, J. and Van Ranst, E. (2012) The Nature and Significance of Variations In Gypsum Crystal Morphology In Dry Lake Basins. *Journal of Sedimentary Research*, 82, 37–52.

Mei, M., Latif, K., Mei, C., Gao, J. and Meng, Q. (2020) Thrombolitic clots dominated by filamentous cyanobacteria and crusts of radio-fibrous calcite in the Furongian Changshan Formation, North China. *Sedimentary Geology*, 395, 105540.

Meister, P., Reyes, C., Beaumont, W., Rincon, M., Collins, L., Berelson, W., Stott, L., Corsetti, F. and Nealson, K.H. (2011) Calcium and magnesium-limited dolomite precipitation at Deep Springs Lake, California. *Sedimentology*, 58, 1810–1830.

Merz, M.U.E., 1992, The biology of carbonate precipitation by cyanobacteria: Facies, v. 26, p. 81–101, doi:10.1007/BF02539795.

Mildrexler, D.J., Zhao, M., and Running, S.W., 2011, Satellite Finds Highest Land Skin Temperatures on Earth: Bulletin of the American Meteorological Society, v. 92, p. 855–860, doi:10.1175/2011BAMS3067.1.

Moore, L.S., and Burne, R.V., 1994, The Modern Thrombolites of Lake Clifton, Western Australia, *in* Bertrand-Sarfati, J. and Monty, C. eds., Phanerozoic Stromatolites II, Dordrecht, Springer Netherlands, p. 3–29, doi:10.1007/978-94-011-1124-9_1.

Nickel, E. (1983) Environmental Significance of Freshwater Oncoids, Eocene Guarga Formation, Southern Pyrenees, Spain. In: *Coated Grains* (Ed Peryt, T.M.), Springer, Berling Heidelberg, pp. 308-329.

Olsen-Valdez, J., Widlansky, S., Trower, E., Snell, K., and Clyde, W., 2025, Carbonates and microbialites record a dynamic lake basin evolution in the Late Cretaceous to Eocene Sheep Pass Formation, Nevada, USA: Sedimentology, p. sed.13264, doi:10.1111/sed.13264.

Pagel, M., Barbin, V., Blanc, P., and Ohnenstetter, D. (Eds.), 2000, Cathodoluminescence in Geosciences: Berlin, Heidelberg, Springer Berlin Heidelberg, doi:10.1007/978-3-662-04086-7.

Pagani, M., Huber, M. and Sageman, B. (2014) Greenhouse Climates. In: *Treatise on Geochemistry*, *Elsevier*, 281–304.

Palacios-Festa, M.R., Cohen, A.S. and Anadón, P. (1994) Use of ostracodes as paleoenvironmental tools in the interpretation of ancient lacustrine records. *Revista española de paleontología*, 9, 145–161.

Parkhurst, D.L., and Appelo, C.A., 2013, Description of input and examples for PHREEQC version 3—a computer program for speciation, batch-reaction, one-dimensional transport, and inverse geochemical calculations: US Geological Survey Techniques and Methods 6-A43, 497 p., https://pubs.usgs.gov/tm/06/a43/.

Pentecost, A. (1978) Blue-Green Algae and Freshwater Carbonate Deposits. *Proceedings of the Royal Society of London. B.*, 200, 43–61.

Petersen, S.V., Dutton, A., and Lohmann, K.C., 2016, End-Cretaceous extinction in Antarctica linked to both Deccan volcanism and meteorite impact via climate change: Nature Communications, v. 7, p. 12079, doi:10.1038/ncomms12079.

Pepin, N., Bradley, R.S., Diaz, H.F., Baraer, M., Caceres, E.B., Forsythe, N., Fowler, H., Greenwood, G., Hashmi, M.Z., Liu, X.D., Miller, J.R., Ning, L., Ohmura, A., Palazzi, E., Rangwala, I., Schöner, W., Severskiy, I., Shahgedanova, M., Wang, M.B., Williamson, S.N. and Yang, D.Q. (2015) Elevation dependent warming in mountain regions of the world. *Nature Climate Change 5*, 424–430.

Platt, N.H. (1989) Lacustrine carbonates and pedogenesis: sedimentology and origin of palustrine deposits from the Early Cretaceous Rupelo Formation, W Cameros Basin, N Spain. *Sedimentology*, 36, 665–684.

Platt, N.H. and Wright, V.P. (1991) Lacustrine Carbonates: Facies Models, Facies Distributions and Hydrocarbon Aspects. In: *Lacustrine Facies Analysis*, 1st edn. (Ed. P. Anadón, Li. Cabrera, and K. Kelts), *Wiley*, 57–74.

Platt, N.H. and Wright, V.P. (2023) Flooding of a carbonate platform: The Sian Ka'an Wetlands, Yucatán, Mexico—A model for the formation and evolution of palustrine carbonate factories around the modern Caribbean Sea and in the depositional record. *The Depositional Record*, 9, 99–151.

Pommer, M., Sarg, J.F. and McFarlin, F. (2023) Environmental and microbial influence on chemistry and dolomite formation in an ancient lake, Green River Formation (Eocene), Uinta basin, Utah, U.S.A. *Journal of Sedimentary Research*, 93, 213–242.

Preuß, A., Schauder, R., Fuchs, G., and Stichler, W., 1989, Carbon Isotope Fractionation by Autotrophic Bacteria with Three Different C0 $_2$ Fixation Pathways: Zeitschrift für Naturforschung C, v. 44, p. 397–402, doi:10.1515/znc-1989-5-610.

Pruss, S.B. and Knoll, A.H. (2017) Environmental covariation of metazoans and microbialites in the Lower Ordovician Boat Harhour Formation, Newfoundland. *Paleogeography, Paleoclimatology, Paleoecology*, 489, 917–929.

Qi, H. et al., 2021, USGS44, a new high-purity calcium carbonate reference material for δ^{13} C measurements: Rapid Communications in Mass Spectrometry, v. 35, p. e9006, doi:10.1002/rcm.9006.

Quade, J., Eiler, J., Daëron, M., and Achyuthan, H., 2013, The clumped isotope geothermometer in soil and paleosol carbonate: Geochimica et Cosmochimica Acta, v. 105, p. 92–107, doi:10.1016/j.gca.2012.11.031.

Rangwala, I., Sinsky, E. and Miller, J.R. (2013) Amplified warming projections for high altitude regions of the northern hemisphere mid-latitudes from CMIP5 models. *Environ. Res. Lett.*, 8, 024040.

Renne, P.R., Sprain, C.J., Richards, M.A., Self, S., Vanderkluysen, L., and Pande, K., 2015, State shift in Deccan volcanism at the Cretaceous-Paleogene boundary, possibly induced by impact: Science, v. 350, p. 76–78, doi:10.1126/science.aac7549.

Richards, M.A., Alvarez, W., Self, S., Karlstrom, L., Renne, P.R., Manga, M., Sprain, C.J., Smit, J., Vanderkluysen, L., and Gibson, S.A., 2015, Triggering of the largest Deccan eruptions by the Chicxulub impact: Geological Society of America Bulletin, v. 127, p. 1507–1520, doi:10.1130/B31167.1.

Riding, R. (2011) Microbialites, Stromatolites, and Thrombolites. *Encyclopedia of geobiology*, 635–654.

Riding, R. (2006) Microbial carbonate abundance compared with fluctuations in metazoan diversity over geological time. *Sedimentary Geology*, 185, 229–238.

Rodriguez-Aranda, J.P. and Calvo, J.P. (1998) Trace fossils and rhizoliths as a tool for sedimentological and paleoenvironmental analysis of ancient continental evaporite successions. *Palaeogeography, Palaeoclimatology, Palaeoecology*, 140, 383–399.

Roehler, H.W. (1993) Eocene climates, depositional environments, and geography, greater Green River basin, Wyoming, Utah, and Colorado. *US Geological Survey Professional Paper 1506-F*, 74 pp.

Rosen, M.R., Miser, D.E., Starcher, M.A. and Warren, J.K. (1989) Formation of dolomite in the Coorong region, South Australia. *Geochimica et Cosmochimica Acta*, 53, 661–669.

Rosenbaum, J., and Sheppard, S.M.F., 1986, An isotopic study of siderites, dolomites and ankerites at high temperatures: Geochimica et Cosmochimica Acta, v. 50, p. 1147–1150, doi:10.1016/0016-7037(86)90396-0.

Sarg, J.F., Suriamin, N., TÌnavsuu-Milkeviciene, K. and Humphrey, J.D. (2013) Lithofacies, stable isotopic composition, and stratigraphic evolution of microbial and associated carbonates, Green River Formation (Eocene), Piceance Basin, Colorado. *Bulletin*, 97, 1937–1966.

Schauble, E.A., Ghosh, P., and Eiler, J.M., 2006, Preferential formation of 13C–18O bonds in carbonate minerals, estimated using first-principles lattice dynamics: Geochimica et Cosmochimica Acta, v. 70, p. 2510–2529, doi:10.1016/j.gca.2006.02.011.

Schieber, J. (2007) Benthic microbial mats as an oil shale component: Green River Formation (Eocene) of Wyoming and Utah. In: Atlas of microbial mat features preserved within the clastic rock record, Schieber, J., Bose, P.K., Eriksson, P.G., Banerjee, S., Sarkar, S. Altermann, W., and Catuneau, O., (Eds.), pp. 225–232. Elsevier, Amserdam, the Netherlands.

Scotese, C.R., Vérard, C., Burgener, L., Elling, R.P., and Kocsis, A.T., 2025, The Cretaceous world: plate tectonics, palaeogeography and palaeoclimate: Geological Society, London, Special Publications, v. 544, p. SP544-2024–28, doi:10.1144/SP544-2024-28.

Seard, C., Camoin, G., Rouchy, J.-M. and Virgone, A. (2013) Composition, structure and evolution of a lacustrine carbonate margin dominated by microbialites: Case study from the Green River formation (Eocene; Wyoming, USA). *Palaeogeography, Palaeoclimatology, Palaeoecology*, 381–382, 128–144.

Shapiro, R. (2000) A Comment on the Systematic Confusion of Thrombolites. *PALAIOS*, 15, 166–169.

Shinn, E.A. (1983) Birdseyes, Fenestrae, Shrinkage Pores, and Loferites: A Reevaluation. *SEPM JSR*, 53, 619–628.

Smith, M.E. and Carroll, A.R. (eds) (2015) Stratigraphy and Paleolimnology of the Green River Formation, Western USA. *Springer Netherlands*, Dordrecht.

Smith, M.E., Carroll, A.R. and Singer, B.S. (2008) Synoptic reconstruction of a major ancient lake system: Eocene Green River Formation, western United States. *Geological Society of America Bulletin*, 120, 54–84.

Snell, K.E. (2011) Paleoclimate and Paleoelevation of the western Cordillera in the United States. *University of California Santa Cruz*, PhD Thesis.

Snell, K.E., Koch, P.L., Druschke, P., Foreman, B.Z. and Eiler, J.M. (2014) High elevation of the 'Nevadaplano' during the Late Cretaceous. *Earth and Planetary Science Letters*, 386, 52–63.

Snell, K.E., Thrasher, B.L., Eiler, J.M., Koch, P.L., Sloan, L.C. and Tabor, N.J. (2013) Hot summers in the Bighorn Basin during the early Paleogene. *Geology*, 41, 55–58.

Sprain, C.J., Renne, P.R., Vanderkluysen, L., Pande, K., Self, S., and Mittal, T., 2019, The eruptive tempo of Deccan volcanism in relation to the Cretaceous-Paleogene boundary: Science, v. 363, p. 866–870, doi:10.1126/science.aav1446.

Sumner, D.Y., 2001, Microbial Influences on Local Carbon Isotopic Ratios and Their Preservation in Carbonate: Astrobiology, v. 1, p. 57–70, doi:10.1089/153110701750137431.

Sundell, K.E., Gehrels, G.E. and Pecha, M.E. (2021) Rapid U-Pb Geochronology by Laser Ablation Multi-Collector ICP-MS. *Geostandard Geoanalytic Res*, 45, 37–57.

Surdam, R.C. and Stanley, K.O. (1979) Lacustrine sedimentation during the culminating phase of Eocene Lake Gosiute, Wyoming (Green River Formation). *Geol Soc America Bull*, 90, 93.

Swain, F.M. (1987) Late Cretaceous? and Paleogene freshwater ostracoda from central and eastern Nevada. *Review Espanola de Micropaleontologia*, 181–227.

Talbot, M.R., 1990, A review of the palaeohydrological interpretation of carbon and oxygen isotopic ratios in primary lacustrine carbonates: Chemical Geology: Isotope Geoscience section, v. 80, p. 261–279, doi:10.1016/0168-9622(90)90009-2.

Tänavsuu-Milkeviciene, K. and Sarg, J.F. (2012) Evolution of an organic-rich lake basin – stratigraphy, climate and tectonics: Piceance Creek basin, Eocene Green River Formation. *Sedimentology*, 59, 1735–1768.

Tänavsuu-Milkeviciene, K., Sarg, J.F. and Bartov, Y. (2017) Depositional Cycles and Sequences In An Organic-Rich Lake Basin: Eocene Green River Formation, Lake Uinta, Colorado and Utah, U.S.A. *Journal of Sedimentary Research*, 87, 210–229.

The Cenozoic CO Proxy Integration Project (CenCOPIP) Consortium*†, Hönisch, B., Royer, D.L., Breecker, D.O., Polissar, P.J., Bowen, G.J., Henehan, M.J., Cui, Y., Steinthorsdottir, M., McElwain, J.C., Kohn, M.J., Pearson, A., Phelps, S.R., Uno, K.T., Ridgwell, A., Anagnostou, E., Austermann, J., Badger, M.P.S., Barclay, R.S., Bijl, P.K., Chalk, T.B., Scotese, C.R., De La Vega, E., DeConto, R.M., Dyez, K.A., Ferrini, V., Franks, P.J., Giulivi, C.F., Gutjahr, M., Harper, D.T., Haynes, L.L., Huber, M., Snell, K.E., Keisling, B.A., Konrad, W., Lowenstein, T.K., Malinverno, A., Guillermic, M., Mejía, L.M., Milligan, J.N., Morton, J.J., Nordt, L., Whiteford, R., Roth-Nebelsick, A., Rugenstein, J.K.C., Schaller, M.F., Sheldon, N.D., Sosdian, S., Wilkes, E.B., Witkowski, C.R., Zhang, Y.G., Anderson, L., Beerling, D.J., Bolton, C., Cerling, T.E., Cotton, J.M., Da, J., Ekart, D.D., Foster, G.L., Greenwood, D.R., Hyland, E.G., Jagniecki, E.A., Jasper, J.P., Kowalczyk, J.B., Kunzmann, L., Kürschner, W.M., Lawrence, C.E., Lear, C.H., Martínez-Botí, M.A., Maxbauer, D.P., Montagna, P., Naafs, B.D.A., Rae, J.W.B., Raitzsch, M., Retallack, G.J., Ring, S.J., Seki, O., Sepúlveda, J., Sinha, A., Tesfamichael, T.F., Tripati, A., Van Der Burgh, J., Yu, J., Zachos, J.C. and Zhang, L. (2023) Toward a Cenozoic history of atmospheric CO_2. *Science*, 382, 5177.

Thompson, J.B. and Ferris, F.G. (1990) Cyanobacterial precipitation of gypsum, calcite, and magnesite from natural alkaline lake water. *Geology*, 18, 995.

Thrasher, B.L., and Sloan, L.C., 2009, Carbon dioxide and the early Eocene climate of western North America: Geology, v. 37, p. 807–810, doi:10.1130/G30090A.1.

Tobin, T.S., Wilson, G.P., Eiler, J.M., and Hartman, J.H., 2014, Environmental change across a terrestrial Cretaceous-Paleogene boundary section in eastern Montana, USA, constrained by carbonate clumped isotope paleothermometry: Geology, v. 42, p. 351–354, doi:10.1130/G35262.1.

Trower, E.J., Hibner, B.M., Lincoln, T.A., Dodd, J.E., Hagen, C.J., Cantine, M.D., and Gomes, M.L., 2024, Revisiting Elevated δ ^{13} C Values of Sediment on Modern Carbonate Platforms: Geophysical Research Letters, v. 51, p. e2023GL107703, doi:10.1029/2023GL107703.

Urey, H., 1947, The Thermodynamic Properties of Isotopic Substances: Journal of the Chemical Society (Resumed), p. 562–581.

Van Der Meulen, B., Gingerich, P.D., Lourens, L.J., Meijer, N., Van Broekhuizen, S., Van Ginneken, S. and Abels, H.A. (2020) Carbon isotope and mammal recovery from extreme greenhouse warming at the Paleocene–Eocene boundary in astronomically-calibrated fluvial strata, Bighorn Basin, Wyoming, USA. *Earth and Planetary Science Letters*, 534, 116044.

Vandervoort, D.S. and Schmitt, J.G. (1990) Cretaceous to early Tertiary paleogeography in the hinterland of the Sevier thrust belt, east-central Nevada. *Geol*, 18, 567.

Vellekoop, J., Esmeray-Senlet, S., Miller, K.G., Browning, J.V., Sluijs, A., Van De Schootbrugge, B., Sinninghe Damsté, J.S., and Brinkhuis, H., 2016, Evidence for Cretaceous-Paleogene boundary bolide "impact winter" conditions from New Jersey, USA: Geology, v. 44, p. 619–622, doi:10.1130/G37961.1.

Vellekoop, J., Sluijs, A., Smit, J., Schouten, S., Weijers, J.W.H., Sinninghe Damsté, J.S., and Brinkhuis, H., 2014, Rapid short-term cooling following the Chicxulub impact at the Cretaceous–Paleogene boundary: Proceedings of the National Academy of Sciences, v. 111, p. 7537–7541, doi:10.1073/pnas.1319253111.

Wanas, H.A. and Sallam, E. (2016) Abiotically-formed, primary dolomite in the mid-Eocene lacustrine succession at Gebel El-Goza El-Hamra, NE Egypt: An approach to the role of smectitic clays. *Sedimentary Geology*, 343, 132–140.

Warden, J.G., Casaburi, G., Omelon, C.R., Bennett, P.C., Breecker, D.O., and Foster, J.S., 2016, Characterization of Microbial Mat Microbiomes in the Modern Thrombolite Ecosystem of Lake Clifton, Western Australia Using Shotgun Metagenomics: Frontiers in Microbiology, v. 7, doi:10.3389/fmicb.2016.01064.

Warren, J.K. (1990) Sedimentology and Mineralogy of Dolomitic Coorong Lakes, South Australia. SEPM JSR. doi: 10.1306/212F929B-2B24-11D7-8648000102C1865D

Westerhold, T., Marwan, N., Drury, A.J., Liebrand, D., Agnini, C., Anagnostou, E., Barnet, J.S.K., Bohaty, S.M., De Vleeschouwer, D., Florindo, F., Frederichs, T., Hodell, D.A., Holbourn, A.E., Kroon, D., Lauretano, V., Littler, K., Lourens, L.J., Lyle, M., Pälike, H., Röhl, U., Tian, J., Wilkens, R.H., Wilson, P.A. and Zachos, J.C. (2020) An astronomically dated record of Earth's climate and its predictability over the last 66 million years. *Science*, 369, 1383–1387.

White, R.A., Soles, S.A., Brady, A.L., Southam, G., Lim, D.S.S., and Slater, G.F., 2020, Biosignatures Associated with Freshwater Microbialites: Life, v. 10, p. 66, doi:10.3390/life10050066.

Widlansky, S.J., Secord, R., Snell, K.E., Chew, A.E. and Clyde, W.C. (2022) Terrestrial carbon isotope stratigraphy and mammal turnover during post-PETM hyperthermals in the Bighorn Basin, Wyoming, USA. *Clim. Past*, 18, 681–712.

Wilf, P., Johnson, K.R., and Huber, B.T., 2003, Correlated terrestrial and marine evidence for global climate changes before mass extinction at the Cretaceous–Paleogene boundary: Proceedings of the National Academy of Sciences, v. 100, p. 599–604, doi:10.1073/pnas.0234701100.

Wilf, P. (2000) Late Paleocene–early Eocene climate changes in southwestern Wyoming: Paleobotanical analysis. *Geological Society of America Bulletin*, 112, 292–307.

Winfrey, W.M. (1960) Stratigraphy, Correlation, and Oil Potential of the Sheep Pass Formation, East-Central Nevada. 126–133.

Wing, S.L., Harrington, G.J., Smith, F.A., Bloch, J.I., Boyer, D.M. and Freeman, K.H. (2005) Transient Floral Change and Rapid Global Warming at the Paleocene-Eocene Boundary. *Science*, 310, 993–996.

Wolfbauer, C.A. and Surdam, R.C. (1974) Origin of Nonmarine Dolomite in Eocene Lake Gosiute, Green River Basin, Wyoming. *Geol Soc America Bull*, 85, 1733.

Woolway, R.I., Kraemer, B.M., Lenters, J.D., Merchant, C.J., O'Reilly, C.M. and Sharma, S. (2020) Global lake responses to climate change. *Nat Rev Earth Environ*, 1, 388–403.

Wright, D.T. and Wacey, D. (2004) Sedimentary dolomite: a reality check. *SP*, 235, 65–74.

Wright, V.P. (1986) The role of fungal biomineralization in the formation of Early Carboniferous soil fabrics. *Sedimentology*, 33, 831–838.

Wright, V.P. and Platt, N.H. (1995) Seasonal wetland carbonate sequences and dynamic catenas: a re-appraisal of palustrine limestones. *Sedimentary Geology*, 99, 65–71.

Wrona, F.J., Prowse, T.D., Reist, J.D., Hobbie, J.E., Lévesque, L.M.J. and Vincent, W.F. (2006) Climate Change Effects on Aquatic Biota, Ecosystem Structure and Function. *AMBIO: A Journal of the Human Environment*, 35, 359–369.

Zachos, J., Pagani, M., Sloan, L., Thomas, E. and Billups, K. (2001) Trends, Rhythms, and Aberrations in Global Climate 65 Ma to Present. *Science*, 292, 686–693.

Zachos, J.C., Dickens, G.R. and Zeebe, R.E. (2008) An early Cenozoic perspective on greenhouse warming and carbon-cycle dynamics. *Nature*, 451, 279–283.

Zeebe, R.E., and Wolf-Gladrow, D., 2001, CO2 in Seawater: Equilibrium, Kinetics, Isotopes: Elsevier, Elsevier Oceanography Series 65.